Electronic and Plasmonic Properties of Real and Artificial Dirac Materials

Claire Woollacott
School of Physics
University of Exeter

A thesis submitted for the degree of
Doctor of Philosophy in Physics
June 2015

Electronic and Plasmonic Properties of Real and Artificial Dirac Materials

Submitted by Claire Woollacott to the University of Exeter as a thesis for the degree of
Doctor of Philosophy in Physics.
June 2015

I certify that all material in this thesis which is not my own work has been identified and that no material has previously submitted and approved for the award of a degree by this or any other university.

Signed: ....
Miss Claire Woollacott

Date: ....

Inspired by graphene, I investigate the properties of several different real and artifical Dirac materials. Firstly, I consider a two-dimensional honeycomb lattice of metallic nanoparticles, each supporting localised surface plasmons, and study the quantum properties of the collective plasmons resulting from the near field dipolar interaction between the nanoparticles. I analytically investigate the dispersion, the effective Hamiltonian and the eigenstates of the collective plasmons for an arbitrary orientation of the individual dipole moments. When the polarisation points close to normal to the plane the spectrum presents Dirac cones, similar to those present in the electronic band structure of graphene. I derive the effective Dirac Hamiltonian for the collective plasmons and show that the corresponding spinor eigenstates represent chiral Dirac-like massless bosonic excitations that present similar effects to those of electrons in graphene, such as a non-trivial Berry phase and the absence of backscattering from smooth inhomogeneities. I further discuss how one can manipulate the Dirac points in the Brillouin zone and open a gap in the collective plasmon dispersion by modifying the polarisation of the localized surface plasmons, paving the way for a fully tunable plasmonic analogue of graphene. I present a phase diagram of gapless and gapped phases in the collective plasmon dispersion depending on the dipole orientation.

When the inversion symmetry of the honeycomb structure is broken, the collective plasmons become gapped chiral Dirac modes with an energy-dependent Berry phase. I show that this concept can be generalised to describe many real and artificial graphene-like systems, labelling them Dirac materials with a linear gapped spectrum. I also show that biased bilayer graphene is another Dirac material with an energy dependent Berry phase, but with a parabolic gapped spectrum. I analyse the relativistic phenomenon of Klein Tunnelling in both types of system.

The Klein paradox is one of the most counterintuitive results from quantum electrodynamics but it has been seen experimentally to occur in both monolayer and bilayer graphene, due to the chiral nature of the Dirac quasiparticles in these materials. The non-trivial Berry phase of π in monolayer graphene leads to remarkable effects in transmission through potential barriers, whereas there is always zero transmission at normal incidence in unbiased bilayer graphene in the *npn* regime. These, and many other 2D materials have attracted attention due to their possible usefulness for the next generation of nano-electronic devices, but some of their Klein tunnelling results may be a hinderence to this application. I will highlight how breaking the inversion symmetry of the system allows for results that are not possible in these system's inversion symmetrical counterparts.

Acknowledgements

Firstly, I would like to give many thanks to Professor Bill Barnes, who not only has been an invaluable source of knowledge, but also for the support a guidance on many issues even those not related to physics. You are a very busy man, but I always felt that you would make time for me, and for that I will be eternally grateful.

Next, I would like to thank Bill's PhD student, Alastair Humphrey, whose insights have been indispensable.

For the majority of my PhD a source of great wisdom has sat behind me, and by that I mean Alex Pearce. Alex, thank you so much for smiling all those times that I've stopped you halfway through a calculation, or when you are trying to think something through, to discuss my problems with me. I have felt very lucky to have you right behind me! Even more that that, thank you for all the barbecues and games nights!

Furthermore, I would like to mention the other PhD students in my office, Tom Sturges, Charles Downing, Lachlan Marnham. Thank you guys for all the laughs as well as the many scientific discussions.

David Ernsting has been my rock throughout this research. Thank you for being understanding when I work late, and encouraging me to do my best. You have also been exceptionally helpful, in just being there when I needed someone to talk through what I'm thinking, and ensuring my understanding makes sense, as well as celebrating with me when things go right and consoling me when things don't quite work out. You are a crucial part of my life. Oh, and thank you for your wonderful proof reading skills.

Lastly I would like to say how very grateful I am to my supervisor Dr Eros Mariani, who, though he would say he is "throwing me in cold water" and wants me to "fight" on my own for the answers, has given me so much guidance when I have needed it. These past few years he has been very patient, and it has been a real pleasure to work with him, so thank you Eros.

Contents

Awards

2014	-	**Most Innovative Poster Award**, University of Exeter Postgraduate Research, Showcase, Exeter, UK - Comprising of a £250 cash prize, For innovatively presenting complex science to lay people
2013	-	**Cavendish Medal (Gold Medal for Physics)**, SET for Britain Awards, House of Commons, UK Parliament - Comprising of a medal and a £3000 cash prize, for presenting my research to experts and lay people including members of parliament with the aim to increase knowledge of current scientific research in the UK
2012	-	**First Prize Poster Award**, IOP CMD-24 (ECOSS-29, ECSCD-11, and CMMP-12) International Conference, Edinburgh, UK - Comprising of a £100 cash prize
2012	-	**First Prize Poster Award**, IOP/EPSRC Graduate Summer School in Condensed Matter Physics - *Physics by the Lake*, Lake District, UK
2011	-	**College Commendation Award**, University of Exeter, UK - For excellent achievements and contributions to the Physics Department

Publications

- Guillaume Weick, **Claire Woollacott**, William Barnes, Ortwin Hess, and Eros Mariani, *Dirac-like Plasmons in Honeycomb Lattices of Metallic Nanoparticles*, Phys. Rev. Lett. **110**, 106801 (2013)

- Thomas Jebb Sturges, **Claire Woollacott**, Guillaume Weick, and Eros Mariani, *Dirac Plasmons in Bipartite Lattices of Metallic Nanoparticles*, IOP 2D Materials, **2**, 014008 (2015)

- **Claire Woollacott**, Alexander Cope, and Eros Mariani, *Klein Tunnelling of Dirac Particles in Systems with Broken Inversion Symmetry*, in preparation, 2015

Grants

- **Sponsored by the BBC** to attend the "Science in the Media" Communications Course at Cumberland Lodge and The BBC Broadcasting House, London
- **IOP Research Student Conference Fund Grant** (from the Thin Films and Surfaces Group) to attend the 2014 APS March Meeting, Denver, Colorado, 02-07/03/14
- **Onassis Foundation Support for Travel, Accommodation and Sustenance** to attend The 2013 Onassis Lectures: Nanoscience and Nanotechnology, Heraklion, Crete, 15-19/07/13
- **Sponsored by ImagineNano Organisers** for travel to attend ImagineNano 2013, Bilbao, Spain, 23-26/04/13
- **Sponsored by the EPSRC** for accommodation and sustenance to attend IOP/EPSRC Graduate Summer School in Condensed Matter Physics - *Physics by the Lake*, Lake District, 22/07/12-03/08/12.
- **EPSRC Summer Vacation Bursary**, for salary and expenses on a research Internship, 2010
- **Nuffield Foundation Bursary**, for salary and expenses on a research Internship, 2010

Outreach Activities

March 2015 - **Manning both the IOP and SPIE stands at The Big Bang Fair**
Nov 2014 - **Organising the Exeter IOP Festival of Physics Event**, Exeter University
June and Sept 2014 - **IOP South West Branch Schools Lecture Tour, "Magic Materials and The Science of Invisibility"** - Preparing and presenting lectures to children and the public in schools across the South West of England
June 2014 - Present - **IOP Theoretical Condensed Matter Committee Member**
March 2014 - Present - **IOP South West Branch Committee Member**
June 2013 - **Guest Speaker at Pilton Community College Presentation Evening**, Barnstaple
March 2013 and 2014 - **IOP SET for Britain Presentations**, UK Parliament

Invited Talks

04/07/14 - “Dirac-like Plasmons in Honeycomb Arrays of Metallic Nanoparticles”,
Cold Atoms and Magnetism Conference 2014, Birmingham UK

Presentations at Conferences

06-09/04/14 - “Systems with an Energy Dependent Berry Phase and its Consequences
on Klein Tunnelling” Exeter Graphene Conference, Exeter University

28-30/03/14 - “The Power of The Honeycomb”,
Exeter University Postgraduate Research Showcase, Exeter, UK

02-07/03/14 - “Dirac-like Plasmons in Honeycomb Lattices of Metallic Nanoparticles,
Z50.00002”, APS March Meeting 2014, Denver, Colorado, USA

23/03/13-16/04/13 - “Graphene Physics in Plasmonic Metamaterials”
ImagineNano 2013, Bilbao, Spain

11/03/13 - “Honeycomb Arrays of Metallic Nanoparticles supporting Dirac-like
Plasmons”, SET for Britain Awards, House of Commons, Parliament, UK

03-07/09/12 - “Tuneable Plasmonic Analogue of Graphene”, IOP CMD-24 (ECOSS-29,
ECSCD-11, and CMMP-12) International Conference, Edinburgh, UK

22/07/12-03/08/12 - “Artificial Graphene Structures of Plasmonic Metamaterials”,
IOP/EPSRC Graduate Summer School in Condensed Matter Physics -
Physics by the Lake, Lake District, UK

Journals For Whom I Referee

- **Journal of Optics** - IOPscience.

Positions of Responsibility

May 2015 - **Assisting with the organisation of a Planned SPIE Conference**, Exeter SPIE Student Chapter, Exeter University

April 2014 - **Assisting with the organisation of the Exeter Graphene Conference**, Exeter University

2012 - 2014 - **Athena Swan Committee Member**

2011-2015 - **Lead Demonstrator for two Undergraduate Physics Courses**, Exeter University

2011-2015 - **Deputy Lead Demonstrator** for another Undergraduate Physics Courses, Exeter University

2011-2015 - **Postgraduate representative for Physics**, Physics Department, Exeter University - Relaying current postgraduates' views and problems to school/college leadership and organising events to boost morale and improve employability etc

2011-2015 - **Quantum Systems Postgraduate Seminar Organiser**, Physics Department, Exeter University - Booking rooms and speakers, organising a schedule and advertisement

2011-2012 - **Voluntary A-level and GCSE Tutor**, Exeter School

2008-2010 - **Physics Buddy System Founder and Coordinator**, Exeter University - A peer support system within the department, where existing students aid new undergraduates

2008-2009 - **Physics Society President**, Exeter University - Organising events (such as Careers Evenings, trips to the London Science Museum, and Paintballing) for approximately 250 members, as well as approximately doubling the societal membership

2008-2009 - **Student Ambassador**, Exeter University

2007-2010 - **Aim Higher Peninsula Programme Student Ambassador**, Exeter University, Plymouth University, Marjon's University and at other HE establishments in the South West

2007-2010 - **Student-Staff Liaison Committee Chair**, Exeter University

2007-2008 - **Students Associate Scheme (SAS)** Teacher Training, Exeter University

Glossary

Notation	Description
$-e$	Electronic charge.
F	The Fano factor.
G	The Ballistic Conductance.
H	The Hamiltonian of the system.
L	Symbol used for both the classical Lagrangian for the system when determining the dispersion, and the length of the barrier when calculating the Klein Tunnelling probabilities.
L_0	The base barrier length needed for KT, defined from the potential V_0.
$M = N_e m_e$	The total mass of the electronic cloud.
N_e	Number of electrons.
Q_i	Total electronic charge in the i-th nanoparticle..
T	The transmission probability through the KT barrier.
T_i	The kinetic energy of the N electron system in the i-th particle.
$V(x)$	The step function representing the position dependent barrier height (potential) in different regions of the KT scheme.
V_0	Barrier height in region 2, shown in figure 5.1.

Notation	Description
V_i	The potential energy of the N electron system in the i-th particle.
$V_{i,j}$	The coupling potentials between neighbouring particles.
W	The total bandwidth of the CP bands.
W^τ	The bandwidth of individual CP bands, indicated by $\tau = \pm$.
Δ	The size of the gap in the dispersion.
$\Delta(x)$	The step function representing the gap size in different regions of the KT scheme.
Λ	The frequency associated with the interaction 'strength' between particles in the classical description (also referred to as the coupling parameter).
Ω	The frequency associated with the interaction 'strength' between particles in the quantum mechanical description.
Ω_{Ang}	Solid angle.
Φ_B	Symbol for Berry phase (BP).
$\Pi_s(\mathbf{R})$	Momentum conjugated to the displacement field.
Ψ	The spinor wavefunction in the sublattice basis (A/B).
Ξ	Charge per unit area.
$\beta^\tau_{\mathbf{q}}$	The bosonic operator which diagonalises the Hamiltonian, H.
$\mathbf{k}$	Electronic or Plasmonic Wavevector. In chapters 5 and 6, $\mathbf{k}$ denotes the wavevector in regions 1 and 3, shown in figure 5.3. Close to the Dirac point in graphene $\mathbf{k}$ is the wavevector measured from a Dirac point such that $\mathbf{k} = \mathbf{q} - \mathbf{K}^\tau$.

Notation	Description
δ	Decay length.
$\delta\omega$	The difference between the natural oscillation frequencies in the A and B sublattices.
$\delta\theta$	The dimensionless Dirac point coordinate in the y-direction.
$\epsilon(\omega)$	Complex dielectric constant as a function of frequency.
ϵ_d	Relative permittivity of the dielectric.
ϵ_m	Relative permittivity of the metal.
γ	The dominant interlayer hoping strength in bilayer graphene.
γ_L	The Landau damping rate.
γ_{rad}	The radiation damping rate.
γ_{tot}	The total damping rate, including only Landau and radiation damping.
$\hat{\mathbf{n}}$	Unit vector in the direction of oscillation for a single dipole or between nearest neighbour particle for the case of multiple nanoparticles.
$\hat{\mathbf{p}}$	Dipolar unit vector.
$\hat{\boldsymbol{\sigma}}$	Pauli matrices in the sublattice space (A, B) given in equation 2.27.
λ	Wavelength of Incident Light.
λ_F	The quasiparticle's Fermi wavelength.
λ_e	Wavelength of the Re-emitted Light.
C_j	The nearest-neighbour coupling strengths in plasmonic arrays.
$\mathcal{I}^{(2)}$	2×2 Identity matrix.
$\mathcal{I}^{(4)}$	4×4 Identity matrix.
$\mathfrak{s}$	The particle pseudospin.
ω	Angular Frequency.

Notation	Description
ω_0	Natural frequency of oscillation (also known as the resonant frequency) of the nanoparticles.
ω_A and ω_B	Natural frequency of oscillation (also known as the resonant frequency) of the nanoparticles in the A and B sublattices, respectively.
ω_p	Plasma Frequency.
$\omega_{\mathbf{q}}^{\pm}$	Plasmonic dispersion.
ϕ	Azimuth angle between the projection of $\hat{\mathbf{p}}$ in the xy-plane and the nearest neighbour vector, $\mathbf{n}$.
ϕ_c	The special in-plane polarisation angle where the interaction strength goes to zero.
$\psi_{\mathbf{k},K}^{\pm}$	The CP spinor eigenstates.
$\rho(\mathbf{x})$	Charge Density at position $\mathbf{x}$.
σ_c	The Sample Independent Conductivity.
$\sigma_c(\omega)$	Frequency dependent conductivity.
τ	$= \pm 1$, referring to each valley (or cone) denoted as K and K'.
τ_e	Electronic relaxation time.
MoS_2	Molybdenum disulphide.
θ	Polar angle between $\hat{\mathbf{p}}$ (the dipole unit vector) and $\hat{\mathbf{z}}$.
θ_0	The special out-of-plane polarisation angle where the interaction strength goes to zero.
θ_G	The angle at which there is a line in the phase diagram, shown in figure 3.7 where the dispersion changes from gapped to gapless or visa versa.
$\tilde{\Omega}$	The frequency associated with the interaction 'strength' between particles in the quantum mechanical description extended to include possible sublattice asymmetry.

Notation	Description
$\tilde{v}$	The group velocity of CPs in arrays including sublattice asymmetry.
ε_F	Fermi energy.
$\varepsilon_{\mathbf{q}}$	Energy eigenvalues.
ε_{res}	The resonance energy modes when the barrier length is used to quantise the x-wavevector, such that $k_x L/\pi = n$, where n is an integer.
a	Interparticle distance.
a_2	Next-nearest neighbour particle separation distance.
a_3	Next-next-nearest neighbour particle separation distance.
$a_{\mathbf{R}}$ and $b_{\mathbf{R}}$	Bosonic ladder operators given in equation 3.21.
c	Speed of Light.
$h(\mathbf{q})$	The amplitude of the Fourier component of the electronic centre of mass displacement, h, with wavevector $\mathbf{q}$.
k_F	The Fermi wavevector, and when considering KT this symbol represents the Fermi wavevector in regions 1 and 3.
m	The effective mass of quasiparticles in bilayer graphene.
m_e	Electronic mass.
n_c	Charge density.
q_F	The Fermi wavevector in region 2 of the KT scheme.
r	Nanoparticle Radius.
r_A and r_B	Radius of the nanoparticles in the A and B sublattices, respectively.

Notation	Description
r_{opt}	The suggested optimum size of nanoparticles to minimise damping.
s	$= \pm 1$ indicates the bands of the dispersion, with $s = +1$ for the conduction band (electrons) and $s = -1$ for the valence band (holes).
t	Time, although t is also used to signify the hopping energy between nearest neighbour sites in graphene, bilayer graphene and transition metal dichalcogenides, and the transmission amplitude for KT shown in chapters 5 and 6, to be consistent with the literature.
v	The group velocity of CPs in arrays of identical particles, and also the symbol used for the velocity in a generalised system.
v_F	Fermi velocity.
$x_D = K_x a$	The dimensionless Dirac point coordinate in the x-direction.
$y_D = K_y a$	The dimensionless Dirac point coordinate in the y-direction.
$\mathbf{A}(\mathbf{x}, t)$	Vector Potential.
$\mathbf{E}$	Electric Field.
$\mathbf{F}_{\text{Res}}$	Restoring Force of electrons in nanoparticles.
$\mathbf{J}(\mathbf{x}, t)$	Current Density.
$\mathbf{K}^{\tau}$	Symbol for the two inequivalent Dirac points, or valleys, in graphene's Brillouin zone, denoted as K and K'. The vector form signifies the wavevector values at which these occur, such that $\mathbf{K} = -\mathbf{K}'$.
$\mathbf{R}$	Nanoparticle Position.

Notation	**Description**
$\mathbf{V}_{\mathbf{k}}^{\pm}$	Unit vector in the Bloch sphere depicting the directions of the eigenspinors shown in equation 4.10.
$\mathbf{d}$	Distance from the point dipole.
$\mathbf{e}_j$	The nearest neighbour vectors in the honeycomb array, given in equation 3.1.
$\mathbf{e}_j^{(2)}$	The next-nearest neighbour vectors given in equation 3.9.
$\mathbf{e}_j^{(3)}$	The next-next-nearest neighbour vectors given in equation 3.13.
$\mathbf{p}$	The dipole moment, or the electronic momentum.
$\mathbf{q}$	Electronic or Plasmonic Wavevector (In chapters 5 and 6, $\mathbf{q}$ denotes the wavevector in region 2, shown in figure 5.3).
$\mathbf{x}$	Position.
$\boldsymbol{\sigma}$	Pseudospin.
$h_i(\mathbf{R})$	Electronic centre of mass displacement field that corresponds to the LSP at position $\mathbf{R}$ relative to the positive ionic background.
$\lvert\langle\psi_1\vert\psi_2\rangle\rvert^2$	The overlap of pseudo-spin states inside and outside the KT barrier.
0D	Zero Dimensional.
2D	Two Dimensional.
3D	Three Dimensional.
ARPES	Angle Resolved Photo Emission Spectroscopy.
BP	Berry phase, denoted by the symbol Φ_B.
BZ	Brillouin zone.

Notation	**Description**
CP	Collective Plasmon.
DOS	The density of states.
DQILGS	Dirac Quasiparticles In Linear Gapped Systems.
DQIPGS	Dirac Quasiparticles in Parabolic Gapped Systems.
DQIPS	Dirac Quasiparticles in Parabolic Systems.
KT	Klein tunnelling.
LSP	Localised Surface Plasmon.
QED	Quantum Electrodynamics.
QHE	The Quantum Hall Effect.
SP	Surface Plasmon.
W	The width of the KT barrier.

List of Figures

1

Introduction

Dirac materials contain quasiparticles that are described by a Dirac Hamiltonian, which emerges from the relativistic treatment of quantum particles. The Dirac equation, derived by Paul Dirac in 1928, describes parity symmetric chiral particles using multi-component wavefunctions, which naturally account for the spin of the particles [1, 2]. Dirac particles were theoretically predicted long before their experimental discovery in 2004, when monolayer graphene was isolated [3]. Graphene, a two-dimensional (2D) monolayer of carbon atoms [3], is the basic building block for graphitic materials of all other dimensionalities [4] and is the first truly 2D crystal and the only known 2D conducting membrane. Since its discovery, graphene has been extensively researched because of its exciting properties, most of which come from the Dirac nature of its electronic quasiparticles [4]. Graphene's unusual band structure, which is characterised by the presence of fermionic massless Dirac quasiparticles close to zero energy, is a result of the hopping of electrons between neighbouring carbon atoms [5–7]. Many of the remarkable properties of graphene are a direct consequence of the chirality associated with these pseudo-relativistic Dirac fermions. Examples of these properties include: a nontrivial Berry phase of π attained in parallel transport [8,9], which is responsible for the anomalous quantum Hall effect [8, 9], as well as the suppression of electronic backscattering from smooth scatterers [10], which is responsible for the very high electron mobility of graphene samples. Thus graphene could be used in many potential applications [4] as well as providing an excellent condensed-matter analogue of (2+1)-dimensional quantum electrodynamics (QED) [4, 11].

Due to these remarkable properties, there has been a lot of interest in studying Dirac particles, leading to other materials containing Dirac particles being uncovered, such as bilayer graphene, and monolayer transition metal dichalcogenides.

Straining Dirac materials has been shown to change their properties [12] allowing materials such as graphene to be optimised for specific technologies [13]. However, tuning the properties of natural Dirac materials to any significant degree, controllably, has proven quite difficult. Undoubtedly it would be exciting to find a Dirac material with properties that could be tuned over a broader range. Similarly, it would be fascinating to explore new systems that support Dirac quasiparticles beyond the atomically thin materials which have been studied since the discovery of graphene. These new Dirac particles could be used to transport information efficiently although not necessarily via their charge. In this thesis I investigate the design of different tunable Dirac materials, and explore novel Dirac particles emerging in two different contexts: 1) natural Dirac materials, such as graphene, bilayer graphene, and transition metal dichalcogenides; and 2) plasmonic metamaterials, which support bosonic chiral Dirac plasmons with a highly tunable bandstructure.

This thesis will thus combine physical concepts that belong to different fields of research, including quantum transport and electronic bandstructures in solid state devices, as well as plasmonics. The latter field of plasmonics, the branch of physics concerned with investigating the interaction of light with metals [14], has been extensively researched both experimentally and theoretically [15]. Plasmonic nanostructures, such as isolated metallic nanoparticles [16], have been created and, when illuminated by external radiation, the electrons in the nanostructures oscillate, forming a localised surface plasmon resonance [17,18]. These localised surface plasmons enhance the subwavelength optical field around the nanostructures [18] and mean that electromagnetic radiation at the resonance wavelength will be strongly scattered or re-radiated [14]. This enhanced local electric field has also been used to improve photovoltaic devices [19, 20].

Although single or few structures form the foundation of plasmonics, the emphasis is rapidly shifting to periodic arrangements of nanostructures, which constitute a bridge into the field of metamaterials. Metamaterials are man-made, or man altered, materials (such as patterned surfaces, or arrays of nanostructures) which can have tunable properties. The desired properties for particular devices can be obtained by designing specific array structures. In fact, an assortment of novel artificial materials have been designed, some of which even exhibit properties beyond those seen in nature, for example: negative refractive index [21–23], electromagnetic invisibility cloaking [24–26], perfect lensing [27, 28] and slow light [29].

For the plasmonic part of this research I consider arrays of metallic nanoparticles which support localised surface plasmon resonances that are dipolar in nature [30]. The interaction between localised surface plasmons on individual nanoparticles in the array generates collective plasmonic modes that extend over the whole array and involve all localised surface plasmons at once [31–43]. As a consequence the collective plasmon modes can exhibit a variety of properties that crucially depend on the lattice structure of the metamaterial, and on the microscopic interactions between localised surface plasmon resonances [31–34, 36, 37]. Whilst there are infinitely many possible nanoparticle arrangements, one structure that has attracted considerable attention in the condensed matter community in recent years is the 2D honeycomb structure of graphene. As the majority of graphene's remarkable electronic properties stem from its structure, one can infer, from Bloch's theorem [44], that collective plasmons in a honeycomb array of metallic nanoparticles would present similar properties. Understanding the nature and properties of collective plasmons in this array is vital, as they are the fundamental modes which guide electromagnetic radiation over macroscopic distances in the metasurface. This is the main aim of the first part of my work. After this, other Dirac materials, real and artificial, are explored which exhibit an energy dependent chirality and Berry phase (BP). To characterise them, I analyse their quantum transport properties in the ballistic regime.

This thesis is organised as follows: In chapter 2 I present the background theory, for both plasmonic metamaterials and Dirac materials, that is needed to understand the work displayed in subsequent chapters. I describe localised surface plasmons in metallic nanoparticles, discuss their interactions in plasmonic arrays, and also detail some of the exceptional properties exhibited by electrons in graphene as well as in other Dirac materials.

In chapter 3 I tackle the primary question faced in this research by investigating the Dirac-like nature of collective plasmons in 2D honeycomb arrays of metallic nanoparticles and unveil the emergence of massless Dirac bosons. I also show the tunability of the plasmonic bandstructure in this metamaterial by analysing in detail the phase diagram of gapless and gapped phases that emerge when tilting the localised surface plasmon dipole orientation.

An advantage of metamaterials over conventional materials is the fact that they can be altered, or designed, to have various properties. I examine one such alteration in chapter 4, where I study the properties of 2D honeycomb arrays of metallic nanoparticles with broken inversion symmetry. This opens a gap in the otherwise linear collective plasmon spectrum and leads to the appearance of ‘massive’ Dirac bosons with an energy dependent Berry phase. I deduce the effective low energy Hamiltonian that describes these particles and show that it can be generalised to also describe some fermionic systems, such as MoS_2. I collectively refer to all of these systems as Dirac materials with a linear gapped spectrum.

In chapter 5 I use this generalised Hamiltonian to examine the ballistic transport properties of these systems by considering their quasiparticles incident on a square potential barrier. I prove that opening a gap in the graphene-like spectrum allows for backscattering from smooth potentials at normal incidence, which is impossible in graphene and could make the fermionic versions of these Dirac materials useful for transistor applications.

In chapter 6 I investigate the ballistic transport properties of other Dirac materials supporting chiral massive Dirac quasiparticles with a gapped spectrum, such as bilayer graphene with an interlayer bias. Again, breaking the inversion symmetry of the system and opening a gap in the spectrum results in properties vastly different from its unbiased counterpart. For example, biasing bilayer graphene can result in perfect transmission at normal incidence, via conventional Fabry-Perot resonant states.

The remarkable properties shown in chapters 5 and 6 are tunable with energy, band gap, and barrier height, allowing for metamaterials, and even natural materials, to be designed for specific device applications.

Finally, I conclude in chapter 7.

2

Background Theory

The interaction between light and matter has been of interest, both scientifically and artistically, for millennia. We all use the properties of light to our advantage and pleasure with objects such as mirrors and stained glass windows. The first lenses and mirrors were created to bend the trajectory of light, leading to a huge variety of practical applications such as imaging objects. Historically, the diffraction limit has seriously hindered our ability to observe microscopic structures with dimensions less than the wavelength of the detecting light [45]. However, this limitation has been overcome with the use of plasmonic nanostructures [14, 46], such as isolated metallic nanoparticles [16]. When illuminated by external radiation, the electrons in the nanostructures oscillate collectively, forming a localised surface plasmon (LSP) resonance [17, 18], which can enhance the subwavelength optical field due to the evanescent field at the surface [18]. This phenomenon can overcome the diffraction limit and hence allow for molecular level resolution [47]. Furthermore, the enhancement of the local electric field has been utilised by placing plasmonic nanostructures on conventional semiconductors to increase the induced photocurrent [19, 20].

Arrays of metallic nanoparticles can have a variety of different collective properties, which can be very different from the response of isolated nanoparticles [48]. This is because the LSP resonances on the individual nanoparticles interact with each other to produce a collective plasmon (CP) mode extended over the whole structure [33, 37]. This phenomenon was theorised [49] (and later confirmed by experiment [50, 51]) to be able to transmit energy along chains of subwavelength particles, which is a step towards prospective plasmonic devices [52]. Such an array of nanoparticles can be considered a plasmonic metamaterial, which are man-made or man-altered materials, constructed in such a way as to produce desired properties. In particular, much research has been conducted into how they scatter light [52, 53].

The properties of the CP depend on the arrangement of the nanoparticles in the array as well as on the dominant type of interactions between particles [18]. It is possible to tune the properties of a metamaterial made of an array of metallic nanoparticles by arranging them into specifice lattice structures. The first part of this chapter is devoted to the fundamental properties of plasmonic metamaterials. I begin in section 2.1 by discussing bulk plasmons, and then reducing dimensionality to consider surface plasmons in two dimensions (2D) and LSPs in metallic nanoparticles, where quantisation effects are more prominent. This treatment is then extended into the realm of metamaterials by considering arrays of metallic nanoparticles, examining the interactions between LSP resonances on multiple nanoparticles. After discussing the coupling between two nanoparticles in section 2.2, I present the general framework of CPs in plasmonic metamaterials, considering a linear chain of metallic nanoparticles in section 2.3, and a 2D square array of metallic nanoparticles in section 2.4.

In principle there are infinitely many possible array structures that one could investigate, however there is one lattice that has recently gained a lot of interest in the condensed matter community due to its remarkable properties, which mostly stem from its structure. This lattice is the honeycomb structure of graphene [3], a 2D monolayer of carbon atoms. It may be possible to replicate some of these exciting properties in a plasmonic metamaterial with a similar structure, which was the primary aim of this project. Thus I present the electronic properties of graphene in section 2.5.

There are also other materials which support Dirac quasiparticles like those seen in graphene, but, due to slight differences in the structure, exhibit different and possibly very useful properties for future device applications. As later extensions of my research involve these “Dirac materials” or take inspiration from them, their properties are described in sections 2.6 and 2.7.

2.1 Plasmonics

A ‘plasma’ is the name given to a state of matter that consists of a gas of charged particles, hence, by envisioning metals (as described in the Drude model [44]) as a lattice of fixed positive ions surrounded by a negatively charged electron gas, metals can be considered plasmas. Quantised collective oscillations in the charge density of the plasma are called plasmons. The oscillations are most commonly produced by external radiation, where the force due to its electric field encourages the electronic centre of mass of the Fermi sea into motion [46, 54].

2.1.1 Bulk Materials and the Drude Model

The Drude model describes conduction in metals, and as such it can be used to describe plasmons. The primary assumption is that, due to the fact that metals are electrically neutral, there are only two types of particles present in an atom: negatively charged electrons, which are considered to be identical solid point particles, and larger, immobile, positively charged ions [44]. When these atoms join together to make a metal, the valence electrons can travel far from their parent ions, and therefore form the *sea* of free electrons, called conduction electrons.

As bulk plasmons are oscillations in the electronic sea in bulk metals, I can use the well known results of the Drude model to describe them. One of these is the dielectric function of the material which leads to the plasma frequency.

Using Maxwell’s Equations, in the presence of a non-zero current density due to the movement of electrons, one deduces the complex dielectric constant [55], $\epsilon(\omega) = 1 + \frac{4\pi i \sigma_c(\omega)}{\omega}$, where $\sigma_c(\omega)$ is the frequency dependent conductivity. If ω is large enough to satisfy the condition $\omega \gg \frac{1}{\tau_e}$ (where τ_e is the electronic relaxation time, which gives the time between collisions, and has typical values of $\sim 10^{-14}$s), then ϵ can be expressed as

$$\epsilon(\omega) = 1 - \frac{\omega_p^2}{\omega^2} \quad , \tag{2.1}$$

where ω_p is the plasma frequency, with typical values of $\sim 10^{15}$rad s^{-1}, given by:

$$\omega_p^2 = \frac{4\pi n_c e^2}{m} \quad . \tag{2.2}$$

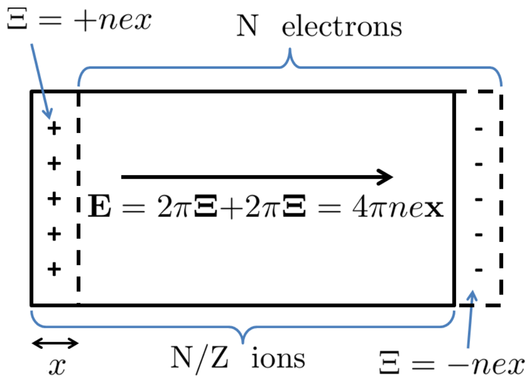

Figure 2.1: Simple model of plasmons. The Fermi sea of conduction electrons is displaced towards the right, creating a net negative charge on the right hand side, and the absence of electrons on the left leads to a resultant positive charge. Here **E** is the induced electric field, N is the number of electrons in the system, n is the electron density, and Ξ is the surface charge density at either end of the slab.

---

where n_c is the charge density.

There are two cases which are of interest here, when:

1. $\omega < \omega_p$: ϵ is real and negative, and the electromagnetic radiation decays exponentially in space, therefore no radiation propagates.

2. $\omega > \omega_p$: ϵ is real and positive, and the solutions are oscillatory, therefore radiation can propagate.

Thus, the plasma frequency is defined as the frequency above which the metals become 'transparent' [44] and where one can approximate the metal as a plasma. This is a valid approximation due to the fact that the assumption of $\omega \gg \frac{1}{\tau_e}$ is satisfied near $\omega \simeq \omega_p$ [44].

A consequence of case (2) is that the electron gas can sustain charge density oscillations which can propagate through the material. These charge density waves are described as plasma oscillations, the quanta of which are called plasmons [44] and interactions with these can explain the energy loss of fast moving electrons through metallic foils [54], which is of the order of $\hbar\omega_p$ [44].

We can model the charge distribution in a bulk plasmon by displacing the entire electron sea through some distance, x, with respect to the fixed positive background of ions [44], as shown in figure 2.1.

The resulting surface charge gives rise to an electric field of magnitude $|\mathbf{E}| = 4\pi|\Xi| = 4\pi n|\mathbf{x}|e$, where Ξ is the charge per unit area at either end of the slab. The electron gas as a whole will obey the equation of motion

$$N_e m_e \ddot{x} \quad = \quad -N_e e|4\pi\Xi| \quad = \quad -N_e e(4\pi n x e) \quad = \quad -4\pi n e^2 N_e x \ , \tag{2.3}$$

where N_e is the number of electrons, m_e is the electronic mass and x is the electronic centre of mass displacement. This harmonic equation of motion [56] leads to oscillations at the plasma frequency, $\omega = \omega_p$, given by equation 2.2.

2.1.2 Surface Plasmons

Surface plasmons (SPs) are defined as 2D electromagnetic excitations at the interface between two materials which involve a collective oscillation of surface charge [54]. For this to occur, one material should have a negative permittivity, and free charge carriers, hence is usually a metal, and the other should have a positive permittivity.

The field generated by the SP perpendicular to the surface is evanescent, depicting the bound nature of SPs. In the dielectric this field has a decay length approximately of the order of half the wavelength of the incident light which excited the SP, whereas in the metal the decay length is determined by the skin depth, $\delta = \frac{c}{\sqrt{\omega_p^2 - \omega^2}}$ [57], where c is the speed of light.

SPs are considered for lots of different device applications, ranging from magneto-optical data storage to solar cells as well as for making biological sensors [14]. The ability of SPs to concentrate and channel light in subwavelength structures could be utilised to produce photonic circuits with length scales much smaller than those already produced [58, 59].

In order for these devices to be realised, there is a problem that needs to be overcome. This is the momentum mismatch between SPs and that of the incident photon, at a certain frequency, which can be seen in figure 2.2. The interaction between an incident electromagnetic field and the surface charge density results in the momentum of the SP, $\hbar\mathbf{k}_{\mathrm{SP}}$, being greater than that of a photon in free space of the same frequency, with momentum $\hbar\mathbf{k}_0$. This increase in momentum is associated with the binding of the SP to the surface. The frequency dependent SP wavevector reads [14]

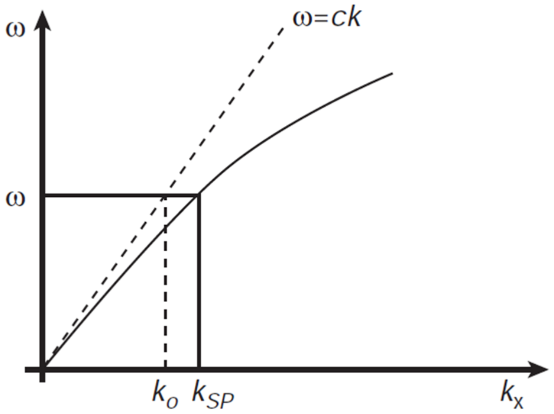

Figure 2.2: A sketch of a surface plasmon dispersion curve compared to the dispersion for light showing the momentum mismatch between SPs (continuous line) and photons (dashed line) of the same frequency [14].

$$k_{\mathrm{SP}} = k_0 \sqrt{\frac{\epsilon_d \epsilon_m}{\epsilon_d + \epsilon_m}} \ , \tag{2.4}$$

where ϵ_m and ϵ_d are the relative permittivities of the metal and the dielectric respectively.

This momentum mismatch must be overcome for the SP to couple with light allowing propagating modes to exist. One way of bridging the momentum mismatch is to use a prism to enhance the momentum of the incident light [60, 61]. Another way is to use a grating on the surface of the metal [62]. Gratings allow the momenta to be matched so that the SP can couple to light controllably, with good efficiency, which is needed for photonic circuits [63, 64].

Although SPs are 2D and of course affected by the boundary, most properties of SP modes can be well described with classical electromagnetic theories provided that the objects supporting the surface plasmons are large enough that they can be described by a dielectric function (or the material permittivity). Quantum mechanics underpins these theories through the dielectric function, which contains all the required information about both the collective excitations and individual particle excitations [65]. The macroscopic concept of a boundary is taken into account by classical electrodynamic theories.

Classical theories can no longer be implemented if the mean free path of the conduction electrons becomes larger than the characteristic dimensions of the system [54]. When reducing the dimensionality of the considered system, for example with localised surface plasmons (LSPs) in metallic nanoparticles, this size limitation must be considered.

2.1.3 Localised Surface Plasmons in Individual Metallic Nanoparticles

Nanostructures have a reduced dimensionality in at least one direction such that at least one of their characteristic lengths is of the order of at most a few hundred nanometres. I consider quasi-zero dimensional (0D) nanoparticles (or nanodots) which have lengths in all three dimensions on the nanometer scale.

When external electromagnetic radiation is incident on metallic nanoparticles LSPs can be excited. When a plasmon is generated by a relatively long wavelength, which is much larger than the size of the nanoparticle, the energy of the incident light will be confined to a volume not much larger than the geometrical volume of the nanoparticle [14, 66]. This has been of great interest in the plasmonics community as it allows for electromagnetic radiation to be trapped in relatively small spatial dimensions.

Under such size restrictions ($\lambda \gg r$), due to the confinement of the conduction electrons, the scattered light fields have a dipolar character [15] so the LSP can be considered dipolar in nature and all higher order oscillations are negligible. A simple way to visualise this dipole-like resonance is to consider an external, static, applied electric field such that the electronic centre of mass moves in the opposite direction to that of the field [14]. This results in a negative charge building up on one side of the particle, and a resultant positive charge on the other side, inducing what can be considered as a dipole [14]. The two oppositely charged 'sides' of the nanoparticle attract each other and the resulting attractive force acts like a restoring force on the electrons, therefore a resonant, oscillating condition can exist [14]. The oscillation of the electronic centre of mass in such a nanoparticle is called a LSP resonance.

Thus, the electron cloud is displaced through some distance x with respect to the static positive background of ions shown in figure 2.3. The oscillating condition for these dipoles is analogous to a harmonic oscillator, similar to that discussed for bulk plasmons but the geometry of the sphere leads to a resonant frequency which is modified from the plasma frequency. In general there will be additional anharmonic corrections to the equation of motion, however these can be neglected as I assume small electronic centre of mass displacements with respect to the characteristic dimensions of the nanoparticle.

For a spherical particle in a dielectric medium, with permittivity ϵ_d, calculating the electric

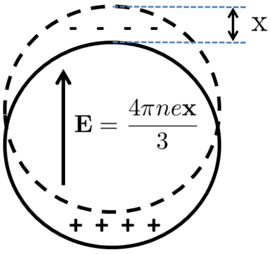

Figure 2.3: Collective electronic excitation of a LSP in a spherical particle in a vacuum, showing the simple model of plasmons, where the displacement of the electronic cloud is exaggerated, and **E** is the induced electric field inside the nanoparticle.

---

field inside the sphere to be $\mathbf{E} = \frac{3\epsilon_d}{2\epsilon_d+1}\mathbf{E}_0$, where $\mathbf{E}_0 = \frac{4\pi n e \mathbf{x}}{3\epsilon_d}$ (which can be found using geometrical arguments), leads to the restoring force on electrons in the particle $\mathbf{F}_{\text{Res}}= \frac{4\pi n e^2}{1+2\epsilon_d}\mathbf{x}$ [57,67]. Therefore the equation of motion for the electrons inside the particle reads

$$\begin{aligned} N m_e \ddot{x} &= -\frac{4\pi N_e n_c e^2 x}{1+2\epsilon_d} , \\ \therefore \omega_0 &= \sqrt{\frac{4\pi n_c e^2}{m_e(1+2\epsilon_d)}} = \frac{\omega_p}{\sqrt{1+2\epsilon_d}} . \end{aligned} \tag{2.5}$$

For the case of a particle in vacuum $\epsilon_d = 1$, giving $\mathbf{E} = \frac{4\pi n e \mathbf{x}}{3}$ as shown in figure 2.3, and the resonant frequency reads $\omega_0 = \frac{\omega_p}{\sqrt{3}}$.

Due to the oscillation of the electronic centre of mass, the electrons are accelerating, leading to the oscillating dipole re-radiating light. This re-radiation by small particles is generally called scattering. The frequency of the scattered, or re-radiated, light is the same as the incident light [14]. Scattering and absorption of light by the electrons in the nanoparticle reduce the transmission. This occurs most dramatically when the frequency of the incident light coincides with the resonant frequency of the nanoparticle. In general, the resonance frequency of individual nanoparticles depends on its shape, size and material constitution. This is in contrast to the resonant frequency, ω_0, in equation 2.5 that was derived for spherical particles (thus having no shape dependence) and does not depend on size. The reason for this discrepancy is due to the fact that the LSP was only considered dipolar in nature during this derivation, while further multipole excitations become

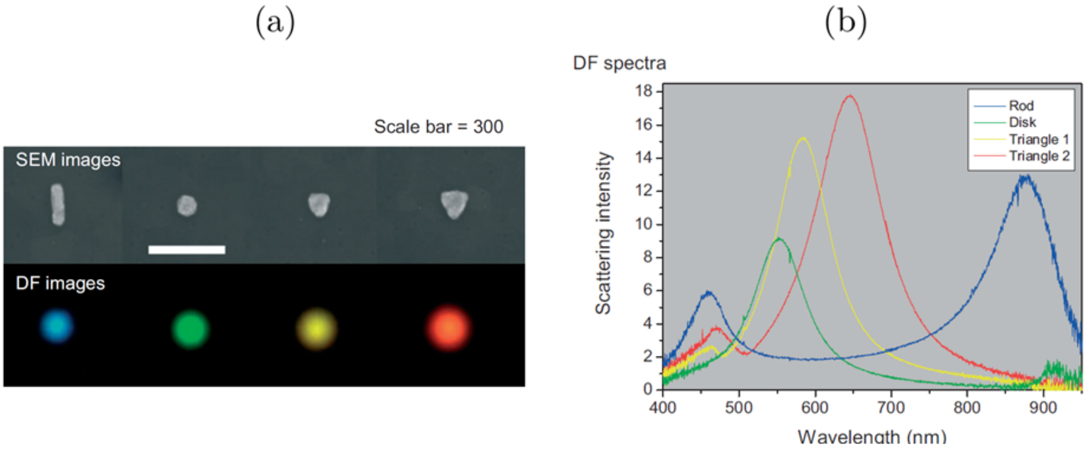

Figure 2.4: Experimental results showing the resonant frequency dependence on shape and size on the nanoparticle. The shapes considered are a rod, a disc, a small triangle and a larger one, made by electron beam lithography [68], shown left to right in the scanning electron micrograph images in the top of panel (a), with corresponding Dark field images underneath, indicating the colour (and therefore the frequency) of the resonant modes. Panel (b) shows dark-field spectra of these nanoparticles. The thickness of these particles was 30 nm and the substrates were silica glass coated with 20 nm of ITO. The scale bar in the top figure is 300 nm [69].

Figure 2.5: The Lycurgus Cup, which dates from the fourth century, is made of glass containing gold and silver dust that change the colour of the cup from an opaque green to a translucent red under different light conditions [70].

more important for larger particles, which affect the resonant frequency. In addition to this effect, nanoparticles of different sizes exhibit different magnitudes of LSP damping, which has an effect on the renormalisation of the of the resonant frequency, ω_0.

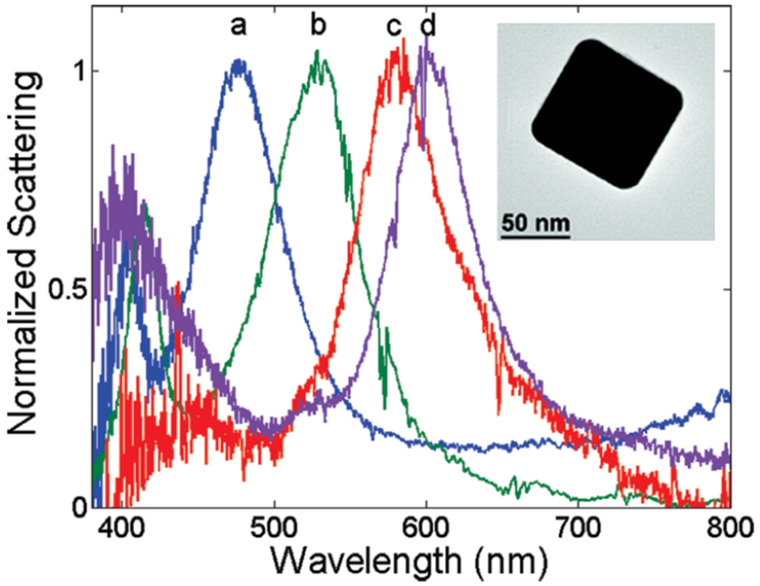

Figure 2.6: The amount of dark-field scattering from nanocubes of similar sizes and rounded courners (shown in the inset), made of either gold or silver, showing the respective resonant frequencies. The line spectra labelled (a) shows silver on a polymer, $\lambda_{\max}$ = 475nm, (b) shows silver on Si_3N_4, $\lambda_{\max}$ = 524nm, (c) shows gold on the same polymer as in panel (a), $\lambda_{\max}$ = 583nm and (d) shows gold on Si_3N_4, $\lambda_{\max}$ = 603nm [71].

Figure 2.4 shows four different sized and shaped particles and their corresponding resonant frequencies. It can be seen that different shaped nanoparticles have differing natural oscillation frequencies and hence re-radiate light of different colours. It can also be seen, in figure 2.4, that the size of the nanoparticles has an effect on the resonant frequency. This is evident in the resonance of the third and fourth nanoparticles from the left, which are approximately the same shape but different sizes. As the particle size is increased the resonant frequency is red shifted. This is a phenomenon that has been used for centuries in stained glass windows, where metallic nanoparticles were used to change the colour of the transmitted and reflected light through the glass. Nanoparticles were also famously utilised in the Roman Empire to make the Lycurgus Cup, shown in figure 2.5, where the noble metal nanoparticles embedded in the glass change the colour of the cup under differing light conditions.

As the resonant frequency of the LSP depends on the dielectric function of the material, nanoparticles made of different materials have distinctly different resonance frequencies. The different resonance frequency of both gold and silver nanoparticles is shown in figure 2.6, where the effect of different substrate materials can also be seen. Nanoparticles can be designed to have resonant frequencies that would be most useful for device applications. For example gold and silver nanoparticles, that are approximately 5 – 150nm in diameter, have resonant frequencies in the visible range, as can bee seen in figure 2.6. Hence, due to the resonantly driven LSPs, these nanoparticles exhibit particularly strong optical absorption in this part of the spectrum [15], which is the relevant spectral range used in most photonic devices. LSPs can enhance the local electric field and so selectively increase or decrease the light absorption by the nanoparticles [18], therefore exciting LSPs, at resonance frequencies, in noble metal nanoparticles could then lead to many possible applications.

A rigorous treatment of the coupling of light with metallic nanoparticles has been presented by Gustav Mie in 1908 [72], when he solved the problem of scattering of light by a spherical particle made of an arbitrary material. Mie's solution encompassed both the electromagnetic effects (which were solved from first principles) and the details of the material, which he tackled by proposing the phenomenological dielectric function $\epsilon(\omega)$ [18]. Mie was the first to outline light scattering by small spherical particles using Maxwell's electromagnetic theory. The solution represented the light scattered by the particles as a sum of partial waves, and can be used to approximately describe the oscillation of the electronic centre of mass, which, depending on the size of the nanoparticle, could either be approximated as a dipolar excitation, or further multipole excitations need to be considered. The different types of excitations explain the size dependence for nanoparticles with diameters greater than $\sim$ 10nm. For smaller nanoparticles the dielectric function of the material can be different from bulk results due to the intrinsic size effects that influence the damping in the particle [18]. Intrinsic effects are caused by the increased localisation of the electrons and changes in the atomic structure [18].

2.2 Interacting Dimers

So far I have examined individual nanoparticles but I now move on to consider arrangements of multiple nanoparticles. I start by exploring nanoparticle pairs, or dimers. The LSPs interact with each other forming a collective mode over the whole system, whose properties depend on the arrangement of the nanoparticles and the interaction between them. Depending on the separation of the nanoparticles either near- or far- field coupling is dominant. Both of these are described in the next section, but as I will later focus on closely spaced nanoparticles, near-field coupling is discussed in more detail.

2.2.1 Near and Far Field Coupling

Far-field effects become increasingly more important as the interparticle spacing (multiplied by the refractive index of the embedding medium) exceeds the wavelength of the electromagnetic wave at the LSP resonance [67]. Particles separated by these distances interact with their scattered fields [46], and the retardation of this scattered light over the distance must also be considered [15]. However, when the nanoparticles are in close proximity near field coupling dominates, and the radiated electric field can be viewed as quasi-static, allowing the interaction to be described by instantaneous dipole-dipole interactions. Near-field coupling dominates under the conditions that the dipoles are separated by a distance much less than the wavelength, λ_e, of the re-emitted light from the oscillating dipoles [67] due to the short range of the electromagnetic near-fields, which is of the order of tens of nanometres [31, 73]. With increased particle separation, near-field coupling continues to dominate until the distance between them is equal to several times the nanoparticle diameter, then the coupling strength rapidly decreases as the distance between particles is further increased [74]. The limiting separation distance has been theoretically approximated as $\frac{\lambda_e}{6}$ [67].

I now consider the dependence of electric field on distance by calculating the vector potential for an oscillating dipole. The solution for the vector potential, $\mathbf{A}(\mathbf{x}, t)$, at position $\mathbf{x}$ and time t, in the Lorentz gauge, for a localised oscillating source is well known to be [57, 75]

$$\begin{aligned} \mathbf{A}(\mathbf{x}, t) &= \frac{\mu_0}{4\pi} \int d^3\mathbf{x}' \int dt' \frac{\mathbf{J}(\mathbf{x}', t')}{|\mathbf{x}-\mathbf{x}'|} \delta\left[t' + \frac{|\mathbf{x}-\mathbf{x}'|}{c} - t\right] \\ &= \frac{\mu_0 e^{-\mathrm{i}\omega t}}{4\pi} \int \mathbf{J}(x') \frac{e^{\mathrm{i}k|\mathbf{x}-\mathbf{x}'|}}{|\mathbf{x}-\mathbf{x}'|} d^3\mathbf{x}', \end{aligned} \tag{2.6}$$

using $\mathbf{J}(\mathbf{x}, t) = \mathbf{J}(\mathbf{x}) e^{-\mathrm{i}\omega t}$ for the current density , and where $\mathbf{k} = \frac{\omega}{c}$ is the wavevector of the emitted wave, with c being its speed. Outside the current source the electric fields reads $\mathbf{E} = \frac{\mathrm{i}c}{k} \nabla \times (\nabla \times \mathbf{A})$ [75] and as long as the source is confined in a region much smaller than the radiated electric field (i.e. a point dipole source) then the electric field can be approximated in both the near and far field quite simply.

In near field, $r \ll |\mathbf{d}| \ll \lambda_\mathrm{e}$ (where r is the radius of the nanoparticle, $\mathbf{d}$ is the distance from the point dipole, and λ_e is the wavelength of the emitted light), which can be considered as

$k|\mathbf{d}| \ll 1$, the electric field has barely changed from when it was emitted, thus $\mathbf{x} \sim \mathbf{x}'$. The spacial exponent goes to zero and the inverse distance can be expanded using spherical Harmonics giving the vector potential as [57, 75]

$$\lim_{k|\mathbf{d}|\to 0} \mathbf{A}(\mathbf{x},t) = \frac{\mu_0 e^{-\mathrm{i}\omega t}}{4\pi} \sum_{l,m} \frac{4\pi}{2l+1} \frac{Y_{lm}(\theta,\phi)}{|\mathbf{d}|^{l+1}} \int \mathbf{J}(\mathbf{x}')|\mathbf{d}|^l Y^*_{l,m}(\theta',\phi') d^3\mathbf{x}'. \tag{2.7}$$

Therefore near fields have a static character, with harmonic oscillations given by $e^{-\mathrm{i}\omega t}$ but are otherwise quasi-stationary. Using only the first term ($l = 0$), and the continuity equation [44], the electric field can be approximated as

$$\mathbf{E} = \frac{3\hat{\mathbf{n}}(\hat{\mathbf{n}} \cdot \mathbf{p}) - \mathbf{p}}{4\pi\epsilon_0 |\mathbf{d}|^3}, \tag{2.8}$$

where $\hat{\mathbf{n}}$ is the unit vector in the direction of oscillation, and $\mathbf{p}= \int \mathbf{x}'\rho(\mathbf{x}')d^3\mathbf{x}'$ is the dipole moment, where $\rho(\mathbf{x})$ is the charge density at position $\mathbf{x}$.

Whereas in the far field ($k|\mathbf{d}| \gg 1$) the exponential, in equation 2.6, oscillates rapidly. Here one can approximate $|\mathbf{x}-\mathbf{x}'| \sim |\mathbf{d}|-\hat{\mathbf{n}}\cdot\mathbf{x}'$ [57,75], and up to leading terms in $k|\mathbf{d}|$ the vector potential reads

$$\lim_{k|\mathbf{d}|\to\infty} \mathbf{A}(\mathbf{x},t) = \frac{\mu_0 e^{-\mathrm{i}\omega t} e^{\mathrm{i}k|\mathbf{d}|}}{4\pi|\mathbf{d}|} \int \mathbf{J}(\mathbf{x}') e^{-\mathrm{i}k\hat{\mathbf{n}}\cdot\mathbf{x}'} d^3\mathbf{x}'. \tag{2.9}$$

This indicates that the vector potential acts like an outgoing spherical wave in the far field. As $|\mathbf{d}| \gg \lambda$ this can be expanded in k reading [57, 75]

$$\lim_{k|\mathbf{d}|\to\infty} \mathbf{A}(\mathbf{x},t) = \frac{\mu_0 e^{-\mathrm{i}\omega t} e^{\mathrm{i}k|\mathbf{d}|}}{4\pi|\mathbf{d}|} \sum_j \frac{(-\mathrm{i}k)^j}{j!} \int \mathbf{J}(\mathbf{x}')(\hat{\mathbf{n}} \cdot \mathbf{x}')^j d^3\mathbf{x}'. \tag{2.10}$$

The magnitude of terms falls off rapidly with increasing j and the electric field can be well approximated with the first non-vanishing term reading [75]

$$\mathbf{E} = \frac{k^2}{4\pi\epsilon_0}(\hat{\mathbf{n}} \times \mathbf{p}) \times \hat{\mathbf{n}} \frac{e^{\mathrm{i}k|\mathbf{d}|}}{|\mathbf{d}|}. \tag{2.11}$$

Thus in the near field regime the electric field, given in equation 2.8, has a static character with a $1/|\mathbf{r}|^3$ dependence on distance that reflects its dipolar nature. However, in the far field regime, shown in equation 2.11, retardation of the field must be taken into account (i.e. $|\mathbf{x}-\mathbf{x}'| \nsim 0$)

and the r^{-1} dependence is typical of radiation fields [57, 75]. If the dipole were static, $\mathbf{k} \to 0$, the near field regime would extend to infinity.

Near field coupling leads to a strong enhancement of the local electric field in the gap between the particles [76]. Because of this it is possible to selectively increase or decrease the light absorption by the nanoparticles [18, 19], which has lead to the utilisation of near field plasmonic arrays in many plasmonic photovoltaic devices [19, 20]. It has been numerically shown [42] that, with nanoparticles separated by distances much less than the wavelength of the re-emitted light, such that near field coupling dominates, a quasi-static approximation qualitatively reproduces the results of more sophisticated simulations in which retardation effects are included [42]. Therefore, in this regime, I can assume the LSP coupling can be described by dipole-dipole instantaneous interactions [57].

There have been many investigations into the effect the variation in particle separation has on the resonance frequency of the collective mode of the dimer system as a whole [48]. It is interesting to note that the incident light polarisation has an effect on this as well, such that: when light incident on the dimer is p-polarised (i.e. the applied electric field is polarized parallel to the dimer axis so that the dipoles are oscillating parallel to the dimer axis) there is a large redshift in the extinction peak as the nanoparticle separation is reduced; and when the incident light is s-polarised (i.e. the applied field is polarised perpendicular to the dimer axis and the dipoles can be taken as oscillating perpendicular to the axis) there is a small blue shift [48]. I will now discuss the origin of this effect by considering the simple case of two interacting LSPs, which leads on to the tunability of the response of nanoplasmonic arrays.

2.2.2 Interacting Dipolar Excitations

In this section I describe the nature of the coupling between LSPs in different nanoparticles under such size and interparticle distance conditions that near field coupling between point dipoles dominates. Such a quasistatic approximation is reliable if the wavelength associated with each LSP is much greater than the interparticle distance, $\lambda \gg a$ [33], and in the optical regime for such small nanoparticles higher multipole contributions can be neglected [77]. Within this approximation, the electrodynamics interaction between two dipoles $\mathbf{p}$ and $\mathbf{p}'$, located at $\mathbf{R}$ and $\mathbf{R}'$ respectively, reads [57]

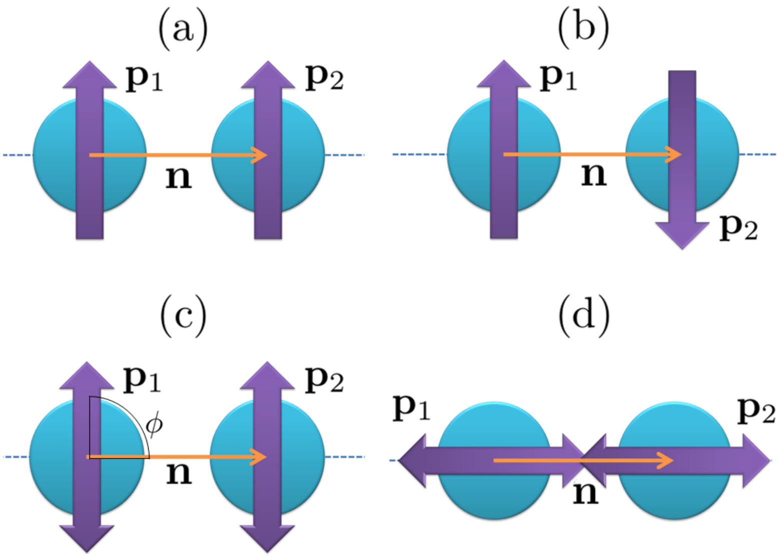

Figure 2.7: Some examples of dipolar oscillation orientations. Panels (a) and (b) show the cases for aligned and anti-aligned dipoles respectively, whereas panels (c) and (d) show two extreme cases for the dipolar polarisations, $\phi = \pi/2$ and $\phi = 0$ respectively (where angles are measured from the interparticle axis).

$$V_{\text{int}} = \frac{\mathbf{p}\cdot\mathbf{p}' - 3(\mathbf{p}\cdot\hat{\mathbf{n}})(\mathbf{p}'\cdot\hat{\mathbf{n}})}{\epsilon_d|\mathbf{R}-\mathbf{R}'|^3} \tag{2.12}$$

with $\hat{\mathbf{n}} = \frac{\mathbf{R}-\mathbf{R}'}{|\mathbf{R}-\mathbf{R}'|}$, the unit vector connecting the two particles shown in figure 2.7 and ϵ_d is the permittivity of the dielectric.

Thus the interaction depends on the orientation of the induced dipoles which can be triggered by external radiation of a given polarisation. In the following I assume that the induced dipoles will be orientated either parallel or antiparallel to each other. This approximation is justified as long as the electric field, which triggers the CPs, is strong enough to suppress fluctuations of the dipoles away from the set polarisation direction. Of course, if the external radiation transfers momentum in the plane of the array it will induce a periodic modulation of the sign of the dipole moment alone the whole structure. The assumption of the global orientation of the dipoles will also hold true if the particles are intrinsically anisotropic, such that they have a preferred dipolar polarisation directions. I parametrize the dipolar orientations as $\hat{\mathbf{p}} = \sin\theta\,(\sin\phi\hat{\mathbf{x}} - \cos\phi\hat{\mathbf{y}}) + \cos\theta\hat{\mathbf{z}}$, where θ is the polar angle between $\hat{\mathbf{p}}$ (the dipole unit vector) and $\hat{\mathbf{z}}$ and ϕ is the angle between the projection of $\hat{\mathbf{p}}$ in the xy-plane and the nearest neighbour vector, $\mathbf{n}$.

For two dipoles in the x-y plane ($\theta = \pi/2$), with $\hat{\mathbf{n}} = \hat{\mathbf{x}}$ and $|\mathbf{R} - \mathbf{R}'| = a$, this interaction potential can be expressed as a function of polarisation angle, as

$$V_{1,2} \approx \frac{p_1 p_2}{\epsilon_d a^3} \left(1 - 3\cos^2\phi\right) \tag{2.13}$$

where p_i is the magnitude of the i-th dipole. Expressed in terms of the charge displacement in the dipoles, the dipole moments can be written as $\mathbf{p}_i = Q_i \mathbf{h}_i = -eN_i h_i(\mathbf{R})\hat{\mathbf{p}}_i$, where $h_i(\mathbf{R})$ is electronic centre of mass displacement that corresponds to the LSP at position $\mathbf{R}$ relative to the positive ionic background and $Q_i = -N_i e$ is the total electronic charge, with N_i the number of electrons on the i-th nanoparticle and $-e$ the electronic charge. For simplicity, in the case of identical nanoparticles, I assume there is an equal number of electrons on each nanoparticle, $N_i = N$, so that the interaction potential can be expressed as:

$$V_{1,2} = \frac{e^2 N^2 h_1 h_2}{\epsilon_d a^3} \left(1 - 3\cos^2\phi\right) \ . \tag{2.14}$$

With this expression and assuming the dipoles act like harmonic oscillators, the classical Lagrangian for the system of two particles can be found, $L = \sum_i \{T_i - V_i\} - V_{1,2}$, where $T_i = \frac{1}{2} N m_e \dot{h}_i^2$ and $V_i = \frac{1}{2} N m_e \omega_0^2 h_i^2$ are the kinetic energy and potential energy of the N electron system in the i-th particle, respectively, and $V_{1,2}$ is the coupling potential in equation 2.14. Substituting this into the Euler-Lagrange equations [78] the equations of motion for each of the nanoparticles in the system can be found:

$$\begin{aligned} \ddot{h}_1 &= -{\omega_0}^2 h_1 - \Lambda^2 \left(1 - 3\cos^2\phi\right) h_2 \\ \ddot{h}_2 &= -{\omega_0}^2 h_2 - \Lambda^2 \left(1 - 3\cos^2\phi\right) h_1 \end{aligned} \tag{2.15}$$

where $\Lambda = \sqrt{\frac{Ne^2}{m_e \epsilon_d a^3}} \sim 10^{10}$rad s^{-1} is a frequency associated with the interaction 'strength' between particles and m_e is the electronic mass. The first two terms in both equations show simple harmonic motion [44] and the last potential-like term is due to the interaction with the other particle.

These equations can now be solved to give the eigenfrequencies of the two collective modes of the system. Due to the dipoles oscillating either parallel or antiparallel to each other, for the case of two interacting nanoparticles, there are always two collective modes possible in the plasmonic dimer (one for parallel and one for antiparallel dipole), which can have different energies depending on the polarisation orientation. With dipoles orientated normal to the interparticle axis the two modes are: the low energy 'bonding' mode, and the higher energy 'antibonding' mode [79]. The high energy mode has parallel dipoles, as shown in figure 2.7(a), which would (over the whole system) lead to a large induced dipole and therefore far from the dimer pair, other particles would experience strong far-field coupling. Such radiative modes, that couple well to the far-field, are often referred to as "bright" plasmon modes [79]. The lower energy, or 'bonding', mode occurs when the dipoles on each individual nanoparticle are anti-parallel, as shown in figure 2.7(b), so that there is no net dipole moment and this system only produces weak far-field coupling [79]. This is called a 'dark' plasmon mode.

For an arbitrary angle, the symmetric electronic centre of mass displacement reads $h_S = h_1 + h_2$, giving the frequency, ω_S [48], and the antisymmetric electronic centre of mass displacement reads $h_A = h_1 - h_2$ with frequency, ω_A [48]. Using h_S and h_A, and taking oscillating solutions of the form $h_i \approx e^{\mathrm{i}\omega t}$, the symmetric and antisymmetric collective modes of the dispersion can be expressed as

$$\begin{aligned} \omega_S &= \omega_0 \sqrt{1 + \frac{\Lambda^2}{\omega_0^2}\left(1 - 3\cos^2\phi\right)} \\ \omega_A &= \omega_0 \sqrt{1 - \frac{\Lambda^2}{\omega_0^2}\left(1 - 3\cos^2\phi\right)} \ , \end{aligned} \tag{2.16}$$

where, as $\Lambda \ll \omega_0$, there can't be imaginary frequency. From this I see that, when $\phi = \frac{\pi}{2}$, $\omega_A < \omega_0 < \omega_S$ as expected.

The polarisation dependence can be explored by considering two extreme cases; 1) when the dipoles are oriented normal to the interparticle axis, and 2) when they are parallel to it, which are shown in figures 2.7(c) and 2.7(d) respectively. Calculating the interaction potential, from equation 2.14, for the first case gives $V_{\text{norm}} = \frac{pp'}{\epsilon|\mathbf{R}-\mathbf{R}'|^3}$, whereas for the parallel case is $V_{\text{para}} = -\frac{2pp'}{\epsilon|\mathbf{R}-\mathbf{R}'|^3}$. Therefore the dipole orientation has a strong effect on the strength of the interaction, and the differing sign can be interpreted in terms of 'attractive' (-) or 'repulsive' (+) forces created between the induced dipoles due to the coupling [48]. It is also evident, from the fact that the above two cases have opposite signs, that there would be some special polarisation angle where the interaction strength goes to zero. This is calculated to be $\phi_c = \arccos\left(\frac{1}{\sqrt{3}}\right)$.

This is very interesting as indeed at $\phi = \phi_c$ the dimer pair should act like two isolated nanoparticles. A simple experiment to test these basic theories could be to illuminate multiple pairs of nanoparticles with varying polarisations of light and to see if at the critical angle the response reverts back to that of individual nanoparticles.

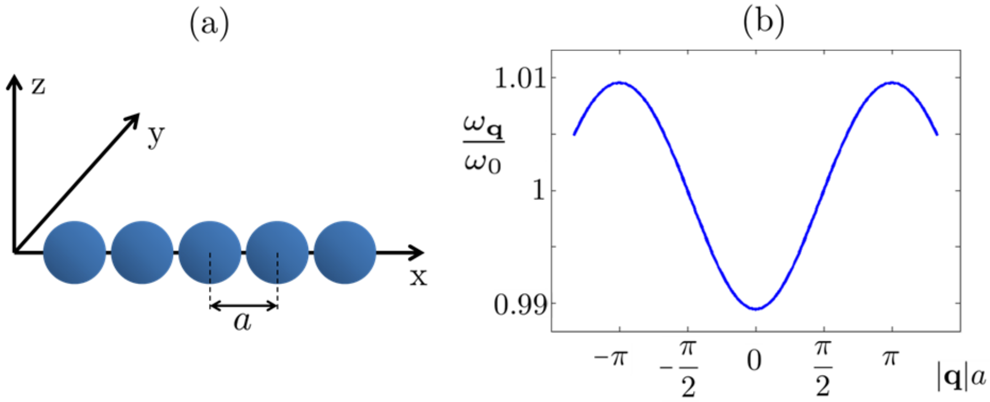

Figure 2.8: Panel (a) shows a schematic of the linear chain of identical spherical nanoparticles separated by a distance a between the centres of the particles. The incident electromagnetic field induces dipolar LSPs in each nanoparticles, which are assumed to all be either parallel or antiparallel to each other. Panel (b) shows the dispersion of an infinite linear chain of oscillating dipoles, up to nearest neighbour particles, with the dipole oscillations perpendicular to the axis of the particles. Here, $\frac{\Delta^2}{\omega_0^2} = 0.01$.

2.3 Infinite 1D Chains of Metallic Nanoparticles

As a simple extension of the previous work, I consider an infinite chain of metallic nanoparticles, like that shown in figure 2.8(a). As in the previous case, when an incident electromagnetic wave is scattered by a chain of nanoparticles the response of the system is modified from the single particle response due to the interaction between particles, an effect which will be evident in the extinction spectrum of the system [67].

The shift in the spectral resonance position compared to that of an isolated particle also depends on the polarisation of the induced dipoles. Figure 2.9 [46] indicates that the restoring force acting on the displaced electrons in each particle in the chain is either increased or decreased by interactions with LSPs on neighbouring particles. This has been investigated experimentally with 1D chains of 50nm gold particles with varying interparticle separations, as shown in figure 2.9(b) [46]. The position of the spectral peak as a function of particle separation and for the two different polarisation is shown in figure 2.9(c) [46]. If no momentum is transferred along the 1D chain, when dipoles are polarised perpendicularly to the chain axis (the transverse mode) there is an increase in the restoring force and the resonance peak is blue shifted, whereas when the dipoles are polarised parallel to the chain (the longitudinal mode) there is a red shift in the resonance peak

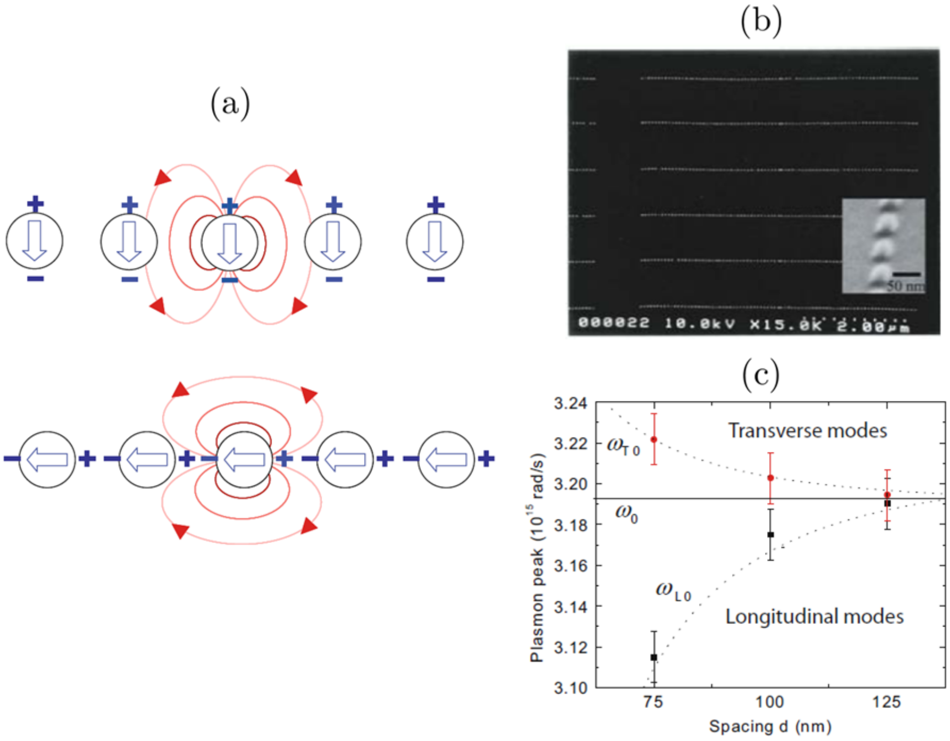

Figure 2.9: Panel (a) shows a schematic of the near-field coupling between a chain of metallic nanoparticles for the two different polarizations, polarised perpendicular to the chain axis (transverse optical polarisation, TO) in the top schematic, and along the chain (longitudinal optical polarisation, LO) in the lower schematic. The arrows indicate the induced dipoles. Panel (b) shows an SEM image of arrays of closely spaced gold nanoparticles and panel (c) shows the dependence of the spectral position of the dipole plasmon resonance on interparticle spacing. The dotted lines show a fit to the r^{-3} dependence of the coupling expected from a point-dipole near field coupling [46].

position.

Figure 2.9(c) [46] also shows that, due to the strong spatial dependence (r^{-3}) of the interaction strength, for large particle separations (of ~ 150nm or more) the response approximately returns to that of isolated particles [46].

The particles in the chain are separated by a distance a, which is much less than the wavelength associated to the LSP, such that near-field coupling dominates and far-field coupling can be neglected. Thus the chain can be considered as an infinite chain of quasi-static dipoles. The optical near field from a chain of metallic nanoparticles is confined in the gaps in between adjacent particles, and it leads to a strong enhancement of the local electric field in between particles [76]. This phenomenon has been helpful in device applications, for example subwavelength metallic structures have boosted the signal enhancement needed in surface-enhanced Raman spectroscopy to allow for the detection of individual molecules [47, 80].

To describe theoretically the 1D plasmonic chain of $n = \infty$ nanoparticles I employ periodic, Born-von Kàrmàn boundary conditions [44, 81]. Also, for this qualitative exploration of the properties I have assumed that only nearest neighbour interactions are significant. The effect of interactions with subsequent neighbours is explored for the case of principal interest in this research later (i.e. the honeycomb case).

The classical Lagrangian of the system reads, $L = \sum_i^n [T_i - V_i - \frac{1}{2}\{V_{i-1,i} + V_{i,i+1}\}]$, where $V_{i,j}$ are the coupling potentials between neighbouring particles given in equation 2.14, and the factor of a half is due to the summation including each interaction twice. Following the same procedure as for dimers, and also transforming the eigenstates into momentum space through $h_i(R) = \mathcal{N}^{-1/2} \sum_{\mathbf{q}} h_i(\mathbf{q}) e^{\mathrm{i}\mathbf{q}\cdot\mathbf{R} - \mathrm{i}\omega t}$, where $\mathbf{q}$ is the wavevector associated with the momentum conjugated to the position $\mathbf{R}$ and $\mathcal{N}$ is the normalisation factor which corresponds to the number of unit cells of the honeycomb lattice, the dispersion of the system reads

$$\omega_{\mathbf{q}} = \omega_0 \sqrt{1 + \frac{\Lambda^2}{\omega_0^2}(1 - 3\cos^2\phi)\cos(qa)} \ , \tag{2.17}$$

where the interaction strength for the chain is $\Lambda = \sqrt{\frac{Ne^2}{m_e \epsilon_d a^3}}$, and again $\Lambda \ll \omega_0$.

This dispersion is shown is shown in figure 2.8(b) for dipoles polarised perpendicular to the chain axis. The wavevector dependence, which appears in equation 2.17 and was not present in the dimer case, is due to the non-localised nature of the chain, *i.e.* that it extends across all space.

2.4 Infinite 2D Arrays of Metallic Nanoparticles

A logical progression after considering an infinite linear chain of particles is to extend the analysis to two dimensions. As well as the effect of different nanoparticle arrangements, both near and far field coupling must again be considered for arrays. The CP properties also depend on interparticle spacing and incident light polarisation [76]. I consider closely spaced nanoparticles, where near-field coupling dominates, as such I use the quasi-static approximation and consider the LSPs as interacting dipoles, meaning retardation effects can be neglected [48]. A lot of research has been conducted into the properties of nanoparticle arrays [15, 76, 82], showing that the interparticle coupling effects give rise to pronounced shifts in the LSP resonance frequency compared to isolated

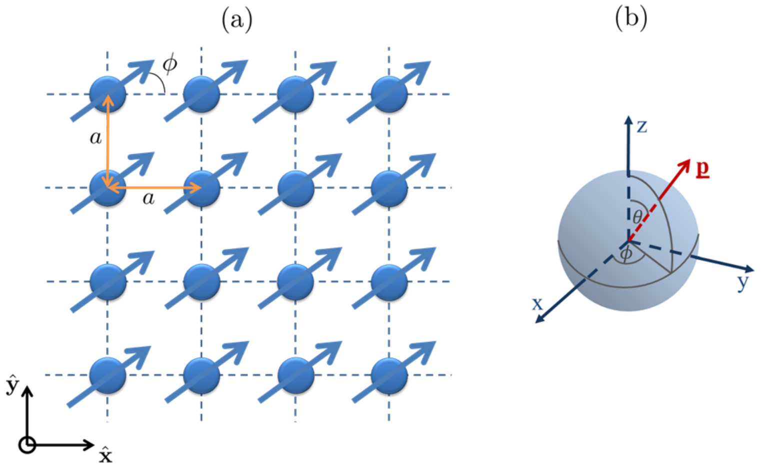

Figure 2.10: Panel (a) shows an infinite square array of metallic nanoparticles with oscillating dipoles at an angle ϕ shown by arrows. The particles are separated by a distances a. In panel (b) the possible orientation of the dipole in three dimensions is presented, showing the polar and azimuthal angles, θ and ϕ respectively.

particles [76].

The simplest 2D array is an infinite square array of metallic nanoparticles, with a structure similar to that shown in figure 2.10. A similar method to that shown previously was implemented, considering only nearest neighbour interactions, such that the Lagrangian for the system reads, $L = \sum_{\mathbf{R}} \left\{T_{\mathbf{R}} + V_{\mathbf{R}} - \frac{1}{2}[V_{\mathbf{R},(Rx,Ry+a)} + V_{\mathbf{R},(Rx,Ry-a)} + V_{\mathbf{R},(Rx+a,Ry)} + V_{\mathbf{R},(Rx-a,Ry)}]\right\}$, where $\mathbf{R}$ indicates the coordinates of the particles. The electronic centre of mass displacement, h, at position $\mathbf{r}$ in the array is the form $h(\mathbf{r}) \approx h(\mathbf{q})e^{\mathrm{i}(q_x x + q_y y - \omega t)}$, where $h(\mathbf{q})$ is the amplitude of the Fourier component with wavevector $\mathbf{q}$.

For identical particles, the Euler-Lagrange equations of motion yield the eigenfrequency

$$\omega_{\mathbf{q}} = \omega_0 \sqrt{1 + \frac{\Lambda^2}{\omega_0^2}\left\{\cos(q_x a)\left[1 - 3\sin^2\theta\cos^2\phi\right] + \cos(q_y a)\left[1 - 3\sin^2\theta\sin^2\phi\right]\right\}}\ . \tag{2.18}$$

where, the coupling parameter $\Lambda = \sqrt{\frac{Ne^2}{\epsilon m_e a^3}}$ obeys $\Lambda \ll \omega_0$, and the polar and azimuthal angles (θ and ϕ respectively) are shown in figure 2.10(b). Here I choose to measure the in-plane angle ϕ, from the nearest neighbour vector that I have denoted as being along the x-axis. From this expression the rotational symmetry of the dispersion is clear, due the rotational symmetry of the square lattice. For purely in-plane dipole polarisations, the dispersion is equivalent (although

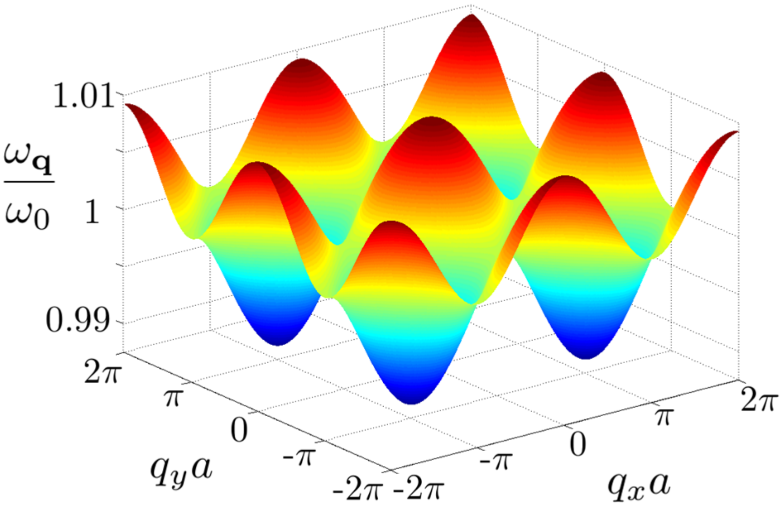

Figure 2.11: The CP dispersion for a 2D square array of metallic nanoparticles with dipoles polarised normal to the plane of the array ($\theta = 0$). Only nearest neighbour interactions are included, and the parameters are taken as $\frac{\Lambda^2}{\omega_0^2} = 0.01$.

rotated) under rotations of the dipole moment through in-plane angles of $\frac{\pi}{2}$ radians.

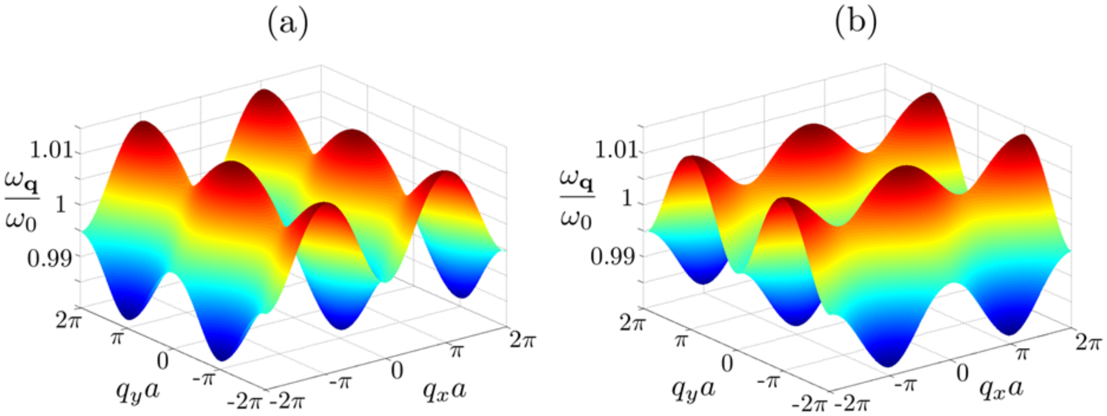

Figure 2.12: The CP dispersion for a 2D square array of metallic nanoparticles with dipoles oriented in the plane along (a) $(\theta, \phi) = \left(\frac{\pi}{2}, 0\right)$ and (b) $(\theta, \phi) = \left(\frac{\pi}{2}, \frac{\pi}{2}\right)$. The dispersions at angles $(\theta, \phi) = \left(\frac{\pi}{2}, \pi\right)$ and $(\theta, \phi) = \left(\frac{\pi}{2}, \frac{3\pi}{2}\right)$ produce the same result as those shown in panels (a) and (b) respectively, due to the lattice symmetry. Only nearest neighbour interactions are included and the parameters are taken as $\frac{\Lambda^2}{\omega_0^2} = 0.01$.

This dispersion, for the case of dipoles oriented normal to the plane ($\theta = 0$), can be seen in

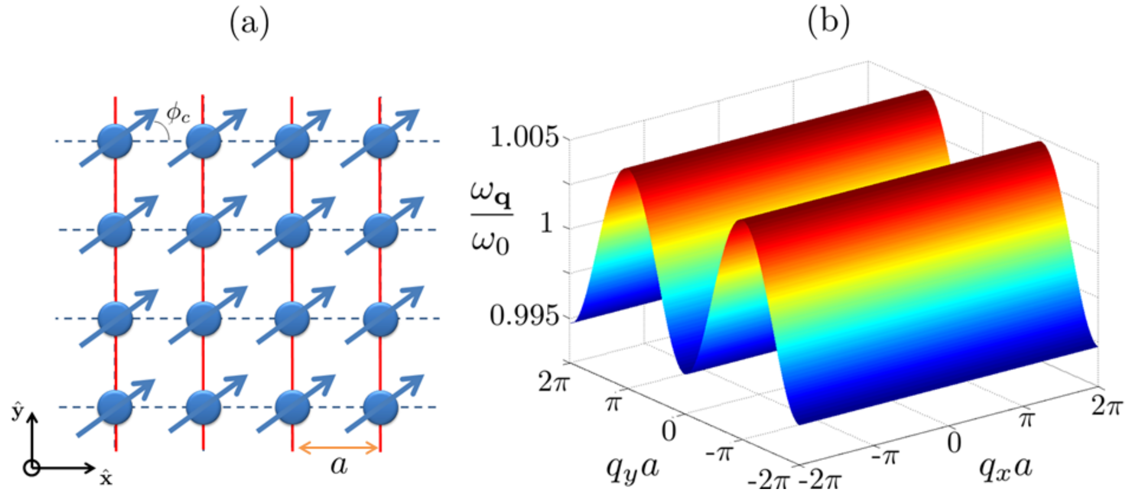

Figure 2.13: Panel (a) shows a diagram of an 2D infinite square array of metallic nanoparticles, like that shown in figure 2.10 but now for a specific dipole polarisation. The oscillating dipoles, indicated by arrows, are polarised along $(\theta, \phi) = (\theta, \phi_c) = \left(\frac{\pi}{2}, \arccos\left[\frac{1}{\sqrt{3}}\right]\right)$ measured from the nearest neighbour vector along the x-axis, meaning that one of the nearest neighbour interactions go to zero. The nearest neighbour interactions that survive at the angle ϕ_c are shown with red lines. Panel (b) shows the CP dispersion corresponding to the array in panel (a). Here it can be seen that the dispersion is invariant along the q_x axis. Again, only nearest neighbour interactions are included and the parameters are taken as $\frac{\Lambda^2}{\omega_0^2} = 0.01$.

---

figure 2.11, and for the case of dipoles oriented in the plane, along one of the nearest neighbour vectors, can be seen in figure 2.12. The in-plane dispersions with dipole oscillations at $\phi = 0, \frac{\pi}{2}, \pi$ and $\frac{3\pi}{2}$ are the same but rotated in reciprocal space by $\pi/2$ due to the symmetry of the lattice.

Similar to the dimer case, there are critical in-plane angles where the coupling to one of the nearest neighbour vectors goes to zero. These angles occur are $\phi_{c,j} = \arccos\left(\frac{1}{\sqrt{3}}\right) + \frac{\pi}{2}(j-1)$ for $j = 1, 2, 3, 4$. At these angles the problem is decoupled into parallel channels, so the system behaves as a set of 1D wave guides showing no dispersion along certain directions. An example of one of these wave guides is shown in figure 2.13(a), where the red lines indicate the remaining non-vanishing interactions, and the corresponding dispersion is shown in figure 2.13(b). By setting $\phi = \phi_{c,1} = \arccos\left(\frac{1}{\sqrt{3}}\right)$ the interactions along the x-axis vanish and the dispersion becomes invariant along the q_x axis. It is also interesting to note that the band width of the system is half that seen at $(\theta, \phi) = (0, 0)$. The reason for this is evident from equation 2.18, as it can be seen that, under the square root, the contribution from the x-direction is added to the contribution from the y-direction, and when one of these interactions goes to zero the maximum the total can be is half what it is

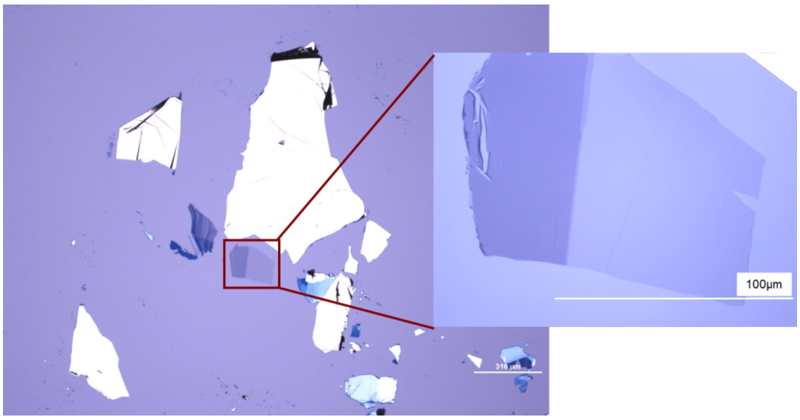

Figure 2.14: An optical microscopy image of several exfoliated graphene flakes with varying layers, on 290 nm thick oxidized silicon wafer. The inset shows a zoom on a single layer region [83].

---

with both contributions. Thus, away from this critical polarisation, the maximum value of the dispersion is $\omega_{\mathbf{q}}|_{\max} = \omega_0 \sqrt{1 + 2\frac{\Lambda^2}{\omega_0^2}} \sim 1.01\omega_0$ (when $\frac{\Lambda^2}{\omega_0^2} = 0.01$) while at the critical polarisation $\omega_{\mathbf{q}}|_{\max} = \omega_0 \sqrt{1 + \frac{\Lambda^2}{\omega_0^2}} \sim 1.005\omega_0$.

Some of the tuneable properties of this array are unique to its lattice structure. Other structures will produce different properties, and one array that has been found to give exciting properties in condensed matter is the honeycomb structure of graphene. I will introduce graphene in the next section, and describe some of its fundamental properties.

2.5 Graphene

Graphene is a single atom thick 2D array of carbon atoms arranged in a honeycomb lattice [4], an optical image of which can be seen in figure 2.14 [83]. It was discovered in 2004 by Andre Geim and Konstantin Novoselov [3], for which they received the Nobel Price in Physics in 2010 [84].

A STEM image of the crystal structure of graphene is shown in figure 2.15 [85], and a schematic diagram is shown in figure 2.16. This structure can be described as two inequivalent triangular sublattices, denoted as A and B, where two neighbouring atoms belong to different sublattices. This structure is produced by each carbon atom using three of its four outer shell electrons to form three covalent bonds with neighbouring atoms, which are separated by a distance $a \simeq 1.42$ Å [7]. Between each of these pairs of atoms there is a shared σ bond due to the sp^2 hybridization

Figure 2.15: Atomic-resolution ADF-STEM image of a defect-free graphene crystal, showing the honeycomb lattice. The scale bar shows 5Å [85]

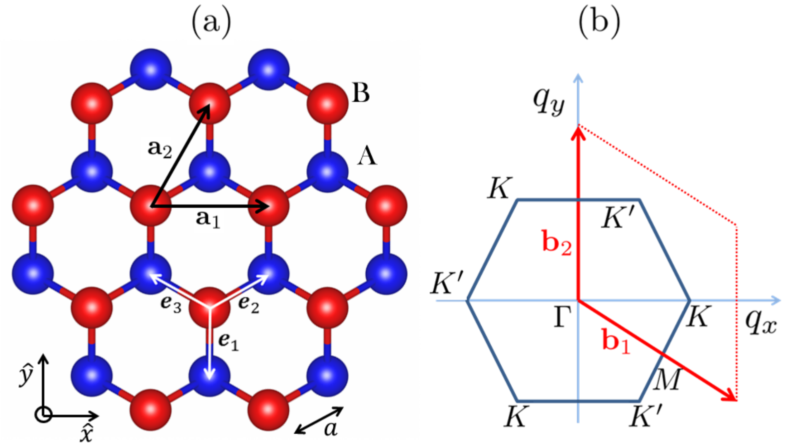

Figure 2.16: (a) The honeycomb lattice of graphene consists of two inequivalent triangular sublattices denoted as A (blue) and B (red), and is invariant under 120° rotations around any lattice site. The sites of one sublattice are at the centers of triangles defined by the other sublattice. There are two atoms per unit cell, one from the A and one from the B sublattice. The atoms are separated by a distance $a = 1.42$Å, and the lattice vectors read $\mathbf{a}_1 = a\left(\sqrt{3}, 0\right)$ and $\mathbf{a}_2 = a\left(\frac{\sqrt{3}}{2}, \frac{3}{2}\right)$. The nearest neighbour lattice vectors, $\mathbf{e}_j$, are given in equation 2.20. (b) The reciprocal lattice of graphene, where the K and K' points and the reciprocal lattice vectors, $\mathbf{b}_1 = \frac{2\pi}{3a}\left(\sqrt{3}, -1\right)$ and $\mathbf{b}_2 = \frac{4\pi}{3a}(0, 1)$, are visible. The red rhombus made by connecting the two reciprocal lattice vectors gives the first reciprocal unit cell for graphene, and the blue hexagon shows the first Brillouin zone which both contain two inequivalent Dirac points.

between one s-orbital and two p-orbitals leading to 2D triangular structure [83, 86]. The fourth electron is in a p_z orbital, which is orientated out of the plane of the lattice [7] and is the bond

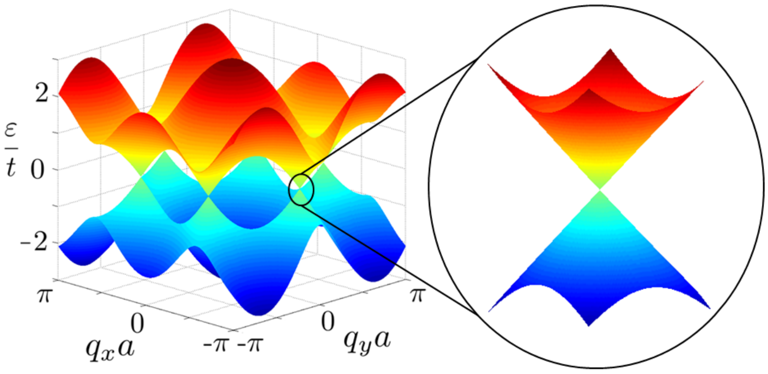

Figure 2.17: The electronic disperion of graphene showing its first Brillouin zone, with energy in units of t (where $t = 2.7eV$ the nearest neighbour hopping strength) and the wavevectors are expressed in units of a (where $a = 1.42$Å is the carbon-carbon distance). The inset shows a zoom in of the dispersion at the cross over point where the conduction and valence bands touch (Dirac point) and the dispersion is locally conical.

---

that would link layers of graphene together; two layers to form bilayer graphene, and many layers to form bulk graphite. Due to the quantum mechanical hopping between sublattices, the p_z orbitals are hybridized across the whole graphene sheet to form the cosine-like conduction and valence bands in the electronic spectrum of graphene, often called the π and π^* bands, respectively. The intersection of these bands at the Brillouin zone (BZ) edge leads to the conical energy spectrum [87]. It is these bands that are responsible for most of the peculiar electronic properties of this atomically thin material [7]. Since each p_z orbital has one extra electron, the electronic band is half-filled [6].

This honeycomb crystal structure leads to most of the extraordinary electronic properties of graphene [7]. It is a zero-gap semiconductor and, rather than the usual Schrödinger equation, its low-energy electronic quasiparticles are described by an effective massless Dirac Hamiltonian [87], derived in the next section.

2.5.1 Tight Binding Electronic Dispersion for Graphene

To derive the electronic properties of graphene we consider the tight-binding Hamiltonian, $\hat{H}$, for the electrons in the honeycomb lattice [5]:

$$\hat{H} = -t \sum_{\mathbf{R}_B} \Big\{ |\mathbf{R}_B\rangle\langle\mathbf{R}_B + \mathbf{e}_1| + |\mathbf{R}_B\rangle\langle\mathbf{R}_B + \mathbf{e}_2| + |\mathbf{R}_B\rangle\langle\mathbf{R}_B + \mathbf{e}_3| \Big\} + H.c. \tag{2.19}$$

where the individual sublattices are denoted A and B, $|\mathbf{R}_A\rangle = |\mathbf{R}_B + \mathbf{e}_j\rangle$ and $|\mathbf{R}_B\rangle = |\mathbf{R}_A - \mathbf{e}_j\rangle$ are the localised states on the lattice sites $\mathbf{R}_A$ and $\mathbf{R}_B$, $t \simeq 2.7eV$ is the hopping energy between nearest neighbour sites [83], and $\mathbf{e}_i$ are the unit vectors [44] for the 2D honeycomb array, shown in figure 2.16 and are [86]:

$$\hat{\mathbf{e}}_1 = a\begin{pmatrix} 0 \\ -1 \end{pmatrix}, \qquad \hat{\mathbf{e}}_2 = a\begin{pmatrix} \frac{\sqrt{3}}{2} \\ \frac{1}{2} \end{pmatrix}, \qquad \hat{\mathbf{e}}_3 = a\begin{pmatrix} -\frac{\sqrt{3}}{2} \\ \frac{1}{2} \end{pmatrix}, \tag{2.20}$$

where the interatomic spacing is $a = 1.42$Å. The Bloch wavefunction for the system given as [88]:

$$|\Psi_{\mathbf{q}}\rangle = \sum_A u_A(\mathbf{q}) e^{i\mathbf{q}\cdot\mathbf{R}_A} |R_A\rangle + \sum_B u_B(\mathbf{q}) e^{i\mathbf{q}\cdot\mathbf{R}_B} |\mathbf{R}_B\rangle \ , \tag{2.21}$$

where $u_A(\mathbf{q})$ and $u_B(\mathbf{q})$ are the wavefunction amplitudes on sites A and B in reciprocal space. The Schrödinger equation [89] can be solved using orthogonality conditions, $\langle \mathbf{R}|\mathbf{R}'\rangle = \delta_{\mathbf{R},\mathbf{R}'}$, as well as the conditions given below:

$$\begin{aligned} \langle \mathbf{R}_A | \varepsilon_{\mathbf{q}} | \Psi_{\mathbf{q}} \rangle &= u_A(\mathbf{q}) \varepsilon_{\mathbf{q}} e^{i\mathbf{q}\cdot\mathbf{R}_A} \\ \langle \mathbf{R}_B + \mathbf{e}_1 | \varepsilon_{\mathbf{q}} | \Psi_{\mathbf{q}} \rangle &= u_A(\mathbf{q}) \varepsilon_{\mathbf{q}} e^{i\mathbf{q}\cdot\mathbf{R}_B} e^{i\mathbf{q}\cdot\mathbf{e}_1} \end{aligned} \tag{2.22}$$

where $\varepsilon_{\mathbf{q}}$ are the energy eigenvalues, $\mathbf{q}$ is the electron wavevector in 2D. Solving the Schrödinger equation [89] gives simultaneous equations for the wavefunction amplitudes, u_A and u_B [5], written here in matrix form:

$$\begin{pmatrix} \varepsilon_{\mathbf{q}} & t\sum_{i=1}^{3} e^{i\mathbf{q}\cdot\mathbf{e}_i} \\ t\sum_{i=1}^{3} e^{-i\mathbf{q}\cdot\mathbf{e}_i} & \varepsilon_{\mathbf{q}} \end{pmatrix} \begin{pmatrix} u_A \\ u_B \end{pmatrix} = 0 \ . \tag{2.23}$$

By setting the determinant of the matrix shown in equation 2.23 to zero to make the secular equation for the system, the full dispersion relation for graphene can be found [5]:

$$\varepsilon_{\mathbf{q}} = \pm t \sqrt{1 + 4\cos\left(\frac{\sqrt{3}q_y a}{2}\right)\cos\left(\frac{3q_x a}{2}\right) + 4\cos^2\left(\frac{\sqrt{3}q_y a}{2}\right)} \ . \tag{2.24}$$

This dispersion relation is shown in figure 2.17, where it can be seen that the conduction and valence bands of graphene's dispersion meet at the so-called Dirac points, making graphene a zero-gap semiconductor [7]. In perfect undoped graphene the Fermi level lies exactly at $\varepsilon_{\mathbf{q}} = 0$, and the spectrum spans a wide range of energy such that the upper band reaches $\varepsilon_{\mathbf{q}}|_{\max} \sim 8\text{eV}$ at the Γ point, corresponding to a temperature of $\sim 3 \times 10^4$K.

For these reasons the vast majority of the electronic properties of graphene are dominated by the low energy spectrum [6]. These are obtained by analysing the dispersion in the vicinity of the two sets of inequivalent so-called Dirac points [7], labelled K and K' in figure 2.16(b). These points make up the six vertices of the hexagonal BZ of graphene in momentum space [6]. These six cones alternate between K and K' as the perimeter of the honeycomb shape is traversed. Figure 2.16(b) also shows the first reciprocal unit cell of graphene, which can be considered a rhombus [6] encasing two of these cones.

The values of q_x and q_y at which these Dirac points occur are determined by setting $\varepsilon_{\mathbf{q}} = 0$ in equation 2.24, and are given by $\mathbf{K}^{\tau}= \tau\frac{4\pi}{3\sqrt{3}a}(1,0)$, as $\mathbf{K} = -\mathbf{K}'$, where $\tau= \pm 1$ refers to each valley (or cone). When studying graphene, these are the primary points of interest [7].

The Hamiltonian describing this system, in the 2×2 space of Bloch amplitudes (u_A, u_B) reads

$$H = \begin{pmatrix} 0 & -t\sum_{i=1}^{3} e^{-\mathrm{i}\mathbf{q}\cdot\mathbf{e}_j} \\ -t\sum_{i=1}^{3} e^{\mathrm{i}\mathbf{q}\cdot\mathbf{e}_j} & 0 \end{pmatrix} . \tag{2.25}$$

Here, the signs in the exponent ensure that the matrix is Hermitian. Expanding this around the Dirac point, $\mathbf{K}^{\tau}$, and introducing the Fermi velocity $v_F= \frac{3ta}{2\hbar} \sim 10^6\text{ms}^{-1}$ [87], the effective low energy Hamiltonian reads

$$\begin{aligned} H^{\tau} &= v_F\hbar \begin{pmatrix} 0 & \tau k_x - \mathrm{i}k_y \\ \tau k_x + \mathrm{i}k_y & 0 \end{pmatrix} , \\ &= v_F\hbar(\tau\sigma_x k_x + \sigma_y k_y), \\ &= v_F\boldsymbol{\sigma}\cdot\mathbf{p} \ , \end{aligned} \tag{2.26}$$

where $\mathbf{p} = \hbar\left(k_x, k_y\right)$ is the electronic momentum in 2D, with $\hbar$ being the reduced Planck constant and the wavevector is measured from a Dirac point such that $\mathbf{k} = \mathbf{q} - \mathbf{K}^{\tau}$ with $|\mathbf{k}| \ll |\mathbf{K}^{\tau}|$, and $\hat{\boldsymbol{\sigma}}= (\hat{\sigma}_x, \hat{\sigma}_y)$ are the Pauli matrices in the sublattice space (A, B), which are given here for clarity (along with others needed later)

$$\sigma_x = \begin{pmatrix} 0 & 1 \\ 1 & 0 \end{pmatrix}, \quad \sigma_y = \begin{pmatrix} 0 & -\mathrm{i} \\ \mathrm{i} & 0 \end{pmatrix}, \quad \sigma_z = \begin{pmatrix} 1 & 0 \\ 0 & -1 \end{pmatrix}. \tag{2.27}$$

By substituting the low energy Hamiltonian, given in equation 2.26, into the Schrödinger equation the eigenvalues of the system can be found, reading

$$\varepsilon_{\mathbf{k}} = s v_F \hbar |\mathbf{k}| \tag{2.28}$$

where $\mathbf{k} = (k_x, k_y)$, and $s=$ sign$(\varepsilon_{\mathbf{k}})$ such that $s = +1$ for the conduction band (electrons) and $s = -1$ for the valence band (holes).

The linear dispersion means that the quasiparticles act as though they are massless. This is similar to the dispersion of other massless relativistic particles (for example photons) [90], but the role of the speed of light is played here by the Fermi velocity, $v_F \simeq \frac{c}{300}$ [87]. The linear dispersion of graphene is valid up to an energy of approximately 2eV. This equates to a temperature of approximately 10^4 K, so for most applications, unless the Fermi level is far removed from the Dirac point by, for example, heavy doping, graphene's dispersion can be considered to be linear. When many-body effects are neglected this description is theoretically accurate [91–93] and has been proven experimentally [8] in the presence of magnetic fields by measuring the Shubnikov-de Haas effect, and most evidently by observing a relativistic analogue of the integer quantum Hall effect [9], which, incidentally, has been reported to occur at room temperature [94].

The linear spectrum is unusual when compared to the often parabolic (free-electron-like) dispersion of conventional metals and semiconductors [44], leading to the expectation of very unusual properties. The electronic properties of graphene and some of its transport properties are further discussed in section 2.5.3.

2.5.2 Massless Dirac Fermions

In this section I consider the eigenstates of monolayer graphene. Using the Hamiltonian given in equation 2.26 along with the dispersion in equation 2.28, I determine the plane wave eigenstate with a wavevector $\mathbf{k}$, reading

$$|\psi^{\tau}_{\mathbf{k},s}\rangle = \frac{1}{\sqrt{2}} \begin{pmatrix} 1 \\ \tau s e^{\mathrm{i}\tau\phi_{\mathbf{k}}} \end{pmatrix} e^{\mathrm{i}\mathbf{k}\cdot\mathbf{r}} = u^{\tau}_{\mathbf{k},s} e^{\mathrm{i}\mathbf{k}\cdot\mathbf{r}} \tag{2.29}$$

where $\phi_{\mathbf{k}} = \arctan\left(\frac{k_y}{k_x}\right)$.

Usually, in condensed matter physics, electrons and holes are described by separate Schrödinger equations [44, 95]. However, in graphene-like systems electron and hole states are interconnected, showing properties analogous to charge-conjugation symmetry in quantum electrodynamics (QED) [91–93]. This symmetry is due to the crystal symmetry, where the two-component wavefunction (describing the system at low energies) is needed to define the relative contributions from the A and B sublattices in the quasiparticle's state [83]. This description is reminiscent of the two-component spinor wavefunctions in QED, where the real spin of the electrons is replaced by the sublattice index in graphene leading to the name "pseudospin" [87].

Dirac fermions in graphene have special properties which are related to this extra internal degree of freedom (pseudospin), and its connection with momentum. Some of these properties are described in the following sections.

2.5.3 Pseudospin Related Electronic Properties of Graphene

Fermi-level tunability with doping and gate voltage

In perfect graphene, the Fermi level sits at the Dirac point, at $\varepsilon_F = 0$ [86, 96]. However, in reality, most graphene flakes have some local doping due to various sources of inhomogeneity. In addition to that, the level of doping in the sample can be changed by applying a gate voltage. A positive gate voltage increases the concentration of electrons and a negative one decreases it, as shown in figure 2.18 [4], which is crucial for device applications.

In fact, figure 2.18 [96] shows the resistivity of graphene at different gate voltages, as the Fermi level is tuned across the neutrality point. There is a peak in the resistivity at zero gate voltage, which corresponds to the Fermi level being at $\varepsilon = 0$. This is because close to the Dirac point the density of states of electrons vanishes linearly, yielding a dramatic suppression of the conductivity. Interestingly, the conductivity does not vanish at the neutrality point. I will discuss the origin of the minimal conductivity in graphene in the following.

Chirality

Graphene's conical dispersion at low energies is due to the intersection of two energy bands [7]. The two bands are indicated by the different coloured lines in figure 2.19. Therefore an electron with energy ε propagating in the positive x-direction (to the right in figure 2.19) originates from

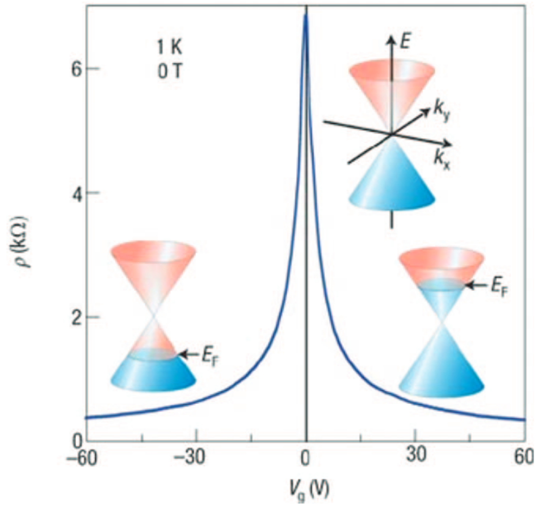

Figure 2.18: Schematic diagram showing the resistivity of monolayer graphene for different gate voltages. Under gate bias, the Fermi level moves above or below the Dirac point to introduce a significant number of free carriers. It has been noticed that, even at the Dirac point, the resistivity does not diverge but remains finite despite the vanishing density of states [4].

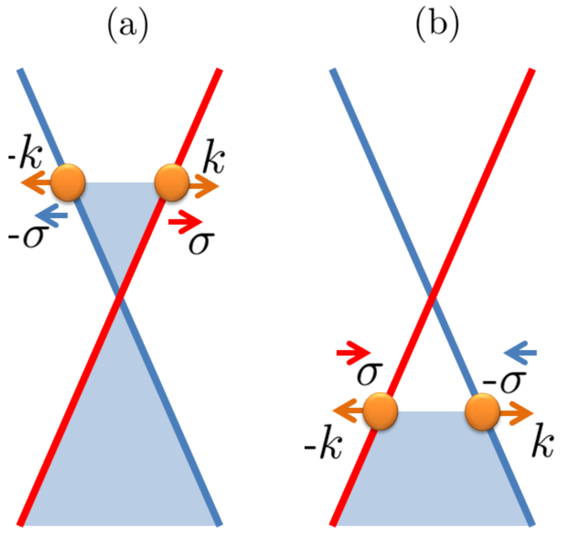

Figure 2.19: A schematic of the low energy linear band structure of graphene in the K valley showing the direction of pseudospin, $\boldsymbol{\sigma}$, for electrons (in panel (a)) and holes (in panel (b)) on both bands.

the same branch of the electronic spectrum as the hole with energy -ε propagating in the opposite direction [87]. As the pseudospin, $\boldsymbol{\sigma}$, points parallel to the electron momentum and antiparallel to the hole momentum, electrons and holes from the same branch have pseudospin pointing in the same direction.

This leads to the introduction of chirality; which is defined as a projection of the pseudospin in the direction of motion (in the K valley it is positive for electrons and negative for holes, and vice-versa in the K' valley) [87].

This can be seen mathematically, by letting the pseudospin and electron momentum be $\boldsymbol{\sigma} = (\sigma_x, \sigma_y, \sigma_z)$, and $\mathbf{p} = (p_x, p_y, 0)$, respectively. In fact, the secular equation in the valley $\tau = +$ (i.e. the K Dirac point) leads to $v_F \boldsymbol{\sigma} \cdot \mathbf{p}\psi = \epsilon\psi = s v_F |\mathbf{p}|\psi$. From this the definition of chirality reads [83]:

$$\frac{\boldsymbol{\sigma} \cdot \mathbf{p}}{|\mathbf{p}|} = s\mathcal{I}^{(2)} \tag{2.30}$$

where $\mathcal{I}^{(2)}$ is 2×2 identity matrix in the sublattice space. Thus in the K valley ($\tau = +1$) the pseudospin of electrons ($s = +1$) is aligned to the momentum, while for holes ($s = -1$) it is anti-aligned.

The chirality eigenvalue is a good quantum number of the eigenstates in graphene and has crucial physical consequences. In fact, the conservation of chirality leads to the absence of elastic backscattering from smooth potentials. This can be seen by writing the matrix element of a smooth impurity potential $\hat{V} = \mathcal{I}^{(2)} V_0$ between two electron states (given in equation 2.29) with opposite wave vectors $\langle \psi_{\mathbf{k}',s'} | \hat{V} | \psi_{\mathbf{k},s} \rangle$. If $\mathbf{k}' = -\mathbf{k}$ the propagation direction is $\phi_{\mathbf{k}'} = \phi_{\mathbf{k}} + \pi$, and the matrix element is proportional to $V_0(1 + ss'e^{i\pi})$. From this it can be seen that the matrix element will vanish for $s = s'$, which is the case for elastic backscattering with $\varepsilon_{-\mathbf{k}} = \varepsilon_{\mathbf{k}}$. Inter-valley scattering is the only way for back scattering processes to occur but, for smooth potentials, this is highly suppressed due to the large momentum transfer it involves, of the order of $\frac{8\pi\hbar}{3\sqrt{3}a}$. The absence of backscattering from impurities with smooth potentials (such as Coulomb scatterers) has important consequences for the calculation of the electrical conductivity of graphene, as only sharp impurities (such as vacancies in the atomic lattice) can cause backscattering. Thus, the low electrical resistivity and high mobility seen in graphene devices is a direct manifestation of the nature of electrons as massless Dirac fermions and is not simply due to particularly high quality samples, nor to a lack of impurities.

Berry Phase

As a particle, in an eigenstate of a quantum system, is transported adiabatically around a closed loop in momentum space it acquires a geometrical phase factor in addition to the dynamical phase factor [97]. The former is called Berry phase (BP) [97]. As the transportation of the particle follows the adiabatic theorem [98], at any instant the system will be in an eigenstate of the instantaneous Hamiltonian [97], and therefore if the Hamiltonian is returned to its original form, then the system will return to its original state apart from some phase factor. The Aharonov-Bohm effect can be interpreted as one such geometrical phase factor [97]. This phase can be observed from the interference between this cycled system and another whose Hamiltonian was not changed [97].

In most semiconductors, which have a parabolic energy spectrum, the quasiparticles often do not accumulate a BP at all. However, as a consequence of the chiral nature of graphene's quasiparticles and the linear spectrum, quasiparticles in graphene possess a non-trivial BP of $\Phi_B = \pi$. In graphene it is the coupling between the pseudo spin and momentum, due to the chirality condition, which leads to a non-trivial geometrical phase being accumulated as the particle travels in a closed loop around a Dirac point.

I can derive this in two ways, the first of which is to explicitly calculate the BP from its definition in terms of the graphene two-component spinors, and substitute the eigenvectors in equation 2.29 into [97]

$$\Phi_{\mathrm{B}} = -\mathrm{i}\oint_{c} \langle \psi(\phi) | \partial_{\phi} \psi(\phi) \rangle \mathrm{d}\phi \ . \tag{2.31}$$

I consider an anti-clockwise path around the Dirac point, in a closed loop, c, yielding $\Phi_B = \pi$ in the K valley, and performing the same analysis on the K' valley yields $\Phi_B = -\pi$.

The second method is to calculate the BP from the definition: $\phi_B = \mathfrak{s}\Omega$, where $\mathfrak{s} = 1/2$ is the particle pseudospin, and Ω_{Ang} is the solid angle subtended by the pseudospin in an adiabatic loop [98]. Taking $\mathbf{p} = |\mathbf{p}|e^{i\phi}$ (where $\mathbf{p} \subseteq \mathbb{C}$) and substituting this into equation 2.30, the pseudospin equation becomes $\boldsymbol{\sigma} \cdot (\cos\phi, \sin\phi, 0) = \pm 1$, where the positive value is taken for the conduction band in the K valley. At $\phi = 0$, the momentum is $p_x = |\mathbf{p}|, p_y = 0$, giving $\boldsymbol{\sigma}(1,0,0) = 1$ meaning that the pseudospin in the conduction band always points outwards, away from the origin of momentum space and the solid angle is given by $\Omega_{Ang} = \int_0^{2\pi}\int_0^{\pi/2} \sin\theta d\theta d\phi = 2\pi$. Therefore the linear Hamiltonian of graphene leads to the massless Dirac fermions having a Berry's Phase given of: $\phi_B = \frac{1}{2}2\pi = \pi$ [99–102].

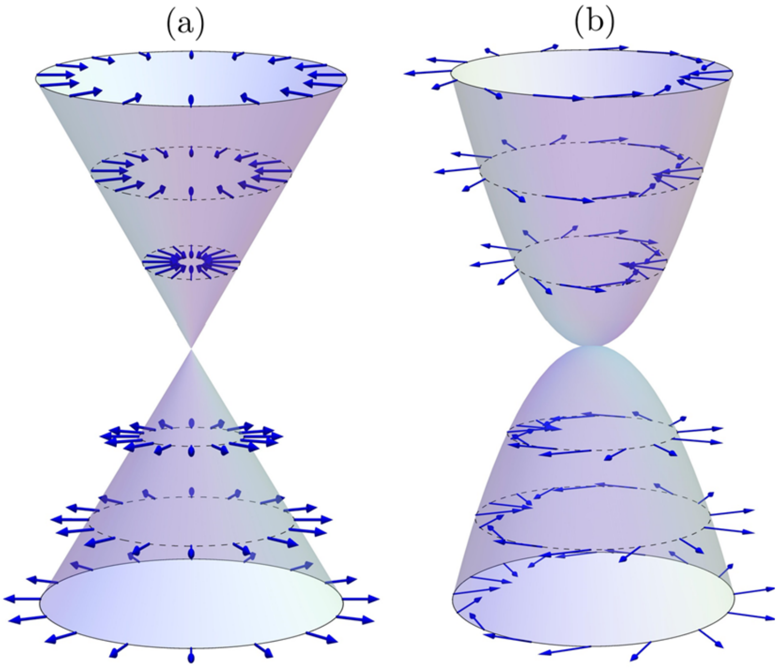

Figure 2.20: The dispersion of (a) monolayer graphene and (b) bilayer graphene in the vicinity of a Dirac point, including arrows indicating the directions of the pseudospin in each case.

Figure 2.20(a) shows the linear dispersion in the vicinity of the Dirac point and the eigenspinor orientations along a closed loop around the Dirac point, where the 2π solid angle enclosed as the pseudo-spin winds once around the loop is also evident. This non-trivial Berry phase can be seen by a shift in the de Haas-van Alphen and Shubnikov-de Haas oscillations [103, 104] and has also been detected, for example, in Quantum Hall Effect (QHE) measurements [8, 105, 106]. Furthermore the peculiar sequence of the Landau levels created in graphene can be seen as a direct consequence of the BP [9].

It is important to note that the BP exists for bosons as well as fermions [97], so it can also be found for the plasmonic systems presented in chapter 3 when analysing scenarios where the Dirac quasiparticles are transported in closed loops.

Graphene's chiral nature and BP lead to interesting tunnelling properties that are discussed in the next section.

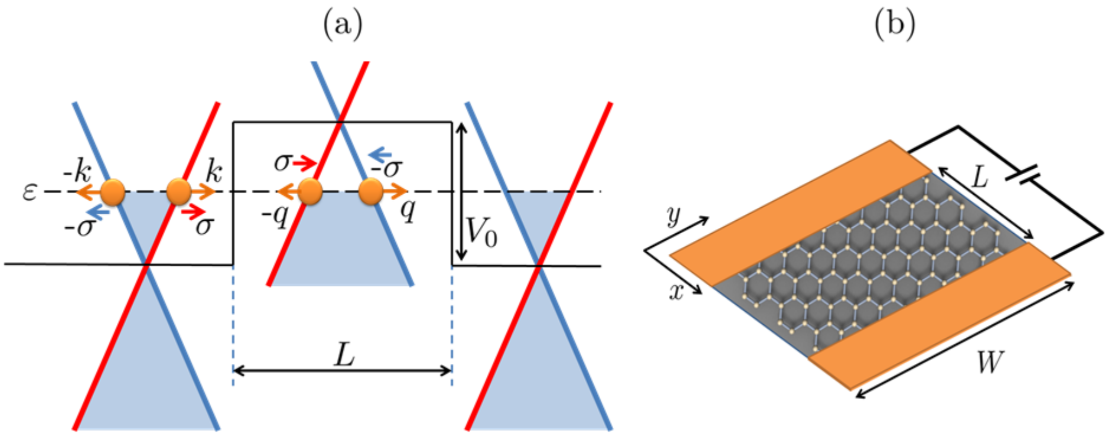

Figure 2.21: Tunnelling through a potential barrier in graphene. Panel (a) shows the potential across the sample, the zero point of the energy is chosen to be at the base of the barrier. The electron dispersion relation in monolayer graphene close to the Dirac point is shown across the sample. The red and blue curves emphasise the origin of the linear spectrum (i.e. the crossing of the energy bands associated with each of the sublattices A and B). The pseudospin, $\boldsymbol{\sigma}$, of the electrons originating from each energy band is illustrated, and is linked with the orbital momentum by the chirality condition. Panel (b) shows the device design considered here, where the material containing the Dirac particles is in a strip between two metal contacts.

Klein Tunnelling

When a conventional massive particle is incident on an electrostatic potential barrier that has a height above its kinetic energy, the associated wavefunction will become evanescent within the barrier. Non-relativistic quantum mechanics dictates that the probability the particle will tunnel through reduces exponentially with increased barrier height and width [7, 89]. This paradigm is overcome in relativistic quantum mechanics, where the Klein paradox describes the process which results in unimpeded tunnelling of relativistic particles through high and wide potential barriers [107]. Counter-intuitively the potential barrier height, V_0, should be at least twice the electron's rest mass energy, $E = mc^2$ (where m is the electron's rest mass and c is the speed of light) [87].

Although, thus far, there have been no realisations of this effect with elementary particles, Klein tunnelling has been experimentally realised in graphene [87]. As a consequence the charge carriers in graphene cannot be easily confined by electrostatic potentials [7]. The general scheme of such a tunnelling experiment is shown in figure 2.21(a), along with a possible device design in figure 2.21(b), where the potential barrier, $V(x)$, is considered to have a rectangular shape and is invariant along the y-axis, such that:

$$V(x) = \begin{cases} V_0 & \text{if } 0 < x < L \\ 0 & \text{otherwise,} \end{cases}$$

where L is the length of the barrier. In order to make a direct analogy to the case usually considered in quantum electro-dynamics (QED) [11, 108] the potential step is assumed to be sharp [87], meaning that the quasiparticle's Fermi wavelength, λ_F, is assumed to be larger than the edge smearing characteristic width. I can also assume that the latter is larger than the lattice constant so that there is no Umklapp scattering between valleys [87].

The potential barrier inverts the charge carriers underneath it, creating holes playing the role of positrons in QED, or vice versa, and tunnelling depends on the conservation of pseudospin outside and inside the barrier.

In the relativistic regime, where the particles are governed by the Dirac equation [7], the transmission probability, T, only weakly depends on the height of the barrier [87], and actually increases with increasing barrier height [7]. The electronic wavefunctions in each of the regions shown in figure 2.21(a) can be expressed from the Dirac spinors in equation 2.29 and the tunnelling probability can be found by implying the continuity of the wavefunctions across the regions [87]. A thorough derivation of the tunnelling probability of electrons in graphene is be presented in chapter 5, where I extend the treatment to include the tunnelling probability of electrons in graphene-like systems with variable amounts of broken inversion symmetry. In this section I only summarise the key results of transmission probability in graphene from the literature to add context to my later explorations.

The tunnelling probability is related to the overlap of the pseudospins outside and inside the barrier, giving selection rules at normal incidence [109–111]. As can be seen from figure 2.21(a) there are parallel pseudospins inside and outside the barrier with equal group velocity [112]. This overlap leads to perfect transmission at normal incidence in graphene [87].

Figure 2.22(a) [87] shows examples of the angular dependent transmission probability T [87] for a step-like potential barrier in monolayer graphene. In the limit of high barriers $|V_0| \gg |\varepsilon|$, the analytical expression for T reads [87]

$$T = \frac{\cos^2\phi}{1 - \cos^2(q_x L)\sin^2\phi} \ . \tag{2.32}$$

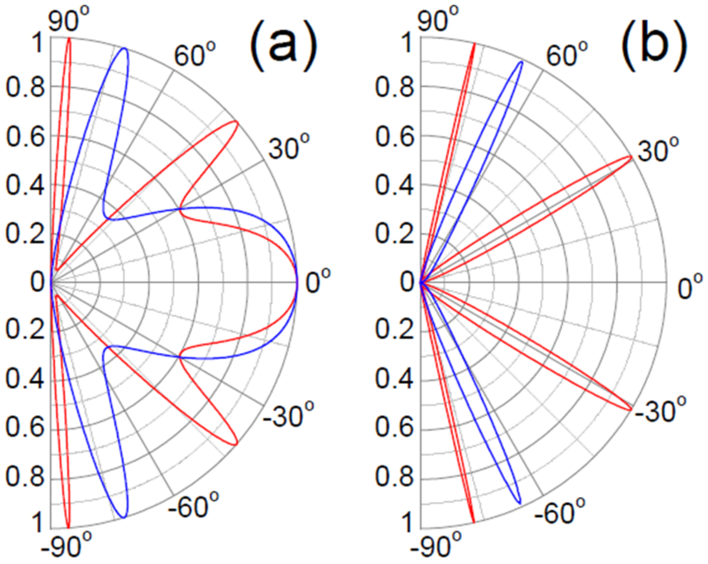

Figure 2.22: Klein tunnelling in Dirac systems. Transmission probability, T through a 100nm long barrier as a function of the incident angle for (a) single- and (b) bi-layer graphene. Considering typical experimental quasiparticle concentrations (the electron concentration outside the barrier is chosen $n = 0.5 \times 10^{12}\text{cm}^2$ for both cases, and inside the barrier, hole concentrations are $p = 1 \times 10^{12}\text{cm}^{-2}$ and $p = 3 \times 10^{12}\text{cm}^2$ for the red and blue curves, respectively). This corresponds to the Fermi energy, ε, of incident electrons as approximately 80 and 17meV for single- and bi-layer graphene, respectively. The barrier heights V_0 are (a) 200 and (b) 50meV (red curves) and (a) 285 and (b) 100meV (blue curves) [87].

---

where q_x is the wavevector in the x-direction inside the barrier.

From this equation it is evident that, under resonant conditions (when $q_xL = n\pi$, where n is an integer) the barrier becomes transparent (T=1) at normal incidence. Even more importantly, perfect transmission is always seen for incident angles close to normal incidence, $\phi = 0$, as seen in figure 2.22. This transparent nature is a feature unique to massless Dirac fermions, and is a direct consequence of the conservation of pseudospin. It is important to note that this perfect transmission is the complete opposite of the perfect reflection in bilayer graphene at normal incidence [87] that is the subject of further investigation in this work.

The perfect transmission of particles in monolayer graphene at small angles has key implications for the transport properties of graphene, including the minimal conductivity at the Dirac point. Although, as the DOS goes to zero at the Dirac point one would normally expect the conductivity to go to zero here as well, apart from in disordered metals [83]. In graphene, the fact that the current operator for Dirac fermions does not commute with the Hamiltonian can be considered

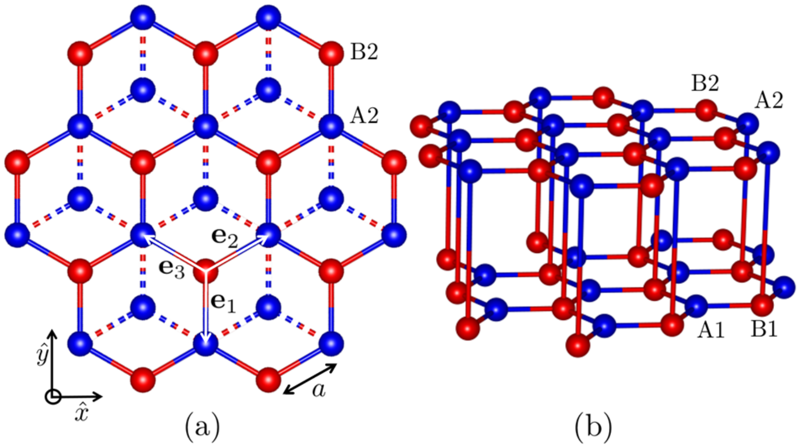

(a) (b)

Figure 2.23: The structure of bilayer graphene, where a) is a top down view showing the honeycomb structure of the top layer of bilayer graphene, and b) is a side view showing the Bernal stacking of the two layers, where the A2 site on the upper layer is directly above the B1 site on the lower layer.

---

as a kind of intrinsic disorder [83], causing the finite minimum conductivity at the neutrality point.

2.6 Bilayer Graphene

There has been increased interest in two-dimensional (2D) atomically thin materials since the discovery of graphene [3] and as such bilayer graphene has become a subject of intense interest in its own right. Similar to monolayer graphene, bilayer graphene has no band gap and its low energy Hamiltonian also describes chiral Dirac quasiparticles, that can be described by spinor wavefunctions [113, 114]. However, unlike monolayer graphene, in bilayer graphene these quasiparticles have a finite mass due to the non-zero second derivative of its energy spectrum. This is due to its parabolic spectrum. This leads to another difference between bilayer graphene and its monolayer counterpart: bilayer graphene has a BP of 2π [113] as opposed to the BP of π in the monolayer system, which gives bilayer graphene different electronic and transport properties to those seen in monolayer graphene.

2.6.1 Tight Binding Calculation for Bilayer Graphene

I consider a sheet of bilayer graphene consisting of two coupled 2D honeycomb lattices. Each layer has inequivalent sites ($A1, B1$ in the bottom sheet, and $A2, B2$ in the top sheet). These are arranged according to Bernal ($A2$-$B1$) stacking as shown in figure 2.23, where every $B1$ site lies directly below an $A2$ site, but $A1$ and $B2$ sites do not lie directly above or below a site in the other layer [114]. The dimers, created by the $A2 - B1$ coupling, lead to higher energy bands in the electronic spectrum. The two layers are separated by an interlayer distance $c = 3.34\text{Å}$.

In analogy to the monolayer case a tight binding analysis can be performed on this system to study the electronic properties of bilayer graphene [114–116]. The tight binding Hamiltonian for electrons in a bilayer Bernal stacked honeycomb lattice, considering all hopping terms between nearest neighbours, reads

$$\hat{H} = -t_{A1,B1}\sum_{\mathbf{R}_B1}\sum_{j=1}^{3}|\mathbf{R}_{B1}\rangle\langle\mathbf{R}_{B1}+\mathbf{e}_j| - t_{A2,B2}\sum_{\mathbf{R}_B2}\sum_{j=1}^{3}|\mathbf{R}_{B2}\rangle\langle\mathbf{R}_{B2}+\mathbf{e}_j| \\ - t_{A2,B1}\sum_{\mathbf{R}_B1}|\mathbf{R}_{B1}\rangle\langle\mathbf{R}_{B1}+c\hat{\mathbf{z}}| + H.c. \tag{2.33}$$

where the nearest neighbour vectors, $\mathbf{e}_j$, are the same as in the monolayer case (given in equation 2.20), $\mathbf{R}_{rl}$ is the position of an atom in the sublattice $r = A, B$ and layer $l = 1, 2$ for the top and bottom layer respectively, and $|\mathbf{R}_{rl}\rangle$ is associated with the corresponding localised orbital. Here, I only consider the dominant terms in the Hamiltonian. Thus this reduced Hamiltonian only takes into account the intralayer hopping ($t_{Al,Bl} \sim 2.6$eV [117]) and the dominant interlayer hopping ($t_{A2,B1} \sim 0.39$eV [118]). Although there are other interactions terms that produce corrections to the results at larger energies, this Hamiltonian explicitly captures the relevant physics of bilayer graphene at low energies, i.e. in the regime corresponding to the temperature range which dominates the vast majority of the electronic properties.

In equation 2.33, I used the identities: (1) $\mathbf{R}_{A1} = \mathbf{R}_{B1} + \mathbf{e}_j$ and $\mathbf{R}_{A2} = \mathbf{R}_{B2} + \mathbf{e}_j$ for the intralayer terms; and (2) $\mathbf{R}_{A2} = \mathbf{R}_{B1} + c\hat{\mathbf{z}}$ for the interlayer terms. Again, in the tight binding approximation, the hopping energy is $t_{rl,r'l'}$ for electrons hopping between sites $\mathbf{R}_{rl}$ and $\mathbf{R}_{r'l'}$.

As is the case in monolayer graphene, the electronic eigenstates in bilayer graphene are described by Bloch states of the form

$$|\psi_{\mathbf{q}}\rangle = \sum_{\mathbf{R}_{A1}} u_{A1}(\mathbf{q})e^{\mathrm{i}\mathbf{q}\cdot\mathbf{R}_{A1}}|\mathbf{R}_{A1}\rangle + \sum_{\mathbf{R}_{B1}} u_{B1}(\mathbf{q})e^{\mathrm{i}\mathbf{q}\cdot\mathbf{R}_{B1}}|\mathbf{R}_{B1}\rangle$$
$$+ \sum_{\mathbf{R}_{A2}} u_{A2}(\mathbf{q})e^{\mathrm{i}\mathbf{q}\cdot\mathbf{R}_{A2}}|\mathbf{R}_{A2}\rangle + \sum_{\mathbf{R}_{B2}} u_{B2}(\mathbf{q})e^{\mathrm{i}\mathbf{q}\cdot\mathbf{R}_{B2}}|\mathbf{R}_{B2}\rangle \tag{2.34}$$

where $u_{rl}(\mathbf{q})$ is the Bloch amplitude of the wavefunction in the sublattice r on layer l with wavevector $\mathbf{q}$. The Hamiltonian in the 4×4 space of Bloch amplitudes $(u_{A1}, u_{B2}, u_{A2}, u_{B1})$ reads

$$\hat{H} = \begin{pmatrix} 0 & 0 & 0 & -tf^*_{\mathbf{q}} \\ 0 & 0 & -tf_{\mathbf{q}} & 0 \\ 0 & -tf^*_{\mathbf{q}} & 0 & -\gamma \\ -tf_{\mathbf{q}} & 0 & -\gamma & 0 \end{pmatrix} \tag{2.35}$$

where $f_{\mathbf{q}} = \sum_{j=1}^{3} e^{\mathrm{i}\mathbf{q}\cdot\mathbf{e}_j}$ and, the intralayer hoping terms are taken as equal, such that $t = t_{A1,B1} = t_{A2,B2}$[1], and the dominant interlayer hoping is denoted as $\gamma = t_{A2,B1}$.

Expanding equation 2.35 around a Dirac point (i.e. measuring the wavevector from the Dirac point, $\mathbf{k} = \mathbf{q} - \mathbf{K}$), gives

$$\hat{H}^{\tau} = \tau \begin{pmatrix} 0 & 0 & 0 & v\hbar k^* \\ 0 & 0 & v\hbar k & 0 \\ 0 & v\hbar k^* & 0 & -\tau\gamma \\ v\hbar k & 0 & -\tau\gamma & 0 \end{pmatrix} \tag{2.36}$$

where the intralayer group velocity is $v = \frac{3at}{2\hbar} \approx 8 \times 10^5 \mathrm{ms}^{-1}$.

The Hamiltonian shown in equation 2.36 can be diagonalised to obtain the four band dispersion:

$$\varepsilon_{\mathbf{k}} = \pm\frac{\gamma}{2} \pm \sqrt{v^2\hbar^2|\mathbf{k}|^2 + \frac{\gamma^2}{4}}\ , \tag{2.37}$$

a cross-section of which, at $k_y = 0$, is shown in figure 2.24. All combinations of the signs on the right hand side are allowed, leading to four possible bands in the dispersion. Expanding this further, in the low energy region $\frac{v\hbar|\mathbf{k}|}{\gamma} \ll 1$ gives

---

[1] The intralayer hoping terms can differ, for example, in supported bilayer samples, where the substrate may lead to different hopping strengths in the two layers.

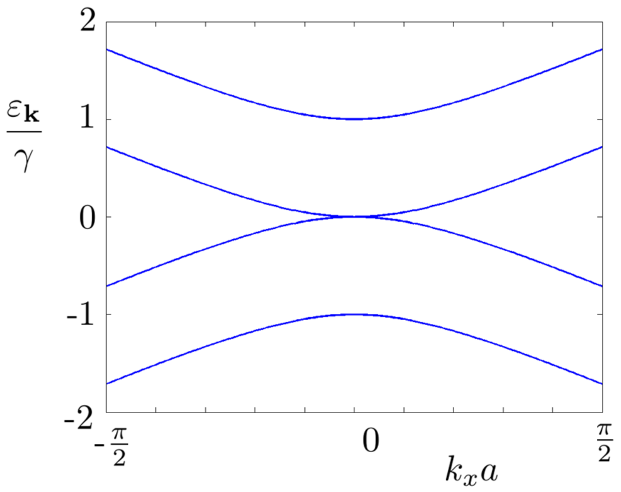

Figure 2.24: Bilayer graphene's four band electronic energy spectrum, where a cut is taken at $k_y = 0$.

$$\varepsilon_{\mathbf{k}} = \pm\frac{\gamma}{2} \pm \frac{\gamma}{2} \pm \frac{\hbar^2|\mathbf{k}|^2}{2m} \ , \tag{2.38}$$

where $m = \frac{\gamma}{2v^2}$ is the effective mass.

Two of the bands shown in equation 2.38 touch at $\varepsilon_{\mathbf{k}} = 0$ while, due to the vertical $B1 - A2$ interlayer hopping, the other two are off-set by an energy $\varepsilon_{\mathbf{k}} = \pm\gamma$. This electronic dispersion is parabolic, therefore it describes 2D massive particles.

The two bands that touch at $\varepsilon_{\mathbf{k}} = 0$ are primarily used to describe bilayer graphene's electronic transport properties at low energy, $|\varepsilon| < \gamma$, and up to an electron density $n_0 = 4 \times 10^{13}\text{cm}^2$, where the higher bands start to be populated [114]. In the $\Psi = (\psi_{A1}, \psi_{B2})$ basis, the 2×2 effective Hamiltonian for the low energy bands reads [114, 119]

$$\hat{H} = \begin{pmatrix} 0 & \frac{\hbar^2(k^\dagger)^2}{2m} \\ \frac{\hbar^2 k^2}{2m} & 0 \end{pmatrix} \ . \tag{2.39}$$

2.6.2 Massive Dirac Fermions

By solving the eigenvalue equation using the Hamiltonian shown in equation 2.39 the electronic eigenstates of bilayer graphene in the low energy approximation can be expressed as:

$$|\psi_{\mathbf{k}}^{\tau}\rangle = \frac{1}{\sqrt{2}}\begin{pmatrix} 1 \\ \tau s e^{\mathrm{i}\tau 2\phi_{\mathbf{k}}} \end{pmatrix} e^{\mathrm{i}\mathbf{k}\cdot\mathbf{r}} = u_{\mathbf{k}}^{\tau} e^{\mathrm{i}\mathbf{k}\cdot\mathbf{r}} \ . \tag{2.40}$$

Similarly to graphene, the two component spinor here again refers to a pseudospin, and in this two band form it relates to the distribution of the electron wavefunction on the $A1$ and $B2$ lattice sites. However, in contrast to the monolayer case, here it can be seen that there is a factor of 2 in the exponent of the phase factor, which arises from the parabolic spectrum at low energies. This factor of 2 means that as an electron travels in a closed loop around the Dirac point in momentum space, its eigenvector winds around twice. This leads to several important properties of massive Dirac fermions; for example, it leads to bilayer graphene having a Berry phase of 2π.

As the rate at which the pseudo spin rotates when an electron travels around the Dirac point is twice that seen in monolayer graphene, electronic states with opposite momenta ($\mathbf{k}$ and $-\mathbf{k}$) are described by the same pseudospin (σ), as illustrated in figure 2.20(b). Thus there can be scattering between states with momentum **k** and -**k**, and therefore, in complete contrast to its monolayer counterpart, in bilayer graphene elastic back scattering from smooth potentials is allowed.

2.6.3 Transport Properties and Klein Tunnelling

Theoretical [116, 120–130] and experimental [8, 9, 131–137] investigations into the unusual transport properties exhibited by bilayer graphene have discovered that the minimum conductivity is twice the value found in monolayer graphene.

I now consider a tunnelling device like that investigated for monolayer graphene, as shown in figure 2.21, and analyse the phenomenon of Klein tunnelling in the bilayer case. The chiral nature of the quasiparticles means that Klein tunnelling can also occur in bilayer graphene, however, the significant differences between the pseudospins in monolayer and bilayer lead to very different tunnelling probabilities [87]. The parabolic spectrum leads to four possible wavevector solutions for a given energy, and a given transverse wavevector k_y; two corresponding to propagating waves and two to evanescent ones. To calculate the transmission probability it is then necessary to satisfy the boundary conditions for the system, which, using the low energy approximation shown in equations 2.39 and 2.40, require both the continuity of the wavefunction and its spatial derivative at the boundaries. A thorough derivation of the transmission probability in bilayer graphene is conducted in a later chapter (chapter 6) where I extend the research to describe transport in biased bilayer graphene, but here I present a summary of the main results of Klein tunnelling in bilayer graphene from the literature.

When $\varepsilon < V_0$ there is perfect reflection at normal incidence [87], which is highly unusual as one would normally expect some tunnelling due to the continuum of electronic states available inside the barrier. Similarly to monolayer graphene, this can be explained by the overlap of the pseudospin outside and inside the barrier, or in this case the lack there of. The absence of conservation of pseudospin at normal incidence can be inferred from figure 2.20(b), and the perfect reflection can be seen in figure 2.22(b).

Considering the simple case of a potential step consisting of a single $p - n$ junction with $V_0 \gg \varepsilon$, the transmission probability for an angle ϕ is given by [87]

$$T = \frac{\varepsilon}{V_0} \sin^2 (2\phi) \tag{2.41}$$

which also gives $T = 0$ for $\phi = 0$.

In figure 2.25 [87] the normal incidence transmission probability of bilayer graphene is compared to that of monolayer graphene, and also to that expected from a non chiral material. The transmission probability for bilayer graphene decays exponentially with the barrier length, even though there are electronic states inside the barrier [87].

2.7 Dirac Materials with Broken Inversion Symmetry

The idea of opening a gap in monolayer graphene's electronic spectrum has gained a lot of attention as this would allow its remarkable properties to be used in devices, where the gap could be used to compensate for the low on/off ratios found in graphene, and hence they may be useful for fabricating transistor devices containing Dirac quasiparticles. This gap can be achieved by breaking the inversion symmetry of graphene; creating a difference between the on-site energies of the A and B sublattice which is described by a σ_z term in the matrix Hamiltonian. Breaking the inversion symmetry of graphene has been attempted in several ways, for example by placing monolayer graphene on top of hexagonal boron nitride, which lacks sublattice inversion symmetry [138]. It is possible that the graphene sheet can inherit this broken inversion symmetry and a band gap can be produced. The gap size depends on the stacking between the layers, and on how many layers are used [139]. This method is especially attractive due to the fact that the measured

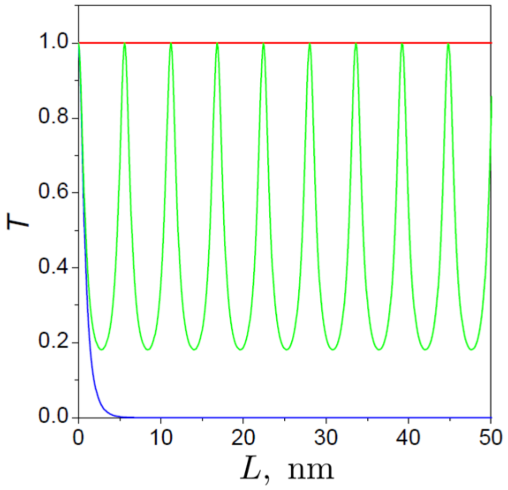

Figure 2.25: Transmission probability T for normally incident electrons in single- and bi- layer graphene (red and blue curves, respectively) and also in a non-chiral zero-gap semiconductor (green curve) as a function of length, L, of the tunnel barrier. The calculations took the same concentration of charge carriers for all three materials ($n = 0.5 \times 10^{12}\text{cm}^2$ and $p = 1 \times 10^{13}\text{cm}^2$ outside and inside the barrier, respectively), with the barrier height taken as 450meV for graphene and 240meV for the other two materials [87].

mobilities of graphene on a hexagonal boron nitride substrate are comparable to that of suspended graphene [139]. Other methods include cutting graphene into nanoribbons, however this has not gained as much interest because lots of graphene's electronic properties are diminished due to the destruction of the honeycomb lattice.

Furthermore, many natural materials exist which already present spectra like that of graphene but with a gap, for example transition metal dichalcogenides. These are a type of layered materials that can be isolated into 2D atomically thin monolayer sheets. These semiconductors are of the type MX_2, where M is a transition metal atom and X is a chalcogen atom, for example MoS_2, $MoSe_2$, and WS_2. This family of semiconductors has a common crystal structure consisting of a series of strongly bonded 2D X-M-X layers loosely coupled to each other by Van der Waals interactions [140, 141], as shown in figure 2.26 for MoS_2. Dirac features appear in these materials because of their planar structure being that of a honeycomb, which can also be seen in figure 2.26. There has been a lot of interest in these semiconductors because, in contrast to their bulk forms, where they have an indirect band gap, monolayers of these materials are direct bandgap semiconductors [142, 143], with a band gap in the optical frequency range, which is ideal for optoelectronic applications [144]. MoS_2 has gained particular interest for optical [145, 146] and electronic de-

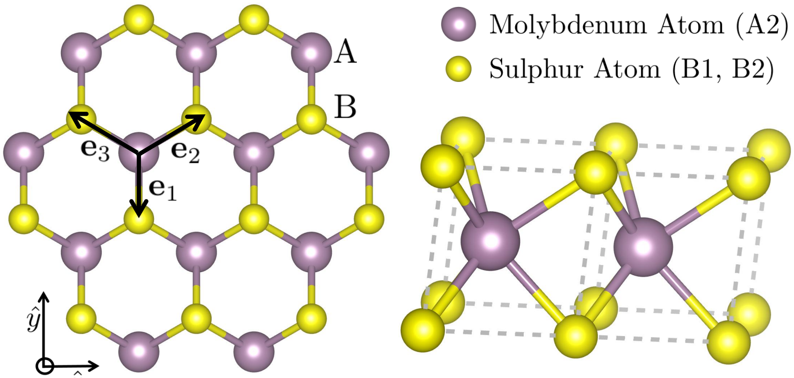

(a) (b)

Figure 2.26: The atomic structure of MoS_2; a) A top down view of the honeycomb lattice with the vectors e_j $(j = 1, 2, 3)$ which connect the A and B sublattices. Two sulphur atoms sit directly above one another to form the honeycomb structure. b) Side view of the lattice showing the three layered structure, representing the ‘monolayer’ of MoS_2.

vices [147, 148] with MoS_2 field effect transistors being experimentally realised to possess room temperature mobilities of $\sim 200\text{cm}^2\text{V}^{-1}\text{s}^{-1}$ [149].

Despite the existence of a band gap, quasiparticles in both materials like graphene on hexagonal boron nitride and transition-metal dichalcogenides behave similarly to those in graphene, and as such can be described by a modified effective low energy Dirac Hamiltonian [144].

Therefore, the general results presented here will also be applicable to any material consisting of a honeycomb lattice with broken inversion symmetry.

The zero energy point is defined to be exactly in the middle of the band gap and the low energy effective Hamilton can be written, including only leading order terms, as

$$\hat{H}^{\tau} = v\hbar\left(\tau_z\sigma_x k_x + \sigma_y k_y\right) - \frac{\Delta}{2}\sigma_z \quad . \tag{2.42}$$

where σ_i are the Pauli matrices in the sublattice space (A, B), τ_i are the Pauli matrices in the valley space (K, K'), and Δ is the gap size, which in MoS_2 is $\sim 1.8\text{eV}$ [146]. This Hamiltonian is written in the basis $\psi = (\psi_A, \psi_B)$ for the A and B sublattices of both graphene on hexagonal boron nitride and transition metal dichalcogenides. In the latter, one sublattice corresponds to the symmetric combination of the orbitals on the X atoms and the other to the M atom.

Here it is important to note that this analysis does not include any spin orbit coupling. In transition metal dichalcogenides spin-obit coupling arises due to the broken inversion symmetry in the honeycomb lattice and the broken spin degeneracy along the $\Gamma - K$ high symmetry line in the BZ. Spin-orbit coupling has been shown to be important for describing some of the transport properties of these materials.

2.8 Chapter Summary

In this chapter I described the relevant theory of plasmonic metamaterials and Dirac materials to provide the basis necessary for understanding the work contained in further chapters. Specifically, I have introduced the fundamental concepts concerning arrays of plasmonic metamaterials, and discussed the electronic properties of some Dirac materials that I aimed to map onto the former. This has included explanations of bulk and surface plasmons, moving on to consider LSP in metallic nanoparticles in more detail. I note that LSPs can be excited in nanoparticles with the use of external electromagnetic radiation, and the interactions between LSP was discussed for different particle separations such that near- and far- field coupling was described. Coupled LSP constitute a bridge to metamaterials, where in some cases patterned surfaces (for example arrays of nanoparticles) are designed to produce properties not seen in nature. I consider nanoparticles close enough together that near-field coupling dominates so the quasi-static approximation can be taken and the LSP interactions can be considered as dipole-dipole interactions. Then some results are presented for CPs in dimers, linear chains and 2D square arrays of metallic nanoparticles.

As the properties of the CP in arrays depends on the array structure, and there are infinitely many possible structures, some materials which have recently exhibited exciting properties due to their structures have been presented. First I considered graphene, a natural Dirac material. Its electronic and transport properties, have been displayed. The chiral nature of the Dirac quasiparticles leads to an absence of back scattering from smooth scatterers which increases the intrinsic conductivity of graphene. This fundamental result is due to the honeycomb structure of graphene, and as such is one of the things my research attempts to mimic in plasmonic metamaterials.

Then other materials with different honeycomb structures were considered to analyse the properties arising from variations on the lattice structure. In particular I have discussed some of the electronic properties of bilayer graphene and Dirac materials with broken inversion symmetry.

3

Honeycomb Array of Metallic Nanoparticles

The research presented in this chapter is work I conducted with guidance from Eros Mariani that resulted in the recent papers [150, 151], in collaboration with Guillaume Weick, Bill Barnes, Ortwin Hess, Eros Mariani and Thomas Sturges.

The evanescent field at the surface of a metallic nanoparticle, associated with the LSP resonance [18], produces strong optical field enhancement in the subwavelength region, allowing one to overcome the diffraction limit and achieve resolution at the molecular level [14, 46, 47]. While the field of plasmonics mostly focuses on single or few structures, the creation of ordered arrays of nanoparticles constitutes a bridge to the realm of metamaterials. Plasmonic metamaterials can exhibit unique properties, even beyond those seen in nature. The interaction between LSPs on individual nanoparticles generates extended plasmonic modes involving all LSPs at once [31–34, 36, 37]. Understanding the nature and properties of these plasmonic modes, referred to as collective plasmons (CPs), is of crucial importance as they are the channel guiding electromagnetic radiation with strong lateral confinement over macroscopic distances.

CPs in periodic arrays of metallic nanoparticles are an active area of research in plasmonics because interactions between the LSP resonances can lead to dramatic changes in the overall optical response of such structures. The properties of the combined system can be very different to those of individual nanoparticles, for example, it was both predicted [152, 153] and observed [30, 154, 155] that the plasmonic response of a periodic array of nanoparticles could be significantly narrowed with respect to the single particle response. The dispersion of CPs and their physical nature critically depend on the lattice structure of the metamaterial and on the microscopic interaction between LSPs. A lattice which has recently generated remarkable interest in the condensed matter community is the honeycomb structure of graphene [3]. Here, the hopping of electrons between neighbouring atoms gives rise to a rich band structure characterised by the presence of fermionic massless Dirac quasiparticles at low energies [5, 6]. The chirality associated with pseudo-relativistic Dirac fermions results in several of the remarkable properties of graphene, such as a nontrivial Berry phase accumulated in parallel transport [8,9] and the suppression of electronic backscattering from smooth scatterers [10], as described in section 2.5. Most of graphene's exceptional properties stem from its honeycomb structure. Undoubtedly, it would be exciting to harvest the remarkable physical properties of electrons in graphene in suitably designed plasmonic metamaterials by analysing the Hamiltonian and the consequent nature of CP eigenmodes in 2Dhoneycomb lattices of metallic nanoparticles. This is the purpose of the present chapter.

The outline of this chapter is as follows: Initially, in section 3.1, I outline the key physical parameters and assumptions considered in this chapter. In section 3.2, I first discuss the problem of mapping the Dirac-like nature onto a plasmonic metamaterial classically, utilising the methods described in chapter 2. The result is a conical CP dispersion of classical plasmons in a honeycomb lattice of nanoparticles, which has been discussed numerically in the past though only for out-of-plane or purely inplane polarisation [156]. In quite different physical systems (*e.g.*, photonic crystals [157–161], acoustic waves in periodic hole arrays [162], and cold atoms [163]), conical dispersions were also found in artificial graphene due to the honeycomb symmetry. However, the existence of a conical dispersion is not sufficient to prove the physical analogy between quantum CPs in honeycomb plasmonic lattices and electrons in graphene [164]. In order to achieve that, in section 3.3, I analytically show how the problem of interacting LSPs in the honeycomb structure can be quantum mechanically mapped to the kinetic problem of electrons hopping in graphene, yielding massless Dirac-like bosonic CPs in the vicinity of two Dirac points in the Brillouin zone (BZ). I then further consider the tunability of the plasmonic metamaterial with LSP polarisation, where I show it is possible to open a gap in the CP spectrum. As this system is fully tunable with respect to the polarisation angle of the LSPs, I investigate in detail the CP dispersion relation for different dipole orientations and identify a rich phase diagram of gapped as well as gapless phases, where the CPs are shown to behave as massless Dirac bosonic excitations. Moreover, I locate regions away from the graphene-like case (when the dipoles are polarised normal to the plane) that also support massless Dirac bosons, deducing that, in some cases, these cones can have differing phase velocities in orthogonal directions. These Dirac cones move around in wavevector space as the polarisation angle is varied, coming together to annihilate each other in order to open a gap. This leads to the possibilty of a fully tunable plasmonic analogue of graphene.

3.1 Arrangement Description

I consider an ensemble of identical spherical metallic nanoparticles of radius r forming a 2D honeycomb lattice with lattice constant a, shown in figure 3.1, embedded in a dielectric medium with dielectric constant ϵ_d. The nanoparticles are located at positions $\mathbf{R}_s$, where $s = A, B$ is a sublattice index which distinguishes the inequivalent lattice sites. The nearest neighbour vectors, $\mathbf{e}_j$, are given by

$$\mathbf{e}_1 = a\begin{pmatrix} 0 \\ -1 \end{pmatrix}, \qquad \mathbf{e}_2 = \frac{a}{2}\begin{pmatrix} \sqrt{3} \\ 1 \end{pmatrix}, \qquad \mathbf{e}_3 = \frac{a}{2}\begin{pmatrix} -\sqrt{3} \\ 1 \end{pmatrix}. \tag{3.1}$$

Each individual spherical nanoparticle supports a LSP resonance which can be triggered by an oscillating external electric field with wavelength $\lambda \gg r$. Under such a condition, the LSP is a dipolar collective electronic excitation with a resonant frequency, ω_0. This frequency depends on the nanoparticle's environment [18] and typically lies in the visible or near-infrared parts of the electromagnetic spectrum [18]. Also, providing this wavelength is much larger than the nanoparticle separation, I assume each of the LSPs are polarised along a common direction (either parallel or antiparallel to each other), as described in chapter 2.

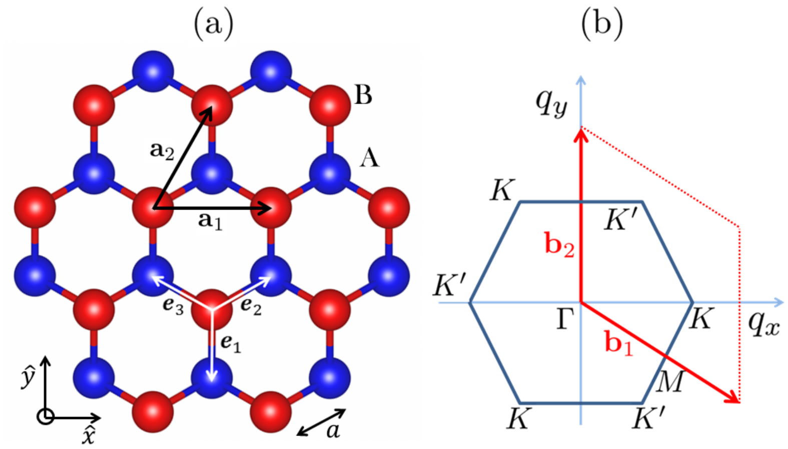

Figure 3.1: Panel (a) shows a schematic diagram of a honeycomb array of metallic nanoparticles inspired by the lattice of graphene. This structure consists of two inequivalent triangular sublattices noted here as A and B, shown as blue and red, respectively, that is invariant under 120° rotations around any lattice site. The nanoparticles are separated by a distance a and the lattice vectors read $\mathbf{a}_1 = a\left(\sqrt{3}, 0\right)$ and $\mathbf{a}_2 = a\left(\frac{\sqrt{3}}{2}, \frac{3}{2}\right)$. The nearest neighbour lattice vectors, $\mathbf{e}_j$, are given in equation 3.1. In panel (b), I show the first reciprocal unit cell of the honeycomb lattice in reciprocal space made by connecting the two reciprocal lattice vectors $\mathbf{b}_1 = \frac{2\pi}{3a}\left(\sqrt{3}, -1\right)$ and $\mathbf{b}_2 = \frac{4\pi}{3a}(0, 1)$, as a red rhombus. The K and K' points are visible, which alternate around the honeycomb Brillouin zone shown here in blue. Both of these can be seen to contain two inequivalent Dirac points.

3.2 Classical Approach

In contrast to graphene, where the interparticle hoping strength decays exponentially, the interaction strength in plasmonic arrays is inversely proportional to the distance cubed, so that further neighbour interactions can have a noticeable effect on the system. However, in the subsequent sections, it will be seen that contributions from further neighbours have no qualitative effect on the resulting properties, and thus a model that includes only nearest neighbour interactions is adequate.

Using the same method described in chapter 2, again taking the approximation of aligned dipole moments, the Lagrangian of the system reads

$$
\begin{aligned}
L = \sum_{\mathbf{R}_A} \frac{1}{2} N m_e \dot{h}_A^2(\mathbf{R}_A) + \sum_{\mathbf{R}_B} \frac{1}{2} N m_e \dot{h}_B^2(\mathbf{R}_B) - \sum_{\mathbf{R}_s} \frac{1}{2} N m_e {\omega_0}^2 h_s^2(\mathbf{R}_s) \\
- \sum_{j} \sum_{\mathbf{R}_A} \frac{N^2 e^2}{\epsilon_d a^3} h_A(\mathbf{R}_A) h_B(\mathbf{R}_A + e_j) \left[1 - 3\sin^2\theta \cos^2\phi_j\right] \ , \qquad (3.2)
\end{aligned}
$$

where θ is the polar angle and ϕ_j is the azimuthal angle, measured from the nearest neighbour vectors, $\mathbf{e}_j$. The equations of motion for this system can be found by substituting this Lagrangian into Euler-Lagrange equations [78] (with respect to A and B sites), and assuming oscillatory motion $\mathbf{h}_s(\mathbf{R}_s) \propto e^{\mathrm{i}\omega t}$, giving

$$
\begin{aligned}
-\omega^2 \mathbf{h}_A(\mathbf{R}_A) &= -{\omega_0}^2 \mathbf{h}_A(\mathbf{R}_A) - \tfrac{Ne^2}{\epsilon_d m_e a^3} \textstyle\sum_j \mathbf{h}_B(\mathbf{R}_A + \mathbf{e}_j) \left[1 - 3\sin^2\theta\cos^2\phi_j\right] \ , \\
-\omega^2 \mathbf{h}_B(\mathbf{R}_B) &= -{\omega_0}^2 \mathbf{h}_B(\mathbf{R}_B) - \tfrac{Ne^2}{\epsilon_d m_e a^3} \textstyle\sum_j \mathbf{h}_A(\mathbf{R}_B - \mathbf{e}_j) \left[1 - 3\sin^2\theta\cos^2\phi_j\right] \ .
\end{aligned} \qquad (3.3)
$$

Using the threefold rotational symmetry of the honeycomb structure, I can define all of the in-plane angles (ϕ_j) relative to each other, and measure them from the nearest neighbour vector $\mathbf{e}_1$. Therefore, $\phi_j = \phi - \frac{2\pi}{3}(j-1)$. Taking the Fourier transform of the displacements, such that they are of the form: $h_s(\mathbf{x}) \propto \sum_{\mathbf{q}} h_s(\mathbf{q}) e^{i\mathbf{q}\cdot\mathbf{x}}$, the equations 3.3 become:

$$
\begin{aligned}
(\omega_{\mathbf{q}}^2 - {\omega_0}^2) h_A(\mathbf{q}) &= \tfrac{Ne^2}{\epsilon_d m_e a^3} h_B(\mathbf{q}) \textstyle\sum_j \left[1 - 3\sin^2\theta\cos^2\left(\phi - \frac{2\pi(j-1)}{3}\right)\right] e^{i\mathbf{q}\cdot\mathbf{e}_j} \ , \\
(\omega\mathbf{q}^2 - {\omega_0}^2) h_B(\mathbf{q}) &= \tfrac{Ne^2}{\epsilon_d m_e a^3} h_A(\mathbf{q}) \textstyle\sum_j \left[1 - 3\sin^2\theta\cos^2\left(\phi - \frac{2\pi(j-1)}{3}\right)\right] e^{-i\mathbf{q}\cdot\mathbf{e}_j} \ .
\end{aligned} \qquad (3.4)
$$

These yield solutions for the normal modes of the system, reading

$$
\omega_{\mathbf{q}}^{\pm} = \omega_0 \sqrt{1 \pm \frac{\Lambda^2}{\omega_0^2} \left|f_{\mathbf{q}}\right|} \ , \qquad (3.5)
$$

where I have introduced $\Lambda = \sqrt{\frac{Ne^2}{\epsilon_d m_e a^3}}$ that parametrises the interaction strength. This model is only valid in the regime $\frac{\Lambda}{\omega_0} \ll 1$ meaning $\omega_{\mathbf{q}}^{\pm}$ cannot be imaginary. The dipole polarisation is encoded into the function $f_{\mathbf{q}}$ given by

$$
f_{\mathbf{q}} = \sum_j C_j e^{i\mathbf{q}\cdot e_j} \ , \qquad (3.6)
$$

with polarisation dependent interaction parameters, reading

$$C_j = \left[1 - 3\sin^2\theta\cos^2\left(\phi - \frac{2\pi(j-1)}{3}\right)\right] \ . \tag{3.7}$$

For the case of dipole moments orientated out of the plane ($\theta = 0$), $f_{\mathbf{q}}$ is the same as is found in the graphene case:

$$\begin{aligned} f_{\mathbf{q}} &= e^{i\frac{q_y a}{2}}\left\{e^{-i\frac{3q_y a}{2}} + 2\cos\left(\frac{\sqrt{3}q_x a}{2}\right)\right\} \\ |f_{\mathbf{q}}| &= \sqrt{1 + 4\cos^2\left(\frac{\sqrt{3}q_x a}{2}\right) + 4\cos\left(\frac{\sqrt{3}q_x a}{2}\right)\cos\left(\frac{3q_y a}{2}\right)} \end{aligned} \tag{3.8}$$

The dispersion from equation 3.5 is plotted in figure 3.2(a) for the case where the LSPs are polarised normal to the plane. Upon comparing this dispersion to the band structure of graphene, seen in figure 2.17, the qualitative resemblance is striking. It is immediately evident that both spectra are gapless and, similar to graphene, the CP dispersion displays a linear, conical dispersion. There are differences, however. For example, in graphene this linear dispersion occurs at low energies, close to $\varepsilon \approx 0$, whereas the CP dispersion exhibits a global energy shift of $\hbar\omega_0$ such that the band cross-over (at which the conical dispersion is present) occurs around the natural frequency of a single oscillating dipole, ω_0. Nevertheless, this is only a minor difference as, in graphene, the energy axis is set so that the Fermi energy equals zero at the Dirac point. This linear dispersion implies the existence of Dirac particles, however, the emergence of a conical dispersion is not sufficient to prove the physical analogy between CPs in honeycomb plasmonic lattices and electrons in graphene [164]. In order to achieve that, the CPs must be considered to be quantum bosonic modes such that their Hamiltonian can be compared to the Dirac Hamiltonian. This analysis is undertaken in section 3.3.

Prior to investigating this problem quantum mechanically, I will address the effect further neighbour contributions have on the CP spectrum.

3.2.1 Including Next-Nearest Neighbour Interactions

In this section I discuss the effect the inclusion of next-nearest neighbour interactions has on the CP spectrum. Each particle has six next-nearest neighbour particles, separated by the distance: $a_2 = \sqrt{3}a$. The next-nearest neighbour vectors, $\mathbf{e}_j^{(2)}$, are shown in figure 3.3(a) and given by:

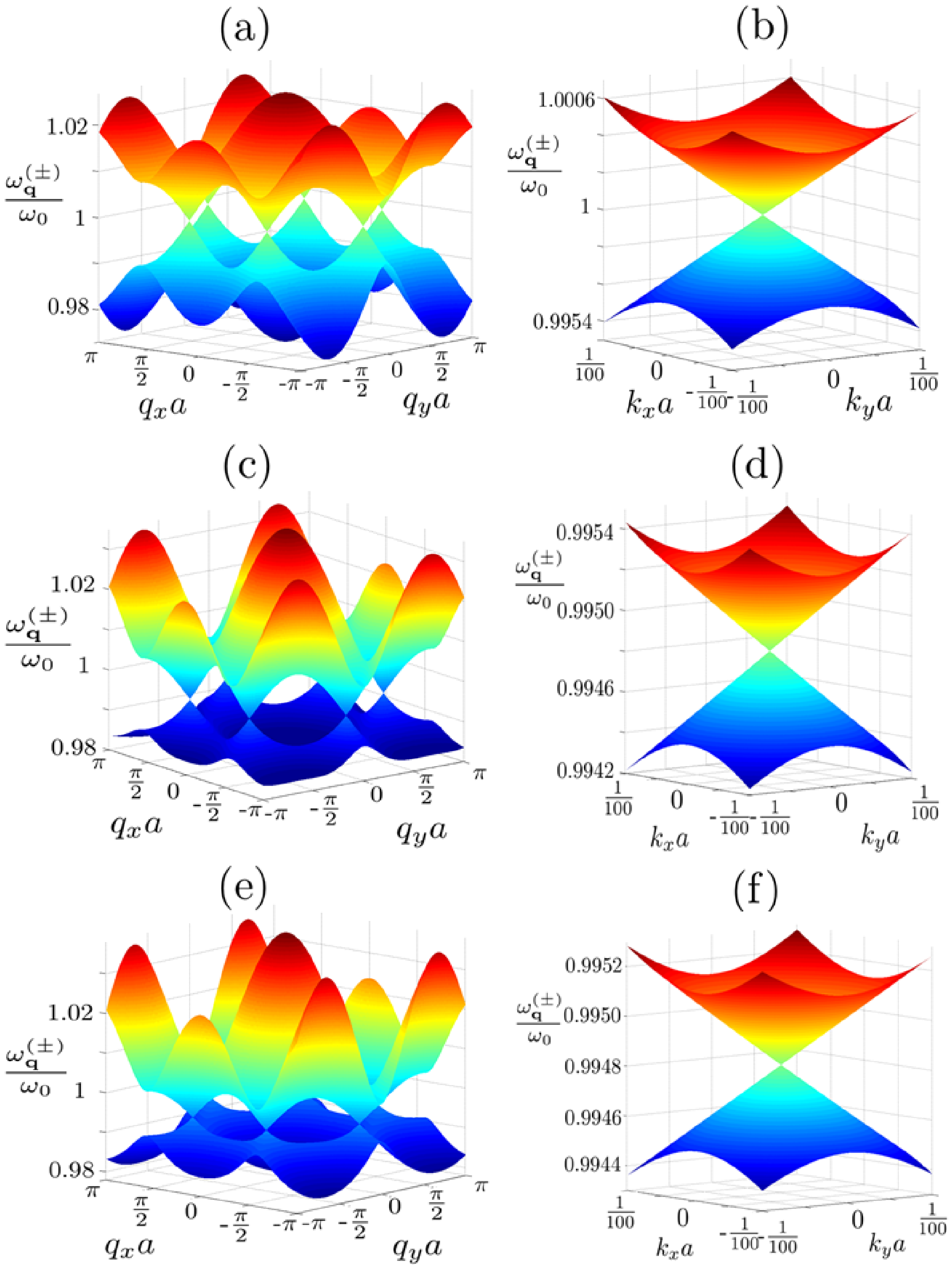

Figure 3.2: The CP dispersion including different amounts of nearest neighbour interactions, at LSP polarisation $(\theta, \phi) = (0, 0)$. In panel (a) only nearest neighbour interactions are included, in panel (c) next-nearest neighbour interactions are included and in panel (e) next-next-nearest neighbour interactions are included. Panels (b), (d), (f), show a close up on one of the Dirac-like cones at the point where the two bands touch for the corresponding CP dispersions in panels (a), (c) and (e), respectively. In each panel $\frac{\Lambda^2}{\omega_0^2} = 0.01$.

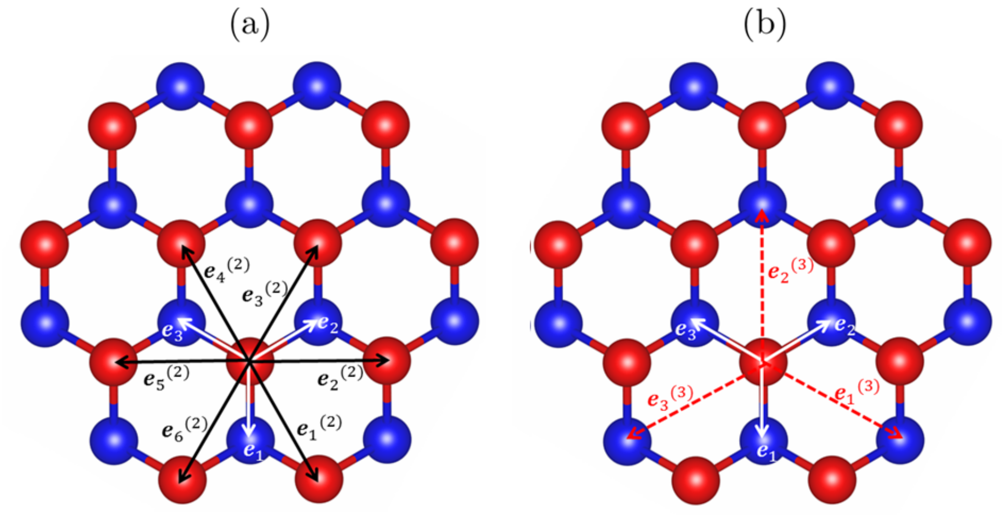

Figure 3.3: Schematic diagram of the honeycomb structure detailing: in panel (a) the next-nearest neighbour vectors, denoted by $\mathbf{e}_j^{(2)}$, which are expressed in equation 3.9; and in panel (b) the next-next-nearest neighbour vectors, denoted by $\mathbf{e}_j^{(3)}$, which are expressed in equation 3.13. The interactions between particles connected by the next-nearest and the next-next-nearest neighbour vectors are included in sections 3.2.1 and 3.2.2, respectively.

$$
\begin{aligned}
\mathbf{e}_1^{(2)} &= \mathbf{e}_1 - \mathbf{e}_3 = a\begin{pmatrix} 0 \\ -1 \end{pmatrix} - \frac{a}{2}\begin{pmatrix} -\sqrt{3} \\ 1 \end{pmatrix} = \frac{a}{2}\begin{pmatrix} \sqrt{3} \\ -3 \end{pmatrix}, \\
\mathbf{e}_2^{(2)} &= \mathbf{e}_2 - \mathbf{e}_3 = \frac{a}{2}\begin{pmatrix} \sqrt{3} \\ 1 \end{pmatrix} - \frac{a}{2}\begin{pmatrix} -\sqrt{3} \\ 1 \end{pmatrix} = \begin{pmatrix} \sqrt{3}a \\ 0 \end{pmatrix}, \\
\mathbf{e}_3^{(2)} &= \mathbf{e}_2 - \mathbf{e}_1 = \frac{a}{2}\begin{pmatrix} \sqrt{3} \\ 1 \end{pmatrix} - a\begin{pmatrix} 0 \\ -1 \end{pmatrix} = \frac{a}{2}\begin{pmatrix} \sqrt{3} \\ 3 \end{pmatrix}, \\
\mathbf{e}_4^{(2)} &= \mathbf{e}_3 - \mathbf{e}_1 = \frac{a}{2}\begin{pmatrix} -\sqrt{3} \\ 1 \end{pmatrix} - a\begin{pmatrix} 0 \\ -1 \end{pmatrix} = \frac{a}{2}\begin{pmatrix} -\sqrt{3} \\ 3 \end{pmatrix}, \\
\mathbf{e}_5^{(2)} &= \mathbf{e}_3 - \mathbf{e}_2 = \frac{a}{2}\begin{pmatrix} -\sqrt{3} \\ 1 \end{pmatrix} - \frac{a}{2}\begin{pmatrix} \sqrt{3} \\ 1 \end{pmatrix} = \begin{pmatrix} -\sqrt{3}a \\ 0 \end{pmatrix}, \\
\mathbf{e}_6^{(2)} &= \mathbf{e}_1 - \mathbf{e}_2 = a\begin{pmatrix} 0 \\ -1 \end{pmatrix} - \frac{a}{2}\begin{pmatrix} \sqrt{3} \\ 1 \end{pmatrix} = \frac{a}{2}\begin{pmatrix} -\sqrt{3} \\ -3 \end{pmatrix}.
\end{aligned}
\tag{3.9}
$$

The CP dispersion, including these next-nearest neighbour interactions as well as the nearest neighbour interactions, reads

$$\omega^{\pm}_{\mathbf{q}} = \omega_0 \sqrt{1 + \frac{\Lambda^2}{\sqrt{27}\omega_0^2} f^{(2)}_{\mathbf{q}} \pm \frac{\Lambda^2}{\omega_0^2} \left| f_{\mathbf{q}} \right|} \ , \tag{3.10}$$

where it can seen that the second term inside the square root, which stems from including next-nearest neighbour interactions, should be $\approx 1/\sqrt{27}$ the size of the final term, which comes from nearest neighbour interactions. The function $f_{\mathbf{q}}$ is the same as for the nearest neighbour case, given in equation 3.6, and $f^{(2)}_{\mathbf{q}}$ is given by:

$$f^{(2)}_{\mathbf{q}} = \sum_{j=1}^{6} C^{(2)}_j e^{i\mathbf{q}\cdot\mathbf{e}^{(2)}_j} \ , \tag{3.11}$$

where $C^{(2)}_j = \left[1 - 3\sin^2\theta\cos^2\left(\phi - \frac{\pi}{6} - \frac{\pi(j-1)}{3}\right)\right]$. With dipoles oriented perpendicular to the plane, $f^{(2)}_{\mathbf{q}}$ becomes

$$f^{(2)}_{\mathbf{q}} = 4\cos\left(\frac{\sqrt{3}a}{2}q_y\right)\cos\left(\frac{3a}{2}q_x\right) + 2\cos\left(\sqrt{3}aq_y\right). \tag{3.12}$$

The dispersion in equation 3.10 is plotted in figure 3.2(c), for the case where the LSPs are polarised normal to the plane. The general shape is of the same form as the dispersion which only includes nearest neighbour interactions (shown in figure 3.2(a)) as there is no band gap and a hexagonal geometry connecting all the Dirac-like points. Therefore, it can be seen that the inclusion of further neighbour contributions does not qualitatively change the CP spectrum. However, the ratio of the widths of the upper and lower bands is greatly altered. Here, the upper band has a larger spread in energy than the lower band.

The Dirac-like points, one of which is shown in figure 3.2(d), still occur at the K and K' points with the same wavevectors as for the nearest neighbour case shown in figure 3.2(b). However, as well as the global frequency shift of ω_0 seen in the nearest neighbour case, when next nearest neighbour interactions are included it can be seen that there is an additional frequency shift due to the extra term in the dispersion (see equation 3.10). With the interaction strength set as $\Lambda^2 = 0.01\omega_0^2$, the energy at which the Dirac-like point occurs is $0.995\omega_0$. The band touching occurs when $|f_{\mathbf{q}}| = 0$, so the frequency of the Dirac-like point (when next-nearest neighbour contributions are included) is given by $\omega^{\pm}_{\mathbf{q}} = \omega'_0 = \omega_0\sqrt{1 + \frac{\Lambda^2}{\omega_0^2\sqrt{27}} f^{(2)}_{\mathbf{q}}(K)}$, which with dipoles polarised normal to the plane is $\omega^{\pm}_{\mathbf{q}} = \omega'_0 = \omega_0\sqrt{1 + \frac{\Lambda^2}{\omega_0^2\sqrt{27}}\left(4\cos\left(\frac{2\pi}{\sqrt{3}}\right) + 2\right)}$. Therefore, it can easily be seen that whilst including the interaction contributions from the next-nearest neighbour particles alters the dispersion, the ‘Dirac-like’ point is robust. This is not quite the case in graphene. Due to the different nature of coupling in the two cases, the effect further neighbours have on graphene’s dispersion is minimal, however it does happen and this leads to trigonal warping [165, 166].

3.2.2 Including Next-Next-Nearest Neighbour Interactions

Each particle has three next-next-nearest neighbour vectors. The distance separating next-next-nearest neighbour particles is $a_3 = 2a$. The next-next-nearest neighbour vectors, $\mathbf{e}_j^{(3)}$, are shown in figure 3.3 and given by:

$$\begin{aligned}
\mathbf{e}_1^{(3)} &= \mathbf{e}_1 - \mathbf{e}_3 + \mathbf{e}_2 &&= a\begin{pmatrix} 0 \\ -1 \end{pmatrix} - \tfrac{a}{2}\begin{pmatrix} -\sqrt{3} \\ 1 \end{pmatrix} + \tfrac{a}{2}\begin{pmatrix} \sqrt{3} \\ 1 \end{pmatrix} &&= a\begin{pmatrix} \sqrt{3} \\ -1 \end{pmatrix}, \\
\mathbf{e}_2^{(3)} &= \mathbf{e}_3 - \mathbf{e}_1 + \mathbf{e}_2 &&= \tfrac{a}{2}\begin{pmatrix} -\sqrt{3} \\ 1 \end{pmatrix} - a\begin{pmatrix} 0 \\ -1 \end{pmatrix} + \tfrac{a}{2}\begin{pmatrix} \sqrt{3} \\ 1 \end{pmatrix} &&= \begin{pmatrix} 0 \\ 2a \end{pmatrix}, \\
\mathbf{e}_3^{(3)} &= \mathbf{e}_1 - \mathbf{e}_2 + \mathbf{e}_3 &&= a\begin{pmatrix} 0 \\ -1 \end{pmatrix} - \tfrac{a}{2}\begin{pmatrix} \sqrt{3} \\ 1 \end{pmatrix} + \tfrac{a}{2}\begin{pmatrix} -\sqrt{3} \\ 1 \end{pmatrix} &&= a\begin{pmatrix} -\sqrt{3} \\ -1 \end{pmatrix}.
\end{aligned} \tag{3.13}$$

Including the interactions from these particles, the CP dispersion reads

$$\begin{aligned}
\omega_{\mathbf{q}}^{\pm} &= \omega_0\sqrt{1 + \frac{\Lambda^2}{\omega_0^2\sqrt{27}} f_{\mathbf{q}}^{(2)} \pm \sqrt{\left(\frac{\Lambda^2}{\omega_0^2}\right)^2 \left[f_{\mathbf{q}} + \frac{f_{\mathbf{q}}^{(3)}}{8}\right]\left[{f_{\mathbf{q}}}^* + \frac{\left(f_{\mathbf{q}}^{(3)}\right)^*}{8}\right]}} \\
&= \omega_0\sqrt{1 + \frac{\Lambda^2}{\omega_0^2\sqrt{27}} f_{\mathbf{q}}^{(2)} \pm \frac{\Lambda^2}{\omega_0^2}\sqrt{\left[f_{\mathbf{q}}^{(3)\prime}\right]\left[\left(f_{\mathbf{q}}^{(3)\prime}\right)^*\right]}} \\
&= \omega_0\sqrt{1 + \frac{\Lambda^2}{\omega_0^2\sqrt{27}} f_{\mathbf{q}}^{(2)} \pm \frac{\Lambda^2}{\omega_0^2}\left|f_{\mathbf{q}}^{(3)\prime}\right|},
\end{aligned} \tag{3.14}$$

where $f_{\mathbf{q}}^{(3)\prime}$ is given by:

$$f_{\mathbf{q}}^{(3)\prime} = f_{\mathbf{q}} + \frac{1}{8} f_{\mathbf{q}}^{(3)}, \tag{3.15}$$

with the function $f^{(3)}_{\mathbf{q}}$, and the corresponding interaction parameters, $C^{(3)}_j$, given by

$$f^{(3)}_{\mathbf{q}} = \sum_{j=1}^{3} C^{(3)}_j e^{\mathbf{iq}\cdot\mathbf{e}^{(3)}_j} \quad , \qquad C^{(3)}_j = 1 - 3\sin^2\theta\cos^2\left(\phi - \frac{\pi}{2} - \frac{2\pi(j-1)}{3}\right) \quad . \tag{3.16}$$

With dipolar polarisation pointed normal to the plane the function $f^{(3)\prime}_{\mathbf{q}}$ reads

$$f^{(3)\prime}_{\mathbf{q}} = e^{-iq_y a}\left\{1 + 2e^{iq_y 3a/2}\cos\left(\frac{\sqrt{3}a}{2}q_x\right) + \frac{1}{4}\cos\left(\sqrt{3}aq_x\right) + \frac{1}{8}e^{iq_y 3a}\right\}. \tag{3.17}$$

The dispersion in equation 3.14 is plotted in figure 3.2(e) for the case where the LSPs are polarised normal to the plane. Again, there is qualitative agreement between this dispersion and that where only nearest neighbour interactions are included as there is still a zero band gap and a hexagonal geometry connecting all the Dirac points. However, similar to the dispersion including up to next-nearest neighbour contributions (shown in figure 3.2(c)) the amplitude of the upper band is much larger than the lower band and the 'Dirac-points', one of which is shown in figure 3.2(f), occur at the same additionally shifted frequency of $\omega_0' \sim 0.995\omega_0$ (when $\Lambda^2 = 0.01\omega_0^2$) as with the previous case. This is, again, due to the term containing $f^{(2)}_{\mathbf{q}}$ in the dispersion shown in equation 3.14. In this equation there is also a further additional term (compared to equation 3.10) containing $f^{(3)}_{\mathbf{q}}$ due to the next-next-nearest neighbour interactions. This term could affect the wavevector values at which $\omega^+_{\mathbf{q}} = \omega^-_{\mathbf{q}}$, *i.e.* the extra term in $|f^{(3)\prime}_{\mathbf{q}}|$ could make the Dirac-like point occur at different wavevector coordinates. However, the k_x and k_y coordinates which satisfy $|f^{(3)\prime}_{\mathbf{q}}| = 0$ are the same as in the previous two cases, meaning that the Dirac point occur at the same position. Thus, the Dirac-like points occur at the same wavevector and frequency values seen for the previous case. The effect of including third nearest neighbour contributions is to scale the gradient of the Dirac cones and the extra term has more of an effect at energies away from the Dirac-like points, as is evident in figure 3.4.

The reason for the differing effects the different neighbour contributions have on the CP dispersion become clear by realising that the different neighbour vectors connect particles either on the same sublattice or different ones: nearest neighbour interactions occur between particles on different sublattices; next-nearest neighbour particles are situated in the same sublattice (either both in A or both in B); and next-next-nearest neighbour particles, again involve interactions between the sublattices. Thus, it is evident that interactions between particles in the same sublattice

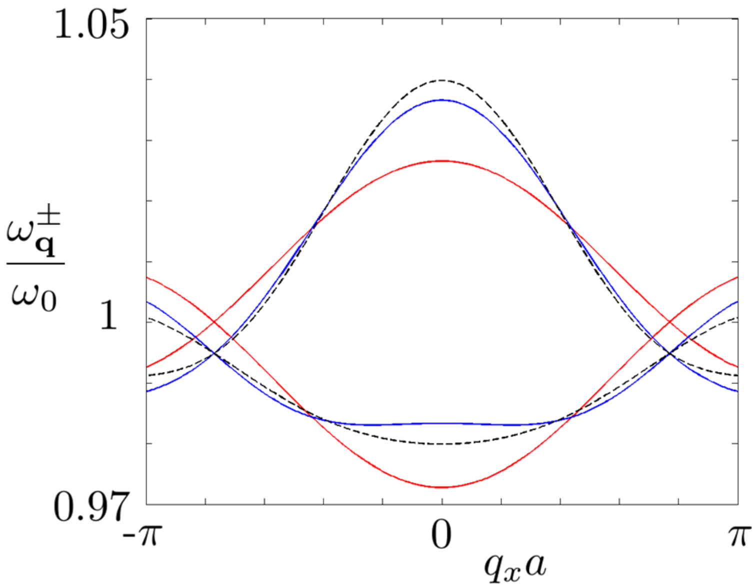

Figure 3.4: A cut of the CP dispersion at $q_y = 0$. The red line indicates the dispersion if only nearest neighbour contributions are included, the blue line indicates contributions included up to next nearest neighbour, and the black dashed line shows the dispersion when contributions up to next-next nearest neighbours are included. Here, $\frac{\Lambda^2}{\omega_0^2} = 0.01$.

---

add additional terms which have the same sign in both the upper and lower bands of the spectrum, shifting the energy of the Dirac-like point, whereas interactions between sublattices lead to terms which have different signs in either bands, that could act to shift the wavevectors at which the Dirac points occur.

3.2.3 Including Further Neighbour Interaction Contributions

From the previous sections a decrease in the magnitude of the contribution to the dispersion from subsequent neighbour interactions can be seen. This is because the coupling strength between particles reduces with distance, and later neighbouring particles are separated with larger and larger distances. Thus one would expect after including a certain number of neighbour interactions in the expression there will come a point where the next contribution would be negligible, and so there is some finite (but large) number of neighbour interactions that need to be included. However, from the treatment considered so far, it appears that this argument could perceivably be extended forever, where the more interactions that are included the more accurate the results. This is not the case, due to the assumptions that have been made: specifically only considering near field coupling. This model breaks down when particles are separated by large distances such that far field coupling dominates. Nonetheless, as far field coupling is much weaker than near field coupling, these additional interactions are expected to have an imperceptible effect. In fact, it has been shown that models using only the quasistatic approximation (and thus only including near field coupling) qualitatively reproduce the results of more sophisticated models, in which both near field and far field coupling effects are included [42]. Therefore it is reasonable to believe that only including interactions up to the limiting distance between these two regimes is sufficient. To approximate this distance I first consider the regime when far field coupling dominates: when particles are separated by distances greater than $\sim \lambda_e/6$, where λ_e is the wavelength of the re-emitted light [14]. Assuming resonance in noble metal nanoparticles, the scattered wavelength should be in the visible region of the electromagnetic spectrum, leading to the assumption of purely near field coupling will break down if particles are separated by distances greater than $\sim$ 80nm. Making another assumption to estimate the size and separation of the nanoparticles: assuming one of the smallest length scales experimentally possible for a nanoparticle of $\sim$ 10nm, and a separation distance to maximise dipolar coupling of $a \sim$ 30nm, the next-nearest neighbour vectors would have a magnitude of $|\mathbf{e}_j^{(2)}| = a_2 = \sqrt{3}a \approx$ 52nm, and that of next-next-nearest neighbour vectors would be $|\mathbf{e}_j^{(3)}| = a_3 = 2a \approx$ 60nm. Thus, there aren't many more successive interactions that could be included within this model. Furthermore, when the next few neighbour interactions where included, the effects where negligible, and the Dirac point, which is the main point of interest in this research, was still robust. Therefore, it seems that a qualitatively accurate picture of the spectrum can be obtained by only including contributions up to the next-next-nearest neighbour particles. Moreover, as the spectrum does not qualitatively change from the nearest-neighbour case, it can be concluded that the only including nearest neighbour interactions provides a qualitative overview of the system. Consequently, although producing some inaccuracies, I assume that the properties of the system can still be approximated with only nearest neighbour contributions included.

This information is utilised in the next section, where the problem is tackled quantum mechanically, and only nearest neighbour interactions are included.

3.3 Quantum Bosonic Mode

The LSP corresponding to the electronic center-of-mass excitation can generally be considered as a quantum bosonic mode, particularly when the size of the nanoparticle is such that quantization effects are important [167–175]. This quantum description of a honeycomb array of metallic nanoparticles allows one to compare the metamaterial directly with graphene.

The noninteracting part of the Hamiltonian describing the independent LSPs on the honeycomb lattice sites reads

$$H_0 = \sum_{s=A,B} \sum_{\mathbf{R}_s} \left[\frac{\Pi_s^2(\mathbf{R}_s)}{2M} + \frac{1}{2} M\omega_0^2 h_s^2(\mathbf{R}_s) \right] \ , \tag{3.18}$$

where $\Pi_s(\mathbf{R})$ is the momentum conjugated to the displacement field, $h_s(\mathbf{R})$, at position $\mathbf{R}$, and $M = N_e m_e$ is the mass of the electronic cloud, with N_e the number of valence electrons in each nanoparticle [170–173].

In the near field approximation, each LSP can be considered as a point dipole with dipole moment $\mathbf{p} = -eN_e h_s(\mathbf{R})\hat{\mathbf{p}}$ (see section 2.2) and within such a quasistatic approximation, the interaction between two dipoles, $\mathbf{p}$ and $\mathbf{p}'$, located at $\mathbf{R}$ and $\mathbf{R}'$, respectively, is given in section 2.2, and here, for completeness, reads

$$V = \frac{\mathbf{p} \cdot \mathbf{p}' - 3(\mathbf{p} \cdot \mathbf{n})(\mathbf{p}' \cdot \mathbf{n})}{\epsilon_d |\mathbf{R} - \mathbf{R}'|^3} \ . \tag{3.19}$$

Here, I assume that in a CP eigenmode all nanoparticles are polarized in the same direction parametrised by θ and ϕ which are the angle between $\hat{\mathbf{p}}$ and $\hat{\mathbf{z}}$, and the angle between the projection of $\hat{\mathbf{p}}$ in the xy plane and $\mathbf{e}_1$, shown in figure 3.1, respectively. This polarisation can be achieved by an external electric field associated with light of suitable polarization. Therefore, I can write the total Hamiltonian of our system of coupled LSPs as $H = H_0 + H_{\text{int}}$, where the dipole-dipole interaction term reads

$$H_{\text{int}} = \frac{(eN_e)^2}{\epsilon_d a^3} \sum_{\mathbf{R}_B} \sum_{j=1}^{3} C_j h_B(\mathbf{R}_B) h_A(\mathbf{R}_B + \mathbf{e}_j) \ , \tag{3.20}$$

with C_j given in equation 3.7. From investigations in section 3.2, it can understood that interactions beyond nearest neighbour do not qualitatively change the CP spectrum, so, in equation 3.20, I only consider the dipole-dipole interaction between nearest neighbours.

The analogy between the properties of the quasiparticles in this honeycomb plasmonic metamaterial and the electronic properties of graphene becomes apparent by introducing the bosonic ladder operators

$$a_{\mathbf{R}}|b_{\mathbf{R}} = \sqrt{\frac{M\omega_0}{2\hbar}}h_{A|B}(\mathbf{R}) + i\frac{\Pi_{A|B}(\mathbf{R})}{\sqrt{2\hbar M\omega_0}} \ , \tag{3.21}$$

which annihilate an LSP on a nanoparticle located at position **R** belonging to the A or B sublattice, respectively. These operators satisfy the commutation relations $[a_{\mathbf{R}}, a^\dagger_{\mathbf{R}'}] = [b_{\mathbf{R}}, b^\dagger_{\mathbf{R}'}] = \delta_{\mathbf{R},\mathbf{R}'}$ and $[a_{\mathbf{R}}, b^\dagger_{\mathbf{R}'}] = 0$. Such operators not only give access to the plasmon dispersion (which can be calculated classically as well, as shown in section 3.2), but also unveil the nature of the CP quantum states. The harmonic Hamiltonian, H_0, can be written in terms of the above-mentioned bosonic operators as

$$H_0 = \hbar\omega_0 \sum_{\mathbf{R}_A} a^\dagger_{\mathbf{R}_A} a_{\mathbf{R}_A} + \hbar\omega_0 \sum_{\mathbf{R}_B} b^\dagger_{\mathbf{R}_B} b_{\mathbf{R}_B} \ , \tag{3.22}$$

while equation 3.20 transforms into

$$H_{\text{int}} = \hbar\Omega \sum_{\mathbf{R}_B} \sum_{j=1}^{3} C_j b^\dagger_{\mathbf{R}_B}(a_{\mathbf{R}_B+\mathbf{e}_j} + a^\dagger_{\mathbf{R}_B+\mathbf{e}_j}) + H.c. \ , \tag{3.23}$$

where I now define the interaction strength as $\Omega = \frac{\Lambda^2}{2\omega_0}$ (which is different from the classical description because of the definition of the operators $a_{\mathbf{R}}$ and $b_{\mathbf{R}}$. Using equations 2.2 and 2.5, this interaction strength can be expressed as $\Omega = \omega_0 \left(\frac{r}{a}\right)^3 \frac{(1+2\epsilon_d)}{2\epsilon_d}$. The bosonic operators above can be converted to momentum space through

$$a_{\mathbf{R}}|b_{\mathbf{R}} = \frac{1}{\sqrt{\mathcal{N}}} \sum_{\mathbf{q}} \exp(i\mathbf{q}\cdot\mathbf{R}) a_{\mathbf{q}}|b_{\mathbf{q}} \tag{3.24}$$

with $\mathcal{N}$ being the number of unit cells of the honeycomb lattice. Thus, the Hamiltonian $H = H_0 + H_{\text{int}}$ transforms into

$$H = \hbar\omega_0 \sum_{\mathbf{q}} (a^\dagger_{\mathbf{q}} a_{\mathbf{q}} + b^\dagger_{\mathbf{q}} b_{\mathbf{q}}) + \hbar\Omega \sum_{\mathbf{q}} \left[f_{\mathbf{q}} b^\dagger_{\mathbf{q}} \Big(a_{\mathbf{q}} + a^\dagger_{-\mathbf{q}} \Big) + f^*_{\mathbf{q}} \Big(a^\dagger_{\mathbf{q}} + a_{-\mathbf{q}} \Big) b_{\mathbf{q}} \right] \tag{3.25}$$

with all the information on the LSP polarisation encoded in $f_{\mathbf{q}}$, which is given in equation 3.6.

3.3.1 Exact Diagonalisation

To find the normal modes of the system, by diagonalizing the the Hamiltonian, I introduce a new bosonic operator

$$\beta_{\mathbf{q}}^{\tau} = w_{\mathbf{q}}^{\tau} a_{\mathbf{q}} + x_{\mathbf{q}}^{\tau} b_{\mathbf{q}} + y_{\mathbf{q}}^{\tau} a_{-\mathbf{q}}^{\dagger} + z_{\mathbf{q}}^{\tau} b_{-\mathbf{q}}^{\dagger} \tag{3.26}$$

where $\tau = \pm 1$, and impose that the Hamiltonian shown in equation 3.25, is diagonal within this basis, such that

$$H = \sum_{\tau} \sum_{\mathbf{q}} \hbar \omega_{\mathbf{q}}^{\tau} \beta_{\mathbf{q}}^{\tau\dagger} \beta_{\mathbf{q}}^{\tau} \ . \tag{3.27}$$

By satisfying the Heisenberg equation of motion, $\left[\beta_{\mathbf{q}}^{\tau}, \hat{H}\right] = \hbar\omega_{\mathbf{q}}^{\tau}\beta_{\mathbf{q}}^{\tau}$, I obtain the eigenvalue problem

$$\begin{pmatrix} \omega_0 & \Omega f_{\mathbf{q}} & 0 & -\Omega f_{\mathbf{q}} \\ \Omega f_{\mathbf{q}}^{*} & \omega_0 & -\Omega f_{\mathbf{q}}^{*} & 0 \\ 0 & \Omega f_{\mathbf{q}} & -\omega_0 & -\Omega f_{\mathbf{q}} \\ \Omega f_{\mathbf{q}}^{*} & 0 & -\Omega f_{\mathbf{q}}^{*} & -\omega_0 \end{pmatrix} \begin{pmatrix} w_{\mathbf{q}}^{\tau} \\ x_{\mathbf{q}}^{\tau} \\ y_{\mathbf{q}}^{\tau} \\ z_{\mathbf{q}}^{\tau} \end{pmatrix} = \omega_{\mathbf{q}}^{\tau} \begin{pmatrix} w_{\mathbf{q}}^{\tau} \\ x_{\mathbf{q}}^{\tau} \\ y_{\mathbf{q}}^{\tau} \\ z_{\mathbf{q}}^{\tau} \end{pmatrix} . \tag{3.28}$$

This procedure yields the CP dispersion,

$$\omega_{\mathbf{q}}^{\tau} = \omega_0 \sqrt{1 + 2\tau \frac{\Omega}{\omega_0} |f_{\mathbf{q}}|} \ , \tag{3.29}$$

along with the coefficients of $\beta_{\mathbf{q}}^{\tau}$, which are

$$w_{\mathbf{q}}^{\tau} = \frac{\cosh\theta_{\mathbf{q}}^{\tau} f_{\mathbf{q}}}{\sqrt{2}|f_{\mathbf{q}}|} \ , \quad x_{\mathbf{q}}^{\tau} = \tau \frac{\cosh\theta_{\mathbf{q}}^{\tau}}{\sqrt{2}} \ , \quad y_{\mathbf{q}}^{\tau} = \frac{\sinh\theta_{\mathbf{q}}^{\tau} f_{\mathbf{q}}}{\sqrt{2}|f_{\mathbf{q}}|} \ , \quad z_{\mathbf{q}}^{\tau} = -\tau \frac{\sinh\theta_{\mathbf{q}}^{\tau}}{\sqrt{2}} \ . \tag{3.30}$$

Here,

$$\cosh\theta_{\mathbf{q}}^{\tau} = \frac{1}{\sqrt{2}} \left(\frac{1 + \tau\frac{\Omega}{\omega_0}|f_{\mathbf{q}}|}{\sqrt{1 + \tau 2 \frac{\Omega}{\omega_0}|f_{\mathbf{q}}|}} + 1 \right)^{\frac{1}{2}} , \qquad \sinh\theta_{\mathbf{q}}^{\tau} = -\tau \frac{1}{\sqrt{2}} \left(\frac{1 + \tau\frac{\Omega}{\omega_0}|f_{\mathbf{q}}|}{\sqrt{1 + \tau 2 \frac{\Omega}{\omega_0}|f_{\mathbf{q}}|}} - 1 \right)^{\frac{1}{2}} \ . \tag{3.31}$$

This Bogoliubov operator, which describes the diagonalised system, obeys the commutation relation $\left[\beta^{\tau}_{\mathbf{q}}, \beta^{\tau\dagger}_{\mathbf{q}'}\right] = \left[w^{\tau}_{\mathbf{q}} w^{\tau}_{\mathbf{q}'} + x^{\tau}_{\mathbf{q}} x^{\tau}_{\mathbf{q}'} + y^{\tau}_{\mathbf{q}} y^{\tau}_{\mathbf{q}'} + z^{\tau}_{\mathbf{q}} z^{\tau}_{\mathbf{q}'}\right] \delta_{\mathbf{q},\mathbf{q}'}$. When the number operator, $\hat{N} = \beta^{\tau\dagger}_{\mathbf{q}} \beta^{\tau}_{\mathbf{q}}$, acts on state $|n\rangle$ (such that $\langle n|n\rangle = 1$) the resulting eigenvalue is the number of quasiparticles, n, such that $\hat{N}|n\rangle = n|n\rangle$. Also, $\beta^{\tau}_{\mathbf{q}}|n\rangle$ and $\beta^{\tau\dagger}_{\mathbf{q}}|n\rangle$ are eigenstates of $\hat{N}$, but give eigenvalues $n-1$ and $n+1$, respectively, making the nature of the annihilation and creation operators evident. Therefore $\beta^{\tau}_{\mathbf{q}}|n\rangle$ is related to $|n-1\rangle$, and similarly $\beta^{\tau\dagger}_{\mathbf{q}}|n\rangle$ is related to $|n+1\rangle$, using the normalisation factors:

$$\begin{aligned} \beta^{\tau}_{\mathbf{q}}|n\rangle &= \sqrt{n}\,|n-1\rangle \\ \beta^{\tau\dagger}_{\mathbf{q}}|n\rangle &= \sqrt{n+1}\,|n+1\rangle \ . \end{aligned} \tag{3.32}$$

The states $|n\rangle$ must be positive integers, and, as such when the annihilation operator acts on the lowest state, $n = 0$, no new eigenstates are generated: $\beta^{\tau\dagger}_{\mathbf{q}}|0\rangle = \sqrt{0}|0\rangle = 0$. Thus, the state $|0\rangle$ can be considered “the vacuum state” due to the fact that applying the annihilator to it produces a vanishing eigenvalue, signifying that there are no quasiparticles left to annihilate.

To first order in $\Omega/\omega_0 \ll 1$, the coefficients $\cosh\theta^{\tau}_{\mathbf{q}} \approx 1$ and $\sinh\theta^{\tau}_{\mathbf{q}} \approx 0$, respectively, and the two CP branches reduce to $\omega^{\tau}_{\mathbf{q}} \approx \omega_0 \pm \Omega|f_{\mathbf{q}}|$ for which the Bogoliubov operators take the simpler form $\beta^{\tau}_{\mathbf{q}} \approx \frac{1}{2}\left[\frac{f_{\mathbf{q}}}{|f_{\mathbf{q}}|} a_{\mathbf{q}} + \tau b_{\mathbf{q}}\right]$.

Incorporating these approximations into equation 3.27, the system can be effectively described by the Hamiltonian

$$\hat{H} \approx \hbar\omega_0 \sum_{\mathbf{q}} \left(a^{\dagger}_{\mathbf{q}} a_{\mathbf{q}} + b^{\dagger}_{\mathbf{q}} b_{\mathbf{q}}\right) + \hbar\Omega \sum_{\mathbf{q}} \left(f_{\mathbf{q}} b^{\dagger}_{\mathbf{q}} a_{\mathbf{q}} + f^{*}_{\mathbf{q}} a^{\dagger}_{\mathbf{q}} b_{\mathbf{q}}\right). \tag{3.33}$$

This expression demonstrates that the non-resonant terms in the interaction Hamiltonian (which are the fourth and sixth term on the right hand side of equation 3.25) are irrelevant for the description of CPs in the honeycomb array of metallic nanoparticles, as long as $\Omega/\omega_0 \ll 1$.

It is evident, by the form of $f_{\mathbf{q}}$ in equation 3.6, that the two CP branches of the dispersion, shown in equation 3.29, crucially depend on the dipole orientation (θ, ϕ). In section 3.3.3, I will explore the polarisation dependence, and several relevant cases that highlight the tunability of the CP band structure, but first I will look specifically at the ‘trivial’ graphene-like case, where the LSPs are polarised normal to the plane.

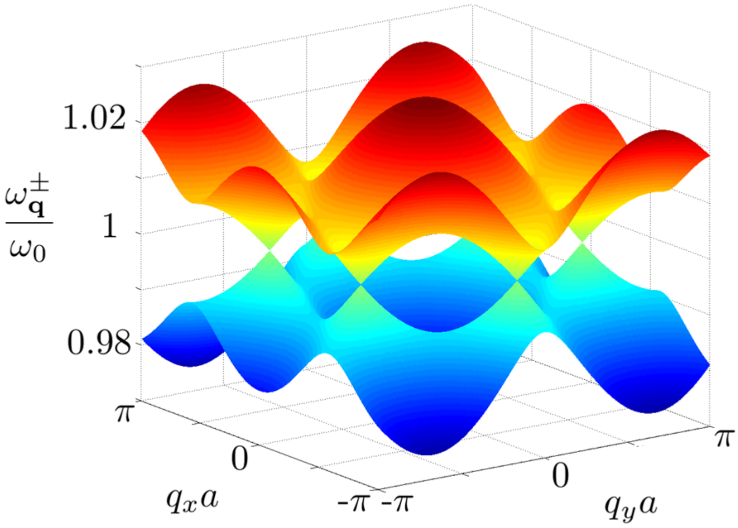

Figure 3.5: The CP dispersion when LSPs are polarised along $(\theta, \phi) = (0, 0)$, with $\frac{\Omega}{\omega_0} = 0.01$.

3.3.2 Dirac-like nature of the Collective Plasmon Quasiparticles

The polarisation dependence of the CP spectrum can be seen in the function $f_{\mathbf{q}}$, given in equation 3.6. In this section, I discuss the properties of the system when the LSP polarisation points normal to the plane ($\theta = 0$), and in further sections I consider tuning this polarisation.

When $\theta = 0$ the interaction parameters C_j are all equal to 1, which is directly analogous to the electronic tight-binding problem in pristine graphene, where the hopping parameters between nearest neighbour atoms are all equal. A plot of the dispersion, given in equation 3.29, is shown in figure 3.5 for the case of a polarization $\hat{\mathbf{p}}$ perpendicular to the plane of the honeycomb lattice. The spectrum presents gapless modes and, what I later prove to be inequivalent Dirac cones centered at the K and K' points located at $\pm\mathbf{K}_D = \frac{4\pi}{3\sqrt{3}a}(\pm 1, 0)$ in the first BZ, shown in figure 3.1(b). These Dirac cones occur at a frequency $\omega_{\mathbf{q}}^{\pm} = \omega_0$. Close to the Dirac points the function $f_{\mathbf{q}}$ expands as $f_{\mathbf{q}} \approx -\frac{3a}{2}(\pm k_x + ik_y)$ where $\mathbf{k} = (k_x, k_y)$ is the wavevector away from the Dirac point ($\mathbf{q} = \pm\mathbf{K}_D + \mathbf{k}$ where $|\mathbf{k}| \ll |\mathbf{K}_D|$). As such, the CP dispersion in equation 3.29 is linear and forms a Dirac cone, $\omega_{\mathbf{k}}^{\pm} \approx \omega_0 \pm v|\mathbf{k}|$, with group velocity $v = 3\Omega a/2 \sim 1 \times 10^6 \mathrm{ms}^{-1}$ when $\Omega = 0.01\omega_0$ and the separation is taken as 30nm. This feature is consistent with numerical analysis [156]. Moreover, by expanding the Hamiltoninan given in equation 3.33 in the vicinity of the Dirac points, I can identify the effective Hamiltonian $H^{\mathrm{eff}} = \sum_{\mathbf{k}} \hat{\mathbf{\Psi}}_{\mathbf{k}}^{\dagger} \mathcal{H}_{\mathbf{k}}^{\mathrm{eff}} \hat{\mathbf{\Psi}}_{\mathbf{k}}$ that adequately describes the

CPs. Here $\hat{\mathbf{\Psi}}_{\mathbf{k}} = (a_{\mathbf{k},K}, b_{\mathbf{k},K}, b_{\mathbf{k},K'}, a_{\mathbf{k},K'})$ is a spinor operator, where K and K' denote the valley indices associated with the inequivalent Dirac points, and the 4×4 Hamiltonian reads

$$\mathcal{H}_{\mathbf{k}}^{\mathrm{eff}} = \hbar\omega_0 \mathcal{I}^{(4)} - \hbar v \tau_z \otimes \boldsymbol{\sigma} \cdot \mathbf{k} \ . \tag{3.34}$$

In this notation, τ_z is the Pauli matrix acting on the valley space (K, K'), while $\boldsymbol{\sigma} = (\sigma_x, \sigma_y)$ is the vector of Pauli matrices acting on the sublattice space (A,B) and $\mathcal{I}^{(4)}$ corresponds to the 4×4 identity matrix in both the valley and sublattice space. Up to a global energy shift of $\hbar\omega_0$, equation 3.34 corresponds to a massless Dirac Hamiltonian that is fulfilled by CPs, in complete analogy with electrons in graphene [5, 6]. The corresponding CP spinor eigenstates of equation 3.34 are, $\psi^{\pm}_{\mathbf{k},K} = \frac{1}{\sqrt{2}}(1, \mp e^{i\xi_{\mathbf{k}}}, 0, 0)$ and $\psi^{\pm}_{\mathbf{k},K'} = \frac{1}{\sqrt{2}}(0, 0, 1, \mp e^{i\xi_{\mathbf{k}}})$ with $\xi_{\mathbf{k}} = \arctan(k_y/k_x)$. These eigenstates represent Dirac-like massless bosonic excitations that are chiral in nature, characterized by $\boldsymbol{\sigma} \cdot \hat{\mathbf{k}} = \pm\mathcal{I}^{(2)}$, where $\mathcal{I}^{(2)}$ is the 2×2 identity matrix in the sublattice space. As a consequence, CPs present similar effects to those of electrons in graphene such as a Berry phase of π [8, 9] and the absence of backscattering from smooth inhomogeneities [10]. This could have crucial implications for the efficient plasmonic propagation in array-based metamaterials.

3.3.3 Tunable Nature of the CPs with LSP Polarisations

In the previous section I have shown that, at the particular case of dipole polarisation pointing normal to the plane, the CP in this metamaterial can present similar properties to electrons in graphene. However, in addition to this, a difference between graphene and this plasmonic metamaterial is the tunability of the CP properties with dipole polarisation, which leads to properties not seen in graphene. Therefore, I now depart form the specific case of LSPs polarised perpendicular to plane, where there is a one-to-one correspondence between graphene and our metamaterial of metallic nanoparticles, and explore the polarisation dependence.

Figure 3.6 shows some examples of CP dispersions at different polarisation angles: figure 3.6(a) replicates the spectrum shown in figure 3.5 of the graphene-like case when $\theta = 0$; figure 3.6(b) shows the case of an in-plane polarization, along a nearest neighbour vector, in this case $\mathbf{e}_1$, such that $(\theta, \phi) = (\pi/2, 0)$; figure 3.6(c) shows the special case with $(\theta, \phi) = (\arcsin(\sqrt{1/3}), 0)$, where one of the nearest neighbour interactions goes to zero; and figure 3.6(d) shows another special case, with $(\theta, \phi) = \left(\sin^{-1}\left(\frac{2}{3}\right), \frac{\pi}{6}\right) \approx \left(\frac{41.8}{180}\pi, \frac{\pi}{6}\right)$, where two of the nearest neighbour interactions go to zero.

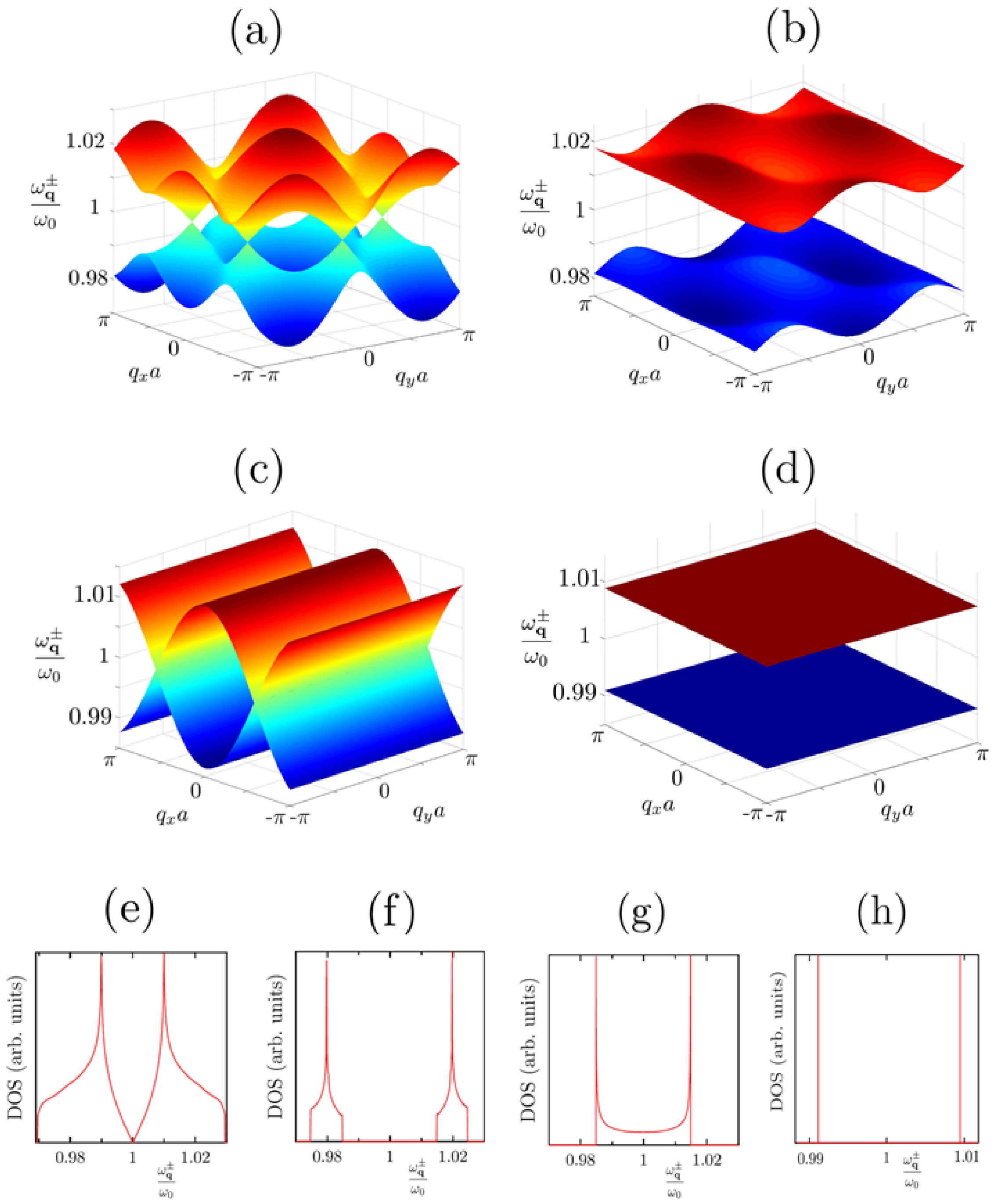

Figure 3.6: The CP dispersion when LSPs are polarised along (a) $(\theta, \phi) = (0, 0)$, (b) $(\theta, \phi) = \left(\frac{\pi}{2}, 0\right)$, (c) $(\theta, \phi) = \left(\arcsin\left[\frac{1}{\sqrt{3}}\right], 0\right)$ and (d) $(\theta, \phi) = \left(\sin^{-1}\left(\frac{2}{3}\right), \frac{\pi}{6}\right) \approx \left(\frac{41.8}{180}\pi, \frac{\pi}{6}\right)$. The corresponding density of states plots are shown in panels (e), (f), (g), and (h), respectively. In each figure $\frac{\Omega}{\omega_0} = 0.01$.

In the first of these cases I see a gapless spectrum presenting Dirac cones while in the second case (figure 3.29(b)), the modes are gapped, meaning that at energies $\hbar\omega^{\pm}_{\mathbf{q}} \approx \hbar\omega_0$ the system has changed from transparent (conducting) to opaque (insulating). Thus, changing the polarization allows one to drastically change the CP spectrum. However, considering just a small perturbation in polarisation angle away from the $\theta = 0$ case, then the effect is not so dramatic. Here, the fact that $\theta \neq 0$ means that all the interaction parameters are no longer equal, but they are positive, which is analogous to making the particles closer together or further apart. Thus this case can be considered analogous to strained graphene. This is true in the polarisation region $0 < \theta < \theta_0$, where $\theta_0 = \arcsin\left(\frac{1}{\sqrt{3}}\right)$. At $\phi = 0$, θ_0 corresponds to a polarization at which one of the interaction parameters is zero, *i.e.* $C_1 = 0$ (where C_j is given in equation 3.7). The dispersion at this polarisation is shown in figure 3.6(c), meaning that the bonds linked by $\mathbf{e}_1$ (see figure 3.1) are ineffective. The system is effectively translationally invariant along one direction, and can be considered as a set of one dimensional (1D) waveguides. Hence, the CP dispersion in 3.6(c) does not depend on q_y and presents Dirac lines.

Beyond this polarisation ($\theta > \theta_0$) the interaction parameters are not necessarily all positive, and negative interaction parameters can be thought of as analogous to attractive couplings (positive parameters can be thought of as repulsive ones) which are not possible in graphene. Thus, the analogy to graphene breaks down and it is possible to open a gap in the spectrum, as illustrated in figure 3.29(b).

Figure 3.6(d) shows the CP dispersion corresponding to a polarisation where two of these nearest neighbour interactions equal zero, such that the system acts like a decoupled array of isolated dimers. Hence the CP spectrum is non-dispersive and presents two flat bands.

Note, in figure 3.6, the panels (e) - (h) show the density of states (DOS) corresponding to the spectrum illustrated in the panels (a) - (d). The DOS will facilitate a comparison between the theoretical predictions of the CP dispersion and any future experiments. It characterises the density of wavevectors, $\mathbf{q}$, that correspond to a value of energy, $\varepsilon = \hbar\omega$, or in this case frequency ω. This was numerically calculated using $\frac{dN}{d\omega} = \frac{dN}{d\mathbf{q}}\frac{d\mathbf{q}}{d\omega}$ (where N is the number of states available) by running a loop over the frequencies and assessing whether the value for the spectrum at each wavevector corresponds to the given frequency, within a certain numerical range, which depends on the difference that was taken between each wavevector and frequency value, $d\mathbf{q}$ and $d\omega$, respectively. If these two frequency values were in suitable agreement, then the numerical matrix element that corresponded to that wavevector was given a value of $\frac{d\mathbf{q}}{d\omega} = \frac{d\mathbf{q}}{d\omega^{\pm}_{\mathbf{q}}}$ at that wavevector value, and if not that wavevector was allocated a value of zero. The sum of each of these elements for a given frequency provided the DOS value for that frequency. As the DOS describes the number of available states per interval of frequency, it is evidently limited by the numerical resolution of both the wavevector and the frequency. Therefore, I ensured that this resolution was high enough that further reductions did not noticeably change the resulting DOS. In figure 3.6(e)-(h) it is interesting to notice the tunability of the DOS with the direction of the polarization, as well as the emergence of van Hove singularities. The latter are associated with Lifshitz transitions [176] in the topology of equipotential lines that percolate at specific energies. The tunability of van Hove singularities in the spectrum could be of crucial importance to increase the coupling of light of different wavelengths with extended CP modes.

Thus, it can be seen that very different properties can be produced by changing the polarisation of the LSPs. For an arbitrary polarization of the LSPs, I examine the robustness of the Dirac points by determining at which polarisations the CP dispersion is gapless. For the CP dispersion to be gapless, I impose $|f_{\mathbf{q}}| = 0$ in equation 3.29. Setting $|f_{\mathbf{q}}| = 0$ in equation 3.6 and considering the polarisations where the real and imaginary parts both equal zero, lead to the condition for having gapless plasmonic modes:

$$0 \leq \frac{(C_2 + C_3)^2 - C_1^2}{4C_2C_3} \leq 1 \ . \tag{3.35}$$

This allows for the production of a rich phase diagram of gapped and gapless CP band structures that emerge by tilting the LSP polarisation. This phase diagram, shown in figure 3.7, indicates the polar and azimuthal polarisation angles (θ and ϕ respectively) for which the band structure is gapless (white regions) or gapped (coloured regions). The colour scale indicates the size of the gap Δ (in units of the coupling Ω), defined as the difference in energy between the minimum of the upper (+) and the maximum of the lower (−) band which, for $\Omega/\omega_0 \ll 1$, reduces to $\Delta \approx 2\Omega\min\left\{|f_{\mathbf{q}}|\right\}$.

In figure 3.7, the black solid, dashed and dotted lines indicate the angles where one of the nearest-neighbour coupling strengths, C_j, defined in 3.7, equals zero, reducing the system to a collection of non-interacting 1D chains. This condition renders the system equivalent to waveguides with a dispersion that is translationally invariant along one direction, as can be seen in figure 3.6(c). As shown in figure 3.7, there are also points where two of these lines intersect,

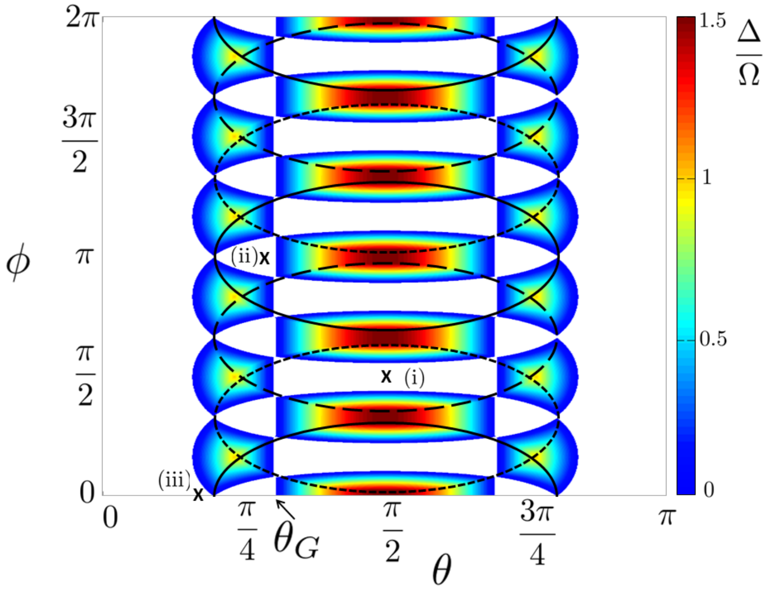

Figure 3.7: The phase diagram of gapless and gapped phases for different LSP polarisations. The phase diagram indicates the polar and azimuthal polarisation angles (θ and ϕ respectively) for which the band structure is gapless (white regions) or gapped (coloured regions). The colour scale indicates the size of the gap Δ (in units of the coupling Ω). Polarisations in some of the topologically disconnected gapless phases have been investigated in the text, here they are labelled with an 'X' which correspond to polarisations: (i) $(\theta,\phi) = (\pi/2,\pi/2)$, (ii) $(\theta,\phi) = (\pi/4,\pi)$, and (iii) $(\theta,\phi) = (\pi/6,0)$. The transitions from gapped to gapless phases (and vice versa) are investigated at θ_G= $\arcsin\left(\sqrt{\frac{2}{3}}\right)$. In the figure $\frac{\Omega}{\omega_0} = 0.01$.

---

signalling that two nearest-neighbour bonds go to zero and the system can effectively be described as isolated dimers, leading to flat bands with no wavevector dependence, as shown in figure 3.6(d).

The white areas in figure 3.7 demonstrate that there are many polarization angles where the spectrum is gapless, indicating the possibility of regions of stability of a massless Dirac spectrum in the (θ,ϕ) parameter space for which one has gapless plasmon modes, an example of which is shown in figure 3.5. Although the presence of a gapless conical dispersion is not sufficient to prove the quasi-particles possess a Dirac-like nature, I predict Dirac physics in these gapless regions, even in pockets of the phase diagram topologically disconnected from the 'trivial' graphene-like case for which $\theta = 0$ (see section 3.3.2). To explore this, I expand the Hamiltonian at various polarisations within different regions. I have investigated three different gapless positions: (i) $(\theta,\phi) = \left(\frac{\pi}{2},\frac{\pi}{2}\right)$, (ii) $(\theta,\phi) = \left(\frac{\pi}{4},\pi\right)$, and (iii) $(\theta,\phi) = \left(\frac{\pi}{6},0\right)$, as indicated by crosses in figure 3.7. In all three cases there are gapless modes with two cones centred at the two inequivalent Dirac points $\pm\mathbf{K}_D$. In cases (i) and (ii), these are located at $\pm\mathbf{K}_D = \frac{2}{\sqrt{3}a}\arccos\left(\frac{2}{5}\right)(\pm 1, 0)$, and for case (iii), $\pm\mathbf{K}_D = \frac{2}{\sqrt{3}a}\arccos\left(-\frac{2}{13}\right)(\pm 1, 0)$. Close to the two inequivalent Dirac points, the function $f_{\mathbf{q}}$ in equation 3.6 expands as (i) $f_{\mathbf{q}} \approx \frac{3a}{2}\left(\pm\frac{\sqrt{7}}{2}k_x - \mathrm{i}k_y\right)$, (ii) $f_{\mathbf{q}} \approx \frac{3a}{4}\left(\mp\frac{\sqrt{7}}{2}k_x + \mathrm{i}k_y\right)$, and (iii) $f_{\mathbf{q}} \approx -\frac{3a}{8}\left(\pm\frac{\sqrt{55}}{2}k_x - \mathrm{i}k_y\right)$, where $\mathbf{q} = \pm\mathbf{K}_D + \mathbf{k}$, with $|\mathbf{k}| \ll |\mathbf{K}_D|$. These expansions show that the CP dispersion, shown in equation 3.29, forms elliptical cones in the vicinity of the Dirac points above, as the magnitude of the k_x and k_y components of $f_{\mathbf{q}}$ are not equal, unlike in the purely out-of-plane polarization case, shown in section 3.3.2. These are illustrated in figure 3.8. Moreover, by expanding equation 3.33 in the vicinity of the Dirac points, an effective Hamiltonian can be identified for each case that adequately describes the CPs and, up to a global energy shift of $\hbar\omega_0$, corresponds to a massless Dirac Hamiltonian. Thus, Dirac-like physics can be recovered in other gapless regions away from the case where the polarization points normal to the plane ($\theta = 0$). Therefore, having further explored the gapless regions of the phase diagram it can be seen that at an arbitrary angle (provided it is in the gapless region) the CP dispersion presents Dirac cones. These are not necessarily in the same positions in wavevector space. In fact, I will show that as the dipolar polarisation angle is varied the Dirac cones travel around in momentum space, and the emergence of a gap in the CP spectrum occurs due to the annihilation of Dirac points, with opposite BP, at specific polarisation angles.

The positions of the Dirac points can be found using these analytical expressions

$$\begin{aligned} x_D &= \frac{1}{\sqrt{3}}\cos^{-1}\left\{\frac{\pm\left[C_2^2 + C_3^2 - C_1^2\right]}{2C_2C_3}\right\}, \\ y_D &= \frac{1}{3}\cos^{-1}\left\{\frac{\pm\left[C_1^2\left(C_2^2 + C_3^2\right)\right] - \left[C_2^2 - C_3^2\right]^2}{2C_1^2C_2C_3}\right\}, \end{aligned} \tag{3.36}$$

where $x_D = K_x a$ and $y_D = K_y a$ are the dimensionless Dirac point coordinates in the x and y regions respectively.

In figure 3.9 I track the position of the Dirac points, whilst continuously varying the polarisation angle from $\phi \approx \frac{\pi}{10}$ to $\phi \approx \frac{\pi}{5}$ while keeping $\theta = \frac{\pi}{2}$ constant (purely in-plane polarization). These two critical angles are denoted by A and B in the inset of the figure, which reproduces part of the phase diagram of figure 3.7. As can be seen from figure 3.9, the Dirac points move in momentum space as ϕ is increased (see the arrows in the figure that indicate the direction of the motion). At the angles where a gap opens, the two inequivalent Dirac points merge and annihilate

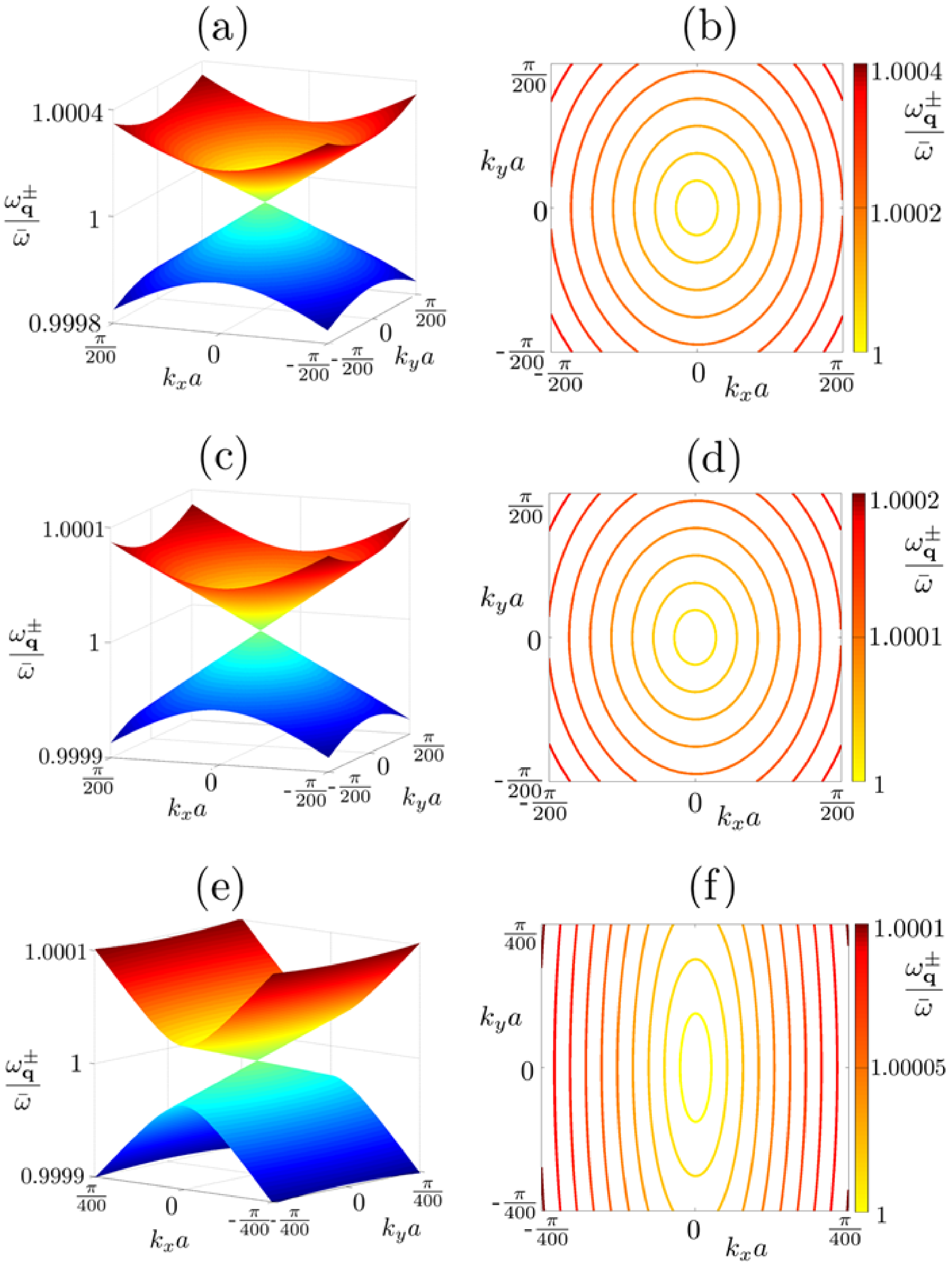

Figure 3.8: Panels (a), (c) and (e) show the collective plasmon dispersion in the vicinity of the Dirac point, for (a) in-plane polarisation $(\theta, \phi) = \left(\frac{\pi}{2}, \frac{\pi}{2}\right)$ with the Dirac point located at $\mathbf{K}_D = \frac{2}{\sqrt{3}a} \arccos\left(\frac{2}{5}\right)(1,0)$, (c) $(\theta, \phi) = \left(\frac{\pi}{4}, \pi\right)$ with the Dirac point located at $\mathbf{K}_D = \frac{2}{\sqrt{3}a} \arccos\left(\frac{2}{5}\right)(1,0)$, and (e) $(\theta, \phi) = \left(\frac{\pi}{6}, 0\right)$ with the Dirac point located at $\mathbf{K}_D = \frac{2}{\sqrt{3}a} \arccos\left(-\frac{2}{13}\right)(1,0)$. The Panels (b), (d) and (f) show the corresponding isoenergetic lines of the upper $\omega^{+}_{\mathbf{q}}$ branch. In the figure, $\Omega/\omega_0 = 0.01$ and $\mathbf{k} = \mathbf{q} - \mathbf{K}_D$.

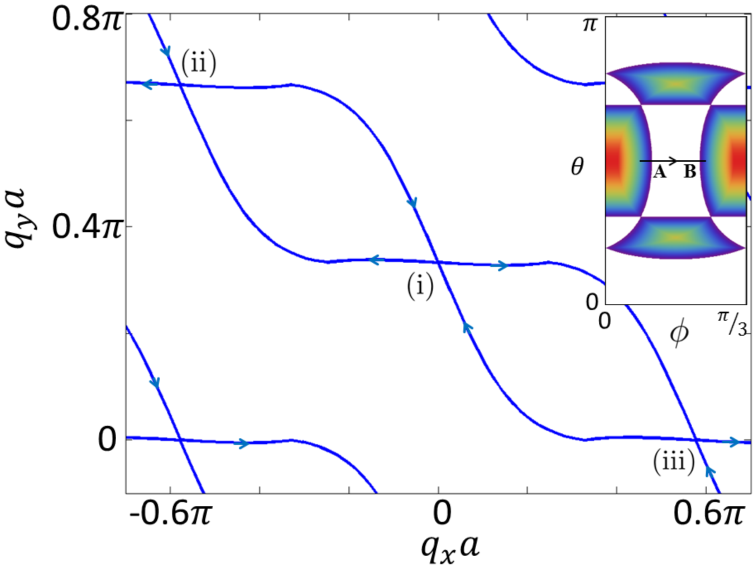

Figure 3.9: Positions in momentum space of the Dirac points as the LSP polarization is changed from $\phi \approx \pi/10$ to $\phi/5$, while keeping $\theta = \pi/2$ constant (purely in-plane polarization), see points A and B in the inset, respectively. The arrows in the figure indicate the direction of the motion of the Dirac points while ϕ increases. Inset: section of the phase diagram from figure 3.7 showing the polarisation angles considered here. In the figure, $\Omega/\omega_0 = 0.01$.

---

each other. Hence in the gapped regions there are no longer two distinct valleys created by the two sublattices. The two merging Dirac points have opposite chirality and Berry phase, so these are conserved after the merger. At the angle labelled A in the inset of figure 3.9 ($\theta = \frac{\pi}{2}, \phi \approx \frac{\pi}{10}$), the gap in the spectrum closes and the two Dirac points in each BZ appear at the same position, for example two at point (i), two at point (ii) and two at point (iii). At the angle labelled B in the inset of the figure ($\theta = \frac{\pi}{2}, \phi \approx \frac{\pi}{5}$) the two Dirac points in each BZ coalesce to open a gap in the spectrum, for example one that started at point (ii) and one that started at point (iii) coalesce at point (i).

The phenomenon described in figure 3.9 is reminiscent of Dirac point merging in graphene that has been predicted to occur with large mechanical deformations of the lattice [177,178]. While these deformations seem to be impossible to reach experimentally in real graphene, other systems such as cold atoms in optical lattices [163] or microwaves in artificial deformed honeycomb structures [179, 180] have been realized and Dirac point merging has been observed. The experimental feasibility of our proposal to observe this phenomenon only requires the external light polarization to be varied.

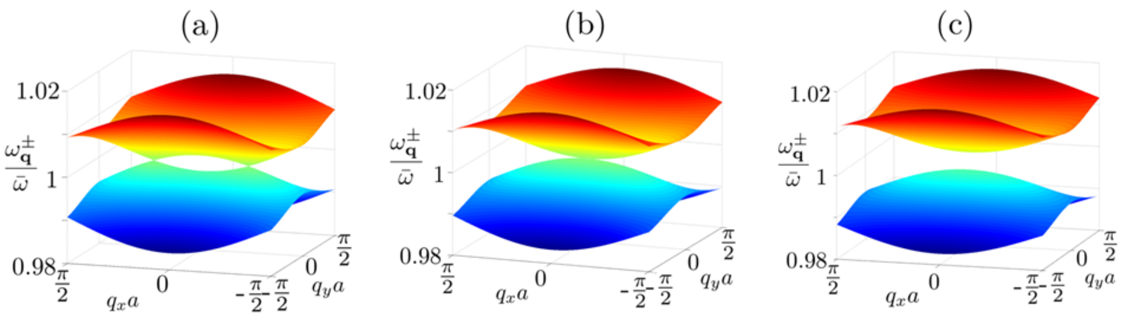

Figure 3.10: Collective Plasmon dispersion for (a) $\theta = \frac{52}{180}\pi$, (b) $\theta = \theta_G \approx \frac{54.7}{180}\pi$, and (c) $\theta = \frac{58}{180}\pi$, with $\phi = 0$ and $\Omega/\omega_0 = 0.01$.

The phase diagram in figure 3.7 shows a symmetry line at $\theta_G = \arcsin\left(\sqrt{\frac{2}{3}}\right) \approx \frac{54.7}{180}\pi$, where the dispersion for a given ϕ either changes from gapped to gapless or vice versa when θ is increased. In figure 3.10, I investigate for $\phi = 0$ the dispersion at θ values just below θ_G (figure 3.10(a)), exactly at $\theta = \theta_G$ (figure 3.10(b)), and just above θ_G (figure 3.10(c)). For small gap sizes the low energy expansions of the dispersion will still be valid. Thus, only a small change in angle is considered. It is evident from the figure that two inequivalent Dirac cones annihilate at $\mathbf{q} = 0$ when $\theta = \theta_G$, subsequently opening a gap and forming two paraboloids for $\theta > \theta_G$. Indeed, this becomes obvious when expanding $f_{\mathbf{q}}$ in the vicinity of $\mathbf{q} = 0$. Introducing $\theta = \theta_G + \delta\theta$ with $0 \leq \delta\theta \ll \theta_G$, I find

$$f_{\mathbf{q}} \approx -3\left[\sqrt{2}\delta\theta + \frac{1}{8}(q_x a)^2\right] + \mathrm{i}\frac{3}{2}q_y a \ , \tag{3.37}$$

and,

$$|f_{\mathbf{q}}| \approx 3\sqrt{2}\delta\theta + \frac{3\sqrt{2}}{16}\left[\sqrt{2}(q_x a)^2 + \frac{1}{\delta\theta}\left(q_y a\right)^2\right] \ . \tag{3.38}$$

Therefore, any finite positive $\delta\theta$ leads to the formation of a gap in the CP spectrum at $\mathbf{q} = 0$ (see equation 3.29). In the vicinity of this point, the bands are parabolic with two inequivalent effective masses whose ratio is controlled by $\delta\theta$ (see figure 3.10). In this case, the gap in the spectrum is due to the non-vanishing $f_{\mathbf{q}}$ at $\mathbf{q} = 0$ (see equation 3.38) and does not require breaking of the symmetry between the two sublattices (as described in chapter 4). At this point, the system no longer has two distinct valleys and can no longer be described by a Dirac Hamiltonian.

3.4 Comparison between the Metamaterial and Graphene

The obvious similarity between graphene and the honeycomb array of metallic nanoparticles is their structure. Apart from the global energy shift of $\hbar\omega_0$, the metamaterial's Hamiltonian given in equation 3.34 strongly resembles the electronic tight-binding Hamiltonian of graphene [5, 6]. However, there are three major differences. I will first explain these in general, and then examine how they affect the special case considered in section 3.3.2.

The first difference is to do with the types of particles involved in each system. The Hamiltonian of graphene describes fermionic particles (electrons), while the LSPs I consider in this metamaterial are bosonic excitations. These types of particles are very different as bosons have no chemical potential or a fixed particle number and a finite lifetime. These differences affect the experimental feasibility of this system and will be clarified in section 3.5. However, even before I conducted this analysis, I expected some of the properties of this system to be similar to those of graphene, because Bloch's theorem does not depend on the quantum statistics of the particles considered in the system, but only on the structure of the periodic lattice. It is this fact that is also responsible for the conical dispersion presented by other systems with honeycomb symmetry [157–163]. Yet, although I have seen these similarities in the case of purely out of plane polarisation, there is a caveat to this expectation when considering other polarisations as this tunability changes the interaction strengths to go beyond what is possible in graphene.

The second difference is to do with the coupling mechanism in both systems: in graphene, an electron hops from one lattice site to a neighbouring one, *i.e.*, the underlying mechanism linking the two inequivalent sublattices is purely kinetic; whereas, in this metamaterial, the mechanism coupling the two sublattices is purely induced by near-field (dipolar) interactions. These dipolar interactions lead to the creation of an LSP excitation at lattice site $\mathbf{R}_B$ and the annihilation of another LSP at a nearest neighbour located at $\mathbf{R}_B + \mathbf{e}_j$. The very different nature of this latter coupling method opens up the possibility of a tunable system, which is not possible in graphene.

Finally, in (unstrained) graphene, the hopping matrix element between two neighbouring atoms is the same for all three bonds. In contrast, in the present case the three energy scales $\hbar\Omega C_j$, with C_j given in equation 3.7, are, in general, different and can be tuned by the direction of the polarization $\hat{\mathbf{p}}$ of the CP eigenmode, which can be controlled by means of an external light field. For $\theta = 0$, all $C_j = 1$, which is analogous to graphene, but for other polarisations this is not necessarily the case. For $0 < \theta \leq \theta_0$ and $\pi - \theta_0 \leq \theta < \pi$ with $\theta_0 = \arcsin(\sqrt{1/3})$, the coefficients

C_j are all positive for any ϕ and have different values, resulting in different couplings between the bonds, thus mimicking the effect of strain in the lattice [181, 182]. For $\theta_0 < \theta < \pi - \theta_0$, the signs of the coefficients C_j depend on ϕ, and the analogy with strained graphene is no longer valid.

Although there are many differences, I have seen that the CP spectrum can resemble that of the electronic band structure in graphene (especially in the special case of $\theta = 0$, considered in section 3.3.2), which is expected from Bloch's theorem. Nonetheless, even in this very special case, there are slight differences between the CP dispersion and the electronic band structure of graphene. The first term in the Hamiltonian, given in equation 3.33, has the effect of producing a global energy shift of $\hbar\omega_0$, such that the Dirac points occur at $\varepsilon = \hbar\omega_0$, rather than $\varepsilon = 0$ as is the case in graphene. This is a minor difference, however, as in graphene the energy is usually scaled so that a zero Fermi energy coincides with the Dirac point. A further difference is that the term $\propto b^{\dagger}_{\mathbf{R}_B} a^{\dagger}_{\mathbf{R}_B+\mathbf{e}_j}$ in equation 3.23 introduces corrections of order $(\Omega/\omega_0)^2$ to the spectrum. Although this does change the spectrum significantly, the effects are only really noticeable far away from the Dirac point, so the approximation of taking energies close to $\varepsilon \approx \hbar\omega_0$ can still be compared to the low energy approximation in graphene.

3.5 Experimental Considerations

In this section I examine some of the considerations that are necessary for experimental research conducted into CP in a metamaterial due to the differences between it and graphene. One of these differences is the fact that the quasi-particles contained within the metamaterial are bosonic in nature, whereas in graphene I consider electrons, which are fermionic. These two types of particles are very different: electrons in graphene have an infinite lifetime, whereas the bosonic excitations in the metamaterial can be created and destroyed such that they only have a finite lifetime. Therefore, a crucial question that has to be addressed in the quest to design arrays of metallic nanoparticles supporting Dirac-like CPs is the effect the inherent damping has on the system. The experimental observability of the CP dispersion will be limited by this plasmonic damping, which tends to blur the resonance frequencies. I will now compare the bandwidth of the CP dispersion to the losses in individual nanoparticles in order to estimate the feasibility of such experiments.

LSPs in individual metallic nanoparticles are subject to three main sources of dissipation

[18]: (i) absorption (Ohmic) losses, that do not depend on the size of the nanoparticle; (ii) radiation damping that scales with the volume of the nanoparticle, with decay rate $\gamma_{\mathrm{rad}}= 2r^3\omega_0^4/3c^3$ [183] (where c is the speed of light) which dominates for larger nanoparticle sizes; and (iii) Landau damping, which is a purely quantum-mechanical effect whose associated decay rate is inversely proportional to the nanoparticle radius, with decay rate $\gamma_L= 3v_F g/4r$ [18, 167–169, 171–173] (where v_F is the bulk Fermi velocity and g a constant of the order of one) which dominates for smaller sizes. The latter two damping mechanisms dominate in particles of different sizes, suggesting there exists an optimal size $r_{\mathrm{opt}}= (3v_F gc^3/8)^{\frac{1}{4}}/\omega_0$ for which the total damping $\gamma_{\mathrm{tot}}= \gamma_{\mathrm{rad}}+\gamma_L$ is minimal. For silver nanoparticles, I find $r_{\mathrm{opt}} = 8\mathrm{nm}$ for which $\gamma_{\mathrm{tot}} = 0.1\mathrm{eV}/\hbar$. Taking an interparticle distance (which maximizes the dipolar coupling between nanoparticles [33,37]) of $a = 3r_{\mathrm{opt}}$, I find that the bandwidth is of the order of $W= \omega^+_{\mathrm{max}} - \omega^-_{\mathrm{min}} = \omega_0/9 = 0.6\mathrm{eV}/\hbar$ at the center of the BZ (for $\epsilon_m = 1$, and for the out-of-plane polarization). Thus, W is sufficiently large when compared to γ_{tot} that the plasmon excitation is well defined and, hence, clearly measurable. Moreover, the appropriate use of active (gain-enhanced) media [184] might increase the observability of the CP dispersion.

Hence, with appropriately sized metallic nanoparticles, the phenomena discussed in this chapter should be observable. However, the interaction between the LSPs may change the picture above. Indeed, recent theoretical results on metallic nanoparticle dimers [185] suggest that while Landau damping is weakly influenced by the dipolar interaction, radiation damping strongly depends of the wavelength of the collective mode. Further work will be needed in order to investigate this important issue.

Although I have discussed the properties of the CPs created on this array, I have neglected to detail the mechanisms for exciting such quasiparticles. The CPs considered in this chapter present the normal modes of the system, and constitute the building blocks for the analysis of the optical properties of Dirac materials. There are many ways in which plasmons can be excited, but the most common is to use external photons incident on the array to give sufficient energy to excite a dipolar resonance in the nanoparticles. In order for the CPs to be excited using external photons, the photons in question have to have a matching in-plane momentum to the plasmonic one. In this case, the plasmons can couple to the incident photon, creating plasmon polaritons, which are generally the mechanism used to propagate energy across a sample [46]. This could result in tunable plasmon polaritons that may inherit some of the effective Dirac-like properties studied in the present work. A preliminary work in this direction [186] has shown that plasmon polaritons in a simple 3D cubic array of metallic nanoparticles present a band structure that is tunable with the polarization of light, leading to birefringence which is purely due to interaction effects between dipolar LSPs. Nonetheless, in my case, the vicinity of the Dirac points typically lies outside the light cone [90]. In order to overcome this momentum mismatch and observe the Dirac plasmons, one might add an extra periodic modulation of the lattice to allow grating coupling between the incident light and the desired collective modes [46]. Another alternative method might be to use a non-linear technique to overcome the momentum mismatch [187].

3.6 Chapter Summary

In this chapter, I have demonstrated the strong analogies between the physical properties of electrons in graphene and those of collective plasmon modes in a 2D honeycomb lattice of metallic nanoparticles. In particular, the similarities between the dispersion shown in figure 3.5 and the electronic band structure of graphene [5, 6] are striking. These similarities exist despite the differences in the quantum statistics of the particles in the two respective cases. Thus, as electronic states of graphene can be described by massless Dirac fermions, the CP eigenstates are found to correspond to massless Dirac-like bosonic excitations. This description means that these bosons have similar properties to fermions in graphene, for example, a Berry phase of π and chirality leading to the absence of backscattering, which opens up the potential to use this system in novel plasmonic device applications.

The massless Dirac nature of these CPs is not all that can be recovered from this metamaterial. The CP spectrum can be fully tuned by the polarization of an external light field, opening exciting new possibilities for controlling the propagation of electromagnetic radiation with subwavelength lateral confinement in plasmonic metamaterials. In this chapter I have unveiled the full Dirac Hamiltonian of quantum CPs as well as the pseudospin structure of the CP eigenmodes for dipolar LSPs with arbitrary orientation. The existence of Dirac points is robust for a small inplane component of the polarization, where the system maps to strained graphene [181, 182], while band gaps can emerge for increasing in-plane polarization. At energies away from the Dirac point, van Hove singularities emerge in the CP DOS, associated with Lifshitz transitions in the topology of equipotential lines [176]. My analysis highlights the physical nature of CP eigenmodes as well as the tunability of their dispersion relation (and of the corresponding DOS) with the polarization of light, which can be crucial for enhancing the coupling of light with the plasmonic metamaterial at different wavelengths.

I have explored in detail the rich phase diagram of gapless and gapped phases emerging from tilting the polarization of the dipole moments and shown that each topologically disconnected gapless phase supports CPs that are effectively described by a massless Dirac Hamiltonian. The emergence of gapped phases from gapless ones occurs via the coalescence of Dirac cones driven by progressively tilting the dipole orientation. This is reminiscent of Dirac point merging in real graphene that has been predicted to occur with extreme mechanical deformations of the lattice [177, 178] but has yet to be seen experimentally [177, 178]. This is more experimentally feasible in the plasmonic metamaterial because the mechanism needed to induce this Dirac point merging is simply the polarisation of the incident light. The fact that the CP dispersion presents a band gap in the vicinity of ω_0 at many polarisation angles unveils the transition of the metamaterial at these frequencies from transparent (conducting) to opaque (insulating).

Although there are systems which have a band gap and still exhibit Dirac-like quasiparticles, of which transition metal dichalcogenides are an example (see section 2.7) [140, 141], the gaps in these systems are produced by inversion symmetry breaking, which is not the case in our metamaterial. As the Dirac points merge in the CP to create a gap, the two valley physics is broken, and the system can no longer be described by a Dirac Hamiltonian. Thus, the Dirac nature of the CP excitations is not robust for all dipole polarisations.

Taking inspiration from transition metal dichalcogenides, in the following chapter I will explore the effect broken inversion symmetry has on a honeycomb array of metallic nanoparticles.

4

Honeycomb Plasmonic Metamaterial with Broken Inversion Symmetry

In this chapter I present the work I conducted, which resulted in the recent paper [151], in collaboration with Guillaume Weick, Eros Mariani and Thomas Sturges.

This chapter directly follows on from the work presented in chapter 3. Advances in high-precision electron beam lithography as well as other techniques, such as self-assembly, permit the creation of well defined ordered arrays of nanostructures, so that they can be made to reproduce lattices seen in nature, like the honeycomb structure of graphene and many more. Because the properties of the CPs crucially depend on the lattice structure of the metamaterial, variations of that structure are considered. These artificial graphene systems could greatly benefit both theorists and device-physicists as, unlike its carbon based counterpart, almost every parameter of the system can be manipulated to tailor the properties of the material.

In this chapter I take advantage of such tunability and study in detail the CP dispersion relation of bipartite hexagonal arrays of nanoparticles that have been adapted from the graphene-like case, such that the inversion symmetry is broken. Further, I explore the effect of breaking the inversion symmetry by envisaging that the basis nanoparticles of each of the two sublattices have inequivalent plasmon resonance frequencies. Ways to achieve this experimentally are described in the next section.

4.1 Arrangement Description

I consider the perfect honeycomb array of spherical metallic nanoparticles, as before, but now with broken inversion symmetry by envisaging that the LSPs on the A and B sublattices have inequivalent resonance frequencies, ω_A and ω_B, respectively. As the LSP resonance frequency depends on the particle size, shape and material constitution, the particles on each sublattice can have different resonance frequencies if any of these parameters are inequivalent for the different sublattices. Thus the differing frequencies could be realised experimentally by either manufacturing the two sublattices out of different materials or by constructing them to be different sizes [18].

Other than this change the honeycomb shape is considered to be the same as in the previous chapter, as shown in figure 3.1, where the nearest neighbour vectors $\mathbf{e}_j$ are given in equation 3.1 and the centres of the nanoparticles are still considered to occur at the $\mathbf{R}_s$ positions, with $s = A, B$ the sublattice index. For the quasistatic approximation of point-like interacting dipoles to hold I still assume that both radii (r_A and r_B) of the particles in the two sublattices are much smaller than λ.

4.2 Generic Effective Hamiltonian and Dispersion Relation

As, in this chapter I elect to break the inversion symmetry of the system, I can re-embrace the Hamiltonian, $H = H_0 + H_{\text{int}}$, given in chapter 3 (see equations 3.22 and 3.23 respectively), and express it in the more general form as

$$\begin{aligned} H_0 &= \hbar\omega_A \sum_{\mathbf{R}_A} a^{\dagger}_{\mathbf{R}_A} a_{\mathbf{R}_A} + \hbar\omega_B \sum_{\mathbf{R}_B} b^{\dagger}_{\mathbf{R}_B} b_{\mathbf{R}_B}, \\ H_{\text{int}} &= \hbar\tilde{\Omega} \sum_{\mathbf{R}_B} \sum_{j=1}^{3} C_j b^{\dagger}_{\mathbf{R}_B} (a_{\mathbf{R}_B+\mathbf{e}_j} + a^{\dagger}_{\mathbf{R}_B+\mathbf{e}_j}) + H.c. \end{aligned} \tag{4.1}$$

where $\tilde{\Omega}=\ \sqrt{\omega_A\omega_B}\left(\frac{r_A r_B}{a^2}\right)^{3/2}\frac{1+2\epsilon_m}{6\epsilon_m}\ =\ \sqrt{\frac{\omega_A\omega_B}{\omega_0^2}}\left(\frac{r_A r_B}{r^2}\right)^{3/2}\Omega$ and the bosonic ladder operators read

$$a_{\mathbf{R}_A}|b_{\mathbf{R}_B} = \sqrt{\frac{M_{A|B}\omega_{A|B}}{2\hbar}}\, h_{A|B}(\mathbf{R}_{A|B}) + \frac{i\Pi_{A|B}(\mathbf{R}_{A|B})}{\sqrt{2\hbar M_{A|B}\omega_{A|B}}}. \tag{4.2}$$

which obey the same commutation relations as seen in chapter 3. By converting the ladder operators into momentum space, using equation 3.24, the Hamiltonian can be written as

$$H = \hbar\sum_{\mathbf{q}}\left(\omega_A a_{\mathbf{q}}^{\dagger}a_{\mathbf{q}} + \omega_B b_{\mathbf{q}}^{\dagger}b_{\mathbf{q}}\right) + \hbar\tilde{\Omega}\sum_{\mathbf{q}}\left[f_{\mathbf{q}}b_{\mathbf{q}}^{\dagger}\left(a_{\mathbf{q}} + a_{-\mathbf{q}}^{\dagger}\right) + f_{\mathbf{q}}^{*}\left(a_{\mathbf{q}}^{\dagger} + a_{-\mathbf{q}}\right)b_{\mathbf{q}}\right] \tag{4.3}$$

As in chapter 3, the information regarding the polarisation of the LSPs, in equation 4.3, is encoded in the function $f_{\mathbf{q}} = \sum_{j=1}^{3} C_j \exp(i\mathbf{q}\cdot\mathbf{e}_j)$, which is ultimately the source of the wavevector dependence in the dispersion relation, where $C_j = \left[1 - 3\sin^2\theta\cos^2\left(\phi - \frac{2\pi(j-1)}{3}\right)\right]$.

A trivial extension of the logic presented in chapter 3 leads to the eigenmodes of the system, $\beta_{\mathbf{q}} = wa_{\mathbf{q}} + xb_{\mathbf{q}} + ya_{-\mathbf{q}}^{\dagger} + zb_{-\mathbf{q}}^{\dagger}$, now with inequivalent sublattice basis nanoparticles. These diagonalise the Hamiltonian, reading

$$H = \sum_{\tau=\pm}\sum_{\mathbf{q}}\hbar\omega_{\mathbf{q}}^{\tau}\beta_{\mathbf{q}}^{\tau\dagger}\beta_{\mathbf{q}}^{\tau}, \tag{4.4}$$

where the general operator obeys the Heisenberg equation of motion $\left[\beta_{\mathbf{q}}, H\right] = \hbar\omega_{\mathbf{q}}\beta_{\mathbf{q}}$. This eigenvalue problem may again be written in matrix form as $\psi\mathbf{M}\mathbf{X} = \omega_{\mathbf{q}}\beta_{\mathbf{q}} = \omega_{\mathbf{q}}\psi\mathbf{X}$, where $\psi = (a_{\mathbf{q}}, b_{\mathbf{q}}, a_{-\mathbf{q}}^{\dagger}, b_{-\mathbf{q}}^{\dagger})$, $\mathbf{X} = (w, x, y, z)^T$ and

$$\mathbf{M} = \begin{pmatrix} \omega_A & \tilde{\Omega}f_{\mathbf{q}} & 0 & -\tilde{\Omega}f_{\mathbf{q}} \\ \tilde{\Omega}f_{\mathbf{q}}^{*} & \omega_B & -\tilde{\Omega}f_{\mathbf{q}}^{*} & 0 \\ 0 & \tilde{\Omega}f_{\mathbf{q}} & -\omega_A & -\tilde{\Omega}f_{\mathbf{q}} \\ \tilde{\Omega}f_{\mathbf{q}}^{*} & 0 & -\tilde{\Omega}f_{\mathbf{q}}^{*} & -\omega_B \end{pmatrix}, \tag{4.5}$$

from which the CP dispersion can be found,

$$\omega_{\mathbf{q}}^{\pm} = \sqrt{\frac{\omega_A^2 + \omega_B^2}{2} \pm \sqrt{\left(\frac{\omega_A^2 - \omega_B^2}{2}\right)^2 + 4\omega_A\omega_B\tilde{\Omega}^2|f_{\mathbf{q}}|^2}}\ . \tag{4.6}$$

It is convenient to express the two LSP frequencies in a symmetric form as $\omega_A = \bar{\omega} + \frac{\delta\omega}{2}$

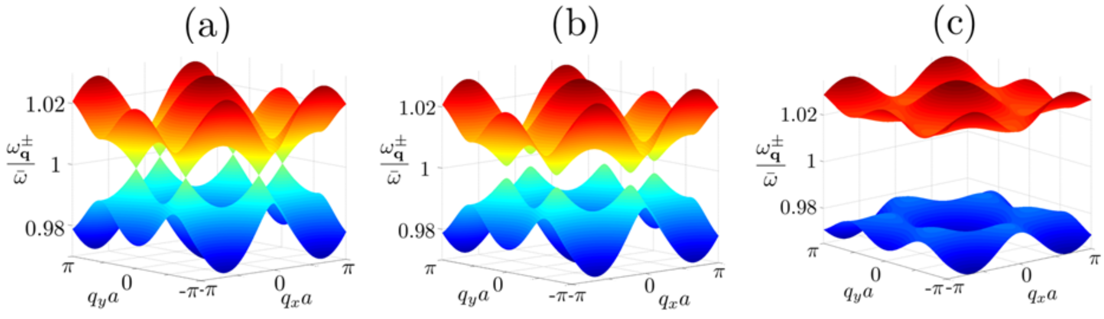

Figure 4.1: Collective plasmon dispersions from equation 4.7 with LSP polarisation normal to the plane ($\theta = 0$), for (a) no asymmetry such that $\frac{\delta\omega}{\bar{\omega}} = 0$, (b) $\frac{\delta\omega}{\bar{\omega}} = 0.004$ and (c) $\frac{\delta\omega}{\bar{\omega}} = 0.04$. In the figure $\tilde{\Omega}/\omega_0 = 0.01$.

and $\omega_B = \bar{\omega} - \frac{\delta\omega}{2}$, with $\bar{\omega}$ being the average frequency and $\delta\omega$ being the difference in frequency[1]. This allows us to tune the asymmetry, $\delta\omega$. Thus the CP spectrum given in equation 4.6, becomes

$$\omega_{\mathbf{q}}^{\pm} = \sqrt{\bar{\omega}^2 - (\delta\omega)^2 \pm 2\bar{\omega}\sqrt{(\delta\omega)^2 + \left(1 - \frac{(\delta\omega)^2}{\bar{\omega}^2}\right)\tilde{\Omega}^2|f_{\mathbf{q}}|^2}}\,. \tag{4.7}$$

4.3 Tunable Properties with Asymmetry

In figure 4.1 I plot the dispersion, given in equation 4.7, for the special case where the polarisation points perpendicular to the 2D plane ($\theta = 0$), for different amounts of asymmetry: $\frac{\delta\omega}{\bar{\omega}} = 0$ (figure 4.1(a)); $\frac{\delta\omega}{\bar{\omega}} = 0.004$ (figure 4.1(b)); and $\frac{\delta\omega}{\bar{\omega}} = 0.04$ (figure 4.1(c)). As would be expected, when $\delta\omega = 0$ (thus $\omega_A = \omega_B = \omega_0$), as shown in figure 4.1(a), the two CP branches return to the same form as has already been seen in chapter 3. However, it can be seen from the figure that any finite difference in the LSP frequencies ($\delta\omega \neq 0$) introduces an asymmetry into the system that corresponds to a gap of size $\delta\omega$ opening in the spectrum, while the extrema of the two bands still occur at the K and K' points in the Brillouin zone. I will show in section 4.4 that, by expanding equation 4.4 close to these extrema, I can identify an effective Hamiltonian that comprehensively describes the CPs and, interestingly, corresponds to a *massive* Dirac Hamiltonian, again up to a global shift of $\hbar\omega_0$.

Notice also that the symmetry-breaking term, $\delta\omega$, affects the bandwidth of each plasmonic

---

[1] For definitiveness I assume that $\delta\omega \geq 0$, without loss of generality.

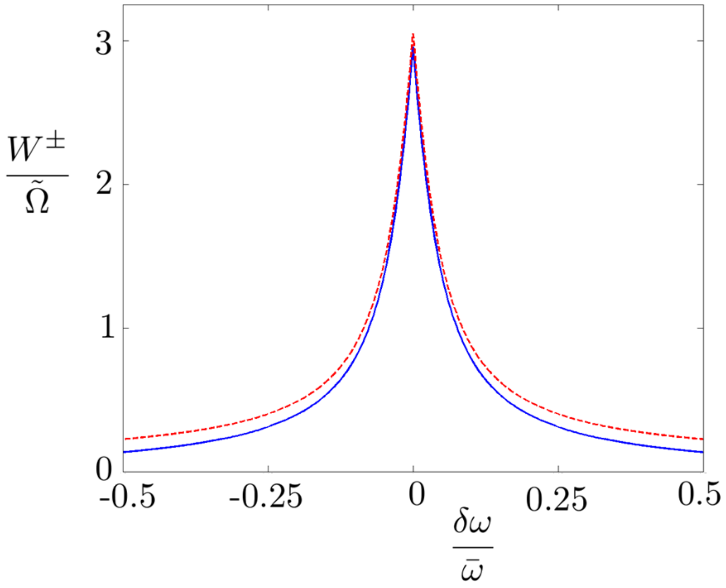

Figure 4.2: Widths, W^{+} and W^{-}, of the upper and lower plasmonic bands (blue solid and red dashed lines), respectively, in units of $\tilde{\Omega}$ as a function of the asymmetry, $\frac{\delta\omega}{\bar{\omega}}$. In the figure $\tilde{\Omega}/\omega_0 = 0.01$.

---

subband, defined as $W^{\tau} = \max\left\{\omega_{\mathbf{q}}^{\tau}\right\} - \min\left\{\omega_{\mathbf{q}}^{\tau}\right\}$ (where $\tau = \pm$ for the upper and lower bands, respectively), as shown in figure 4.2. In particular, increasing $|\delta\omega|$ leads to an algebraic decrease of both bandwidths, such that, as the asymmetry is increased, the dispersion is essentially flattened. This will have an effect on the observability of these CPs, as discussed in section 4.6.

Figure 4.3 shows the width of an individual band compared to the total width of the entire dispersion, measured from the minima of the lower band to the maxima of the upper band. As there is a strong linear dependence of total band width on asymmetry for larger asymmetries, and the band gap size is linearly proportional to the asymmetry, it is evident that the total band width is dominated by the gap size for large asymmetry.

4.4 Dirac-like Nature of the Collective Plasmon Quasiparticles

As can be seen from figure 4.1(b), although there is a gap in the spectrum the extrema of the bands still occur at the K points in the Brillouin zone. Substituting the symmetric terms for $\omega_A = \bar{\omega} + \delta\omega$ and $\omega_B = \bar{\omega} - \delta\omega$ into the Hamiltonian (given in equation 4.4) and expanding it in the vicinity of each extrema, in the basis $\hat{\Psi}_{\mathbf{k}} = (a_{\mathbf{k},K}, b_{\mathbf{k},K}, a_{\mathbf{k},K'}, b_{\mathbf{k},K'})$, the effective Hamiltonian reads

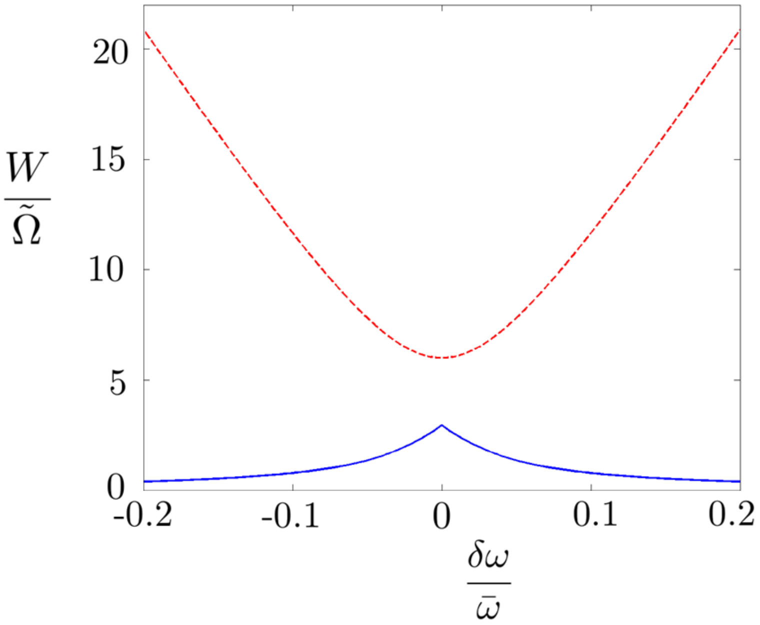

Figure 4.3: The total width of both bands, W, which is measured from the bottom of the lower band to the top of the upper band, such that the band gap size is included (red dashed line), together with the width of just the upper band, W^+ (blue solid line), as a function of asymmetry, $\delta\omega$. In the figure, $\tilde{\Omega}/\omega_0 = 0.01$.

$$\mathcal{H}_{\mathbf{k}}^{\text{eff}} = \hbar\bar{\omega}\mathcal{I} + \frac{\hbar\delta\omega}{2}\tau_z \otimes \sigma_z - \hbar\tilde{v}\left(\tau_x\sigma_x k_x + \tau_y\sigma_y k_y\right) \quad , \tag{4.8}$$

with eigenvalues given by

$$\omega_{\mathbf{k}}^{\pm} = \bar{\omega} \pm \sqrt{\tilde{v}^2|\mathbf{k}|^2 + \left(\frac{\delta\omega}{2}\right)^2} \quad , \tag{4.9}$$

where $\tilde{v} = \frac{3\tilde{\Omega}a}{2}$.

In contrast to the analysis in chapter 3, here, with any non-zero asymmetry, the dispersion is gapped for any value of wavevector and the quasiparticles acquire a finite effective mass, $m^* = \frac{\hbar\delta\omega}{2\tilde{v}^2}$, due to the inversion symmetry breaking term, $\delta\omega \neq 0$. When $\delta\omega \neq 0$ equation 4.8 corresponds to a massive Dirac Hamiltonian (up to a global shift in energy of $\hbar\bar{\omega}$), signifying that the CP eigenmodes can be described as massive Dirac bosons. These are analogous to the massive Dirac fermions in other Dirac materials with broken inversion symmetry, such as transition metal dichalcogenides [140] and graphene on hexagonal boron nitride [138] (seen in section 2.7).

The origin of this massive behaviour is very different from the case in bilayer graphene where the effective mass is due to the curvature of its electronic dispersion and quasiparticles in bilayer graphene act as though they have mass even though there is no gap in the spectrum [113].

4.5 Eigenspinors and Berry Phase

I now utilise the effective Hamiltonian to explore some of the properties of the system, namely the quasiparticles pseudo-spin and Berry phase. The pseudo-spin is a consequence of the bipartite nature of these graphene-like lattices, leading to the need for a two-component wavefunction to define the relative contributions to the quasiparticles from each of the two sublattices. The latter of these, the Berry phase, is a geometric phase acquired by the quasiparticle over the course of a cyclic adiabatic process [97], and is proportional to the solid angle that the pseudospin encloses in that cyclic process [98].

Besides the global energy shift, the effective Hamiltonian, given in equation 4.8, in each valley evolves continuously between a purely out-of-plane Zeeman term $\frac{\hbar\delta\omega}{2}\sigma_z$ (when $\tilde{v}|\mathbf{k}| \ll \delta\omega$) and a 2D massless Dirac Hamiltonian $-\hbar\tilde{v}\boldsymbol{\sigma}\cdot\mathbf{k}$ (when $\tilde{v}|\mathbf{k}| \gg \delta\omega$). The eigenstates of the Hamiltonian in the K valley thus correspond to the normalised vector in the Bloch sphere

$$\mathbf{V}^{\pm}_{\mathbf{k}} = \pm\frac{1}{\sqrt{\tilde{v}^2|\mathbf{k}|^2 + \left(\frac{\delta\omega}{2}\right)^2}}\left(-\tilde{v}k_x, -\tilde{v}k_y, \frac{\delta\omega}{2}\right) \ . \tag{4.10}$$

From this, I can calculate the Berry phase of the pseudospin $\mathfrak{s} = \frac{1}{2}$ Dirac quasiparticles described by the Hamiltonian shown in equation 4.8 as $\phi_B = \mathfrak{s}\Omega_B$, with Ω_B the solid angle enclosed by the Bloch-sphere vector $\mathbf{V}^{\pm}_{\mathbf{k}}$ while the state $|\mathbf{k}\rangle$ is transported anticlockwise in a closed loop around the Dirac point in the 2D wavevector space [98, 188]. The vector $\mathbf{V}^{\pm}_{\mathbf{k}}$ is shown in figure 4.4 for both the case when $\delta\omega = 0$ and $\delta\omega \neq 0$. Depending on the ratio $\frac{\tilde{v}|\mathbf{k}|}{\delta\omega}$, and thus on the quasiparticle energy, the solid angle Ω_B changes (see the figure 4.4(b)). This ranges from $\Omega_B = 0$ at the band gap edges ($\omega = \bar{\omega} \pm \frac{\delta\omega}{2}$, where $\mathbf{V}^{\pm}_{\mathbf{k}=0} = \pm\hat{z}$) to $\Omega_B \approx 2\pi$ if $\tilde{v}|\mathbf{k}| \gg \frac{\delta\omega}{2}$ (where $\mathbf{V}^{\pm}_{\mathbf{k}}$ rotates in the xy plane).

Interestingly, I find that CPs in honeycomb arrays with broken inversion symmetry are naturally described as Dirac quasiparticles in a gapped spectrum with an energy-dependent Berry phase (defined up to integer multiples of 2π), reading

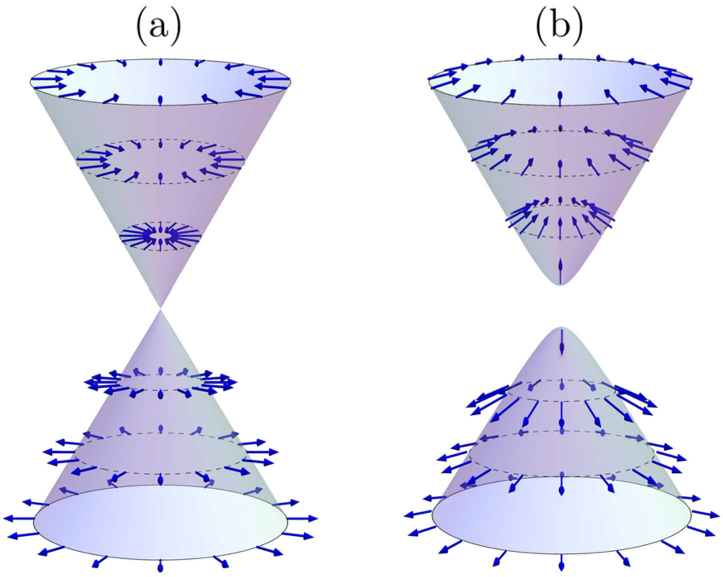

Figure 4.4: Sketch of the CP dipsersion in the vicinity of the (K) Dirac point in the first Brillouin zone, while the arrows depict the unit vector $\mathbf{V}_{\mathbf{k}}^{\pm}$ defined in the equation 4.10, for (a) the case where $\delta\omega = 0$ and the dispersion is gapless and the pseudo-spin resembles that of graphene; and (b) where $\delta\omega \neq 0$.

$$\phi_B(\omega) = \pi \frac{|\omega - \bar{\omega}| - \frac{\delta\omega}{2}}{|\omega - \bar{\omega}|} \quad , \tag{4.11}$$

in the K valley if $|\omega - \bar{\omega}| \geq \frac{\delta\omega}{2}$. A similar analysis yields an equal and opposite Berry phase for the K' valley.

When $\delta\omega = 0$, shown in figure 4.4(a), the pseudospin always points antiparallel (parallel) to the wavevector in the upper (lower) band and the Berry phase returns to π which is the same as in monolayer graphene. However, with a non-zero asymmetry the direction of the pseudospin is energy dependent, thus enclosing different solid angles and the Berry phase depends on energy: at the minima of the top band ($\omega_{\mathbf{q}}^{(+)} - \bar{\omega} \approx \delta\omega$) the Berry phase tends to zero whilst at high energies ($\omega_{\mathbf{q}}^{(+)} - \bar{\omega} \gg 2\delta\omega$) it tends to π, the latter case being analogous to that found for electrons in monolayer graphene [8, 9]. Thus, this massive behaviour is most evident at lower energies, close to the extrema of the bands.

The explicit connection between pseudo spin and orbital degrees of freedom evident in the effective Hamiltonian, given in equation 4.8, is at the very heart of several properties exhibited by quasiparticles in real and artificial graphene systems, such as the suppression of elastic backscattering from smooth impurity potentials [10], weak antilocalisation [189, 190] as well as the anomalous quantum Hall effect [8, 9]. In chapter 5, I analyse in detail the consequences of the energy-dependent geometric phase of the CP on the quantum transport properties of gapped Dirac quasiparticles.

4.6 Experimental Observability of the Collective Plasmon Quasiparticles

As explained in section 3.5, the observation of the remarkable phenomena associated with these CPs is limited by plasmonic damping which tends to blur the resonance frequencies of the CP dispersion. To estimate the feasibility of resolving these features experimentally, it is useful to compare the CP band width to the typical losses in individual nanoparticles. I have previously indicated that both radiation damping [183] and Landau damping [18, 167–172, 174, 175] can be minimised for nanoparticles of an optimal size. For example, with silver nanoparticles, $r_{\text{opt}} = 8\text{nm}$ gives a total damping rate of $0.1\text{eV}/\hbar$. With particles separated by $a = 3r_{\text{opt}}$, to maximise the dipolar coupling, the width of an individual band $\sim 0.6\text{eV}/\hbar$. Therefore, for no asymmetry, the bandwidth can be sufficiently large compared with the total damping rate.

However, the width of the individual bands reduces drastically with increased asymmetry, thus there will be a maximum asymmetry in frequencies (corresponding to a minimum band width) that will allow for the observation of the CP dispersion. From figure 4.2 it can be deduced that the CP bandwidth will be comparable to the blurring due to damping if there is a difference in resonant frequencies of $\frac{\delta\omega}{\bar{\omega}} \sim 0.1$. Thus, the asymmetry must be much less then this for the CP spectrum to be clearly visible. This experimental restriction cooperates nicely with the low energy approximation (*i.e.* energies close to the Dirac point) taken here.

4.7 Comparison with Other Systems and Generalisation

It is interesting to note that, although the lattice design was inspired by graphene and then an adaptation was taken to break the inversion symmetry, due to the crystal symmetry properties, the Hamiltonian and dispersion relation that have been found in this chapter are are very similar to those of several other natural and artificial materials, which recently generated a lot of interest in the scientific community. This Hamiltonian is also of the same form as that for graphene with a staggered sublattice potential [191], and similarly that which will describe graphene on hexagonal Boron Nitride [192, 193]. Furthermore, a Hamiltonian of this form describes transition metal dichalcogenides, for example MoS_2 [194–196] as each sublattice consists of different atoms, breaking the inversion symmetry, as shown in section 2.7. There has been great interest in MoS_2 due to its band gap, as there it is possible that using this material could allow Dirac particles to be used in devices such as transistors by overcoming the lack of an on/off ratio that is found in graphene. However, MoS_2 has a very large band gap which may make it impractical for device applications [140, 141].

It is possible to generalise my current treatment in order to allow for the prediction of the properties of, not only the plasmonic metamaterials considered here, but those of other materials as well. First, I can generalise the low energy Hamiltonian to be

$$H^{(\tau)} = v\hbar(\tau k_x\hat{\sigma}_x + k_y\hat{\sigma}_y) + \frac{\Delta}{2}\hat{\sigma}_z \ , \tag{4.12}$$

where v is the group velocity of the quasiparticles in the given system, $\tau = \pm 1$ is a valley index, $\hat{\boldsymbol{\sigma}} = (\hat{\sigma}_x, \hat{\sigma}_y)$ are the Pauli matrices, Δ is the size of the band gap given by the minimum energy of the upper band minus the maximum energy of the lower band, $\Delta = \varepsilon^{(+)}_{\text{min}} - \varepsilon^{(-)}_{\text{max}}$. For comparison to our plasmonic case, $\Delta = \hbar\delta\omega$ and the global energy shift, $\hbar\bar{\omega}$, is encompassed in the symmetric energy eigenvalue, defined from the centre of the band gap in any material as $\varepsilon^{\pm}_{\mathbf{k}} = \hbar(\omega^{\pm}_{\mathbf{k}} - \bar{\omega})$. The Hamiltonian in equation 4.12 has energy eigenvalues, $\varepsilon^{\pm}_{\mathbf{k}} = \pm\sqrt{v^2\hbar^2|\mathbf{k}|^2 + \frac{\Delta^2}{4}}$, and spinor eigenstates,

$$\psi = \begin{pmatrix} \psi_A \\ \psi_B \end{pmatrix} = \sqrt{\frac{\varepsilon + \frac{\Delta}{2}}{2\varepsilon}} \begin{pmatrix} 1 \\ \frac{v\hbar\mathbf{k}}{\varepsilon + \frac{\Delta}{2}} \end{pmatrix} . \tag{4.13}$$

These materials belong to a new class of systems with an energy dependent Berry phase, of the general form

$$\Phi_{\text{B}} = \pi\left(\frac{|\varepsilon| - \frac{\Delta}{2}}{|\varepsilon|}\right) \ , \tag{4.14}$$

in the K valley when $|\varepsilon| > \frac{\Delta}{2}$. Performing the same analysis on the K' valley yields the equal and opposite result. This can be calculated from a generalised version of the normalised vector in the Bloch sphere, given by

$$\mathbf{V}_{\mathbf{k}}^{\pm} = \pm \frac{1}{\sqrt{v^2\hbar^2|\mathbf{k}|^2 + \left(\frac{\Delta}{2}\right)^2}} \left(-v\hbar k_x, -v\hbar k_y, \frac{\Delta}{2}\right) \ . \tag{4.15}$$

4.8 Chapter Summary

In this chapter, I have extended the analysis conducted in chapter 3 to consider a lattice with broken inversion symmetry. As such, the two sublattices A and B of the honeycomb array are inequivalent and are considered to have different natural oscillation frequencies ω_A and ω_B, respectively. Having analysed the band structure of CPs stemming from the near field dipolar coupling between LSPs in individual nanoparticles, I unveil that CPs are effectively described as Dirac particles with a gapped linear spectrum. The Hamiltonian describing the system is Dirac like with additional σ_z terms that open a gap in the CP spectrum. This Hamiltonian, and the chiral nature of the spinor wavefunctions, lead to the bosonic excitations having an energy dependent Berry phase. Moreover, I show that the general form of the effective Hamiltonian that describes these CPs is not unique to this system and, in fact, by generalising the Hamiltonian, dispersion and eigenvectors, I have discovered properties universal to all these systems. Thus, I can describe a new class of system, with an energy dependent Berry phase. The energy dependent chirality and Berry phase of such systems lead to the fact that other properties are energy dependent. The effect this has on the quantum transport properties of quasiparticles in gapped Dirac materials is explored in the chapter 5.

Thus, by considering this simple change to the basic honeycomb lattice analysed previously, I have discovered the further adaptability of this plasmonic metamaterial, such that it could be modified to have the properties needed for multiple device applications. Furthermore, although in graphene on boron nitride and in transition metal dichalcogenides the band gap is fixed, in the plasmonic metamaterial it can be tuned with asymmetry, thus a gap size that best fits the proposed application can be manufactured. This variability could make this metamaterial pertinent for many different implementations.

It is interesting to note that there are many further adaptations that can be taken, which could be seen as future work along this line of research, some of which have been undertaken by members of my research group. For example, we have considered changing the honeycomb structure itself. The Dirac nature of the CPs contained in these systems is a direct consequence of the bipartite nature of the honeycomb array (*i.e.* that one can describe it with two inequivalent sublattices), which for a time-reversal symmetric and parity-invariant 2D lattice leads to a four-component wavefunction [197]. However, the honeycomb lattice considered here is a particular case of a large family of hexagonal bipartite lattices which can also be described in this way, and as such would lead us to expect the others to also contain Dirac quasiparticles, along with much of the accompanying quantum phenomena which I revealed in chapter 3 for the particular case of the perfect honeycomb structure. The properties of hexagonal bipartite lattices have been investigated in more generality in a recent paper [151]. The formation of such lattices was accomplished by starting with the honeycomb structure and displacing the second basis particle, in essence shifting one of the sublattices with respect to the other. Investigating these 'non-honeycomb' bipartite lattices lead to the discovery that massless Dirac bosons can indeed be recovered and, interestingly, the emergence of topological phase transitions in the evolution of the phase diagram for a succession of different lattices was observed. Therefore, the honeycomb lattice should no longer be considered unique in hosting Dirac quasiparticles.

5

Klein Tunnelling in Dirac Materials with a Linear Gapped Spectrum

The research presented in this chapter is work I conducted, whilst assisting a summer student (Alex Cope), that will be exhibited in a forthcoming paper [198], in collaboration with Eros Mariani and Alex Cope.

When a particle is incident on a potential barrier non-relativistic quantum mechanics dictates that the probability the particle will tunnel through reduces exponentially with increased width and height of the barrier [89]. This paradigm is overcome in relativistic quantum mechanics, where the Klein paradox describes the process which results in unimpeded tunnelling of relativistic particles through high and wide potential barriers [107].

The Klein paradox is one of the most counterintuitive results from quantum electrodynamics and has been discussed in particle-, nuclear-, and astro-physics, but direct testing using elementary particles has so far proved impossible [87]. Nevertheless, there have been conceptually simple experiments of the phenomenon in condensed matter using monolayer and bilayer graphene, due to the chiral nature of the Dirac quasiparticles in these materials [199] and the presence of states in the barrier [87], see section 2.5.3. Electron-hole conversion and conservation of pseudospin explain the perfect tunnelling at normal incidence in monolayer graphene [87], which is the complete opposite of the perfect reflection seen in bilayer graphene at normal incidence due to the lack of conservation of pseudospin [87], see section 2.6.3. The unusual behaviour of monolayer graphene is reflected in its non-trivial Berry phase [97] of π [100–102], which has been detected, for example, in Quantum Hall Effect (QHE) measurements [8, 105, 106]. These, and many other 2D materials have attracted attention due to their possible usefulness for the next generation of nano-electronic devices, but some of their Klein tunnelling (KT) results may be a hinderence to this application. However, this may be overcome by breaking the inversion symmetry of these systems or considering Dirac materials which already have broken inversion symmetry. The Berry phase is usually fixed for a given system, however breaking the inversion symmetry of Dirac materials opens a gap in their linear spectra and leads to them exhibiting an energy dependent Berry phase, as described in chapter 4. This energy dependent Berry phase has a substantial effect on the materials ballistic transport properties, which could make them even more useful in nano-electronic or nano-plasmonic devices [200, 201].

In the current chapter I analyse this relativistic phenomenon for Dirac particles in systems with broken inversion symmetry (and thus a gapped spectrum) in materials with a linear spectrum like monolayer transition metal dichalcogenides and graphene on hexagonal boron nitride, as well as broken inversion symmetric honeycomb arrays of metallic nanoparticles. These are a new class of system with an energy dependent Berry phase that leads to energy dependent transmission probabilities, which can be tuned with barrier height and gap size. Breaking the inversion symmetry of the system allows for previously unseen results, which are often the complete opposite to those of their inversion symmetric counterparts. I theoretically prove the concept of KT of Dirac particles in systems with a gapped linear spectrum, with a generalised approach, in order for the results to be applicable to a large number of materials. The possible experimental platforms are characterised by massless Dirac Hamiltonians, and additional σ_z terms due to broken inversion symmetry.

It is important to specify that in the literature, quasiparticles in both bilayer graphene and in systems like transition metal dichalcogenides behave like massive Dirac particles, but they have distinctly different Hamiltonians. In bilayer graphene the massive behaviour is due to the curvature of the dispersion and occurs even without a gap in the spectrum but, in systems like transition metal dichalcogenides the massive behaviour is due to the band gap produced by broken inversion symmetry. Consequently, to avoid confusion, Dirac quasiparticles in systems with a linear gapped spectrum, such as in transition metal dichalcogenides, are here referred to as Dirac Quasiparticles In Linear Gapped Systems (DQILGS), and Dirac quasiparticles in systems with a parabolic spectrum, like bilayer graphene, are referred to as Dirac Quasiparticles in Parabolic Systems (DQIPS).

In order to examine the quantum transport properties of this system I envisage quasiparticles incident on a potential barrier and investigate the KT probabilities of those particles through the barrier. The device design for both fermionic and bosonic systems are described in the next section.

5.1 Experimental Design

The Klein tunnelling potential scheme considered here is illustrated in figure 5.1. I consider a potential barrier with a rectangular shape, which is invariant along the y-axis (leading to the assumption that the y-component of the wavevector is invariant across the device), so that:

$$V(x) = \begin{cases} V_0 & \text{if } 0 < x < L \\ 0 & \text{otherwise.} \end{cases}$$

I assume the width (W) of the barrier is much greater than the length (L), so that edge effects can be be neglected [121]. In order to make a direct analogy to the case usually considered in quantum electro-dynamics (QED) [11, 108], and to simplify the problem, I assume the potential step is sharp [87]. This assumption holds true as long as: 1) in fermionic systems, the quasiparticle's Fermi wavelength, λ_F, is much larger than the edge smearing characteristic width (which in turn should be larger than the lattice constant to make Umklapp scattering between different valleys forbidden) [87]; or 2) in plasmonic systems, the wavelength of the CP mode (which encompasses the LSPs across the system) is much greater than the dimensions of the nanoparticles in the array.

In Dirac materials that contain fermionic carriers, these barriers can be created with an electric field using thin local electrostatic gates above the system, or by local chemical doping [3, 8, 106, 202]. A schematic diagram of a suggested tunnelling device for fermionic systems is

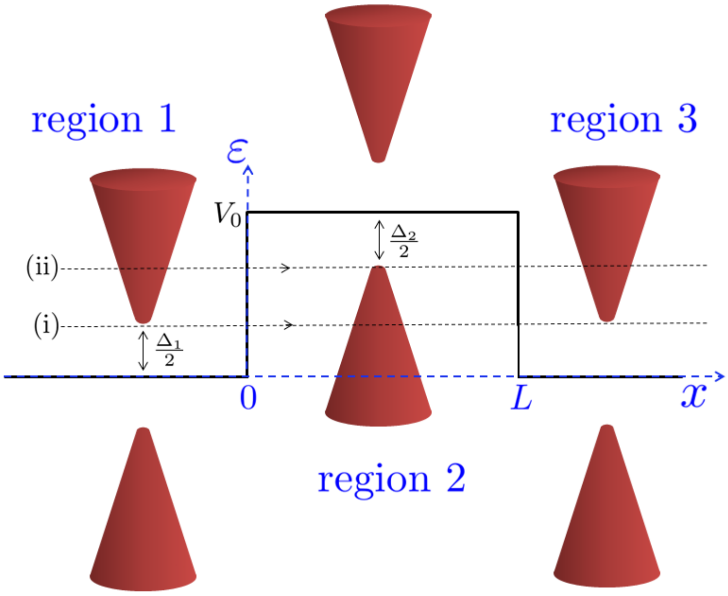

Figure 5.1: Schematic diagram for tunnelling through a potential barrier, where the zero point of the energy is chosen to be at the base of the barrier. For generality the gap size is allowed to be different inside and outside the barrier, such that the gap size in regions 1 ($x \leq 0$) and 3 ($x \geq L$) is Δ_1, and in region 2 ($0 < x < L$) is Δ_2. Lines (i) and (ii) show the specific cases corresponding to the conductance lines in figure 5.10: (i) corresponds to E_1, where $\varepsilon = \frac{\Delta_1}{2}$, (ii) corresponds to E_2, where $\varepsilon = V_0 - \frac{\Delta_2}{2}$.

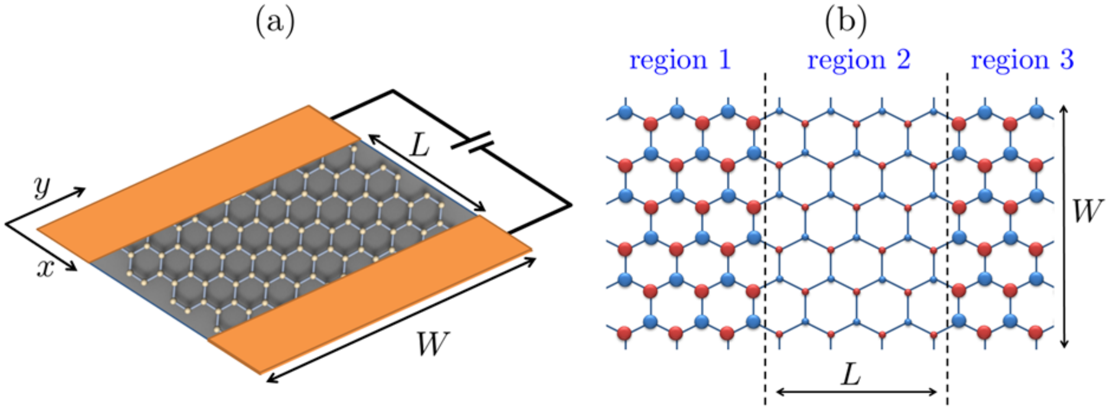

Figure 5.2: Tunnelling devices for materials containing particles with different quantum statistics. Panel (a) shows the device design considered for fermionic quasiparticles, where the material containing the gapped Dirac particles is in a strip between metal contacts. The metal contacts (or leads) constitute regions 1 and 3, shown in figure 5.1, and the central Dirac material is region 2. Panel (b) shows the device design for plasmonic systems, specifically a honeycomb array of metallic nanoparticles. The 'potential' increase in region 2 is created by varying the size of the particles, and thus changing their average resonant frequency, $\bar{\omega}$.

---

shown in figure 5.2(a).

In plasmonic metamaterials this barrier could be produced by locally shifting the average natural frequency $\bar{\omega}$. This could be done, for example, by making a step change in the respective sizes of all the nanoparticles in the barrier region, as shown in figure 5.2(b). The gap ($\Delta = \hbar[\omega_A - \omega_B]$) can either stay the same, or differ in different regions.

5.2 Method

The systems considered in this section have a graphene-like honeycomb structure but with broken inversion symmetry, as described in section 4.7. To obtain the gap in the spectrum the inversion symmetry of the system must be explicitly broken, therefore there must be a difference between the two sublattices, and then, close to the K points, the dispersion is well described by DQILGSs [144].

The quasiparticles in this bipartite lattice are described by two-component eigenvectors, $\psi_{\mathbf{k}} = (\psi_A, \psi_B)$, similar to spinor wavefunctions in quantum electrodynamics, where the components, ψ_A and ψ_B, define the relative contributions from the A and B sublattices, respectively. In this basis, to first order in k, the two-band Hamiltonian, $\hat{H}$, for these DQILGSs with a generic scalar potential included has the form:

$$\hat{H}^{(\tau)} = \begin{pmatrix} \frac{\Delta(x)}{2} + V(x) & vp^{\dagger} \\ vp & -\frac{\Delta(x)}{2} + V(x) \end{pmatrix} , \tag{5.1}$$

with $p = \hbar(\tau k_x + ik_y)$ being the complex representation of the quasiparticle momentum, v the quasiparticle's velocity and with the assumption that the gap and potential barrier height are local in each region, such that $\Delta(x)$ and $V(x)$, respectively, represent step functions, the general normalised two-component spinor eigenvector describing the system is given by:

$$\psi = \sqrt{\frac{\varepsilon + \frac{\Delta(x)}{2} - V(x)}{2[\varepsilon - V(x)]}} \begin{pmatrix} 1 \\ \frac{vp}{\varepsilon + \frac{\Delta(x)}{2} - V(x)} \end{pmatrix} , \tag{5.2}$$

where ε is the incident electron (or CP) energy. The general expression for the wavevector in the x-direction is given by:

$$k_x = \sqrt{\frac{[\varepsilon - V(x)]^2 - \frac{\Delta(x)^2}{4}}{v^2} - k_y^2} \ . \tag{5.3}$$

Taking these general expressions, the wavefunction, $\Psi(x, y)$, describing each region of the system can be found, and due to the invariance of the potential in the y-direction, it can be written as $\Psi(x, y) = \Psi(x)e^{ik_y y}$ so only $\Psi(x)$ need be considered. To do this I define different symbols for the wavevectors outside and inside the barrier, such that in regions 1 and 3 ($x < 0$ and $x > L$) I define $k_x = k$, and in region 2 ($0 \leq x \leq L$) $k_x = q$. For generality, I allow the gap size to be different inside and outside the barrier, such that in regions 1 and 3 I define $\Delta(x) = \Delta_1$, and in region 2, $\Delta(x) = \Delta_2$. Finally, as the y-component of the wavevector is conserved, it is given by

$$k_y = k_F \ \sin(\phi) = \sqrt{\frac{\varepsilon^2 - \frac{\Delta_1^2}{4}}{v^2}} \ \sin(\phi) \, , \tag{5.4}$$

where ϕ is the incident angle of the electron (or CP) on the barrier from region 1 (where $x < 0$), and k_F is the Fermi wavevector in regions 1 and 3, shown in figure 5.3.

Thus, the wavefunctions in the three regions read

$$\Psi_1(x) = \xi_1 \left\{ \begin{pmatrix} 1 \\ \frac{vp_1}{\varepsilon + \frac{\Delta_1}{2}} \end{pmatrix} e^{ikx} + r \begin{pmatrix} 1 \\ \frac{-vp_1^*}{\epsilon + \frac{\Delta_1}{2}} \end{pmatrix} e^{-ikx} \right\} \ , \tag{5.5}$$

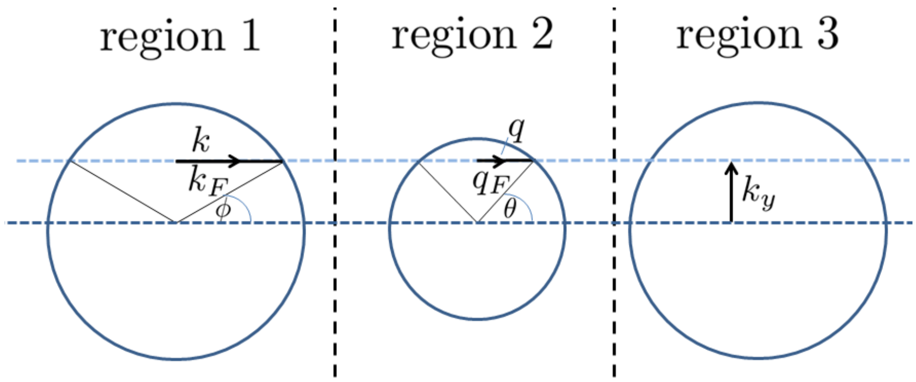

Figure 5.3: Sketch of the top down view across all three regions shown in figure 5.1, with a circle representing the equipotential line at the Fermi surface in each region. The conservation of the k_y across each of the regions is evident. In regions 1 and 3 the x-component of the wavevector is $k_x = k$, such that $k_F = \sqrt{k^2 + k_y^2}$, and in region 2, $k_x = q$, such that $q_F = \sqrt{q^2 + k_y^2}$.

$$\Psi_2(x) = \xi_2 \left\{ A \begin{pmatrix} 1 \\ \frac{vp_2}{\epsilon - V_0 + \frac{\Delta_2}{2}} \end{pmatrix} e^{iqx} + B \begin{pmatrix} 1 \\ \frac{-vp_2^*}{\epsilon - V_0 + \frac{\Delta_2}{2}} \end{pmatrix} e^{-iqx} \right\} \quad , \tag{5.6}$$

$$\Psi_3(x) = \xi_1 \left\{ t \begin{pmatrix} 1 \\ \frac{vp_1}{\epsilon + \frac{\Delta_1}{2}} \end{pmatrix} e^{ik(x-L)} \right\} \quad , \tag{5.7}$$

where I assume the coefficient of the incoming wavevector (in the x-direction) from region 1 is unity, r is the coefficient of reflection at the $x = 0$ boundary from region 1, A and B are the amplitudes of transmission and reflection in region 2 respectively, and t is the amplitude of transmission in region 3 through the boundary at $x = L$. The momenta in each region read $p_1 = \hbar(\tau k + ik_y)$, $p_2 = \hbar(\tau q + ik_y)$, and

$$\xi_1 = \sqrt{\frac{\varepsilon + \frac{\Delta_1}{2}}{2\varepsilon}} \quad , \qquad \xi_2 = \sqrt{\frac{\varepsilon + \frac{\Delta_2}{2} - V_0}{2[\varepsilon - V_0]}} \quad , \tag{5.8}$$

with

$$k = \sqrt{\frac{\varepsilon^2 - \frac{\Delta_1^2}{4}}{v^2} - k_y^2} \quad , \qquad q = \sqrt{\frac{[\varepsilon - V_0]^2 - \frac{\Delta_2^2}{4}}{v^2} - k_y^2} \quad . \tag{5.9}$$

At $x = 0$, $\Psi_1 = \Psi_2$, and at $x = L$, $\Psi_2 = \Psi_3$, which lead to four simultaneous equations, reading

$$\frac{\alpha}{\gamma\beta}\{1 + r\} \quad = \quad A + B \quad ,$$

$$\begin{aligned}
\frac{\beta}{\gamma\alpha}\left\{\mathbf{p}_1 - r p_1^*\right\} &= A p_2 - B p_2^* \ , \\
\frac{\gamma\beta}{\alpha}\left\{A e^{iqL} + B e^{-iqL}\right\} &= t \ , \\
\frac{\gamma\alpha}{\beta}\left\{A\mathbf{p}_2 e^{iqL} - B p_2^* e^{-iqL}\right\} &= t p_1 \ ,
\end{aligned} \tag{5.10}$$

where

$$\begin{aligned}
\alpha &= \sqrt{\varepsilon + \frac{\Delta_1}{2}} \ , \\
\beta &= \sqrt{\varepsilon + \frac{\Delta_2}{2} - V_0} \ , \\
\gamma &= \sqrt{\frac{\varepsilon}{\varepsilon - V_0}} \ .
\end{aligned} \tag{5.11}$$

Solving these simultaneous equations gives an expression for the transmission amplitude,

$$t = -\frac{2e^{-ikL} k q \alpha^2 \beta^2}{2kq\alpha^2\beta^2 \cos(Lq) - \mathrm{i}\sin(Lq)\nu} \ , \tag{5.12}$$

where

$$\nu = q^2\alpha^4 + k^2\beta^4 + k_y^2(\alpha^2 - \beta^2) \ . \tag{5.13}$$

5.3 Results and Discussion

In this section I will use the expression I have calculated for the transmission amplitude, given in equation 5.12, to investigate the tunnelling probability ($T = |t|^2$) for different incident energies, gap sizes and barrier heights.

In order for transmission to be possible there must be injected quasiparticles, therefore I take $\varepsilon \geq \frac{\Delta_1}{2}$ corresponding to an $n-$type region 1 and 3. Assuming $V_0 \geq \frac{\Delta_1}{2} + \frac{\Delta_2}{2}$ the Fermi energy can be taken at such a level that the system becomes an *npn* junction, and the local potential barrier inverts charge carriers underneath it; electron-like injected particles transform to hole-like states that play the role of positrons in QED [87].

To explore this further I first consider $\Delta_1 = \Delta_2 = \Delta$, thus $\varepsilon \geq \frac{\Delta}{2}$ and $V_0 \geq \Delta$ to allow for the possibility of an *npn* junction where states are available. Cases satisfying these two conditions are shown in figure 5.4, but for differing energies. In figure 5.4(a) the energy of the incident particles is much greater than the gap size ($\varepsilon \gg \Delta$), and there is perfect transmission at normal incidence, similar to the results seen in graphene, whereas in figure 5.4(b) the energy is taken to be just

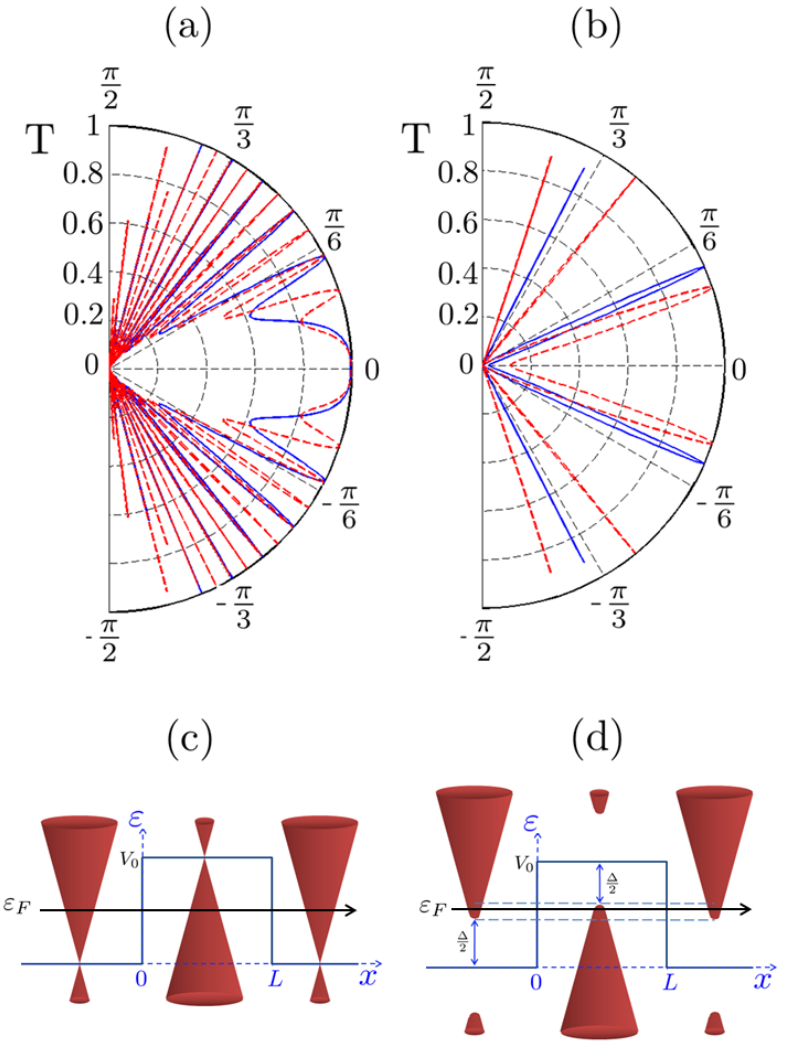

Figure 5.4: Klein tunnelling in a system of DQILGSs: The transmission probability through a barrier of length $L = 10L_0 \approx 200$nm (where $L_0 = \frac{v\pi\hbar}{\bar{V}_0}$, with $\bar{V}_0 \sim 0.1$eV) as a function of incident angle for different barrier heights and incident electrons energies is shown in panels (a) and (b), with a sketch of the corresponding band structure shown in figures (c) and (d) respectively. I consider two regimes; $V_0 \gg \Delta$ shown in panels (a) and (c), and $V_0 \approx \Delta = \Delta + \delta V$ shown in panels (b) and (d). In panel (a) I show the transmission for $V_0 = 10\Delta$ at $\varepsilon = 5\Delta$ (blue line) and $V_0 = 20\Delta$ at $\varepsilon = 10\Delta$ (red dashed line). In panel (b) I consider $V_0 = 1.1\Delta$ at $\varepsilon = 0.55\Delta$ (blue line) and $V_0 = 1.2\Delta$ at $\varepsilon = 0.6\Delta$ (red dashed line). In the first panel the gap has little effect on the transmission, and I recover $T \rightarrow 1$ at $\phi = 0$, however, for the latter case the energy is taken closer to the gap where it has more of an effect and the spinor overlap inside and outside the central region is suppressed, leading to a suppression of forward scattering.

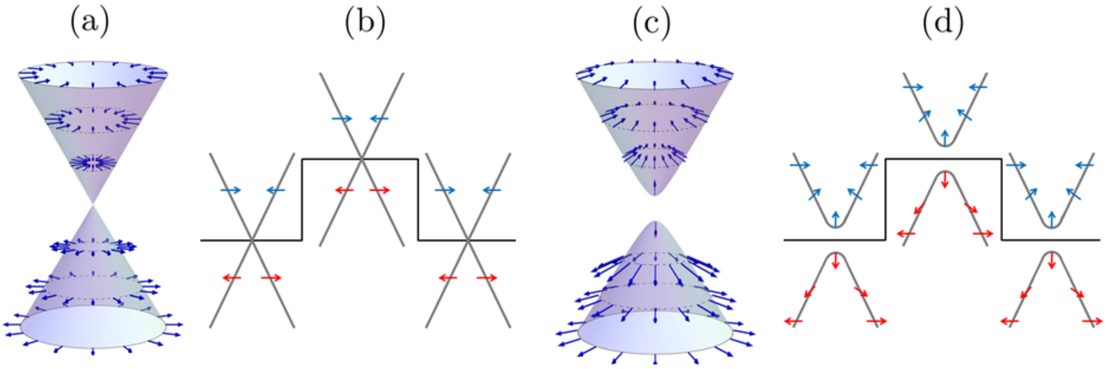

Figure 5.5: Panel (a) shows the conical graphene-like dispersion around $\varepsilon \sim \varepsilon_F$, with no asymmetry, and energy independent pseudospin. Panel (c) shows a sketch of the dispersion for a system described by the Hamiltonian given in equation 4.12, with $\Delta \neq 0$ close to the band gap, on which the directions of the Blöch vector at different energies can be seen. With the addition of a gap, the asymmetry leads to an energy dependent pseudospin. Panels (b) and (d) show the Klein Tunnelling scheme considered here, for the case of zero asymmetry and non-zero asymmetry respectively. The directions of the Bloch vector in each of the bands, inside and outside the barrier, are shown for $k_y = 0$.

above the band minima of the upper band ($\varepsilon = \frac{\Delta}{2} + \delta\varepsilon$, where $\delta\varepsilon \ll \Delta$), and I seen near perfect reflection at normal incidence, the complete opposite. Therefore, from figure 5.4 it is evident that the transmission through the system is energy dependent and, as the transmission probability depends on the overlap of the spinor wavefunctions inside and outside the barrier, it is interesting to compare this to the effect that the asymmetry between the sublattices has on the eigenspinor orientation, shown in section 4.5.

To do this, I can take the generalised normalised vector in the Bloch sphere from equation 4.15, and include a generic potential:

$$\mathbf{V}^{\pm}_{\mathbf{k}1} = \frac{1}{V(x) \pm \sqrt{v^2\hbar^2|\mathbf{k}|^2 + \left(\frac{\Delta}{2}\right)^2}} \left(-v\hbar k_x, -v\hbar k_y, \frac{\Delta}{2}\right), \tag{5.14}$$

which provides an analytical expression for the orientation of the eigenspinor in the presence of a gap, and is graphically shown in figure 5.5, where panel (a) shows the case of no asymmetry and panel (c) shows finite asymmetry. I can also write the Berry phase of the system, shown in equation 4.14, in the presence of a generic (but locally static) potential, as

$$\Phi_{\mathrm{B}}(\varepsilon, V, \Delta) = \pi \left(\frac{|\varepsilon - V(x)| - \frac{\Delta(x)}{2}}{|\varepsilon - V(x)|} \right) \quad , \tag{5.15}$$

in the K valley when $|\varepsilon - V(x)| > \frac{\Delta(x)}{2}$, with both the potential and gap size being constant in each region.

Where the Zeeman terms in the effective Hamiltonian (shown in equation 4.12) are of greater importance (i.e. at the band extrema) the Bloch vector has a greater out-of-plane component. Thus, at $\varepsilon = \pm\frac{\Delta}{2}$, $\Phi_B \to 0$ (as $V^{\pm}_{\mathbf{k}=0} = \pm\hat{z}$), whereas when $\frac{|\varepsilon|}{\Delta} \gg 1$, $\Phi_B \to \pm\pi$ (and $V^{\pm}_{\mathbf{k}}$ rotates in the $x-y$ plane), similar to graphene. Therefore in full generality allowing the gap inside and outside the barrier to be different, the overlap of the spinors, ψ, (from equation 5.2) in regions 1 and 2 at normal incidence, as a function of the Berry phase, reads

$$\begin{aligned} |\langle\psi_1|\psi_2\rangle|^2 &= \frac{1}{4\,|\varepsilon(\varepsilon - V_0)|}\Bigg[\sqrt{\left(\varepsilon + \frac{\Delta_1}{2}\right)\left(\varepsilon + \frac{\Delta_2}{2} - V_0\right)} \\ &\qquad + \sqrt{\left(\varepsilon - \frac{\Delta_1}{2}\right)\left(\varepsilon - \frac{\Delta_2}{2} - V_0\right)}\ \Bigg]^2 \\ &= \frac{1}{4\pi^2}\Big[\ \sqrt{\Phi_B(\varepsilon, -\Delta_1)\Phi_B(\varepsilon, V_0, -\Delta_2)} \\ &\qquad + \sqrt{\Phi_B(\varepsilon, \Delta_1)\Phi_B(\varepsilon, V_0, \Delta_2)}\ \Big]^2 . \end{aligned} \tag{5.16}$$

For zero asymmetry the overlap of these spinors has induced selection rules leading to the counter-intuitive ramification that is perfect tunnelling at normal incidence. It can be seen in figures 5.5(a) and 5.5(b), and calculated from equation 5.16 that, at normal incidence, there can be a perfect overlap of pseudo-spin states inside and outside the barrier, $|\langle\psi_1|\psi_2\rangle|^2 = 1$, leading to 100% transmission. In figures 5.5(c) and 5.5(d), the case when $\Delta \neq 0$ is presented, where due to the asymmetry these selection rules no longer apply. The energy dependent pseudospin orientations allow for the possibility that the spinors inside and outside of the barrier no longer overlap perfectly, and therefore enables some backscattering. There is also the prospect of antiparallel spinors, giving rise to perfect reflection. In fact when $\Delta_1 = \Delta_2 = \Delta$, $V_0 = \Delta$ and $\varepsilon = \frac{\Delta}{2}$, equation 5.16 gives $|\langle\psi_1|\psi_2\rangle|^2 = 0$.

I can now use this expression for the spinor overlap to explain the energy dependent transport shown in figure 5.4. Figure 5.4(a) shows when $V_0 \gg \Delta$ and $\varepsilon = V_0/2$, at normal incidence ($\phi = 0$) the barrier becomes transparent ($T = |t|^2 = 1$, where t is shown in equation 5.12). This perfect tunnelling is possible due to the σ_z terms in the Hamiltonian becoming relatively small and the approximate matching of the directions of pseudospin for quasiparticles inside and outside the barrier [87]. The latter is the same as Klein tunnelling in graphene, and is a feature unique to

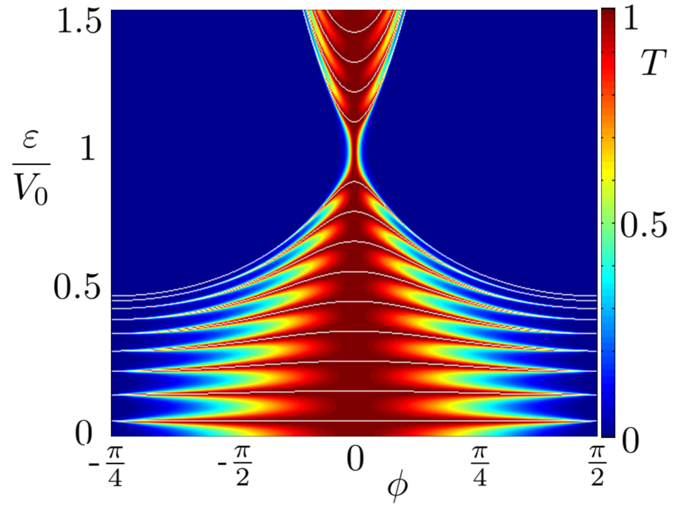

Figure 5.6: Transmission probability of DQILGSs for zero asymmetry through a $L = 10L_0 \approx$ 200nm long barrier as a function of incident angle and electron or CP energy, where the resonance lines, calculated from equation 5.17, are shown in white.

---

massless Dirac fermions [87], so the DQILGSs act like massless Dirac fermions.

When $V_0 \approx \Delta + \delta V$ (where $\delta V \ll \Delta$) and $\varepsilon \sim V_0/2$, as shown in figure 5.4(b), the barrier is opaque ($T = 0$), which is the opposite to monolayer graphene. The blue (solid) line shows this 100% reflection, with $T = 0$ at $\phi = 0$. However the red (dashed) line does not show this completely 100% reflection, even though the transmission is far from what has be seen for the case when $\Delta = 0$. This can be explored by presenting the transmission over all energies as a function of angle. The case of zero asymmetry is shown in figure 5.6, where no matter the energy in the *npn* region ($\varepsilon < V_0$) there is always perfect transmission at normal incidence as expected, due to the conservation of spinors in each region [87]. There are also strong resonance peaks visible, which are due to the resonant tunnelling through Fabry-Perot type states. The locations of these resonance modes ε_{res} can be estimated by quantising k_x as $k_x L/\pi = n$, where n is an integer, yielding the curves,

$$\varepsilon_{\text{res}}^{(n)}(k_y) = V_0 \pm \sqrt{v^2\hbar^2\left[\left(\frac{n\pi}{L}\right)^2 + k_y^2\right]}\ , \tag{5.17}$$

indicated in figure 5.6 by the white lines. There is qualitative agreement between the positions of the resonances, in both the *npn* and *nnn* regions.

In figure 5.7, the transmission probability with different amounts of asymmetry is further explored and can again be seen to have strong resonance peaks. Figure 5.7(a) is the case of no

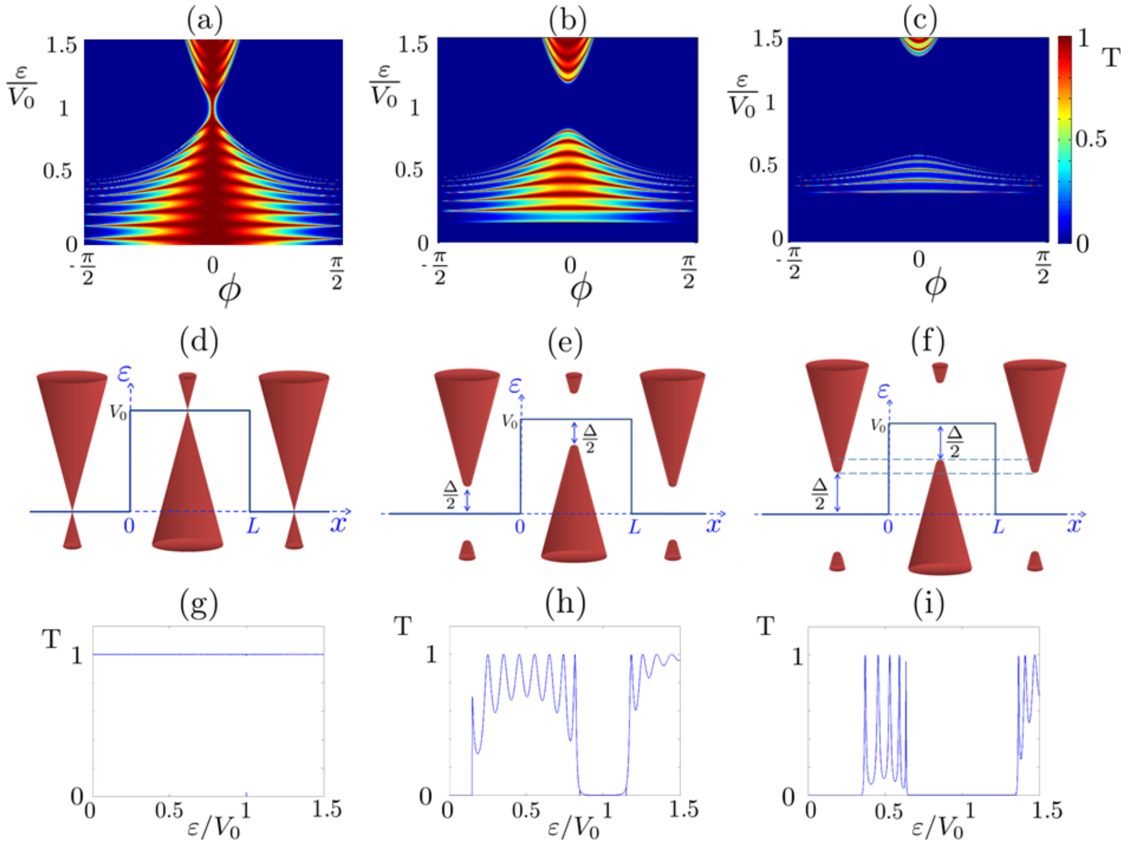

Figure 5.7: Klein tunnelling in a system of DQILGSs for different amounts of asymmetry: Panels (a)-(c) show the transmission probability through a $10L_0 \approx$ 200nm long barrier as a function of incident angle and electron or CP energy, panels (d)-(f) show the corresponding schematics of the band structure and relative barrier heights and gap sizes, and panels (g)-(i) show the transmission probability at normal incidence for the corresponding amounts of asymmetry. In panels (a), (d) and (g) there is no asymmetry ($\Delta = 0$), in panels (b), (e) and (h) $\Delta = 0.3V_0$ and in panels (c), (f) and (i) $\Delta = 0.7V_0$.

---

asymmetry reproduced from 5.6, where there is always perfect transmission at normal incidence. With increased asymmetry [from panels (a) to (c)] the transmission at normal incidence [shown in figures 5.7(d)-(f)] is no longer pinned to $T = 1$. At energies that correspond to these resonances there can still be high transmission but between them the transmission probability can tend to zero. This explains why the transmission lines in figure 5.4(b) do not both present $T = 0$ at $\phi = 0$.

In figure 5.8 the dependence of the transmission probability on pseudospin overlap is displayed. Here I show the transmission through the barrier as a function of energy at normal incidence (blue solid line) and also the spinor overlap at normal incidence (red dashed line) calculated from equation 5.16. The spinor overlap provides an envelope function describing the shape of

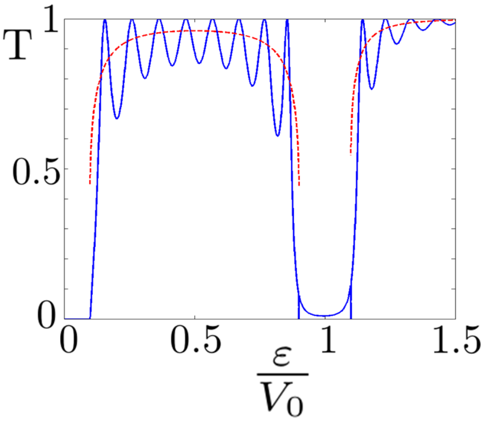

Figure 5.8: The transmission probability at normal incidence for different incident energies (blue solid line) and the modulus square of the pseudospin overlap (red dashed line) calculated from equation 5.16, which acts like an envelope function, when $\Delta = 0.2V_0$ and $L = 10L_0 \approx 200$nm. This helps to explain the general shape of the transmission, aside from the peaks and troughs due to resonant Fabry-Perot type tunnelling.

---

the transmission probability apart from the peaks and troughs due to resonant tunnelling through Fabry-Perot type states. The spinor overlap is a good approximation of the average of the resonant tunnelling probabilities, but this overlap description breaks down inside the gap, as there are no states.

In figure 5.9 I show the transmission probability in the vicinity of $\varepsilon \approx V_0$ to examine the asymmetry effects at this point. With zero asymmetry, shown in figure 5.9(a), the transmission peak is localised in angle but not in energy. It can also be seen that even when there is a gap inside the barrier, shown in figures 5.9(b) and 5.9(c), for very small gaps and as long as there are incident electrons (or CPs) there can be transmission through the barrier via evanescent waves. This non-zero transmission is seen most clearly in figure 5.9(d).

I can exploit the transmission probability above to calculate the ballistic conductance, G, through the barrier, given by the Landauer formula [203–205]:

$$G = \frac{We^2}{\pi h} g \int_{-k_F}^{k_F} T(k_y) \mathrm{d}k_y \tag{5.18}$$

where W is the width of the barrier, and $g = g_v g_s = 4$ is the total degeneracy of the system made up of the valley degeneracy, $g_v = 2$, and the spin degeneracy, $g_s = 2$.

Having numerically evaluated G as a summation over k_y, in figure 5.10 I plot the sample

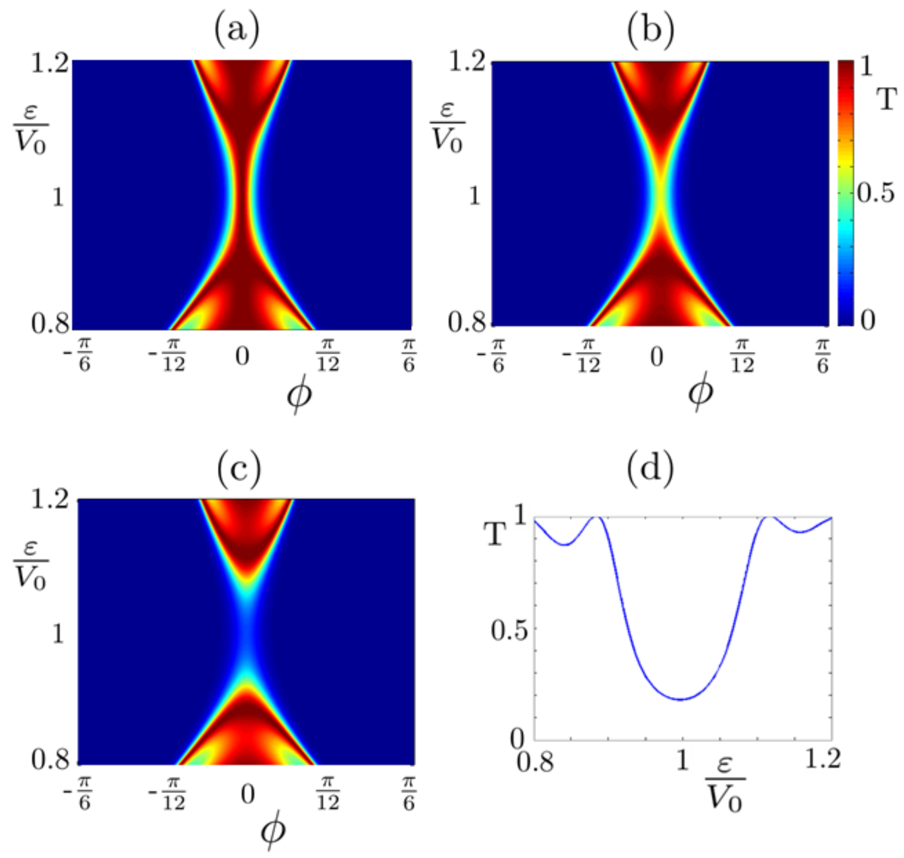

Figure 5.9: A close up on the transmission probability of DQILGSs around $\varepsilon \approx V_0$ for different amounts of asymmetry when $L = 10L_0 \approx 200$nm: Panel (a) shows the transmission probability for $\Delta = 0$, in panel (b) $\Delta = 0.05V_0$ and in panel (c) $\Delta = 0.1V_0$. Panel (d) shows the transmission probability at normal incidence when $\Delta = 0.1V_0$.

---

independent conductivity, $\sigma_c = G\frac{L}{W}$, as a function of dimensionless barrier height and incident electron energy, $\frac{V_0}{\Delta}$ and $\frac{\varepsilon}{\Delta}$ respectively. As the gap is relatively large compared to both the incident energy and the barrier height, there are two distinct regions of zero conductivity, the diagonal line across the figure (between $\varepsilon = V_0 - \frac{\Delta}{2}$ and $\varepsilon = V_0 + \frac{\Delta}{2}$) and the horizontal line between $0 \leq \varepsilon \leq \frac{\Delta}{2}$, which correspond to energies inside the gap in region 2 and region 1, respectively.

Inside the barrier, in the region labelled B, which corresponds to an *npn* junction, the conductivity increases with increased V_0, as the larger the barrier height is with respect to the gap, the less of an effect the gap has. It is interesting to note that the most prominent increase in conductivity arises when $\varepsilon \approx \frac{V_0}{2}$, which agrees with our previous conclusion that the transmission becomes more graphene-like when the dispersion can be considered approximately linear, i.e. at energies

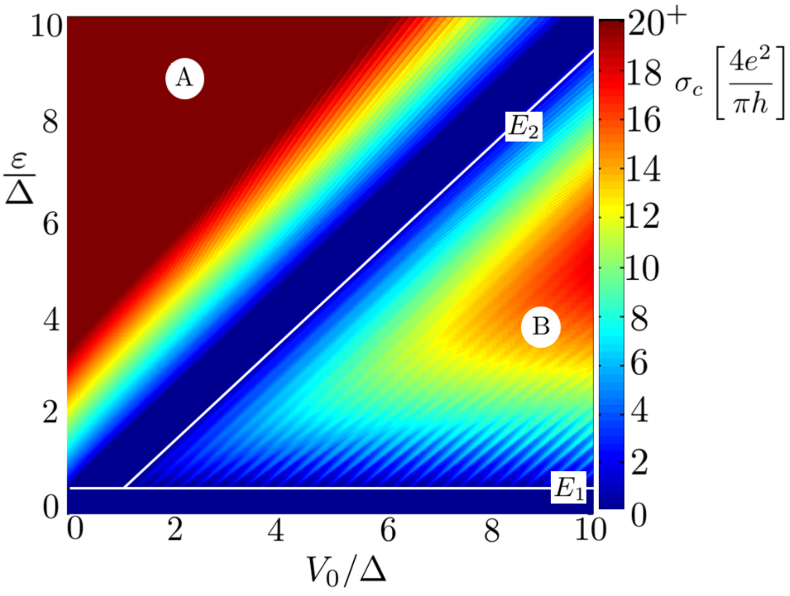

Figure 5.10: Conductivity as a function of barrier height, V_0, and incident quasiparticle energy, ε, which are both normalised to the gap size, when $L = 32L_0 \approx 660$nm. The colour bar has been adjusted to show more detail for lower values of conductance (which are of interest in the $\varepsilon < V_0$ region), and everything above $\sigma = 20G_0 = \frac{160e^2}{h}$ is indicated as red. The regions associated with non-vanishing conductivity are labelled A and B. They identify the *nnn* and *npn* regions respectively, and the lines labelled E_1 and E_2 correspond to $\varepsilon = \frac{\Delta}{2}$ and $\varepsilon = V_0 - \frac{\Delta}{2}$, respectively, which correspond to the lines (i) and (ii) in figure 5.1 respectively.

---

greater than $\Delta/2$, but also less than $V_0 - \Delta/2$, making the best approximation for linear dispersions both outside and inside the barrier occur at $\varepsilon \sim \frac{V_0}{2}$.

In region A, $\varepsilon > V_0$, so the system corresponds to an *nnn* junction. At $\varepsilon > \frac{\Delta}{2}$ the conductivity increases with energy as the density of states (DOS) increases higher in the dispersion. However, in region B $V_0 > \varepsilon$, such that electron-like states convert into hole-like states at the barrier and back again after it. Therefore there must be an overlap in the electron-like and hole-like wavefunctions to facilitate transmission. As a result the conductivity is suppressed in region B with respect to region A, due to the mostly destructive interference of the spinor wave functions (for inside and outside of the barrier). This is most pronounced at the tips of the dispersions, as the spinors inside and outside of the barrier are approximately antiparallel.

There are more prominent fluctuations in the conductivity parallel to the line labelled E_1 (which corresponds to $\varepsilon = \frac{\Delta}{2}$) than parallel to the line labelled E_2 ($\varepsilon = V_0 - \frac{\Delta}{2}$). This can be understood by examining the situation at each line, shown in figure 5.1. In figure 5.1, the line

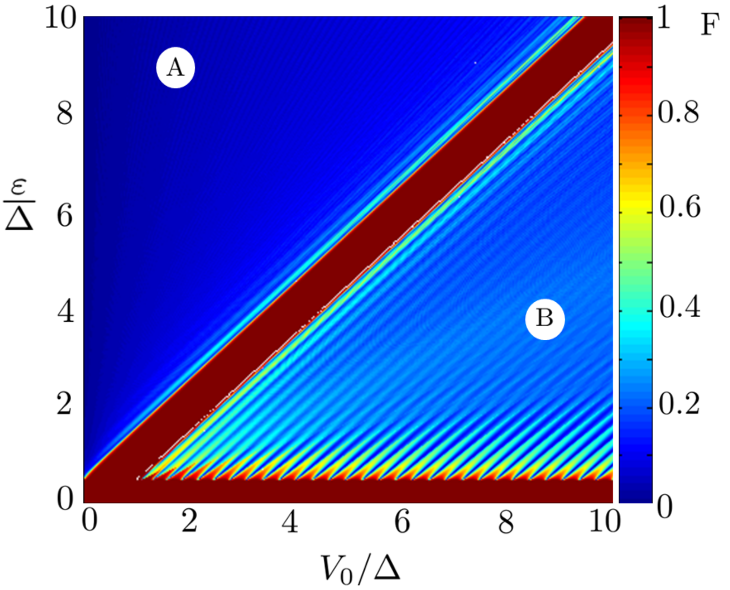

Figure 5.11: The Fano factor, F, as a function of the barrier height, V_0, and incident quasiparticle energy, ε, both normalised to the gap Δ. Non-unity regions are labelled A and B for ease of identification. In the figure $L = 32L_0 \approx 660$nm.

---

labelled (i) shows the case considered along E_1, where there are increased fluctuations. In this case there are only a small amount of injected quasiparticles: the incident quasiparticles are taken from the tip of the conduction band outside of the barrier. However, there are a large number of states available inside the barrier. Inside the barrier there can be quasi-resonant tunnelling due to Fabry-Perot type states [206] leading to the observed increases and decreases in conductivity. Along the line labelled (ii) (figure 5.1), corresponding to E_2 (figure 5.10), it can be determined that there are very few states inside the barrier for the incident electrons to tunnel into, so there are less fluctuations in conductivity.

This system can be further explored by considering the Fano factor, F, which is the ratio between noise power and average current [207] and is determined by the relation [205]:

$$F = \frac{\int_{-k_F}^{k_F} T(k_y)\left[1 - T(k_y)\right] \mathrm{d}k_y}{\int_{-k_F}^{k_F} T(k_y) \mathrm{d}k_y} \quad . \tag{5.19}$$

For tunnelling through insulating barriers, or where there is a gap, the Fano factor is expected to be unity, and tends to zero for ballistic transport [204].

By numerically evaluating F the colour plot in figure 5.11 was produced. The red diagonal and horizontal lines are present due to F = 1 in the gap, as expected. In agreement with the conductivity, there is a strong asymmetry between the two regions, A and B. In region A, F→ 0 indicating ballistic transport above the barrier. In region B, similar to G, oscillations are also encountered in F which are again associated with the quasi-resonant Fabry-Perot type states inside the barrier. However these states have the opposite effect (decreasing F when there is an increase in G). The widths of these oscillations depend on the length of the barrier [206], and the doping in the system [208], which can also be controlled. The value of F in region B is on average higher than in A, however, it reduces further from the gapped regions. Away from the gap, the average of F over several oscillations can be seen to tend to $1/3$, which is the value of F at the neutrality point in graphene [209]. This shows that there is pseudo-diffusive transport via evanescent waves in the regions where transport is performed by quasiparticles travelling through the barrier.

So far I have assumed that the gap is uniform across the sample, as would be the case for the existing gap in transition metal dichalcogenides and graphene on hexagonal boron nitride. However, in artificial graphene systems it is possible to vary the gap size throughout the system. Furthermore, in some of the graphene-like systems that can be described by the Hamiltonian shown in equation 4.12 it is possible that outside the barrier there would be no gap but the doping or top gate that causes the barrier could also induce a gap inside the barrier, thus $\Delta_1 = 0$ and $\Delta_2 \neq 0$. In this case, the eigenspinor outside the barrier, where there is no gap, will again be purely in the plane and orientated antiparallel to the wavevector, but the eigenspinor inside the barrier is not restricted to this. Thus, the maximum difference between pseudospin orientation angles inside and outside the barrier will be $\pi/2$, as opposed to π in the case of a constant gap. From equation 5.16, I can calculate the spinor overlap, which will range between $\frac{1}{2}$ and 1 (as opposed to 0 and 1 that was seen for the case of a constant gap). Seeing this difference in maximum and minimum spinor overlap between these cases leads to the expectation that the transmission for this case may well not go to zero.

The transmission for the case where $\Delta_1 = 0$ and $\Delta_2 \neq 0$ is shown in figure 5.12. Figure 5.12 shows the transmission near to $\varepsilon \sim 0$ differs from that which was previously seen, as $T \rightarrow 1$ at $\phi = 0$. However at higher energies, close to $\varepsilon \sim V_0$ (which are the most experimentally relevant energies), the transmission is closer to the case with a uniform gap shown in figure 5.7. Nonetheless, although the transmission is no longer pinned to unity, it does not reach zero at any point, as it does when $\Delta_1 = \Delta_2 \neq 0$.

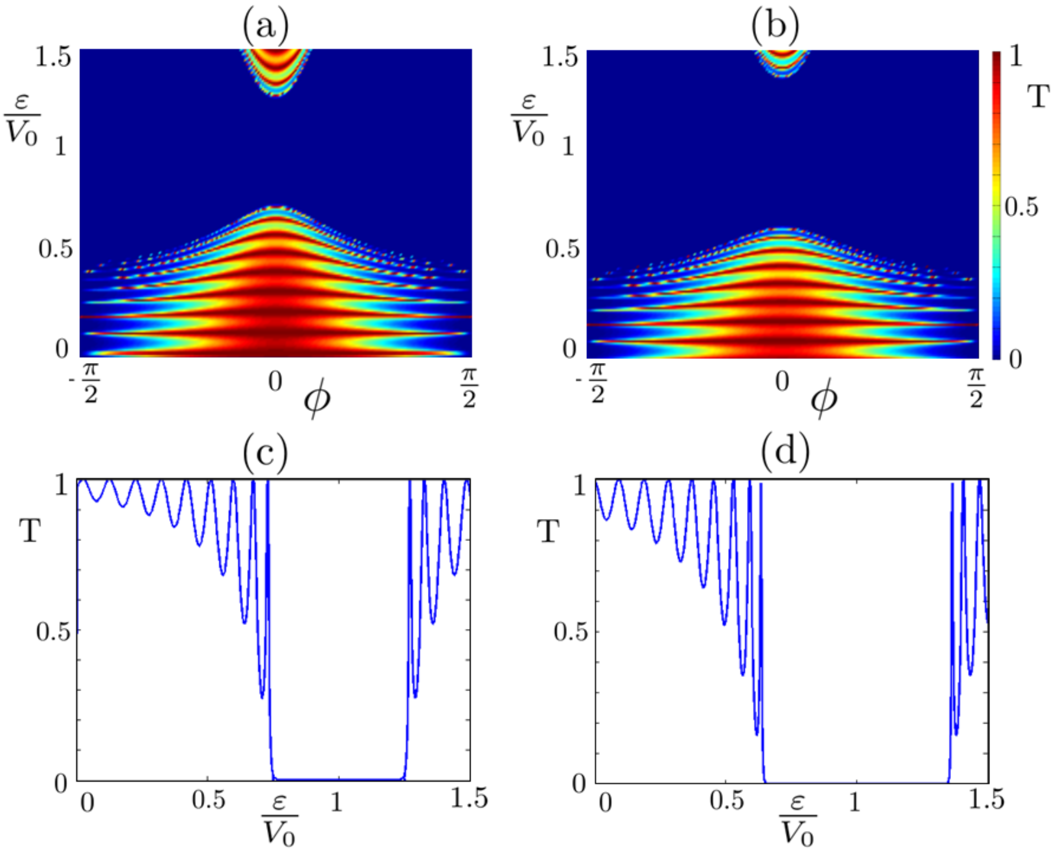

Figure 5.12: Transmission probability with $\Delta_1 = 0$ and $\Delta_2 \neq 0$. Panel (a) shows the case where $\Delta \sim 0.5V_0$ and panel (b) shows the case where $\Delta \sim 0.7V_0$. Panels (c) and (d) show the transmission at normal incidence for the cases shown in panels (a) and (b) respectively. In the figure $L = 10L_0 \approx$ 200nm.

Thus, I have shown that transmission can be suppressed in graphene-like systems by opening a gap in their linear band structures, as the broken inversion symmetry leads an energy depend Berry phase. This opens up the possibility of using these materials in transistors and therefore should expand on their possible device applications.

5.3.1 Experimental Feasibility

In this chapter the concept of Klein Tunnelling with Dirac quasiparticles in ballistic systems with linear gapped spectra (DQILGSs) has been demonstrated, and I have suggested some experimental platforms to verify this. Transition metal dichalcogenides have been considered, however, due to the large disorder present in these materials, high mobilities are difficult to achieve, and as such this transmission may only be evident for very short barriers, which maybe experimentally inaccessible. Nonetheless, a mobility of $200\text{cm}^2\text{V}^{-1}\text{s}^{-1}$ has been realised in room temperature transistors [210, 211], thus using the approximate effective mass at the Dirac point of MoS_2 ($m \approx 0.5m_e$) [211] and the Drude conductivity formula giving mobility as $\mu = \frac{e\tau}{m} = \frac{el_s}{v_F m}$, where l_s is the scattering length, I estimate that a Klein tunnelling device would need a barrier width of less than 30nm to render these results, which may be feasible. Another experimental difficulty with using MoS_2 is the size of its band gap ($\Delta = 1.66\text{eV}$ [144]), as producing high enough barriers to be comparable to this gap may also be impractical, whereas experiments conducted on some of the other systems (plasmonic metamaterials for example) have the advantage of a tunable band gap.

5.4 Chapter Summary

In this chapter I have investigated the tunnelling probabilities of Dirac quasiparticles contained in ballistic systems with a linear gapped spectrum. For a uniform gap throughout, taking the limiting case of high barriers, $V_0 \gg \Delta$, and $\varepsilon \gg \Delta$ where $\Phi_B \to \pi$, the dispersion can be approximated as linear and the transmission resembles that of monolayer graphene, implying that the quasiparticles behave like chiral massless Dirac particles. Whereas with barriers only slightly larger than the gap ($V_0 \sim \Delta + \delta V$) at $\varepsilon \sim \frac{V_0}{2}$, with $\Phi_B \sim 0$, the transmission as a function of angle no longer mirrors that of monolayer graphene as there can be perfect reflection at normal incidence.

With a finite gap, the selection rule requiring perfect transmission at normal incidence breaks down and the transmission probability is energy dependent, as is the Berry phase. This energy dependent transmission follows from the energy dependence of the pseudospin orientations, and thus of the overlap of the pseudospin states in the different regions. Therefore the broken inversion symmetry has allowed for the possibility of backscattering, and thus confinement, and the possibility of a large on/off ratio. This further broadens the usefulness of these graphene-like materials as it opens up the possibility of using these materials in transistors.

The conductivity and Fano factor as a function of barrier height reflect the energy dependent transmission. Moreover, for the *npn* case there are large oscillations in both the conductivity and the Fano factor which correspond to each other. These are due to quasi-resonant tunnelling through Fabry-Perot type states leading to periodic increases (decreases) in the conductivity (Fano factor).

Of the many possible experimental platforms to which this research is applicable, MoS_2 has gained a lot of attention. However, for this material a correction to these results will need to

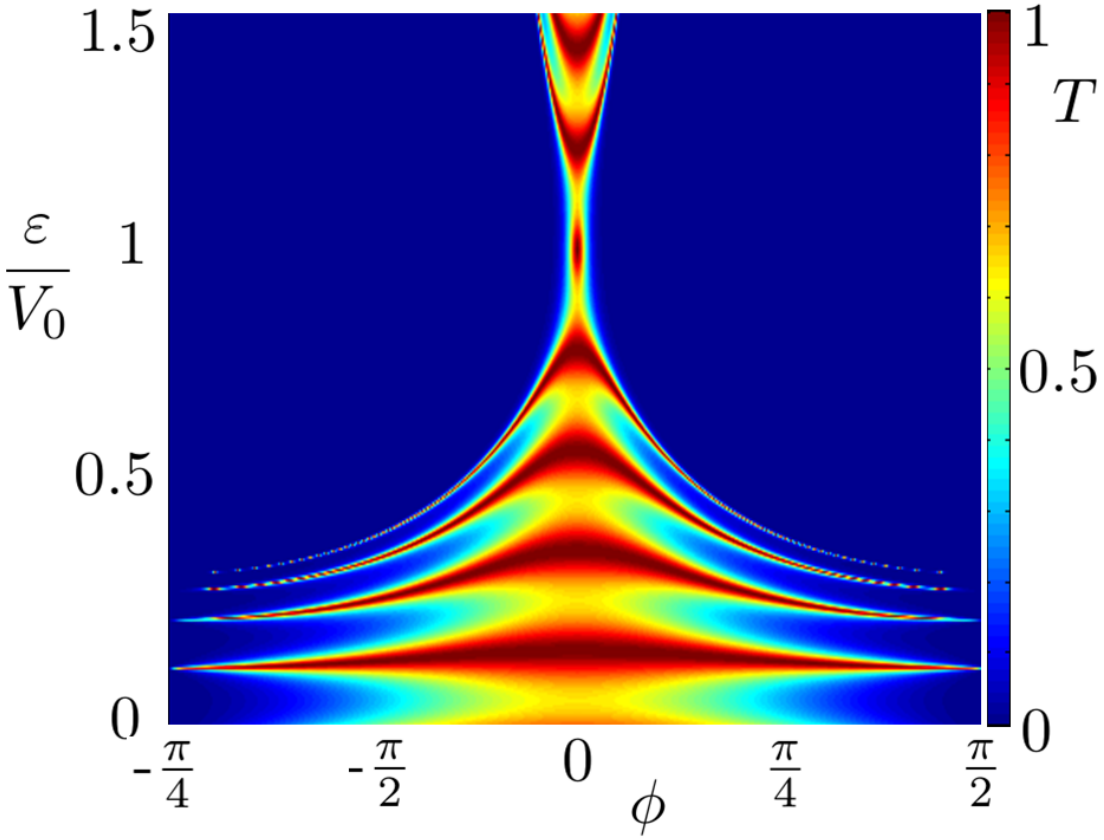

Figure 5.13: Transmission probability with $\Delta_1 = \Delta_2 = 0$ but $v_2 = 2v_1$, where v_i is the speed in the i-th region. In the figure $L = 10L_0 \approx 200$nm.

---

be taken, as it has strong spin orbit coupling which has not been considered in this thesis.

For systems with a tunable band gap it is possible that the gap size could be different inside and outside the barrier and in the case when $\Delta_1 = 0$ and $\Delta_2 \neq 0$, due to the impossibility of attaining orthogonal pseudo-spins inside and outside the barrier, it is no longer possible to retrieve perfect reflection at normal incidence. It is evident, however, that the transmission is not pinned to unity, as in the gapless case.

The energy dependence of the pseudo-spin orientation should also affect several other properties exhibited by carriers in both real and artificial graphene systems, leading to energy dependent weak antilocalisation and energy dependent anomalous quantum Hall effect, for example.

Finally, it is interesting to note that another possible consequence of manufacturing regions with different barrier heights, $V(x)$, (or different $\bar{\omega}$ values) in a metamaterial is that the group velocity could be different in the different regions (especially if the different regions house nanoparticles of different consisting materials). Figure 5.13 shows the transmission probability when there is no gap in the spectrum but different velocities inside and outside the barrier. Here it is evident that the asymmetry between the different regions has a similar effect to the asymmetry in the sublattices in that due to this difference there is no longer perfect transmission as is seen in graphene at normal incidence. The fluctuations in transmission probability at normal incidence are caused by the lack of uniformity across the sample. This shows the further tunability of the metamaterial, and opens up more possibilities for adaptation to a specific purpose.

6

Klein Tunnelling in Dirac Materials with a Parabolic Gapped Spectrum

The research presented in this chapter is work I conducted that will be exhibited in a forthcoming paper [198], in collaboration with Eros Mariani and Alex Cope.

There has been increased exploration of two-dimensional (2D) atomically thin materials since the discovery of graphene [3] and as such bilayer graphene has become a subject of intense interest in its own right. Similar to monolayer graphene, unbiased bilayer graphene has no band gap, and its low energy Hamiltonian also supports chiral Dirac quasiparticles that can be described by spinor wavefunctions [113, 114]. However, unlike monolayer graphene, in bilayer graphene these quasiparticles have a finite mass due to the curvature of its spectrum even in the absence of a gap. The nature of this effective mass is very different from that of the quasiparticles considered in chapter 5, where the massive behaviour is due to the band gap produced by broken inversion symmetry. In bilayer graphene it is possible to combine both causes of massive behaviour by creating an asymmetry between the layers which opens a gap in the parabolic spectrum. This asymmetry changes the properties of the system, which should be more evident when the gap is sizeable with respect to the kinetic energy of the Dirac quasiparticles [212]. This asymmetry can be created in many ways, for example, by doping or applying a potential difference between the layers [213, 214].

Even without a gap, the parabolic spectrum leads to other differences between bilayer graphene and its monolayer counterpart, for example electronic states in bilayer graphene have a BP of 2π [113] as opposed to the BP of π in graphene. They also have very different Klein tunnelling probabilities [87, 113, 114]: perfect transmission is seen at normal incidence in monolayer graphene in the *npn* regime, due to conservation of pseudospin [87] inside and outside the barrier (as seen in section 2.5.3); but the complete opposite is discovered in unbiased bilayer graphene (see section 2.6.3). Due to the parabolic spectrum, the pseudospin in bilayer graphene winds twice as quickly as in its monolayer counterpart, and the resulting mismatch in pseudospin orientations inside and outside the barrier explain the perfect reflection seen at normal incidence [87, 131, 132]. However, this perfect reflection is highly unusual as one would usually expect some tunnelling due to the continuum of electronic states on the other side of the barrier [89]. The extent to which these transport properties are affected if a bias is applied to bilayer graphene, opening a gap in its dispersion, is explored here.

In this chapter I expand on the research conducted in chapter 5, in which KT was investigated in Dirac materials with a linear gapped spectrum. Here, I extend this to produce a description for tunnelling in Dirac materials with a gapped spectrum with parabolic spectra, like biased bilayer graphene. I theoretically prove the concept of KT of Dirac particles in systems with a massive Dirac Hamiltonian as well as the additional σ_z terms, due to broken inversion symmetry. I prove that opening a gap in bilayer graphene's electronic dispersion can allow for perfect transmission at normal incidence, at certain energies. The ability to tune the opening of a gap can thus be used to tailor the transmission properties, making bilayer graphene an important candidate for the next generation of nano-electronic devices [200, 201].

Note, to avoid confusion the Dirac quasiparticles in systems with a *gapless* parabolic spectrum, like bilayer graphene, are referred to as DQIPS, and the Dirac quasiparticles in systems with a *gapped* parabolic spectrum, like in biased bilayer graphene, are referred to as DQIPGS.

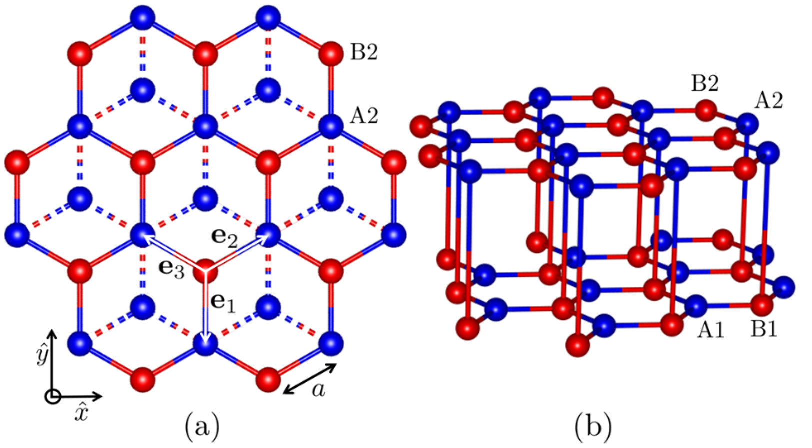

Figure 6.1: The structure of bilayer graphene, where a) is a top down view showing the honeycomb structure of the layer of graphene that makes up the top layer of bilayer graphene, and b) a side view showing the Bernal stacking of the two layers, where A2 site on the upper layer is directly above the B1 site on the lower layer. This is reproduced from figure 2.23 for ease of reading.

6.1 Biased Bilayer Graphene

The electronic dispersion of bilayer graphene has been modelled using density functional theory [215–217] and the tight binding model [114, 115, 120, 133, 218–223], both of which have predicted that an asymmetry between the layers leads to a tunable gap between the conduction and valence bands. The dependence of the gap size on external gate voltage has been modelled taking into account screening within the tight binding model [133, 217, 223], and such calculations appear to be in good agreement with observations made in the regime of the quantum Hall effect [133], ARPES measurements [224], and density functional calculations [217].

I consider a sheet of bilayer graphene consisting of two coupled 2D honeycomb lattices, with inequivalent sites ($A1$, $B1$ in the bottom sheet, and $A2$, $B2$ in the top sheet). These are arranged according to Bernal ($A2 - B1$) stacking as shown in figure 6.1, where every $B1$ site lies directly below an $A2$ site, but $A1$ and $B2$ sites do not lie directly above or below a site in the other layer [114]. The dimers, created by the $A2 - B1$ coupling, lead to high energy bands in the electronic spectrum.

To explore the transport properties of bilayer graphene it is convenient to use a low energy Hamiltonian that describes effective hopping between the non-dimer sites, $A1 - B2$, i.e. that are not strongly coupled by γ, the interlayer coupling. This two component effective Hamiltonian is applicable within the energy range $|\varepsilon| < \gamma$ [114] and has been derived by McCann and Falko [114] using Green's functions. The effective low energy Hamilton, $\hat{H}_0$, in the case where $v|\mathbf{p}| \ll \gamma$, and in the basis $\Psi_{\mathbf{k}} = (\psi_{A1}, \psi_{B2})$, is given by:

$$H^{(\tau)} = \begin{pmatrix} \frac{\Delta}{2} & \frac{(p^{\dagger})^2}{2m} \\ \frac{p^2}{2m} & -\frac{\Delta}{2} \end{pmatrix} \tag{6.1}$$

where $m = \gamma/2v^2$ is the effective mass of the quasiparticles in unbiased bilayer graphene [114], due to the curvature of the dispersion, and $v = at\sqrt{3}/2\hbar$ is the intralayer velocity [114], with t the intralayer nearest neighbour hopping strength [114]. The complex representation of the quasiparticle momentum is $p = \hbar(\tau k_x + ik_y)$, where k_x and k_y are the wavevectors in the x- and y-directions respectively, and $\tau = \pm 1$ indicates the K, K' valley. The gap, Δ, is a measure of the local asymmetry, and can have different values across the sample (in the leads for example).

By substituting this Hamiltonian into the Schrödinger equation, $H^{(\tau)}\psi_{\mathbf{k}}^{(\tau)} = \varepsilon\psi_{\mathbf{k}}^{(\tau)}$, I define the eigenvalues

$$\varepsilon = \pm\sqrt{\frac{|\mathbf{p}|^4}{4m^2} + \frac{\Delta^2}{4}}\,, \tag{6.2}$$

and the normalised eigenvectors

$$\psi_{\mathbf{k}}^{(\tau)} = \begin{pmatrix} \psi_{A1} \\ \psi_{B2} \end{pmatrix} = \sqrt{\frac{\varepsilon + \frac{\Delta}{2}}{2\varepsilon}} \begin{pmatrix} 1 \\ \frac{p^2}{2m\left(\varepsilon + \frac{\Delta}{2}\right)} \end{pmatrix}\,. \tag{6.3}$$

I can also analytically express the eigenstates as normalised vectors in the Bloch sphere. As the effective Hamiltonian for biased bilayer graphene continuously interpolates between a 2D massive Dirac Hamiltonian, $\frac{\hbar^2}{2m}\left\{\sigma_x\left(k_x^2 - k_y^2\right) + 2\sigma_y k_x k_y\right\}$ $\left(\text{when } \frac{\hbar^2|\mathbf{k}|^2}{2m} \gg \frac{\Delta}{2}\right)$, and an out of plane Zeeman term, $\frac{\Delta}{2}\sigma_z$ $\left(\text{when } \frac{\hbar^2|\mathbf{k}|^2}{2m} \ll \frac{\Delta}{2}\right)$, the normalised vector reads:

$$\mathbf{V}_{\mathbf{k}}^{\pm} = \pm\left[\frac{\hbar^4|\mathbf{k}|^4}{4m^2} + \frac{\Delta^2}{4}\right]^{-1/2}\left(\frac{\hbar^2(k_x^2 - k_y^2)}{2m}, \frac{2\hbar^2 k_x k_y}{2m}, \frac{\Delta}{2}\right). \tag{6.4}$$

This gives an analytical expression for the orientation of the pseudo-spins, which is graphically shown in figure 6.2 (panel (a) shows the case where $\Delta = 0$, and panel (c) shows a finite asymmetry), and which leads to the Berry phase given by

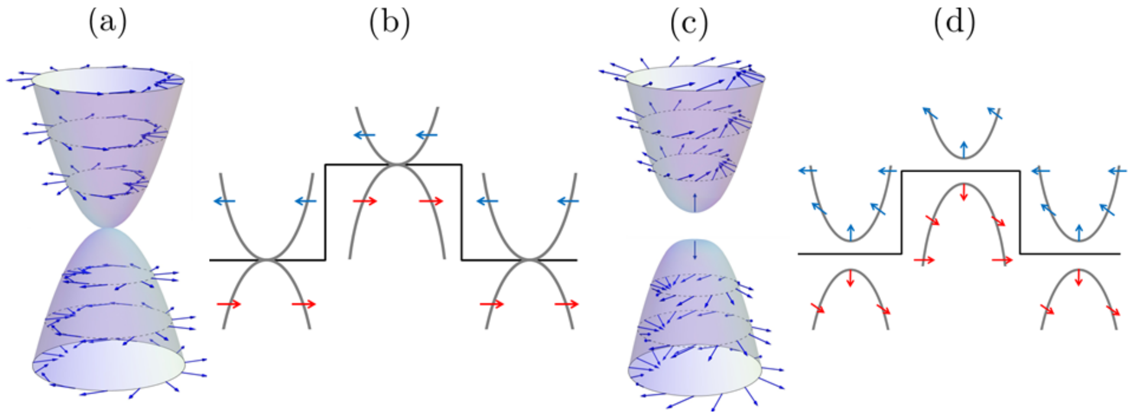

Figure 6.2: Panel (a) shows a the low energy parabolic dispersion of bilayer graphene, with no asymmetry, where the energy independent eigenspinor directions can be seen. Panel (c) shows the the dispersion for the case when there is a non-zero asymmetry, where the Blöch vectors associated with pseudospins acquire an energy dependent component. Panels (b) and (d) show the Klein Tunnelling scheme considered here, for the case of zero asymmetry and non-zero asymmetry respectively. The directions of the pseudospin in each of the bands, inside and outside the barrier, are shown for $k_y = 0$.

$$\Phi_{\mathrm{B}} = 2\pi\left(\frac{|\varepsilon| - \frac{\Delta}{2}}{|\varepsilon|}\right) \quad , \tag{6.5}$$

in the K valley, when $|\varepsilon| > \frac{\Delta}{2}$. Performing the same analysis in the K' valley yields the equal and opposite result.

Here it can be seen that, in the case of no asymmetry (shown in figure 6.2(a)) the pseudospin always lies in the $x - y$ plane and the quasiparticles have a Berry phase of 2π, but with a non-zero asymmetry (shown in figure 6.2(c)), there is an additional out-of-plane component to the pseudospin [225]. I will show that this has interesting effects on the transport properties of biased bilayer graphene.

6.2 Method

I will now calculate the effect the interlayer asymmetry has on KT in ballistic bilayer graphene. Generalising the low energy Hamiltonian given in equation 6.1, for a globally non-uniform gap,

$\Delta(x)$, with a scalar potential, $V(x)$, included, for the K valley I obtain:

$$H^{(\tau)} = \begin{pmatrix} \frac{\Delta(x)}{2} + V(x) & \frac{(p^{\dagger})^2}{2m} \\ \frac{p^2}{2m} & -\frac{\Delta(x)}{2} + V(x) \end{pmatrix} \tag{6.6}$$

where the gap and potential barrier height are assumed to be local in each region, such that $\Delta(x)$ and $V(x)$, respectively, represent step functions. The general normalised two-component spinor eigenvector describing the system now reads:

$$\psi_{\mathbf{k}}^{(\tau)} = \begin{pmatrix} \psi_{A1} \\ \psi_{B2} \end{pmatrix} = \sqrt{\frac{\varepsilon + \frac{\Delta(x)}{2} - V(x)}{2[\varepsilon - V(x)]}} \begin{pmatrix} 1 \\ \frac{\mathbf{p}^2}{2m\left(\varepsilon + \frac{\Delta(x)}{2} - V(x)\right)} \end{pmatrix} . \tag{6.7}$$

and the eigenvalues are now given by

$$\varepsilon = V(x) \pm \sqrt{\frac{|\mathbf{p}|^4}{4m^2} + \frac{\Delta(x)^2}{4}} . \tag{6.8}$$

Including this general (but locally static) potential, the normalised vector in the Bloch sphere reads

$$\mathbf{V}_{\mathbf{k}}^{\pm} = \frac{1}{V(x) \pm \sqrt{\frac{\hbar^4|\mathbf{k}|^4}{4m^2} + \frac{\Delta^2}{4}}} \left(\frac{\hbar^2(k_x^2 - k_y^2)}{2m}, \frac{2\hbar^2 k_x k_y}{2m}, \frac{\Delta}{2} \right) , \tag{6.9}$$

and the BP of the system is

$$\Phi_{\mathrm{B}}(\varepsilon, V, \Delta) = 2\pi \left(\frac{|\varepsilon - V(x)| - \frac{\Delta(x)}{2}}{|\varepsilon - V(x)|} \right) , \tag{6.10}$$

in the K valley when $|\varepsilon - V(x)| > \frac{\Delta(x)}{2}$, where both the potential and gap size are constant in each region.

I now insert a particular potential into these expressions. The scheme of the Klein Tunnelling considered here is the same as was taken in chapter 5, and is illustrated in figure 6.3. I consider a potential barrier with a rectangular shape, which is invariant along the y-axis (leading to the assumption that the k_y component of the wavevector is conserved across the device), so that the potential reads:

$$V(x) = \begin{cases} V_0 & \text{if } 0 < x < L \\ 0 & \text{otherwise.} \end{cases}$$

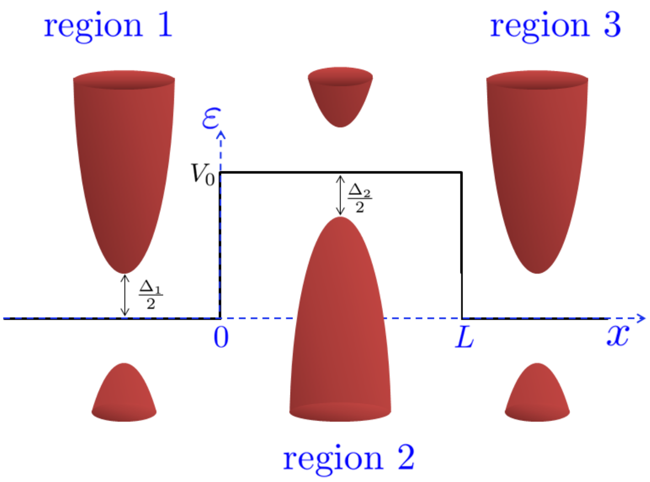

Figure 6.3: Schematic diagram for tunnelling through a potential barrier, where the zero point of the energy is chosen to be at the potential value in regions 1 and 3. For generality the gap size is allowed to be different inside and outside the barrier, and is defined as Δ_1 in regions 1 ($x \leq 0$) and 3 ($x \geq L$), and Δ_2 in region 2 ($0 < x < L$).

I assume the width (W) of the barrier to be much greater than the length (L), so that edge effects can be neglected [226]. In order to make a direct analogy to the case usually considered in quantum electro-dynamics (QED) [11, 108], and to simplify the problem, I assume the potential step is sharp [87]. This assumption holds true as long as the quasiparticle's Fermi wavelength, λ_F, is much larger than the edge smearing characteristic width of the potential step (which itself should be larger than the lattice constant in order to avoid Umklapp scattering between different valleys) [87].

Due to the parabolic energy spectrum there are four possible wavevectors in each region. With the assumption that k_y is conserved, the general expressions for the wavevectors in the x-direction are given by:

$$\begin{aligned} k_x^{(1)} &= \sqrt{\frac{2m}{\hbar^2}\sqrt{[\varepsilon - V(x)]^2 - \frac{\Delta(x)^2}{4}} - k_y^2}\ , \qquad & k_x^{(2)} &= -k_x^{(1)}\ , \\ k_x^{(3)} &= \mathrm{i}\sqrt{\frac{2m}{\hbar^2}\sqrt{[\varepsilon - V(x)]^2 - \frac{\Delta(x)^2}{4}} + k_y^2}\ , \qquad & k_x^{(4)} &= -k_x^{(3)}\ . \end{aligned} \tag{6.11}$$

When $\Delta(x) = 0$, $k_x^{(3)}$ and $k_x^{(4)}$ are the evanescent wavevectors in the positive and negative x-direction, respectively. However, with $\Delta(x) \neq 0$ any of the four wavevectors can be real, imaginary or complex, depending on the values of the parameters.

The wavefunction, $\Psi(x, y)$, in each region of figure 6.3 can now be calculated as a coherent superposition of four solutions, and due to the invariance of the potential in the y-direction, it can be written as $\Psi(x, y) = \Psi(x)e^{ik_y y}$, such that only $\Psi(x)$ need be considered. I also define the x-component of the wavevector in regions 1 and 3 as $k_x^{(i)} = k_i$ and in region 2 as $k_x^{(i)} = q_i$. Furthermore, as the gap is locally constant but can be different in each region, I use the same assumption as in chapter 5, that the gap in the regions outside the barrier is the same, but could be different inside the barrier. I define the gap in regions 1 and 3 as Δ_1, and in region 2 as Δ_2. The wavevector in the y-direction reads

$$k_y = k_F \ \sin(\phi) = \sqrt{\frac{2m}{\hbar^2}\sqrt{\varepsilon^2 - \frac{\Delta_1^2}{4}}} \ \sin(\phi) \, , \tag{6.12}$$

and is conserved over all regions, where ϕ is the incident angle of the electron on the barrier from region 1, such that $k_1 = k_F e^{i\phi}$, where k_F is the Fermi wavevector in regions 1 and 3, as indicated in figure 5.3 for the monolayer case.

Thus, the wavefunctions in each region read

$$\begin{aligned}
\Psi_1(x) &= \xi_1 \left\{ \begin{pmatrix} 1 \\ \frac{\hbar^2 (k_1 + \mathrm{i}k_y)^2}{2m\left(\varepsilon + \frac{\Delta_1}{2}\right)} \end{pmatrix} e^{\mathrm{i}k_1 x} + r \begin{pmatrix} 1 \\ \frac{\hbar^2 (k_2 + \mathrm{i}k_y)^2}{2m\left(\varepsilon + \frac{\Delta_1}{2}\right)} \end{pmatrix} e^{\mathrm{i}k_2 x} + C_1 \begin{pmatrix} 1 \\ \frac{\hbar^2 (k_3 + \mathrm{i}k_y)^2}{2m\left(\varepsilon + \frac{\Delta_1}{2}\right)} \end{pmatrix} e^{\mathrm{i}k_3 x} \right\} \\
\Psi_2(x) &= \xi_2 \Bigg\{ A_2 \begin{pmatrix} 1 \\ \frac{\hbar^2 (q_1 + \mathrm{i}k_y)^2}{2m\left(\varepsilon + \frac{\Delta_2}{2} - V_0\right)} \end{pmatrix} e^{\mathrm{i}q_1 x} + B_2 \begin{pmatrix} 1 \\ \frac{\hbar^2 (q_2 + \mathrm{i}k_y)^2}{2m\left(\varepsilon + \frac{\Delta_2}{2} - V_0\right)} \end{pmatrix} e^{\mathrm{i}q_2 x} + \\
&\qquad C_2 \begin{pmatrix} 1 \\ \frac{\hbar^2 (q_3 + \mathrm{i}k_y)^2}{2m\left(\varepsilon + \frac{\Delta_2}{2} - V_0\right)} \end{pmatrix} e^{\mathrm{i}q_3 x} + D_2 \begin{pmatrix} 1 \\ \frac{\hbar^2 (q_4 + \mathrm{i}k_y)^2}{2m\left(\varepsilon + \frac{\Delta_2}{2} - V_0\right)} \end{pmatrix} e^{\mathrm{i}q_4 x} \Bigg\} \\
\Psi_3(x) &= \xi_1 \left\{ t \begin{pmatrix} 1 \\ \frac{\hbar^2 (k_1 + \mathrm{i}k_y)^2}{2m\left(\varepsilon + \frac{\Delta_1}{2}\right)} \end{pmatrix} e^{\mathrm{i}k_1 x} + D_3 \begin{pmatrix} 1 \\ \frac{\hbar^2 (k_4 + \mathrm{i}k_y)^2}{2m\left(\varepsilon + \frac{\Delta_1}{2}\right)} \end{pmatrix} e^{\mathrm{i}k_4 x} \right\} \ .
\end{aligned} \tag{6.13}$$

where

$$\xi_1 = \sqrt{\frac{\varepsilon + \frac{\Delta_1}{2}}{2\varepsilon}} \ , \qquad \text{and,} \qquad \xi_2 = \sqrt{\frac{\varepsilon - V_0 + \frac{\Delta_2}{2}}{2\left(\varepsilon - V_0\right)}} \ . \tag{6.14}$$

The boundary conditions at the step edges require the continuity of the wavefunction and

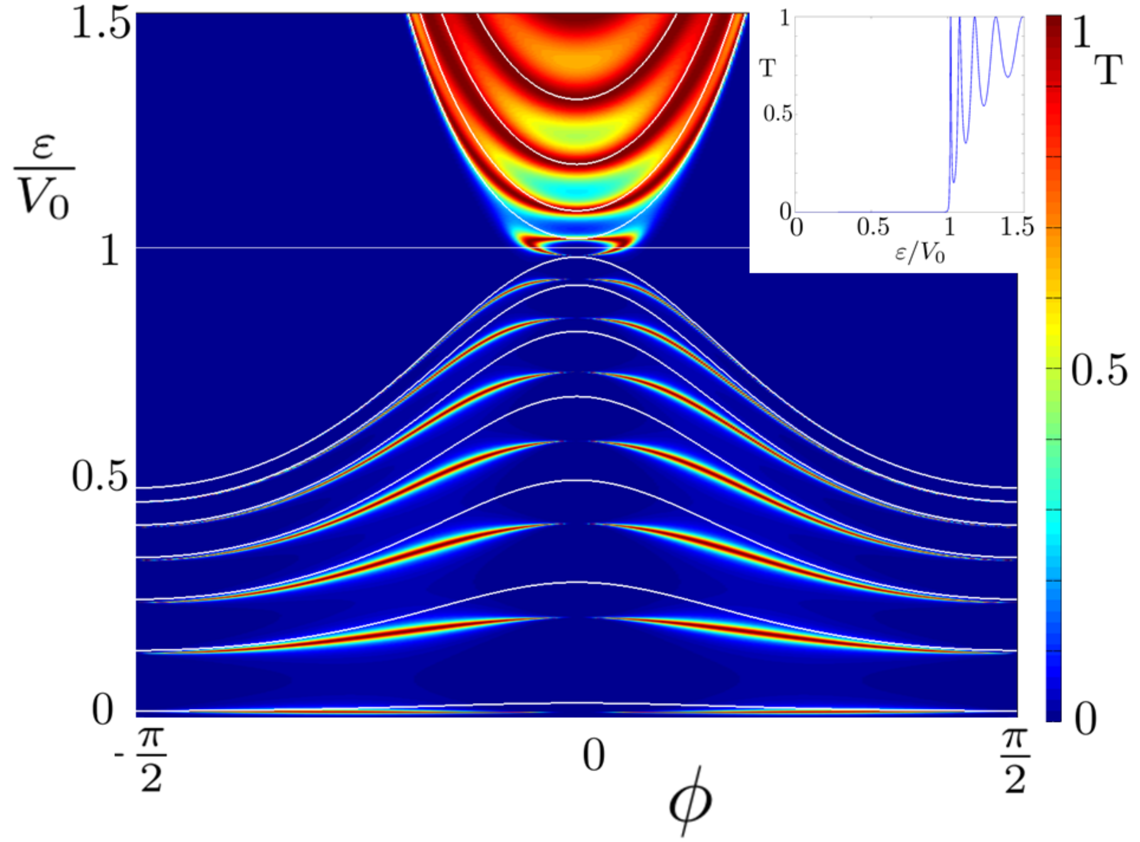

Figure 6.4: Transmission probability in unbiased bilayer graphene through a barrier of height V_0 and width $7L_0 \approx 200$nm (where $L_0 = \frac{\hbar\pi}{\sqrt{2m\bar{V}_0}}$, with $\bar{V}_0 = 0.01$eV). The transmission probability is shown as a function of energy and incident angle, where the white lines indicate where the resonances, from equation 6.15, lie on this spectrum. The inset shows the corresponding transmission at normal incidence.

---

its derivative, *i.e.* at $x = 0$, $\Psi_1 = \Psi_2$ and $\frac{\partial}{\partial x}\Psi_1 = \frac{\partial}{\partial x}\Psi_2$, and at $x = L$, $\Psi_2 = \Psi_3$ and $\frac{\partial}{\partial x}\Psi_2 = \frac{\partial}{\partial x}\Psi_3$, which leads to eight simultaneous equations. Solving these gives an expression for the transmission amplitude, t.

6.3 Results and Discussion

Assuming that $\Delta_1 = \Delta_2 = \Delta$, $T = |t|^2$ was numerically evaluated and is shown as a function of incident electron energy and incident angle, normalised to the barrier height, for the case with no gap in figure 6.4, and with $\Delta \neq 0$ in figure 6.5.

In figure 6.4, I see qualitative similarities in the transmission spectrum to that seen in previous work on unbiased bilayer graphene [121]. I also recover a suppression of the transmission through the barrier at normal incidence in the npn region ($\varepsilon < V_0$) [87], shown in the inset. This is expected due to the orthogonality of spinors at $\phi = 0$.

The locations of resonance modes, ε_{res}, due to Fabry-Perot type states, can be estimated by quantising k_x as $k_xL/\pi = n$, where n is an integer, yielding,

$$\varepsilon_{\text{res}}^{(n)}(k_y) = V_0 \pm \sqrt{\frac{\hbar^4 \left[\left(\frac{n\pi}{L}\right)^2 + k_F^2 \sin^2(\phi)\right]^2}{(2m)^2}} \quad , \tag{6.15}$$

indicated in figure 6.4 by the white lines. There is qualitative agreement between the positions of the resonances, in particular for $\varepsilon > V_0$, in the region $\phi \sim 0$, with a slight disagreement away from this as the resonance lines, from expression 6.15 tend towards the next relative resonance. When $\varepsilon < V_0$ the resonance lines predict the correct number of resonances but there is little agreement at $\phi = 0$, even though there is consensus nearer $\phi = \pm\frac{\pi}{2}$. Also, in figure 6.4 there is an interesting feature close to $\varepsilon = V_0$ and $\phi = 0$. The resonance closest to the Dirac point has a different dependence on wavevector than all other resonances: when $|k_y|$ is increased, rather than producing a parabolic shape as seen for higher modes, it creates a bubble-like shape. This 'bubble' is described as the resonance of evanescent modes [121], and it is these evanescent modes that are seen as responsible for the pseudo-diffusive transport at the Dirac point. Notice that at the bottom of this bubble I still recover $T = 0$ at $\phi = 0$, as demanded by the fact perfect orthogonality of spinors in the n and p regions.

I now consider the effect of asymmetry on the transmission, which has been partially discussed in [212, 227, 228]. Figure 6.5 shows the transmission for varying amounts of asymmetry. When $\Delta \approx V_0/100$, such that $\Delta \ll V_0$, shown in figure 6.5(a) the transmission spectrum again resembles the case where there is no gap. However, at normal incidence, shown in figure 6.5(d), it can be seen that there is now some transmission in the npn regime, which is not present in unbiased bilayer graphene. This effect is more pronounced when the gap is large compared to the energy, for example close to the bottom of the conduction band outside the barrier, at $\varepsilon \sim \Delta/2$, or at $\varepsilon \sim V_0 - \Delta/2$ as is evident from the larger peaks in figure 6.5(d). These peaks in transmission probability are due to the resonant tunnelling permitted by non-orthogonal spinors in the n and p regions, which are crucially only allowed because of the gap.

For a larger gap relative to the barrier, shown in figure 6.5(b), there is no transmission inside the gap ($\varepsilon < \frac{\Delta}{2}$), as expected. However, by opening this gap there is no longer perfect reflection

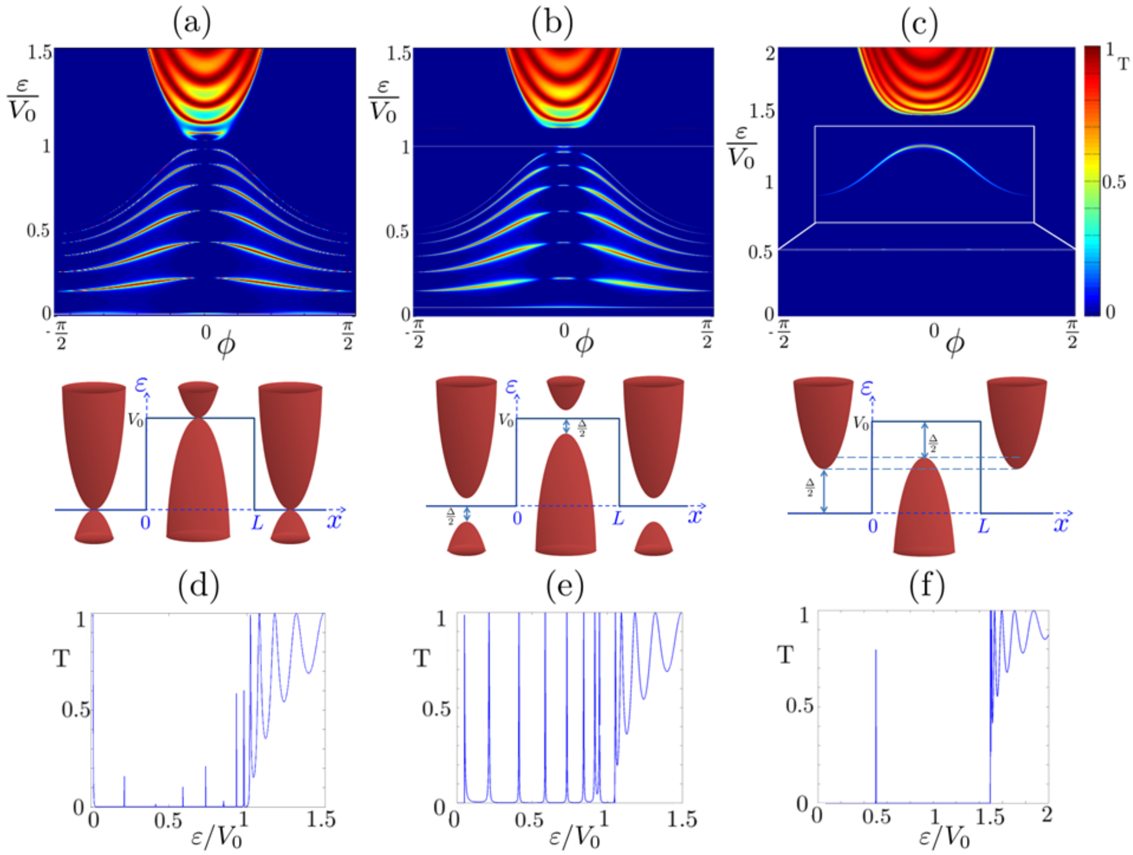

Figure 6.5: Transmission probability in biased bilayer graphene through a barrier of height V_0 and width $7L_0 \approx 200$nm. Panels (a)-(c) show the transmission as a function of energy and incident angle, and (d)-(f) show the corresponding transmission at normal incidence, and the schematics in between these show the barriers and gaps considered in each case. The gap in the spectrum is $\Delta \approx V_0/100$ in panels (a) and (d), $\Delta \approx V_0/10$ in (b) and (e), and $\Delta \approx 0.99V_0$ in (c) and (f). The inset in (c), in the white box, shows a close up of the transmission between $0.50 \leq \varepsilon/V_0 < 0.51$ across the whole ϕ range, which is too small to be seen the main panel.

at normal incidence, and perfect transmission can be found at certain energies, see figure 6.5(e). Hence I have shown that by biasing bilayer graphene, and breaking inversion symmetry, I can recover properties previously thought to be reserved for *massless* Dirac particles. It is interesting to note that these sharp transmission resonances, at approximately normal incidence, are localised around small angles, leading to strong transmission directly across the sample. These may turn out to be useful in angular resolved ballistic devices.

Figure 6.5(c) shows the case where there is only a small overlap of the bands inside and outside the barrier such that $\Delta \sim V_0$. The inset shows a close up on the transmission at this small band overlap, when $\varepsilon \sim V_0/2$. At other energies there is no transmission due to the large gap, until

$\varepsilon \geq V_0 + \Delta/2$ where transmission occurs above the barrier. Therefore transmission can still be recovered at normal incidence through the barrier, even though there is only a small overlap in the bands.

Figures 6.5(a)-6.5(c) also show that, with increased asymmetry, the strength of the 'bubble' shaped transmission peak (seen in figure 6.4, at energies in the vicinity of $\varepsilon \sim V_0$) reduces. In fact, with an increased gap there is no longer a transmission 'bubble' around $\varepsilon \approx V_0$. In figure 6.6 I explore the evolution of this 'bubble' with increased asymmetry, taking gap values smaller than those seen in figure 6.5(b). When $\Delta = 0$, shown in figure 6.6(a), there is zero transmission at the bottom of the 'bubble' as would be expected due to the perfect orthogonality between spinors in the n and p regions. With a small non-zero Δ there can still be a 'bubble' due to transmission across the barrier using the evanescent waves, but as the asymmetry is increased, shown in figures 6.6(b)-6.6(d), the strength of this transmission diminishes. It can also be seen that as the asymmetry is increased, the transmission probability at the bottom of the 'bubble' becomes non-zero and then separates to become the localised transmission peak of highest energy in the npn region, as shown in figure 6.5(b). This isolated transmission peak is produced at $\varepsilon \approx V_0 - \frac{\Delta}{2}$ and $\phi \approx 0$, and is the most localised peak in angle and energy. Notice also that this is the only localised peak that does not have extended 'moustache' peaks at wider angles. This localised nature is shown more clearly in the inset of figure 6.6(f) where the transmission across all angles is shown for this specific energy. This peak resonance could be probed in angular resolved measurements in a device constructed like that shown in figure 6.6(e). Here, inducing a bias between contact 1 and contact 5 one would observe transmission at multiple contacts on the opposite side to contact 1 (due to the 'moustache' resonances) at another energy, but at this energy there would only be transmission detected at contact 5. This specific resonance is extremely sharp, both in energy and in angle, and could be exploited as a switch in ballistic devices.

I also show, in figure 6.6(f), that the transmission resonance is qualitatively analogous to that exhibited by monolayer graphene at the neutrality point [226], at $\varepsilon \approx V_0$, in the limit $V_0 \to \infty$ [121], given by:

$$T_{\text{mono}}\left(\varepsilon \approx V_0 - \frac{\Delta}{2}, k_y\right) = \frac{1}{\cosh^2\left(k_y L\right)} \quad . \tag{6.16}$$

In figure 6.6(f), the red dashed line, which indicates T_{mono}, is in good qualitative agreement

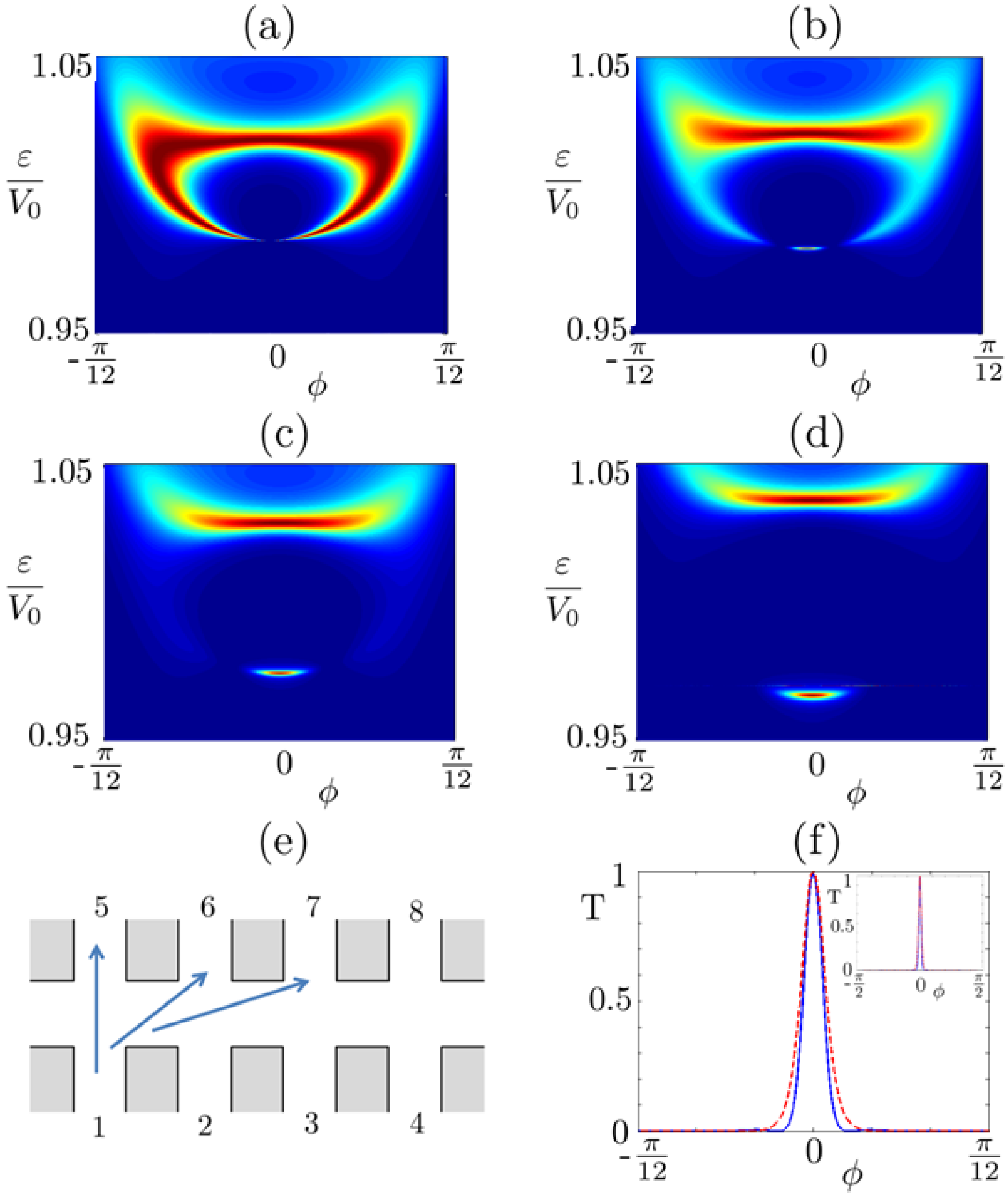

Figure 6.6: Transmission probability near the neutrality point ($\varepsilon \approx V_0$) as the gap size is increased, in biased bilayer graphene through a barrier of height V_0 and width $7L_0 \approx 200$nm. Panels (a) shows a close up on the bubble when $\Delta = 0$, as can also be seen in figure 6.4. Panels (b)-(d) show the evolution of the transmission bubble with increased asymmetry. In panel (b) $\Delta = 0.02V_0$, in panel (c) $\Delta = 0.04V_0$ and in panel (d) $\Delta = 0.06V_0$. Panel (e) shows a schematic of a possible angular resolved device to measure the peak resonances shown in panels (a)-(d). Panel (f) shows a cut of transmission probability as a function of angle at $\Delta = 0.06V_0$ and $\varepsilon \approx 0.97V_0$, where the inset shows the transmission across the entire angular range. The blue solid line in panel (f) is the numerical result, and the red dashed line is calculated from equation 6.16.

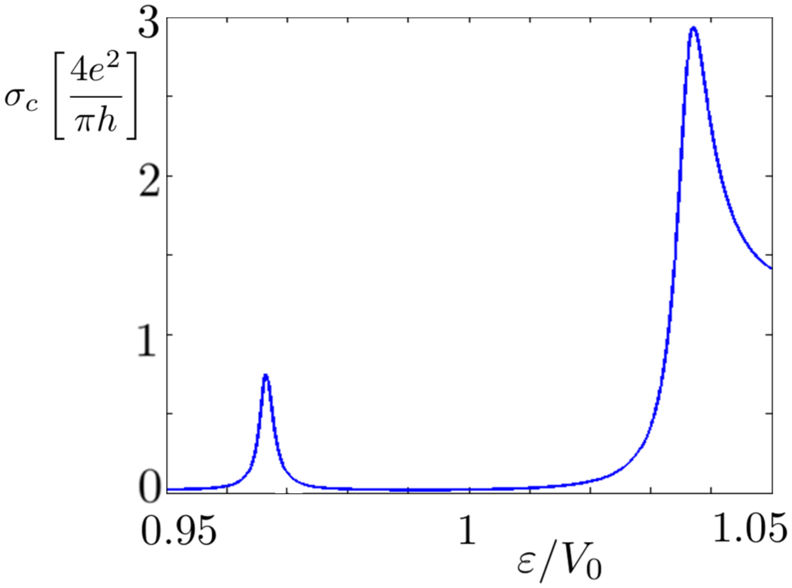

Figure 6.7: The conductivity as a function of energy in the vicinity of the barrier height, with $\Delta = 0.06V_0$. At $\varepsilon \sim V_0 - \frac{\Delta}{2}$ a peak in transmission is evident, which corresponds to the localised transmission peak at the bottom of the bubble in figure 6.6(d). In the figure $L = 7L_0 \approx 200$nm.

---

with the transmission data I have numerically calculated. A transmission resonance of this form, in monolayer graphene, is responsible for the minimal conductivity at the Dirac point, of $\sigma_c = \frac{GL}{W} = \frac{4e^2}{\pi h}$, where G is the conductance. I expect a similar behaviour for the conductivity at this energy in bilayer graphene, due to the resemblance between these transmission spectra. To analysis this, the conductivity across the bubble, which is numerically calculated using equation 5.18, is shown in figure 6.7, and can be seen to be just less than the value expected in monolayer graphene.

It is evident that the additional σ_z terms in the Hamiltonian drastically affect the transmission probabilities and generate supplementary energy dependences. Again the dependence of transmission on energy can be interpreted by considering the energy dependent Berry phase, given in equation 6.5. As was the case in chapter 5, both the transmission and the Berry phase are energy dependent because of the link between the orbital degrees of freedom and the pseudo-spin. Thus the energy dependent transmission can be explained by considering the spinor overlap, inside and outside the barrier. The overlap of the spinors inside and outside the barrier, at normal incidence, for the general case of variable gap and potential barrier in different regions, as a function of the

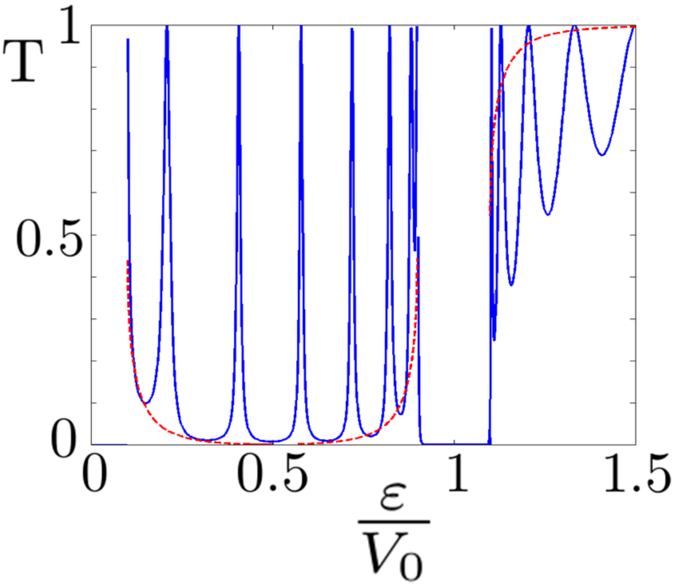

Figure 6.8: The transmission probability at normal incidence for different incident energies (blue solid line) and the pseudospin overlap (red dashed line) from equation 6.17, which acts like an envelope function, when $\Delta = 0.1V_0$. This helps to explain the general shape of the transmission, aside from the peaks and troughs due to resonant tunnelling through to Fabry-Perot states. In the figure $L = 7L_0 \approx 200$nm.

Berry phase, reads

$$\begin{aligned} |\langle\psi_1|\psi_2\rangle|^2 &= \frac{1}{4\,|\varepsilon\,(\varepsilon - V_0)\,|}\Bigg[\sqrt{\left(\varepsilon+\frac{\Delta_1}{2}\right)\left(\varepsilon+\frac{\Delta_2}{2}-V_0\right)} \\ &\quad -\sqrt{\left(\varepsilon-\frac{\Delta_1}{2}\right)\left(\varepsilon-\frac{\Delta_2}{2}-V_0\right)}\ \Bigg]^2 \\ &= \frac{1}{16\pi^2}\Bigg[\sqrt{\Phi_{B2}(\varepsilon,-\Delta_1)\Phi_{B2}(\varepsilon,V_0,-\Delta_2)} \\ &\quad -\sqrt{\Phi_{B2}(\varepsilon,\Delta_1)\Phi_{B2}(\varepsilon,V_0,\Delta_2)}\ \Bigg]^2 . \end{aligned} \tag{6.17}$$

From this the reason for the energy dependent transmission becomes apparent. With no gap, the pseudo-spin rotates in the $x - y$ plane and the quasiparticles have a Berry phase of 2π (as can be calculated from equation 6.5), which has been well documented for unbiased bilayer graphene [113]. With no asymmetry, at normal incidence in the *npn* region, there is no overlap of spinors leading to the selection rules for perfect reflection. These orthogonal pseudospin states, at normal incidence, inside and outside the barrier can be seen in figure 6.2(b), and from equation 6.17 they lead to $\langle\psi_1|\psi_2\rangle = 0$, if $\Delta_1 = \Delta_2 = 0$.

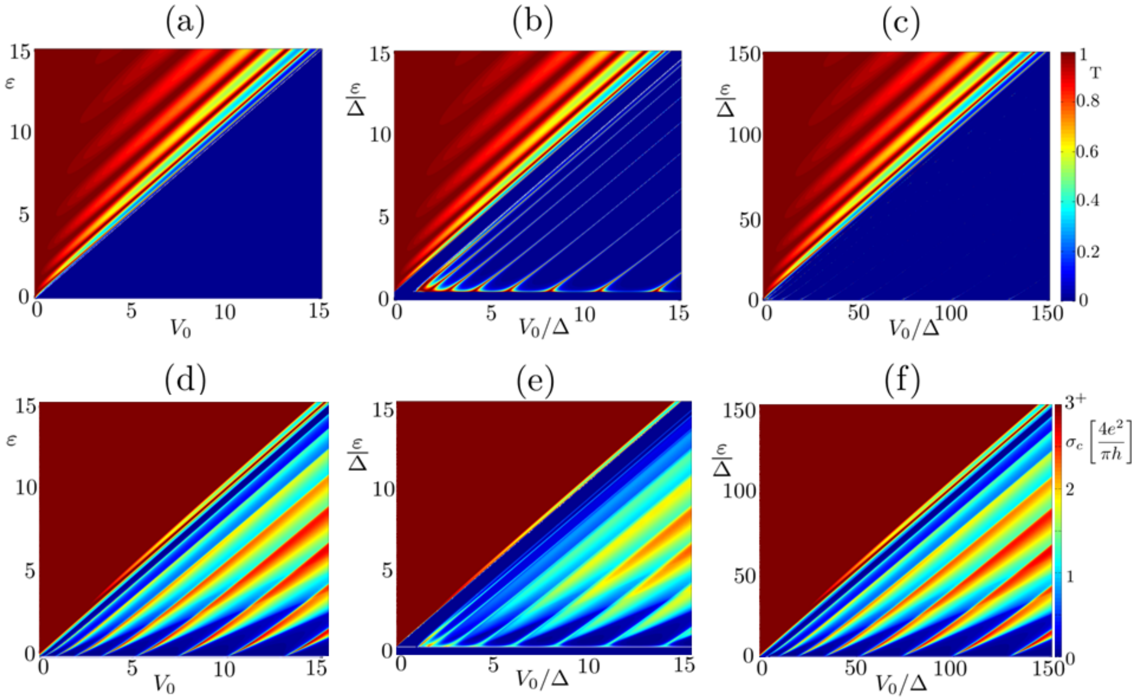

Figure 6.9: Panels (a)-(c) show the transmission probability at normal incidence through the bilayer graphene system as a function of incident electron energy and barrier height for different gap sizes and panels (d)-(f) show the corresponding conductivity. The transmission is shown for zero bias (i.e. $\Delta = 0$) in panel (a) and $\Delta \neq 0$ in panels (b) and (c). With $\varepsilon \gg \Delta$ and $V_0 \gg \Delta$, shown in (c), the transmission probability resembles the case where $\Delta = 0$, however when $\varepsilon \sim \Delta$ and $V_0 \sim \Delta$, shown in (b), the gap has more of an effect. In the conductivity plots, the colour scheme has been adjusted to highlight the conductivity of interest (i.e. $\varepsilon \leq V_0$), thus conductivities of $4e^2/h$ or more are coloured red. In the figure $L = 7L_0 \approx 200$nm.

When $\Delta \neq 0$ the pseudo-spins can be oriented out of the plane, and thus circumvent the selection rule at normal incidence, leading to an energy dependent transmission probability. In figures 6.2(c) and 6.2(d), the case when $\Delta \neq 0$ is presented, where, due to the asymmetry, the selection rules no longer apply. The energy dependent pseudospin directions allow for the possibility of spinor overlap, and therefore some forward scattering at normal incidence. When $\varepsilon \approx \pm\frac{\Delta}{2}$, the Bloch sphere vector is $V^{\pm}_{\mathbf{k}} = \pm\hat{\mathbf{z}}$ and therefore the BP, from equation 6.5, tends to zero.

In figure 6.8 I show the transmission through the barrier as a function of energy at normal incidence (blue solid line) and also the probability of spinor overlap at normal incidence (red dashed line) calculated from equation 6.17 when $\Delta = 0.1V_0$. The spinor overlap provides an envelope function describing the general shape of the transmission probability, whereas the peaks and troughs are due to ordinary resonant tunnelling through Fabry-Perot type states. This overlap description breaks down inside the gap, as there are no states.

I can now explore the effect of changing the barrier height relative to the gap size. For fixed gap sizes, figures 6.9(a)-6.9(c) show the transmission probability at normal incidence as a function of incident electron energy and barrier height. Figure 6.9(a) shows the case for no gap, and as expected there is zero transmission at normal incidence in the *npn* region. In figures 6.9(b) and 6.9(c) there is a finite gap. As $V_0/\Delta \gg 1$ and $\varepsilon/\Delta \gg 1$, shown in figure 6.9(c), the gap has little effect, meaning the transmission resembles that shown in figure 6.9(a). However, when $\varepsilon \sim \Delta$ and $V_0 \sim \Delta$, shown in figure 6.9(b), the gap has more of an effect, and perfect transmission at normal incidence can be seen. There are clear resonances parallel to the $\varepsilon = V_0$ line, which are the same as the resonances in the transmission plots shown in figure 6.4. These are due to ordinary resonant tunnelling through Fabry-Perot type states.

Figures 6.9(d)-6.9(f) show the conductivity, σ_c, as a function of ε and V_0, where the conductance was first calculated from equation 5.18. Figure 6.9(d) shows the case where there is no gap, and in figures 6.9(e) and 6.9(f) $\Delta \neq 0$. Again there are clear resonances parallel to the line $\varepsilon = V_0$ due to Fabry-Perot type states, similar to figure 6.9(b). When ε/Δ and V_0/Δ are both very large, as shown in 6.9(f) the conductivity resembles the case where $\Delta = 0$, however at small ε/Δ and V_0/Δ values, shown in 6.9(e) the gap has more of an effect, and slightly reduces the conductivity. This leads to the conclusion that, although there is increased transmission at normal incidence with broken inversion symmetry, while averaging over the entire ϕ range there is a slightly reduced transmission.

Similar resonances can be seen in the Fano factor, shown in figure 6.10, which is calculated from equation 5.19. The shape of this function is as would be expected from the conductivity plot. The reduction in the resonance peaks of F close $\varepsilon \approx \frac{\Delta}{2}$ indicates that there is pseudo-diffusive transport with $F \sim \frac{1}{3}$, as is the case at the neutrality point in graphene. Close to $V_0 \approx \frac{\Delta}{2}$ F reduces further and indicates a tendency towards ballistic transport.

For this analysis I have used the 2×2 Hamiltonian given in equation 6.1, produced by taking a low energy approximation, to describe the system. However, the full system, in the basis $\Psi_{\mathbf{k}} = (\psi_{A1}, \psi_{B2}, \psi_{A2}, \psi_{B1})$, is described by the 4×4 Hamiltonian [114]

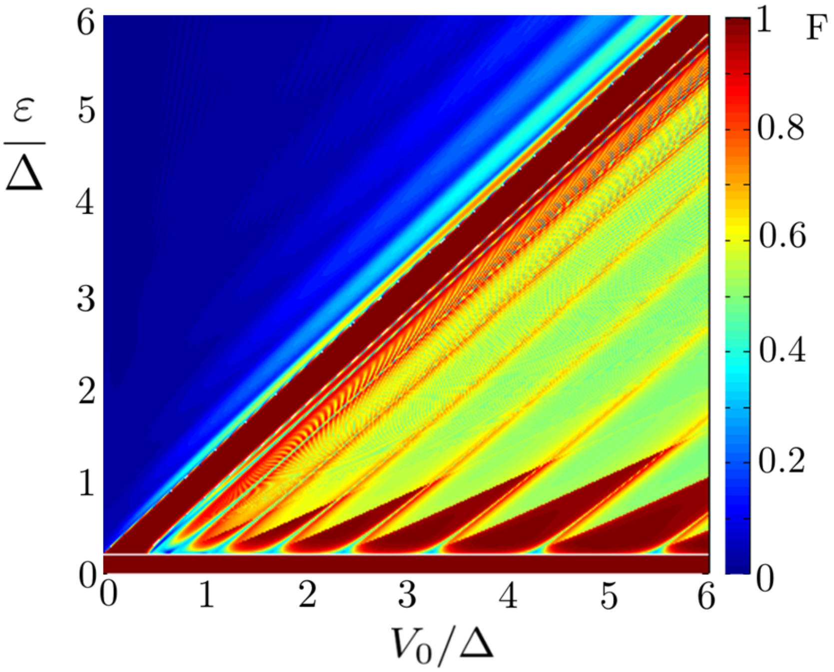

Figure 6.10: The Fano factor for biased bilayer graphene as a function of incident electron energy and barrier height normalised to the band gap size. In the figure $L = 7L_0 \approx 200\text{nm}$.

$$\hat{H} = \begin{pmatrix} V - \frac{\Delta}{2} & 0 & 0 & vp^\dagger \\ 0 & V + \frac{\Delta}{2} & vp & 0 \\ 0 & vp^\dagger & V + \frac{\Delta}{2} & -\gamma \\ vp & 0 & -\gamma & V - \frac{\Delta}{2} \end{pmatrix} , \tag{6.18}$$

which leads to the energy eigenvalues

$$\varepsilon = \sqrt{\frac{\Delta^2}{4} + \frac{\gamma^2}{2} + v^2\hbar^2|\mathbf{k}|^2 \pm \sqrt{\frac{\gamma^4}{4} + v^2\hbar^2|\mathbf{k}|^2\left(\Delta^2 + \gamma^2\right)}} . \tag{6.19}$$

This dispersion has two conduction and two valence bands, and when $\Delta = 0$ all four bands are parabolic, like in the case considered above, as shown in figure 6.11(a). However, when $\Delta \neq 0$, rather than remaining parabolic, as was assumed previously, it creates a *Mexican Hat* shape, shown in figure 6.11(b). Here I briefly analyse the consistency of my results against this modification to the low energy spectrum.

Performing the same analysis on this 4 × 4 Hamiltonian yields qualitatively analogous results as for the low energy approximation (including the 2 × 2 Hamiltonian), except for a slight

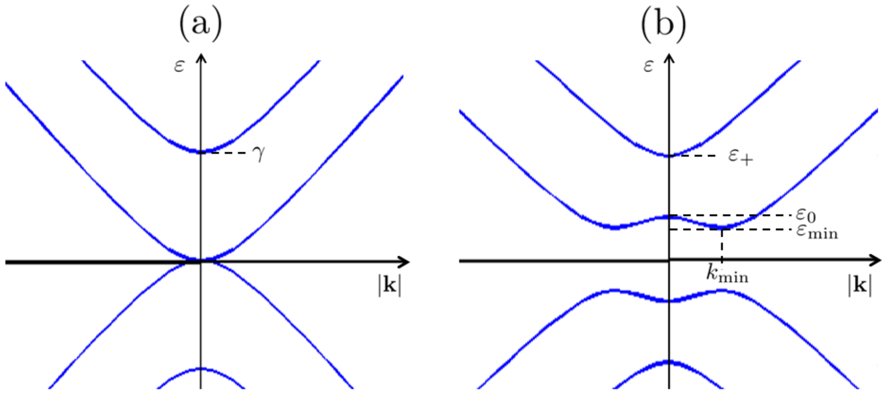

Figure 6.11: The energy and momentum dispersion of bilayer graphene from equation 6.19 with differing bias. In panel (a), with no asymmetry between the layers, bilayer graphene's dispersion is parabolic. In panel (b) the asymmetry can be seen to open a gap in the spectrum and also make changes the general shape of the dispersion. The turning points are $\varepsilon_+ = \sqrt{\frac{\Delta^2}{4} + \gamma^2}$, $\varepsilon_0 = \frac{\Delta}{2}$, $\varepsilon_{\min} = \frac{1}{2}\frac{\gamma\Delta}{\sqrt{\gamma^2+\Delta^2}}$ and $k_{\min} = \frac{\Delta\sqrt{2\gamma^2+\Delta^2}}{2v\hbar\sqrt{\gamma^2+\Delta^2}}$. In the figure $L = 7L_0 \approx 200$nm.

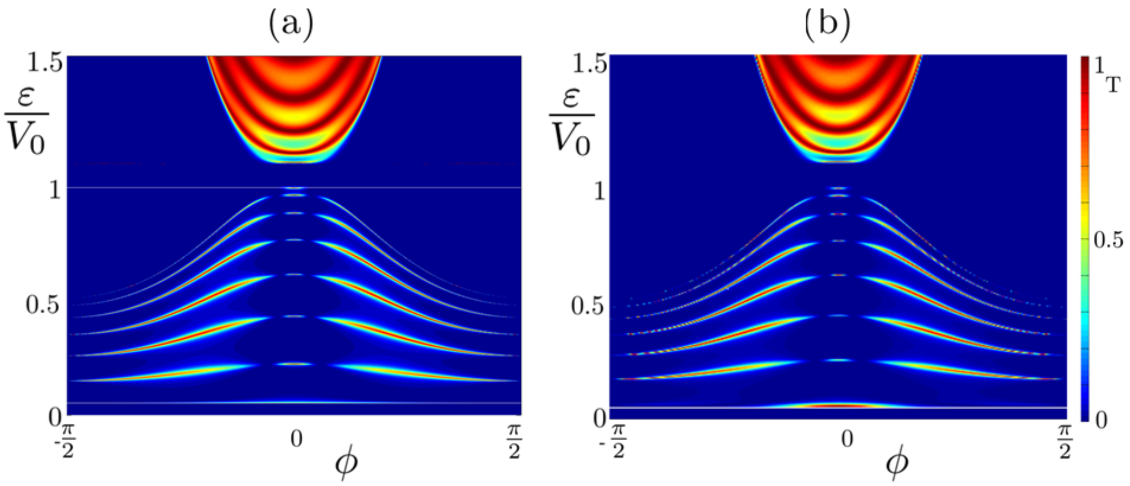

Figure 6.12: Panel (a) is taken from figure 6.5b and panel (b) shows the transmission probability in biased bilayer graphene as calculated using the 4×4 'Mexican Hat' Hamiltonian. The length of the barrier in both figures is taken as $L = 7L_0 \approx 200$nm. The asymmetry is taken as $\Delta = 0.1V_0 = 0.05\gamma$.

difference in the region $\varepsilon_{\min} < \varepsilon < \varepsilon_0$, as shown in figure 6.12. This leads to one caveat: I have assumed there is only a single real and positive solution for k_x in the region $x < 0$ but this may not necessarily be true in the region $\varepsilon_{\min} < \varepsilon < \varepsilon_0$ as can be seen in figure 6.11. I do not make such an assumption inside the barrier, as any of the four wavevectors (from equation 6.11) can be real, imaginary or complex, therefore in figure 6.11, as long as $\varepsilon > \varepsilon_0 = \frac{\Delta}{2}$, I recover essentially the same results.

It may be more realistic to consider the case where $\Delta_1 = 0$ and $\Delta_2 \neq 0$ as the doping or top gate which creates the barrier in the central region can also produce a gapped spectrum, which would not be present in the other regions. In this case the limiting energy at which there is a difference between the full description and the low energy approximation does not apply, and the two models produce essentially the same results for all energies. Examples of the transmission probability for the case of $\Delta_1 = 0$ and $\Delta_2 \neq 0$ are shown in figure 6.13, calculated using the low energy approximation. Figures 6.13(a) and 6.13(b), when compared to figure 6.12(a), show that in the most experimentally relevant energy region (*i.e.* close to $\varepsilon \sim V_0$) the absence of a gap in the leads does not qualitatively change the transmission probability. The highest energy resonance peak (at $\phi = 0$) in the *npn* region, which corresponds to the bottom of the transmission bubble and has no corresponding resonances at other angles, is still present. Therefore the non-unity ratio of gap size inside and outside the barrier should still allow for the angle resolved measurements previously suggested. However, at smaller energies the transmission probability differs from that which was previously seen, as the resonance peaks at $\phi = 0$ are less evident. Nonetheless figures 6.13(c) and 6.13(d) show the transmission probability at normal incidence where it is possible to see that there are still some very sharp non-zero resonances at $\phi = 0$.

6.4 Chapter Summary

In this chapter I have extended on the research conducted in chapter 5 (where systems with a linear gapped spectrum, like MoS_2, containing DQILGSs, were discussed) and investigated the concept of Klein tunnelling in systems with a parabolic gapped spectrum, like biased bilayer graphene, containing DQIPGSs.

Here, I unveil that with even the slightest asymmetry between layers producing a gap in the spectrum, there is no longer perfect reflection at normal incidence for all energies, and that perfect transmission can be discovered at certain energies. With a small uniform gap, $\Delta \ll V_0$, and at large energy, $\varepsilon \sim V_0/2$, the Zeeman term has little effect and the dispersion can be approximated as parabolic giving a BP approaching 2π. Here the transmission as a function of angle tends towards the usual transmission of bilayer graphene, in that there is near-perfect reflection at

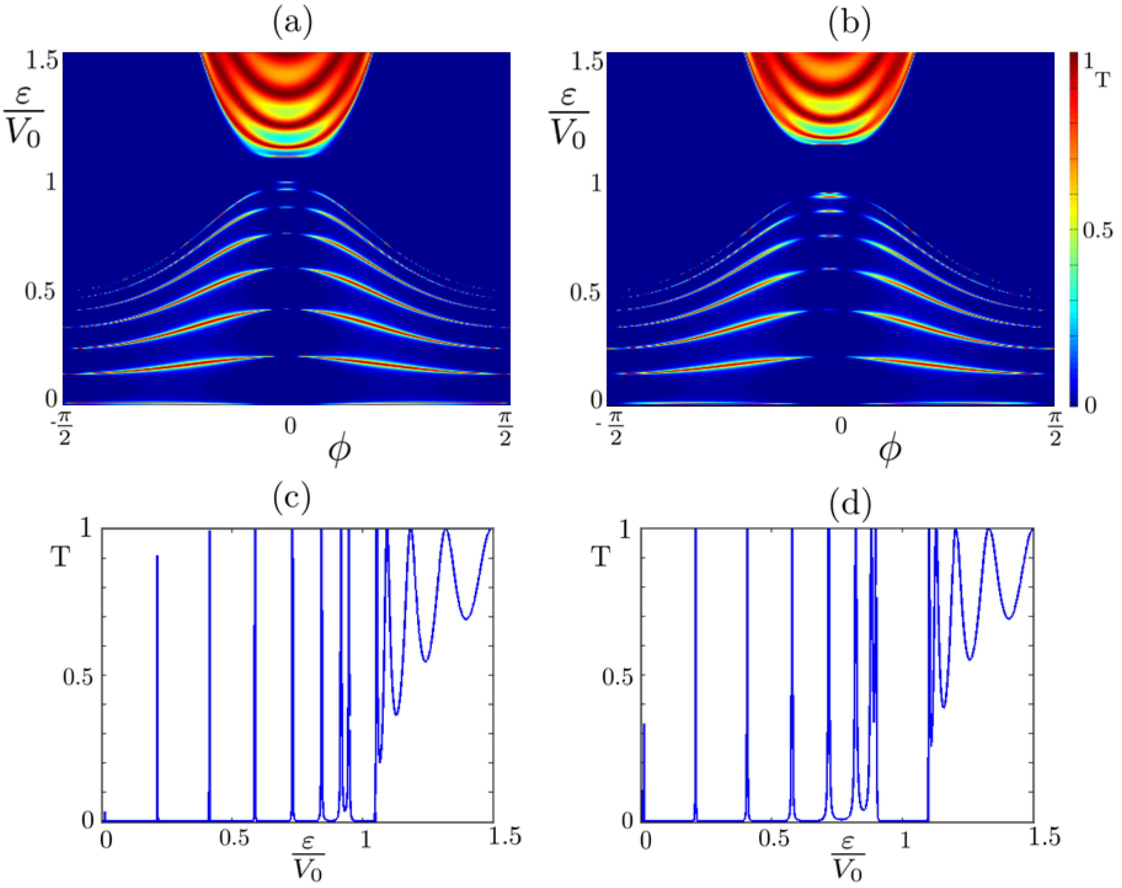

Figure 6.13: Transmission probability when $\Delta_1 = 0$ but $\Delta_2 \neq 0$. In panel (a) $\Delta_2 = 0.1V_0$ and in panel (b) $\Delta_2 = 0.2V_0$. Panels (c) and (d) show the transmission probability at normal incidence for the cases shown in panels (a) and (b) respectively. In the figure $L = 7L_0 \approx 200$nm.

normal incidence. As the gap size is increased this has more of an effect on the transmission, and perfect transmission at normal incidence can occur at certain energies, which can be interpreted as ordinary resonant tunnelling via Fabry-Perot-like states. In fact, the inclusion of a gap in the spectrum allows for non-orthogonal pseudospins between neighbouring regions in the scattering problem, enabling the possibility of tunnelling.

Surprisingly, though the gap causes extra transmission peaks at normal incidence, it decreases the conductivity. Due to the resonances of the Fabry-Perot type states there are clear peaks parallel to the line $\varepsilon = V_0$ in the transmission probability, conductivity, and Fano factor, even in the absence of a gap. This theoretical analysis could be explored in angular resolved measurements in gapped bilayer graphene devices such as that shown in figure 6.6(e).

Finally, although I have specifically discussed this phenomenon for the case of bilayer

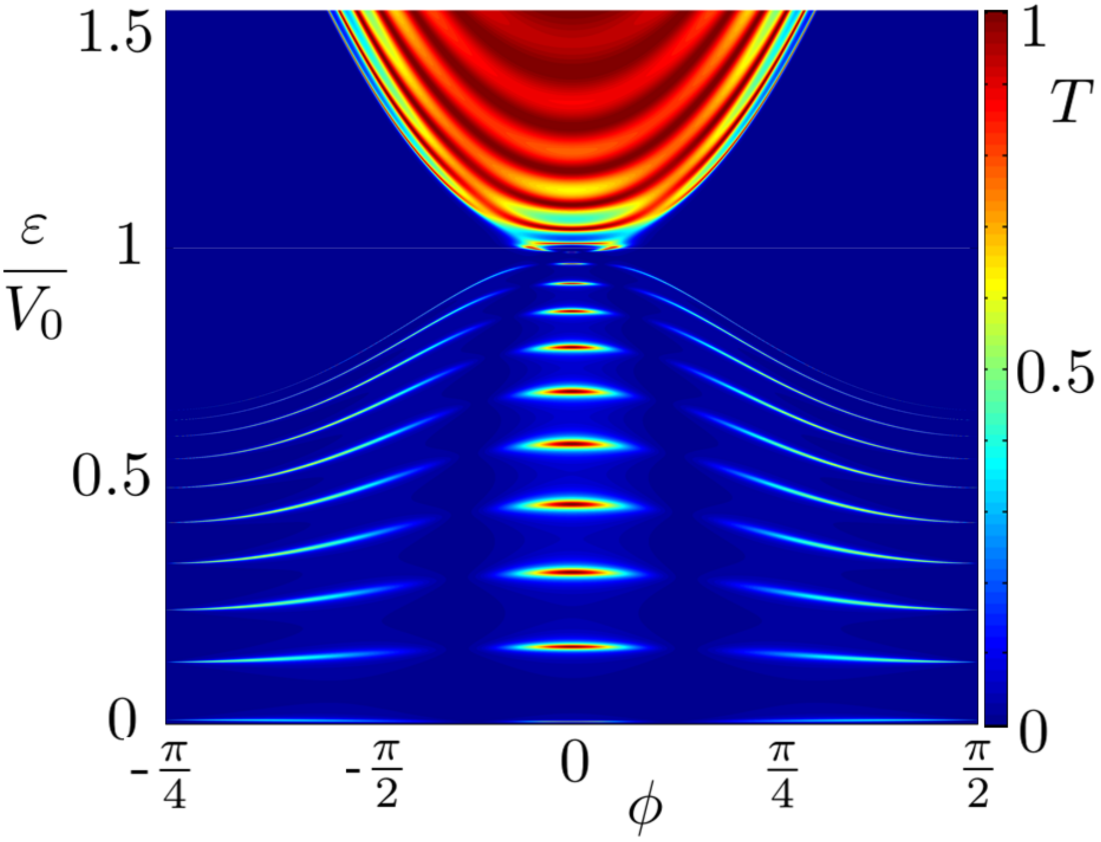

Figure 6.14: Transmission probability with $\Delta_1 = \Delta_2 = 0$ but $m_2 = 2m_1$, where m_i is the quasiparticles' effective mass in the i-th region. In the figure $L = 10L_0 \approx 200$nm.

graphene it is perfectly feasible that a similar dispersion portraying DQIPGS can be produced from arrays of plasmonic metamaterials and therefore, as was shown in the previous chapter, there can be many more adaptations to the device. In plasmonic metamaterials, by manufacturing regions with different barrier heights, $V(x)$, (or different $\bar{\omega}$ values) it is possible to create regions with differing effective masses (especially if the different regions house nanoparticles of different consisting materials). Figure 6.14 shows the transmission probability when there is no gap in the spectrum but different effective quasiparticle masses inside and outside the barrier. Here it is evident that the asymmetry between the different regions has a similar effect to the asymmetry in the sublattices in that due to this difference there is no longer perfect reflection at normal incidence as is seen in unbiased bilayer graphene. The fluctuations in transmission probability at normal incidence are caused by the lack of uniformity across the sample. This shows the further tunability of metamaterials, and opens up more possibilities for adaptation to a specific purpose. Hence, there should be further research conducted into this phenomenon.

7

Conclusions

The research presented in this thesis was motivated by the exceptional properties discovered in Dirac materials, with the aim to explore them further and investigate the possibility of tuning these properties, optimising the materials for specific uses. Inspired by the knowledge that the remarkable electronic properties of graphene mostly stem from its honeycomb structure and, similarly that the properties of metamaterials crucially depend on their lattice structure, initially I explored the possibility of creating Dirac materials from plasmonic metamaterials and later explored novel properties of natural Dirac materials.

Firstly, in a paper I co-authored [150] it was hypothesised that creating honeycomb arrays of metallic nanoparticles could allow plasmonic metamaterials to replicate some of graphene's renowned properties, creating a tunable Dirac system that supports bosonic excitations. The localised surface plasmons in each nanoparticle were approximated as oscillating point dipoles, which interact with each other through an instantaneous dipole-dipole coupling. The resulting collective plasmon modes that span across the whole system were calculated, and the dispersions obtained for arbitrary dipolar angles. The properties of the resulting Hamiltonian and eigenstates were compared to those of electrons in graphene. At certain dipole polarisations, including with dipoles orientated normal to the plane of the lattice, it was shown that the effective Hamiltonian in the vicinity of the Dirac points describes massless Dirac quasiparticles, with a chiral nature and a Berry phase of π. The resulting massless Dirac bosons will affect the response of the metamaterial to light, and could result in unprecedented conductivity of energy by chiral Dirac surface plasmon polaritons due to the absence of backscattering from smooth potentials. For this to be proven, further work is required to ensure that the surface plasmon polaritons inherit the collective plasmon's properties. Honeycomb arrays of metallic nanoparticles thus represent an interesting avenue for the realization of ultrathin tunable metamaterials where the electromagnetic radiation can be transported effectively by chiral pseudo-relativistic Dirac modes.

Moreover, I have shown that the band structure of these collective modes is tunable with the polarization of the incident light that triggers the CPs, a feature which is not available in real graphene devices. By tilting the dipole polarisation away from normal to the plane, an analogy to strained graphene can be made up to a critical out-of-plane angle where one of the interaction parameters goes to zero leading to the system behaving like a one-dimensional wave guide. Here, the CP spectra is invariant along one direction and presents 'Dirac lines'. By further tilting the dipole polarisation the analogy to graphene breaks down and it is possible to open a gap in the CP spectrum by means of the annihilation of inequivalent Dirac points. Therefore at energies in the vicinity of the Dirac point, where at certain polarisations there is a gap, the metamaterial changes from conducting (transparent) to insulating (opaque). It is also interesting to note that strain leads to dramatic consequences in the bandstructure of natural Dirac materials, and, although I have shown that these can be mimicked by tilting the dipole polarisation in this metamaterial, future research could be conducted into the effect of actual strain on the metamaterial. This could be achieved, for example, by embedding the nanoparticles in an elastic medium.

Additionally, as I have shown a honeycomb arrangement of metallic nanoparticles produces an analogous spectrum to that of strained graphene at certain radiation polarisations, it would be interesting to investigate the effect this has further. There could well be possible realisations of artificial gauge fields or other phenomena similar to those produced by straining graphene, and this medium is advantageous as the method of producing these strain-like phenomena is much more experimentally feasible even at extremes.

A major difference between the plasmonic metamaterial and natural Dirac materials is the nature of the quasiparticles contained within each one: the metamaterial supports bosonic quasiparticles whereas in graphene one considers fermions. Electrons in graphene have an infinite lifetime, whereas the bosonic excitations in the metamaterial can be created and destroyed such that they only have a finite lifetime. This plasmonic damping will limit the experimental observability of the CP dispersion, as it blurs the resonance frequencies. Different damping mechanisms dominate for different sized particles, therefore damping can be minimised by selecting an optimal size. By arranging optimally sized particles such that their interparticle distance maximises the dipolar coupling, the total band width of the CP spectrum can be approximated. I estimate this band width to be sufficiently large when compared to the total broadening due to damping, hence the plasmon excitation is well defined and clearly measurable. However, further calculations are required to verify these estimates.

Due to the ability to design and experimentally realise practically any array, this line of research has a broad scope for future investigations, to determine other periodic structures which may be useful for device applications. The logical first step in this direction was to investigate adaptations of the structure already considered, therefore I next considered the same geometrical lattice but with broken inversion symmetry. To achieve this, specifically, the two sublattices A and B of the honeycomb array were considered to be inequivalent so that they have different natural oscillation frequencies, ω_A and ω_B, respectively. I unveil that the resulting CPs are effectively described as Dirac particles with a gapped linear spectrum. This could allow for the remarkable properties of graphene, such as the high conductivity, to be utilised in devices where a large on/off ratio is required. The effective Hamiltonian describing the system at low energies is a massless Dirac Hamiltonian with additional σ_z terms that open a gap in the CP spectrum. This Hamiltonian, and the chiral nature of the spinor wavefunctions, lead to the bosonic excitations having an energy dependent Berry phase, and other energy dependent properties that could be tuned for different implementations. For any amount of asymmetry between the sublattices there is a gap in the CP spectrum, which increases linearly with increased asymmetry, whilst the individual band widths of the dispersion are greatly decreased with increasing asymmetry. In order for the dispersion to be observed, and for a gap in the spectrum to be perceived, the bandwidth must be greater again than the characteristic blurring due to plasmonic damping. Thus I estimated a limitation in the amount of asymmetry possible for the dispersion to be experimentally observable, but, as before, further work is required to verify this.

As this simple change to the honeycomb lattice has altered the properties of the collective plasmons supported within it, in a way that could possibly be useful for several device applications, it leads one to speculate what the effect of other adaptations might be, which could be explored as future work. Furthermore, although both of the lattices examined so far are based on the honeycomb structure there are infinitely many other possible arrangements of metallic nanoparticles whose properties could be investigated. Honeycomb lattices can be described by two inequivalent sublattices, producing spectra with two modes and two Dirac points in the first Brillouin zone with opposite Berry phase (which may also be energy dependent). Non-honeycomb lattices have been recently explored [151], by shifting the position of one of the sublattices, and Dirac physics has again been discovered. It may be interesting to explore this further by considering completely different lattices, for example ones which can be described by N sublattices (where $N \neq 2$) to see if additional Dirac points can be produced, and study their fundamental properties.

The general form of the effective Hamiltonian that describes CPs in honeycomb arrays of metallic nanoparticles with broken inversion symmetry is not unique to this system. By generalising the Hamiltonian, dispersion and eigenvectors, one can realise properties common to a large number of systems, such as transition metal dichalcogenides and graphene on hexagonal boron nitride. These form a new class of system, with an energy dependent Berry phase, which I denote as Dirac systems with a linear gapped spectrum, due to the fact that without the gap the dispersion would be linear.

The energy dependent chirality and Berry phase of such systems are due to the broken inversion symmetry allowing eigenspinors to have a non-vanishing component out of the $x - y$ plane. Indeed, at the band extrema ($\varepsilon \approx \pm\frac{\Delta}{2}$) the spinor points along $\pm\hat{\mathbf{z}}$, leading to a Berry phase of ≈ 0, whereas at energies much larger than the gap the spinor rotates approximately in the $x{-}y$ plane giving rise to a Berry phase of π like in graphene. The effect the energy dependent eigenspinor orientation has on the quantum transport properties of these systems was explored by considering ballistic tunnelling across a barrier. With high barriers and at high energies, such that the effect of the gap is negligible, the transmission probability resembles that of monolayer graphene, implying that the quasiparticles behave like massless-Dirac particles. However, at energies comparable to the gap size, in the *npn* regime, there can be perfect reflection at normal incidence, which is not possible in graphene. Quite in general, the transmission probability of these systems is energy, barrier height, and gap size dependent, which further broadens the usefulness of Dirac materials in a variety of devices. However, as a general treatment has been taken to allow for the description of several systems, when considering a specific material there may be additional details that should be taken into account to fully outline the transport properties. For example, MoS_2 has a strong spin-orbit coupling which has been neglected in this treatment.

A rational extension of this research was to investigate the concept of Klein tunnelling in Dirac materials with a parabolic gapped spectrum, like biased bilayer graphene, or plasmonic metamaterials containing quasiparticles described by the same Hamiltonian. This represents another material with energy dependent pseudospin orientations and Berry phase, leading to energy dependent transport properties, but the nature of the Hamiltonian describing the system means the energy dependence is quite different. With even the slightest bias, producing a gap in the spectrum, there is no longer perfect reflection at normal incidence for all energies (in the *npn* case) as dictated by Klein tunnelling in conventional bilayer devices, and actually perfect transmission can occur at certain energies, via conventional resonant tunnelling. Some of the transmission peaks at normal incidence are very localised in energy and angle allowing for targeted transmission which may be detectable in angular resolved measurements.

In addition to the areas of future work I have already mentioned, I wish to emphasise another problem which has not been addressed in this thesis. I have assumed all the materials are perfect and have ignored inhomogeneities and any effects of disorder. In the case of graphene, if there are smooth inhomogeneities intervalley scattering remains improbable, but sharp, atomic-scale, inhomogeneities allow for states from different valleys to mix [83]. Furthermore, disorder in metamaterial structures has been seen to introduce effective losses into the system [229], which would affect the observability of the collective plasmon. Therefore the effects of disorder need to be explored further.

Furthermore, as I have shown, plasmonic nanostructures can lead to an enhancement in the local electromagnetic field which can itself lead to an amplification of weak non-linear processes [230]. Non-linear optical effects have been found to increase the usefulness of photonic materials such as: allowing one to control the frequency of laser light; optical signal processing and ultra-fast switching [231]. Due to the fact that these useful non-linear effects can be intensified by using plasmonic structures, it would be interesting to consider the consequences of such effects for the plasmonic cases described in this thesis.

Finally, although I have not specified the particular size of nanoparticles considered in this thesis, I have generally considered the LSPs are generated by radiating metallic nanoparticles with light of visible wavelengths. However, the theory and approximations hold true for all ranges of the electromagnetic spectrum, all be it requiring different materials and dimensions for the metallic nanoparticles. One way of facilitating experimental investigations that are less demanding to prove these concepts is to move to a larger wavelength range, for example microwaves. In this wavelength range the particles would correspondingly be larger therefore they would be easier to manufacture and the required uniformity would require less effort, and not need to be as strict. It would then be possible to make arrays of rods (to ensure the assumption of the dipolar nature of the LSP holds true) whose angles could be controlled by wires.

Bibliography

[1] P. A. M. Dirac *Proc. Roy. Soc. A*, vol. 117, p. 610, 1928.

[2] J. L. Mañes, F. Guinea, and M. A. H. Vozmediano *Phys. Rev. B*, vol. 75, p. 155424, 2007.

[3] K. S. Novoselov *et. al., Science*, vol. 306, p. 666, 2004.

[4] A. K. Geim and K. S. Novoselov *Nature Mat.*, vol. 6, p. 183, 2007.

[5] P. R. Wallace *Phys. Rev.*, vol. 71, p. 622, 1947.

[6] A. H. C. Neto *et. al., Rev. Mod. Phys.*, vol. 81, p. 109, 2009.

[7] D. R. Cooper *et. al., ISRN Cond. Matt. Phys.*, vol. 2012, p. 501686, 2011.

[8] K. S. Novoselov *et al, Nature*, vol. 438, p. 197, 2005.

[9] Y. Zhang *it et. al., Nature*, vol. 438, p. 201, 2005.

[10] V. V. Cheianov and V. I. Falko *Phys. Rev. B*, vol. 74, p. 041403(R), 2006.

[11] M. I. Katsnelson and K. S. Novoselov *Sol. Stat. Comm.*, vol. 143, p. 3, 2007.

[12] S. M. Choi, S. H. Jhi, and Y. W. Son *Phys. Rev. B*, vol. 81, p. 081407(R), 2010.

[13] M. A. Bissett, M. Tsuji, and H. Ago *Phys. Chem. Chem. Phys.*, vol. 16, p. 11124, 2014.

[14] W. L. Barnes, A. Dereux, and T. W. Ebbesen *Nature*, vol. 424, p. 824, (2003).

[15] B. Lamprecht *et. al., Phys. Rev. Lett.*, vol. 84, p. 20, 2000.

[16] T. Klar *et. al., Phys. Rev. Lett.*, vol. 80, p. 4249, 1998.

[17] G. F. Bertsch and R. A. Broglia, *Oscillations in Finite Quantum Systems*. Cambridge, England: Cambridge University Press, 1994.

[18] U. Kreibig and M. Vollmer, *Optical Properties of Metal Clusters*. Berlin: Springer-Verlag, 1995.

[19] T. J. Echtermeyer *et. al., Nature Comm.*, vol. 2, p. 458, 2011.

[20] J. Lin *et. al., Appl. Phys. Lett.*, vol. 102, p. 203109, 2013.

[21] V. G. Veselago *Sov. Phys. Usp.*, vol. 10, p. 509, 1968.

[22] D. R. Smith *et. al., Phys. Rev. Lett.*, vol. 84, p. 4184, 2000.

[23] R. A. Shelby, D. R. Smith, and S. Schultz *Science*, vol. 292, p. 77, 2001.

[24] U. Leonhardt *Science*, vol. 312, p. 1777, 2006.

[25] J. B. Pendry, D. Schurig, and D. R. Smith *Science*, vol. 312, p. 1780, 2006.

[26] D. Schurig *et. al., Science*, vol. 314, p. 977, 2006.

[27] J. B. Pendry *Phys. Rev. Lett.*, vol. 85, p. 3966, 2000.

[28] N. Fang *et. al., Science*, vol. 308, p. 534, 2005.

[29] K. L. Tsakmakidis, A. D. Boardman, and O. Hess *Nature*, vol. 450, p. 397, 2007.

[30] B. Auguié and W. L. Barnes *Phys. Rev. Lett.*, vol. 101, p. 143902, 2008.

[31] M. Quinten *et. al., Opt. Lett.*, vol. 23, p. 1331, 1998.

[32] J. R. Krenn *et. al., Phys. Rev. Lett.*, vol. 82, p. 2590, 1999.

[33] M. L. Brongersma, J. W. Hartman, and H. A. Atwater *Phys. Rev. B*, vol. 62, p. R16356, 2000.

[34] S. A. Maier *et. al., Phys. Rev. B*, vol. 65, p. 193408, 2002.

[35] N. Félidj *et. al., Phys. Rev. B*, vol. 66, p. 245407, 2002.

[36] S. A. Maier *et. al., Nature Mat.*, vol. 2, p. 229, 2003.

[37] S. Y. Park and D. Stroud *Phys. Rev. B*, vol. 69, p. 125418, 2004.

[38] W. H. Weber and G. W. Ford *Phys. Rev. B*, vol. 70, p. 125429, 2004.

[39] L. A. Sweatlock *et. al., Phys. Rev. B*, vol. 71, p. 235408, 2005.

[40] A. F. Koenderink and A. Polman *Phys. Rev. B*, vol. 74, p. 033402, 2006.

[41] A. F. Koenderink *Nano. Lett.*, vol. 9, p. 4228, 2009.

[42] D. Han *et. al., Phys. Rev. Lett.*, vol. 102, p. 123904, 2009.

[43] D. K. Polyushkin *et. al., Nano. Lett.*, vol. 11, p. 4718, 2011.

[44] N. W. Ashcroft and N. D. Mermin, *Solid State Physics*. CBS Publishing ASIA LTD, 1976.

[45] M. Born and E. Wolf, *Principles of optics: electromagnetic theory of propagation, interference and diffraction of light*. Cambridge, England: Cambridge University Press, 2002.

[46] S. A. Maier, *Plasmonics: Fundamentals and Applications*. Berlin: Springer-Verlag, 2007.

[47] K. Kneipp *et. al., Phys. Rev. Lett.*, vol. 78, p. 1667, 1997.

[48] W. Rechberger *Optics Communications*, vol. 220, p. 137, 2003.

[49] J. M. Pitarke *et. al., Rep. Prog. Phys.*, vol. 70, p. 1, 2007.

[50] K. H. An, M. Shtein, and K. P. Pipe *Optics Express*, vol. 18, p. 4041, 2010.

[51] Q. C. Sun *et. al., Nano. Letts.*, vol. 14, p. 101, 2014.

[52] F. J. G. de Abajo *Reviews of Modern Physics*, vol. 79, p. 1267, 2007.

[53] J. C. van de Hulst, *Light Scattering by Small Particles*. Dover, England: Dover Publications, Inc., 1981.

[54] D. Sarid and W. Challener, *Modern Introduction to surface Plasmons - Theory, Mathematica Modelling and Applications*. Cambridge, England: Cambridge University Press, 2010.

[55] C. Kittel, *Introduction to Solid State Physics - 6th Edition*. Wiley, 1986.

[56] J. M. Ziman, *Elements of Advanced Quantum Theory*. Cambridge, England: Cambridge University Press, 1969.

[57] J. D. Jackson, *Classical Electrodynamics, 3rd edition*. John Wiley and Sons, 1998.

[58] B. Hecht *et. al., Phys. Rev. Lett.*, vol. 77, p. 1889, 1996.

[59] J. Pendry *Science*, vol. 285, p. 1687, 1999.

[60] E. Kretschmann and H. Raether *Z. Naturforsch A*, vol. 23, p. 2135, 1968.

[61] A. Otto *Z. Phys.*, vol. 216, p. 398, 1968.

[62] R. H. Ritchie *et. al., Phys. Rev. Lett.*, vol. 21, p. 1530, 1968.

[63] J. Moreland, A. Adams, and P. K. Hansma *Phys. Rev. B*, vol. 25, p. 2297, 1982.

[64] P. T. Worthing and W. L. Barnes *Appl. Phys. Lett.*, vol. 79, p. 3035, 2001.

[65] Bohren and Huffman, *Absorption and Scattering of light by small particles*. John Wiley and Sons, 1983.

[66] L. A. Sweatlock *et. al., Phys. Rev. B*, vol. 71, p. 235408, 2005.

[67] A. O. Pinchuk and G. C. Schatz *Materials Science and Engineering B*, vol. 149, p. 251, 2008.

[68] R. F. W. Pease, *Electron Beam Lithography*. Taylor and Francis Online, 2006.

[69] W. A. Murray and W. L. Barnes *Adv. Mat.*, vol. 19, p. 3771, 2007.

[70] "Materials views: The holy grail in plasmonics, the lycurgus cup goes nano, http://www.materialsviews.com/the-holy-grail-in-plasmonics-the-lycurgus-cup-goes-nano/ [accessed 10/02/2015]."

[71] E. Ringe *et. al., J. Phys. Chem. C*, vol. 114, p. 12511, 2010.

[72] G. Mie *Annalen der Physik*, vol. 330(3), p. 377, 1908.

[73] J. C. Weeber *et. al., Phys. Rev. B*, vol. 60, p. 9061, 1999.

[74] M. Quinten and U. Kreibig *Appl. Opt.*, vol. 32, p. 6173, 1993.

[75] H. J. F. Jansen, "Electromagnetic theory lecture notes, oregon state university physics department - www.physics.orst.edu/ leeys/courses/ph633/emch9.pdf [accessed 29/05/2015]."

[76] L. Gunnarsson *et. al., J. Phys. Chem. B*, vol. 109, p. 1079, 2005.

[77] Y. Yamamoto, "Quantum optics and measurements lecture notes, stanford university physics department - web.stanford.edu/ rsasaki/ap387/chap6 [accessed 05/06/2015]."

[78] G. B. Arfken and H. J. Weber, *Mathematical Methods For Physicists, International Edition, Fourth Edition*. California: Academic Press, 1966.

[79] N. J. Halas *et. al., Chem. Rev.*, vol. 111, p. 3913, 2011.

[80] S. M. Nie and S. R. Emery *Science*, vol. 275, p. 1102, 1997.

[81] G. P. Srivastava, *The Physics of Phonons*. Adam Hilger, 1990.

[82] W. Gotschy *et. al., Appl. Phys. B*, vol. 63, p. 381, 1996.

[83] M. I. Katsnelson, *Graphene - Carbon in Two Dimensions*. Cambridge, England: Cambridge University Press, 2012.

[84] "www.nobelprize.org/nobel_prizes/physics/laureates," [Accessed 13/04/2015].

[85] P. Y. Huang *et. al., Nature*, vol. 469, p. 389, 2011.

[86] S. D. Sarma *et. al., Reviews of Modern Physics*, vol. 83, 2011.

[87] M. I. Katsnelson, K. S. Novoselov, and A. K. Geim *Nature Physics*, vol. 2, p. 620, 2006.

[88] R. Saito, G. Dresselhaus, and M. S. Dresselhaus, *Physical Properties of Carbon Nanotubes*. Imperial College Press, 2004.

[89] A. I. M. Rae, *Quantum Mechanics - 5th Edition*. Taylor and Francis Group, 2008.

[90] R. J. A. Lambourne, *Relativity, Gravitation and Cosmology - The Open University*. Cambridge, England: Cambridge University Press, 2010.

[91] J. C. Slonczewski and P. R. Weiss *Phys. Rev.*, vol. 109, p. 272, 1958.

[92] G. W. Semenoff *Phys. Rev. Lett.*, vol. 53, p. 2449, 1984.

[93] F. D. M. Haldane *Phys. Rev. Lett.*, vol. 61, p. 2015, 1988.

[94] K. S. Novoselov *et. al., Science*, vol. 315, p. 1379, 2007.

[95] S. V. Vonsovsky and M. I. Katsnelson, *Quantum Solid State Physics*. Springer, 1989.

[96] M. J. Allen, V. C. Tung, and R. B. Kaner *Chem. Rev.*, vol. 110, p. 132, 2009.

[97] M. Berry *Proc. R. Soc. A*, vol. 392, p. 45, 1984.

[98] J. J. Sakurai, *Modern Quantum Mechanics*. Reading, England: Addison-Wesley, 1994.

[99] E. Mariani, A. J. Pearce, and F. von Oppen *Phys. Rev. B*, vol. 86, p. 165448, 2012.

[100] Y. Zheng and T. Ando *Phys. Rev. B*, vol. 65, p. 245420, 2002.

[101] N. M. R. Peres, F. Guinea, and A. H. C. Neto *Phys. Rev. B*, vol. 73, p. 125411, 2006.

[102] A. H. C. Neto, F. Guinea, and N. M. R. Peres *Phys. Rev. B*, vol. 73, p. 205408, 2006.

[103] G. P. Mikitik and Y. V. Sharlai *Phys. Rev. Lett.*, vol. 82, p. 2147(03), 1999.

[104] S. G. Sharapov, V. P. Gusynin, and H. Beck *Phys. Rev. B*, vol. 69, p. 075104, 2004.

[105] T. Ando, T. Nakanishi, and R. Saito *J. Phys. Soc. Japan*, vol. 67, p. 2857, 1998.

[106] Y. B. Zhang *et al, Nature*, vol. 438, p. 201, 2005.

[107] O. Klein *Zeitschrift für Physik*, vol. 53, p. 3, 1929.

[108] E. Fradkin *Phys. Rev. B*, vol. 33, p. 3263, 1989.

[109] R. K. Su, G. C. Siu, and X. Chou *J. Phys. A*, vol. 26, p. 1001, 1993.

[110] N. Dombey and A. Calogeracos *Phys. Rep.*, vol. 315, p. 41, 1999.

[111] A. Calogeracos and N. Dombey *Contemp. Phys.*, vol. 40, p. 313, 1999.

[112] P. Krekora, Q. Su, and R. Grobe *Phys. Rev. Lett.*, vol. 92, p. 040406, 2004.

[113] K. S. Novoselov *et al, Nature Phys.*, vol. 2, p. 177, 2006.

[114] E. McCann and V. I. Fal'ko *Phys. Rev. Lett.*, vol. 96, p. 086805, 2006.

[115] F. Guinea, A. H. C. Neto, and N. M. R. Peres *Phys. Rev. B*, vol. 73, p. 245426, 2006.

[116] J. Nilsson *et. al., Phys. Rev. B*, vol. 78, p. 045405(07), 2008.

[117] W. W. Toy, M. S. Dresselhaus, and G. Dresselhaus *Phys. Rev. B*, vol. 15, p. 4077(04), 1977.

[118] R. E. Doezema *et. al., Phys. Rev. B*, vol. 19, p. 4224(04), 1979.

[119] J. R. Schrieffer and P. A. Wolff *Phys. Rev.*, vol. 149, p. 491(09), 1966.

[120] M. I. Katsnelson *Eur. Phys. J. B*, vol. 52, p. 151, 2006.

[121] I. Snyman and C. W. J. Beenakker *Phys. Rev. B*, vol. 75, p. 045322, 2007.

[122] M. Koshino and T. Ando *Phys. Rev. B*, vol. 73, p. 245403, 2006.

[123] M. I. Katsnelson *Phys. Rev. B*, vol. 76, p. 073411, 2007.

[124] J. Cserti *Phys. Rev. B*, vol. 75, p. 033405, 2007.

[125] J. Cserti, A. Csordas, and G. David *Phys. Rev. Lett.*, vol. 99, p. 066802, 2007.

[126] K. Kechedzhi *et. al., Phys. Rev. Lett.*, vol. 98, p. 176806, 2007.

[127] S. Adam and S. D. Sarma *Phys. Rev. B*, vol. 77, p. 115436, 2008.

[128] S. D. Sarma, E. H. Hwang, and E. Rossi *Phys. Rev. B*, vol. 81, p. 161407(R), 2010.

[129] M. Trushin *et. al., Phys. Rev. B*, vol. 82, p. 155308, 2010.

[130] E. H. Hwang and S. D. Sarma *Phys. Rev. B*, vol. 82, p. 081409, 2010.

[131] K. S. Novoselov *et. al., Nature Phys.*, vol. 2, p. 177, 2006.

[132] J. B. Oostinga *et. al., Nature Mater.*, vol. 7, p. 151, 2007.

[133] E. V. Castro *et al, Phys. Rev. Lett.*, vol. 99, p. 216802, 2007.

[134] R. V. Gorbachev *et. al., Phys. Rev. Lett.*, vol. 98, p. 176805, 2007.

[135] S. V. Morozov *et. al., Phys. Rev. Lett.*, vol. 100, p. 016602, 2008.

[136] B. E. Feldman, J. Martin, and A. Yacoby *Nature Phys.*, vol. 5, p. 889, 2009.

[137] S. Xiao *et. al., Phys. Rev. B*, vol. 82, p. 041406, 2010.

[138] M. Kindermann, B. Uchoa, and D. L. Miller *Phys. Rev. B*, vol. 86, p. 115415, 2012.

[139] R. Quhe *et. al, NPG Asia Materials*, vol. 4, p. e6, 2012.

[140] Z. Y. Zhu, Y. C. Cheng, and U. Schwingenschlögl *Phys. Rev. B*, vol. 84, p. 153402(10), 2011.

[141] S. Lebègue and O. Eriksson *Phys. Rev. B*, vol. 79, p. 115409(03), 2009.

[142] A. Splendiani *Nano Lett.*, vol. 10, p. 1271, 2010.

[143] K. F. Mak *et al, Phys. Rev. Lett.*, vol. 105, p. 136805, 2010.

[144] D. Xiao *et al, Phys. Rev. Lett.*, vol. 108, p. 196802, 2012.

[145] H. Zeng *et. al., Nature Nano*, vol. 7, p. 490(08), 2012.

[146] K. F. Mak *et. al., Nature Nano*, vol. 7, p. 494(08), 2012.

[147] A. Ayari *et. al., J. Appl. Phys.*, vol. 101, p. 014507, 2007.

[148] H. Wang *et. al., Nano Letters*, vol. 12, p. 4674, 2012.

[149] B. Radisavljevic *et. al., Nature Nano*, vol. 6, p. 147(03), 2011.

[150] G. Weick, C. Woollacott, O. H. W. L. Barnes, and E. Mariani *Phys. Rev. Lett.*, vol. 110, p. 106801, 2013.

[151] T. J. Sturges, C. Woollacott, G. Weick, and E. Mariani *IOP 2D Mater.*, vol. 2, p. 014008, 2015.

[152] K. T. Carron *et. al., J. Opt. Soc. Am. B*, vol. 3, p. 430, 1986.

[153] S. Zou, N. Janel, and G. C. Schatz *J. Chem. Phys.*, vol. 120, p. 10871, 2004.

[154] V. G. Kravets, F. Schedin, and A. N. Grigorenko *Phys. Rev. Lett.*, vol. 101, p. 087403, 2008.

[155] Y. Chu *et. al., Appl. Phys. Lett.*, vol. 93, p. 181108, 2008.

[156] D. Han *et. al., Phys. Rev. Lett.*, vol. 102, p. 123904, 2009.

[157] F. D. M. Haldane and S. Raghu *Phys. Rev. Lett.*, vol. 100, p. 013904, 2008.

[158] O. Peleg *et. al., Phys. Rev. Lett.*, vol. 98, p. 103901, 2007.

[159] R. A. Sepkhanov, Y. B. Bazaliy, and C. W. J. Beenakker *Phys. Rev. A*, vol. 75, p. 063813, 2007.

[160] S. R. Zandbergen and M. J. A. de Dood *Phys. Rev. Lett.*, vol. 104, p. 043903, 2010.

[161] J. Bravo-Abad, J. D. Joannopoulos, and M. Soljacić *Proc. Nat. Acad. Sci. USA*, vol. 109, p. 9761, 2012.

[162] D. Torrent and J. Sánchez-Dehesa *Phys. Rev. Lett.*, vol. 108, p. 174301, 2012.

[163] L. Tarruell *et. al., Nature*, vol. 483, p. 302, 2012.

[164] J. Mei *et. al., Phys. Rev. B*, vol. 86, p. 035141, 2012.

[165] K. Kechedzhi *et. al., Phys. Rev. Lett.*, vol. 98, p. 176806, 2007.

[166] P. Rakyta, A. Kormányos, and J. Cserti *Phys. Rev. B*, vol. 82, p. 113405, 2010.

[167] A. Kawabata and R. Kubo *J. Phys. Soc. Jpn.*, vol. 21, p. 1765, 1966.

[168] C. Yannouleas and R. A. Broglia *Ann. Phys. (NY)*, vol. 217, p. 105, 1992.

[169] R. A. Molina, D. Weinmann, and R. A. Jalabert *Phys. Rev. B*, vol. 65, p. 155427, 2002.

[170] L. G. Gerchikov, C. Guet, and A. N. Ipatov *Phys. Rev. A*, vol. 66, p. 053202, 2002.

[171] G. Weick *et. al., Phys. Rev. B*, vol. 72, p. 115410, 2005.

[172] G. Weick *et. al., Phys. Rev. B*, vol. 74, p. 165421, 2006.

[173] G. Weick *et. al., Eur. Phys. Lett.*, vol. 78, p. 27002, 2007.

[174] C. Seoanez *et. al., Eur. Phys. J. D*, vol. 44, p. 351, 2007.

[175] G.Weick *et. al., Eur. Phys. J. D*, vol. 44, p. 359, 2007.

[176] I. M. Lifshitz *Sov. Phys. JETP*, vol. 11, p. 1130, 1960.

[177] G. Montambaux *et. al., Phys. Rev. B*, vol. 80, p. 153412, 2009.

[178] G. Montambaux *et. al., Eur. Phys. J. B*, vol. 72, p. 509, 2009.

[179] M. Bellec *et. al., Phys. Rev. Lett.*, vol. 110, p. 033902, 2013.

[180] M. Bellec *et. al., Phys. Rev. B.*, vol. 115, p. 115437, 2013.

[181] L. M. Woods and G. D. Mahan *Phys. Rev. B*, vol. 61, p. 10651, 2000.

[182] H. Suzuura and T. Ando *Phys. Rev. B*, vol. 65, p. 235412, 2002.

[183] J. Crowell and R. H. Smith *Phys. Rev.*, vol. 172, p. 436, 1968.

[184] O. Hess *et. al., Nature Mat.*, vol. 11, p. 573, 2012.

[185] A. Brandstetter-Kunc *et. al., Phys. Rev. B*, vol. 91, p. 035431, 2015.

[186] G. Weick and E. Mariani *Eur. Phys. J. B*, vol. 88, p. 7, 2015.

[187] J. Renger *et. al., Phys. Rev. Lett.*, vol. 103, p. 266801, 2009.

[188] J. N. R. A. Sepkhanov and C. W. J. Beenakker *Phys. Rev. B*, vol. 78, p. 045122, 2008.

[189] X. Wu *et. al., Phys. Rev. Lett.*, vol. 98, p. 136801, 2007.

[190] F. V. Tikhonenko *et. al., Phys. Rev. Lett.*, vol. 103, p. 226801, 2009.

[191] D. Soriano and J. Fernández-Rossier *Phys. Rev. B*, vol. 85, p. 195433, 2012.

[192] G. Giovannetti *et al, Phys. Rev. B*, vol. 76, p. 073103, 2007.

[193] E. Doni and G. P. Parravicini *Nuovo Cimento B*, vol. 64, p. 117, 1969.

[194] D. Xiao *et. al., Phys. Rev. Lett.*, vol. 108, p. 196802, 2012.

[195] A. Kormányos *et. al., Phys. Rev. B*, vol. 88, p. 045416, 2013.

[196] E. Cappelluti *et. al., Phys. Rev. B*, vol. 88, p. 075409, 2013.

[197] I. Herbut *Phys. Rev. B*, vol. 83, p. 245445, 2011.

[198] C. Woollacott, A. Cope, and E. Mariani *in preparation*.

[199] M. I. Katsnelson *Eur. Phys. J. B*, vol. 51, p. 157, 2006.

[200] K. S. Novoselov *et al, Proc. Natl. Acad. Sci. U.S.A.*, vol. 102, p. 10451, 2005.

[201] C. Lee *et al, Science*, vol. 328, p. 76, 2010.

[202] A. F. Young and P. Kim *Nature Physics*, vol. 5, p. 222, 2009.

[203] R. Landauer *J. Phys. Condens. Mat.*, vol. 1, p. 8099, 1989.

[204] A. J. Pearce, F. Cavaliere, and E. Mariani *J. Phys.: Condens. Matter*, vol. 25, p. 375301, 2013.

[205] E. B. Sonin *Phys. Rev. B*, vol. 79, p. 195438, 2009.

[206] F. L. Pedrotti and L. S. Pedrotti, *Introduction to Optics - Second Edition*. Prentice-Hall, 1993.

[207] W. van Roosbroeck *Phys. Rev.*, vol. 139, p. A1702, 1995.

[208] F. Capasso, K. Mohammed, and A. Y. Cho *IEEE Journal of Quantum Electronics*, vol. QE-22, p. 99, 1986.

[209] C. H. Lewenkopf, E. R. Mucciolo, and A. H. C. Neto *Phys. Rev. B*, vol. 77, p. 081410(R), 2008.

[210] B. Radisavljevic *et al, Nature Nanotech.*, vol. 6, p. 147, 2011.

[211] Y. Yoon, K. Ganapathi, and S. Salahuddin *Nano Lett.*, vol. 11, p. 3768, 2011.

[212] H. Schomerus *Phys. Rev. B*, vol. 82, p. 165409, 2010.

[213] H. Shioya *et al, Appl. Phys. Lett.*, vol. 100, p. 033113, 2012.

[214] Y. Zhang *et al, Nature*, vol. 459, p. 820, 2009.

[215] S. B. Trickey *et al, Phys. Rev. B*, vol. 45, p. 4460, 1992.

[216] S. Latil and L. Henrard *Phys. Rev. Lett.*, vol. 97, p. 036803, 2006.

[217] H. Min *et al, Phys. Rev. B*, vol. 75, p. 155115, 2007.

[218] K. Yoshizawa, T. Kato, and T. Yamabe *J. Chem. Phys.*, vol. 105, p. 2099, 1996.

[219] C. L. Lu *et al, Phys. Rev. B*, vol. 73, p. 144427, 2006.

[220] J. Nilsson *et al, Phys. Rev. B*, vol. 73, p. 214418, 2006.

[221] M. Koshino and T. Ando *Phys. Rev. B*, vol. 73, p. 245403, 2006.

[222] B. Partoens and F. M. Peeters *Phys. Rev. B*, vol. 74, p. 075404, 2006.

[223] E. McCann *Phys. Rev. B*, vol. 74, p. 161403, 2006.

[224] T. Ohta *et al, Science*, vol. 313, p. 951, 2006.

[225] P. San-Jose *et. al., Phys. Rev. Lett.*, vol. 102, p. 247204, 2009.

[226] J. Tworzydlo *et al, Phys. Rev. Lett.*, vol. 96, p. 246802, 2006.

[227] S. Park *et. al., Phys. Rev. B*, vol. 84, p. 235432, 2011.

[228] A. Varlet *et. al., Phys. Rev. Lett.*, vol. 113, p. 116601, 2014.

[229] T. Hand *et. al., Appl. Phys. Letts.*, vol. 91, p. 162907, 2017.

[230] M. Kauranen and A. V. Zayats *Nature Photonics*, vol. 6, p. 737, 2012.

[231] R. W. Boyd, *Nonlinear Optics - 3rd Edition*. Academic, 2008.